STUDY OF MICROSTRUCTURE AND MICROTEXTURE DURING THERMO-MECHANICAL PROCESSING IN ADVANCED STEELS USING EXPERIMENTAL AND COMPUTATIONAL METHODS

By

Manmath Kumar Dash

Enrolment No.: **ENGG02201418008**

Indira Gandhi Centre for Atomic Research

Kalpakkam 603102, India

A thesis submitted to the

Board of Studies in Engineering Sciences

In partial fulfillment of requirements

for the Degree of

DOCTOR OF PHILOSOPHY

of

HOMI BHABHA NATIONAL INSTITUTE

December 2018

Homi Bhabha National Institute

Recommendations of the Viva Voce Committee

As members of the Viva Voce Committee, we certify that we have read the dissertation prepared by Mr. Manmath Kumar Dash entitled "**Study of Microstructure and Microtexture during Thermo-mechanical processing in Advanced Steels using Experimental and Computational Methods**" and recommend that it may be accepted as fulfilling the thesis requirement for the award of Degree of Doctor of Philosophy.

Chairman – Prof. B. K. Panigrahi	Date: 24/09/19
Guide / Convener – Prof. Saroja Saibaba	Date: 24/09/2019
Examiner - Prof. Indradev Samajdar	Date: 24/09/2019
Member 1- Prof. M. Vasudevan	Date: 24/09/2019
Member 2- Prof. A. Nagesha	Date: 24.9.2019
Technology Advisor- Dr. R. Mythili	Date: 24/09/2019

Final approval and acceptance of this thesis is contingent upon the candidate's submission of the final copies of the thesis to HBNI.

I/We hereby certify that I/we have read this thesis prepared under my/our direction and recommend that it may be accepted as fulfilling the thesis requirement.

Date: 24/09/2019

Place: IGCAR, Kalpakkam

Signature of Guide

STATEMENT BY AUTHOR

This dissertation has been submitted in partial fulfillment of requirements for an advanced degree at Homi Bhabha National Institute (HBNI) and is deposited in the Library to be made available to borrowers under rules of the HBNI.

Brief quotations from this dissertation are allowable without special permission, provided that accurate acknowledgement of source is made. Requests for permission for extended quotation from or reproduction of this manuscript in whole or in part may be granted by the Competent Authority of HBNI when in his or her judgment the proposed use of the material is in the interests of scholarship. In all other instances, however, permission must be obtained from the author.

Manmath Kumar Dash

Manmath Kumar Dash

DECLARATION

I, hereby declare that the investigation presented in the thesis has been carried out by me. The work is original and has not been submitted earlier as a whole or in part for a degree/diploma at this or any other Institution/University.

Manmath Kumar Dash

List of Publications Arising from Thesis

1. Journal

1. Study of crystallographic texture evolution during high-temperature deformation of 18Cr-ODS ferritic steel based on plasticity assessment, Manmath Kumar Dash, R. Mythili, Rahul John, S. Saroja and Arup Dasgupta, *Microscopy and Microanalysis* (2019), 1–6.
   DOI: 10.1017/S1431927619014703
2. EBSD study on processing domain parameters of oxide dispersion strengthened 18Cr ferritic steel, Manmath Kumar Dash, S. Saroja, Rahul John, R. Mythili and Arup Dasgupta, *Journal of Materials Engineering and Performance* 28 (2019) 263–272.
   DOI: 10.1007/s11665-018-3806-8
3. Microstructure and mechanical properties of oxide dispersion strengthened 18Cr-ferritic steel consolidated by spark plasma sintering, Manmath Kumar Dash, R. Mythili, Rahul Ravi, T. Sakthivel, Arup Dasgupta, S. Saroja and S. R. Bakshi, *Materials Science & Engineering A* 736 (2018) 137–147.
   DOI: 10.1016/j.msea.2018.08.093.
4. Effect of annealing treatment on Σ3-type CSL boundaries and its interactions in 304HCu grade austenitic stainless steel, Manmath Kumar Dash, R. Mythili, Arup Dasgupta and S. Saroja, *Metallurgical and Materials Transactions A* 49 (7) (2018) 2843-2853.
   DOI: 10.1007/s11661-018-4613-4
5. Five-parameter grain boundary determination in annealed ferrite structure using electron backscatter diffraction and serial sectioning technique, Manmath Kumar Dash, T. Karthikeyan and S. Saroja, *Trans Indian Inst Met* 70 (1) (2017) 133-143.
   DOI: 10.1007/s12666-016-0868-x.
6. Influence of Texture on Deformation Mechanism of Hot Extruded Oxide Dispersion Strengthened 18Cr Ferritic Steel, Manmath Kumar Dash, R. Mythili, Arup Dasgupta and S. Saroja, *to be communicated*.
7. Evaluation of Deformation and Recrystallization Behavior in Oxide Dispersion Strengthened 18Cr Ferritic Steel, Manmath Kumar Dash, R Mythili, Haraprasanna Tripathy, Saroja Saibaba and Arup Dasgupta, *to be communicated*.

2. Conference Proceedings

1. Evaluation of interface boundaries in oxide dispersion strengthened 18Cr ferritic steel, Manmath Kumar Dash, R. Mythili, Arup Dasgupta and S. Saroja, AIP Conference Proceedings 2115, 030579 (2019).
   DOI: 10.1063/1.5113418
2. Optimization of consolidation parameters of 18Cr-ODS ferritic steel through microstructural and microtexture characterization, Manmath Kumar Dash, R. Mythili, Arup Dasgupta and S. Saroja, AIP Conference Proceedings 1942, 140063 (2018).
   DOI: 10.1063/1.5029194
3. Plasticity assessment based on Schmid factor in deformed 9Cr-1Mo steel, Manmath Kumar Dash, T. Karthikeyan and S. Saroja, Advanced Materials Proceedings, 2017, 2(5), 304-309.
   DOI: 10.5185/amp.2017/505
4. Texture evolution during cold rolling and subsequent annealing in 18%-Cr ODS steel, Manmath Kumar Dash, T. Karthikeyan, Arup Dasgupta and S. Saroja, International Conference on Electron Microscopy and Allied Techniques, EMSI-2017, Mahabalipuram.
   ISBN 978 81 933428 1 7, pp. 6-9.

3. Conference Presentations

1. Consolidation characteristics of 18Cr ODS ferritic steel by spark plasma sintering, Manmath Kumar Dash, R. Mythili, Rahul Ravi, T. Sakthivel, Arup Dasgupta, S. Saroja, Srinivasa Rao Bakshi, International conference on electron microscopy, EMSI-2018, Bhubaneswar.
2. Study of kinetics of secondary phase precipitation in 18Cr ferritic steel using JMatPro@ simulation, Manmath Kumar Dash, R. Mythili, Arup Dasgupta, S. Saroja, RSM-MSENM-2018, Kalpakkam.

(Manmath Kumar Dash)

List of Other Publications during Ph.D.

1. Journal

1. Creep Deformation and Rupture Behavior of P92 Steel Weld Joint Fabricated by NG-TIG Welding Process, T Sakthivel, G Sasikala, Manmath Kumar Dash, P S Rao, *Journal of Materials Engineering and Performance* (2019), 1-15.
   DOI: 10.1007/s11665-019-04157-1
2. Weld overlay coating of Inconel 617M on type 316L stainless steel by cold metal transfer process, Paulson Varghese, E. Vetrivendan, Manmath Kumar Dash, S. Ningshen, M. Kamaraj, U. Kamachi Mudali, *Surface & Coatings Technology* 357 (2018), 1004-1013.
   DOI: 10.1016/j.surfcoat.2018.10.073
3. EBSD based studies on various modes of cyclic deformation at 923 K in a type 316LN stainless steel, Aritra Sarkar, Manmath Kumar Dash, Nagesha, Arup Dasgupta, Materials Science & Engineering A 723 (2018), 229-237.
   DOI: 10.1016/j.msea.2018.02.101
4. Effect of long-term thermal exposures on microstructure and impression creep in 304HCu Grade austenitic stainless steel, Manmath Kumar Dash, T. Karthikeyan, R. Mythili, V.D. Vijayanand and S. Saroja, *Metallurgical and Materials Transactions A* 48 (2017), 4883-4894.
   DOI: 10.1007/s11661-017-4260-1
5. Effect of prior-austenite grain refinement on microstructure, mechanical properties and thermal embrittlement of 9Cr-1Mo-0.1C steel, T Karthikeyan, Manmath Kumar Dash, R Mythili, S Panneer Selvi, A Moitra, S Saroja, *Journal of Nuclear Material* 494 (2017) 260-277.
   DOI: 10.1016/j.jnucmat.2017.07.019
6. Estimation of martensite feature size in a low-carbon alloy steel by microtexture analysis of boundaries, T. Karthikeyan, Manmath Kumar Dash, S. Saroja and M. Vijayalakshmi, *Micron* 68 (2015), 77–90.
   DOI: 10.1016/j.micron.2014.09.008

2. Conference Presentations

1. Microstructural evolution in Spark Plasma Sintered 9Cr - ZrO_2 dispersion strengthened steel with prolonged high temperature exposure, Raghavendra K. G., Arup Dasgupta,

Manmath Kumar Dash, Karthiselva N. S., Jayasankar V and Srinivasa Rao Bakshi, International conference on electron microscopy, EMSI-2018, Bhubaneswar.

2. EBSD Microtexture analysis of tempered martensite microstructure of steel to predict Prior-Austenite, T. Karthikeyan, Manmath Kumar Dash, S. Saroja, and M. Vijayalakshmi, International conference on electron microscopy, EMSI-2015, Mumbai.

(Manmath Kumar Dash)

Acknowledgements

This research work was made possible due to sustained encouragement and amicable work environment at Indira Gandhi Centre for Atomic Research, and I am thankful for the opportunity to pursue my Ph.D study under HBNI.

I am extremely grateful to my research supervisor and mentor Prof. Saroja Saibaba, Associate Director, Materials Characterization Group for providing guidance, care and continuous encouragement during arduous period of research progress. I thank Prof. Saroja Saibaba for her inputs in identifying a challenging problem for the research work and for her unwavering support during difficult times. I got highly benefited by her teaching and through interesting discussions on the thesis work.

I am delighted to record my gratitude to my former and present Doctoral Committee members Prof. K. Laha, Dr. T. Karthikeyan, Prof. B. K. Panigrahi, Prof. M. Vasudevan, Dr. A. Nagesha and Dr. R. Mythili for their kind advice and valuable suggestions at various stages during the course of the work.

I sincerely thank Dr. R. Mythili for sparing her valuable time for critical reading of the thesis and for several discussions to bring out the thesis in the present form. Also, I express my sincere gratitude to Dr. R. Mythili, SAMS for her words of encouragement and insulating me from various upkeep activities of the lab, so that I could complete the thesis writing in time.

This research work is largely based on SEM-EBSD characterization, and I am very grateful in acknowledging Dr. T. Karthikeyan for teaching me SEM-EBSD operation during initial days. I take this opportunity to sincerely thank Dr. Arup Dasgupta, Head, SAMS, and my colleagues Dr. Chanchal Ghosh, Shri. Pradyumna Kumar Parida and Ms. Alphy George for being kind, approachable and earnestly clearing my doubts in the subjects through debate and discussion.

I thank Prof. A. K. Bhaduri, Director, IGCAR, Prof. G. Amarendra, Director, Metallurgy and Materials Group, Dr. Shaju K. Albert, Associate Director, Materials Engineering Group, and Dr. S. Raju, Head, Physical Metallurgy Division for their motivation and support during the entire course of the work.

I wish to express my heartfelt thanks to Dr. K. Jayasankar from IMMT, Bhubaneswar, Prof. B. S. Murty, Prof. Srinivasa Rao Bakshi, Mr. Rahul John, Mr. Rahul Ravi from IIT-Madras, Chennai, Dr. Hara Prasanna Tripathy, Mr. T. Sakthivel, Dr. David Vijayanand from MMG, IGCAR and Dr. V. Srihari from RRCAT, Indore for providing vital experimental support as and when required at different stages of this work.

I kindly acknowledge Mr. Raj Narayan Hajra, Mrs. T. Ezhilarasi, Dr. G. Thirupathi, Mr. M. Sivakumar, Mr. A. Saikumaran, Ms. B. R. Vaishnavi Krupa and other PMD colleagues, whose support has directly and indirectly helped me to reach this far.

My thanks are also due to NFC, Hyderabad for providing the steel used in this study. I also acknowledge the use of experimental facilities at the UGC-DAE consortium.

I wish to acknowledge my beloved parents, sister and brother for their aspirations for pursuing my Ph. D. degree, and my adorable ***Ganesh Ji*** for cheerfully sustaining me in the process.

Manmath Kumar Dash

CONTENTS

Synopsis

List of Figures

List of Tables

List of Abbreviations and General Symbols

Chapter 1

Introduction **1**

1.1. Selection of Radiation Resistant High Temperature Materials 1

1.2. Development of ODS Ferritic Steels 3

1.3. Status of Development of High (>12%) Cr ODS Steel 5

1.4. Fabrication of ODS Ferritic Steels 7

1.5. Anisotropy in High (>12%) Cr ODS Ferritic Steel 9

1.5.1. Cause of Anisotropy in Hot Extruded High (>12%) Cr Ferritic Steel 9

1.5.2 Methods to Overcome Anisotropy 10

1.6. Electron Backscatter Diffraction (EBSD) Characterization of ODS Steels 14

1.7. Scope of the Thesis 15

1.8. Organization of the Thesis 15

Chapter 2

Experimental Details **19**

2.1. Powder Synthesis and Consolidation 20

2.1.1. Mechanical Alloying 20

2.1.2. Cold Isostatic Pressing (CIP) Followed by Sintering 20

2.1.3. CIP Followed by Hot Isostatic Pressing (HIP) 22

2.1.4. Spark Plasma Sintering (SPS) 22

2.1.5. Hot Extrusion (HE) 24

2.2. Processing Treatments 24

2.3. Characterization 27
2.3.1. Specimen Preparation 27
2.3.2. Scanning Electron Microscopy (SEM) 27
2.3.3. Electron Backscatter Diffraction (EBSD) 28
2.3.4. Synchrotron XRD 30
2.3.5 Differential Scanning Calorimetry (DSC) 30
2.4. Evaluation of Mechanical Properties 31
2.4.1. Instrumented Hardness 31
2.4.2. Compression Test (Gleeble Simulator) 32
2.4.3. Tensile Test 33
2.4.4 Creep Test 34
2.5. Serial Sectioning Method and Quaternions 34
2.6. JMatPro® Simulation 36
2.7. Simulation with VPSC5 Code 37
2.8 Summary 38

Chapter 3

Microstructure and Mechanical Properties of Oxide Dispersion Strengthened 18Cr Ferritic Steel Consolidated by Various Methods **39**

3.1. Characterization of Milled Powders 39
3.2. Consolidation of Steel by Cold Isostatic Pressing (CIP) and Sintering 41
3.2.1. Microstructural Analysis 41
3.2.2. Optimization of Sintering Temperature 42
3.3. Characterization of Steel Consolidated by CIP and HIP 44
3.4. Consolidation of 18Cr ODS Ferritic Steel by Spark Plasma Sintering 45
3.4.1. Consolidation and Densification Characteristics 46
3.4.2. Effect of Sintering Temperature on Microstructure 50
3.4.3. Evaluation of Mechanical Property 54
3.5. Characterization of Steel Consolidated by Hot Extrusion 60
3.5.1 Mechanical Properties 62

3.6 Comparison of Various Consolidation Methods 65
3.7 Conclusion 68

Chapter 4

Study of Deformation and Recrystallization Behavior in Oxide Dispersion Strengthened 18Cr Ferritic Steel **71**

4.1. Microstructure and Microtexture Characterization 72
4.1.1. EBSD Characterization of As Received Steel 72
4.1.2. EBSD Characterization of Deformed Steel 73
4.2. Study of Recovery and Recrystallization Kinetics by Differential Scanning Calorimetry (DSC) Analysis 77
4.2.1 Identification of Recovery and Recrystallization Temperature Domain 77
4.2.2 Kinetics of Recovery and Recrystallization 79
4.3. Design of Heat Treatment to Minimize Anisotropy 82
4.3.1. Conventional Recrystallization Treatment 82
4.3.2. Two Step Heat Treatment 84
4.3.3. Characterization of Microstructure after Two Step Heat Treatment 85
4.3.4. Evaluation of Mechanical Properties using Instrumented Hardness 88
4.4. Plasticity Assessment of Tensile Tested Specimen 92
4.4.1. Tensile Test 92
4.4.2. Microtexture Distribution in Room Temperature Tensile Tested Specimen 93
4.4.3. Microtexture Distribution in High Temperature Tensile Tested Specimen 97
4.5. Conclusion 99

Chapter 5

Study of High Temperature Processing Domain in Oxide Dispersion Strengthened 18Cr Ferritic Steel **103**

5.1. Effect of Temperature and Strain Rate on Flow Stress 104

5.2. Hot Deformation Constitutive Equations 106
5.3. Generation of Processing Maps 109
5.4. Evolution of Microstructure and Microtexture during Hot Compression Testing 113
5.5. Prediction of Texture Using VPSC-5 Constitutive Model 118
5.5.1. Model Description 118
5.5.2. Simulated Texture Distribution 121
5.6. Conclusion 122

Chapter 6

Characterization of Interface Boundaries in Advanced Steels using 5-Parameter Description 125

6.1. Evaluation of Grain Boundary Character Distribution in 18Cr ODS Ferritic Steel 126
6.1.1. Characterization of Grain Morphology and Boundary Network 126
6.1.2. Grain Boundary Character Distribution (GBCD) 129
6.2. Evaluation of Grain Boundary Character Distribution in 9Cr-1Mo steel 132
6.2.1. Characterization of Grain Morphology and Boundary Network 132
6.2.2. Grain Boundary Character Distribution (GBCD) 133
6.3. Evaluation of Grain Boundary Character Distribution in 304HCu Austenitic Stainless Steel (SS304HCu) 134
6.3.1. Microstructural Evolution during Annealing Treatments 134
6.3.2. Description of Grain Boundary Character 136
6.3.3. Σ3 Type Boundary and Its Interaction 139
6.3.4 $\Sigma 3^n$ Boundary Migration 141
6.4. Procedure for Estimation of Five Macroscopic Parameters 144
6.4.1. Serial Sectioning Method 144

6.4.2. Fine Alignment of EBSD Scans 145
6.4.3. Estimation of Five Macroscopic Parameters 146
6.5. 5-Parameter Grain Boundary Determination in Annealed BCC Ferrite Structure of 9Cr-1Mo Steel 150
6.5.1. Reconstruction of EBSD Maps 150
6.5.2 Rotation Axis Distribution 151
6.5.3. Grain Boundary Plane Normal Distribution 152
6.5.4. Character of meeting (h k l) Planes 152
6.5.5. Analysis of Tilt or Twist character of Boundaries 154
6.5.6. Comparison with Theoretical Set 155
6.6. 5-Parameter Grain Boundary Analysis in Annealed 304HCu Austenitic Steel 156
6.6.1 Coherency of Σ3 Boundary 156
6.7 Conclusion 160

Chapter 7

Summary **163**

7.1. Summary
7.2. Optimization of Consolidation Conditions for 18Cr Oxide Dispersion Strengthened Ferritic Steel 164
7.3. Design of Deformation and Annealing for Minimizing Anisotropy 165
7.4. High Temperature Processing Domain of 18Cr Oxide Dispersion Strengthened Ferritic Steel 166
7.5. 5-parameter Interface Boundaries Characterization 167
7.6. Scope for Future Work 169

References **171**

List of Figures

Fig. 1.1. Comparison of (a) average thermal expansion coefficient and (b) thermal conductivity of ferritic and austenitic steels.

Fig. 1.2. Texture evolved during various stages of processing.

Fig. 1.3. Schematic development of recrystallization, (a) High stored energy, high anisotropic grain growth velocity, (b) Low stored energy, low anisotropic growth velocity.

Fig. 2.1. (a) Cold isostatic pressing equipment used in the present study and (b) schematic showing the compaction chamber and mould.

Fig. 2.2. Schematic diagram of an SPS unit containing an assembled graphite die and punches.

Fig. 2.3. Illustration of specimen and detector geometry, spherical Kikuchi map construction of crystal plane trace and its gnomonic projection as straight lines collected over a small solid angle covered by the detector screen.

Fig. 2.4. Schematic of tensile specimen of 18Cr ODS ferritic steel after consolidation by hot extrusion (HE) (all dimensions are in mm).
*Note: ED and TD are parallel and perpendicular to extrusion direction respectively.

Fig. 2.5. Schematic of creep specimen of 18Cr ODS ferritic steel after consolidation (all dimensions are in mm).

Fig. 3.1. SE micrograph of (a) 18Cr ferritic steel powder (b) mechanically alloyed steel powder and Y_2O_3 and (c) particle size distribution before and after milling.

Fig. 3.2. Synchrotron X-ray diffraction pattern of 18Cr-ferritic steel powders with and without Y_2O_3 dispersoids.

Fig. 3.3. SE micrograph of cold isostatic pressed (green compact) 18Cr ODS ferritic steel (more compactly packed region is circled).

Fig. 3.4. Change in (a) relative density and (b) size and area fraction of pores as a function of sintering temperature in CIP product.

Fig. 3.5. (a) EBSD crystal orientation map and (b) inverse pole figure along the axial direction of cylindrical specimen of 18Cr ODS ferritic steel after CIP and sintering at 1423 K (1150 ºC).

Fig. 3.6. EBSD (a) crystal orientation map and (b) inverse pole figure of HIP product.

Fig. 3.7. Relative variation of (a) density and (b) densification rate (Marked regions indicate 1- localized deformation, 2- bulk deformation, 3-mass transport phenomena) as a function of time, (c) plot of ln($\dot{D}$) with respect to 1/T and (d) density variation with temperature during consolidation by SPS.

Fig. 3.8. EBSD crystal orientation maps superimposed with grain boundary (misorientation angle 5-15º- Gray and >15º - Black) of 18Cr ODS ferritic steel powder consolidated by SPS at (a) 1273 K (1000 °C),(b) 1323 K (1050 °C), (c) 1373 K (1100 °C), (d) 1423 K (1150 °C) and the clustering of grains with [110] orientation are circled in (b-d) and (e) grain size distribution at different sintering temperatures.

Fig. 3.9. Inverse pole figure (with contour intensity level better than random: 2.4 to 2.8) with respect to applied direction of pressure during consolidation (denoted as [001]) of 18Cr ODS ferritic steel by SPS at (a) 1273 K (1000 °C),(b) 1323 K (1050 °C), (c) 1373 K (1100 °C), (d) 1423 K (1150 °C). (encircled region shows the alignment of crystallographic plane with respect to crystal coordinate axis).

(*Note: A uniform legend (intensity value from 0-2.831) has been used for ease of reading and individual maximum intensity has been included in respective inverse pole figure)

Fig. 3.10. Fig. 3.10. EBSD (a) image quality and (b) crystal orientation map of 18Cr ferritic steel powder consolidated by SPS at 1323 K (1050 °C) showing deformation bands (yellow arrows) and sub-grains (red arrows).

Fig. 3.11. Instrumented indentation hardness profile of 18Cr ferritic steel with (along axial and transverse direction of applied pressure in SPS) and without dispersoid consolidated at 1323 K (1050 °C) (a) load-displacement curves and (b) penetration profile.

Fig. 3.12. Creep analysis of 18Cr ODS steel consolidated by SPS at 1323 K (1050 ºC) tested at 300MPa stress, (a) Creep curves at various temperatures, (b) creep rate variation with time, and (c) Arrhenius type relationship between the steady state creep rate (h^{-1}) and temperature.

Fig. 3.13. Prediction of creep properties in 18Cr ferritic steel, calculated using 'JMatPro®'; predicted and experimentally determined variation of (a) steady state creep rate, (b) rupture life with temperature and (c) Arrhenius type

relationship between minimum creep rate in steady state region and temperature.

Fig. 3.14. SEM fractographs of SPS consolidated 18Cr ODS ferritic steel creep tested at (a) 873 K (600 ºC) and (b) 973 K (700 ºC) showing ductile failure.

Fig. 3.15. Overlay image of inverse pole figure and image quality maps obtained by EBSD along (a) extruded, and (b) transverse directions of hot extruded 18Cr ODS ferritic steel and (c) and (d) inverse pole figures along ED and TD respectively showing a strong (110) or α-fiber texture.

Fig. 3.16. Comparative analysis of instrumented indentation hardness profile of ED and TD sections of hot extruded 18Cr ODS ferritic steel.

Fig. 3.17. Creep curves of hot extruded 18Cr ODS ferritic steel at a stress of 300MPa along (a) ED, (b) TD , variation of (c) creep rate and (d) rupture life with temperature.

Fig. 3.18. SEM fractographs from (a) ED and (b) TD surfaces of hot extruded 18Cr ODS ferritic steel and creep tested at 973 K (700 ºC).

Fig. 4.1. (011) pole figure of hot-extruded 18Cr ODS ferritic steel for (a) ED and (b) TD sections.

Fig. 4.2. Schematic of sampling and direction of rolling from hot extruded 18Cr ODS ferritic steel.

*Note: ED, TD and R stands for extrusion, transverse and rolling direction respectively.

Fig. 4.3. Overlay image of EBSD inverse pole figure and image quality maps of hot-extruded 18 Cr ODS ferritic steel obtained after 50% cold rolling along the (a) extruded, and (b) transverse direction; (c,d) (011) pole figure after rolling along ED and TD respectively and discrete {0 1 1} pole figure distribution of (d) retained cellular structure of matrix region (marked red square box in Fig. 4.3(b)) and (e) cellular structure in shear band (marked blue square box in Fig. 4.3(b)) after deformation.

Fig. 4.4. Comparison of three DSC traces: as-received hot extruded steel, Run#1 on 50% cold worked and Run#2 is successive of Run#1 under identical experimental conditions; inset corresponds to the marked region in the on heating DSC thermogram showing distinct thermal arrests due to recovery and recrystallization.

Fig. 4.5. Fractional (a) recovery and (b) recrystallization as a function of temperature under different heating rates for 50% cold worked 18Cr ODS ferritic steel.

Fig. 4.6. Plot showing the Arrhenius type relationships for the steady state (a) recovery and (b) recrystallization.

Fig. 4.7. Overlaid EBSD crystal orientation and IQ maps of (a) AEDR and (b) ATDR steel.(Fine grain region marked)

Fig. 4.8. Overlay image of EBSD crystal orientation and image quality maps of 50% cold rolled 18Cr ODS ferritic steel followed by two step heat treatment (a) A_1EDR (1^{st}), (b) A_2EDR (2^{nd}) and (c) A_3EDR (3^{rd}) iteration of deformation followed by 2 step heat treatment and (c), (d) and (e) relevant (011) pole figures. (ED- Extruded direction, Marked region: fine grain structure- black arrow, elongated deformation band- white arrow)

*Note: A uniform legend (intensity value from 0-3) has been used for ease of interpretation

Fig. 4.9. Comparison of variation of grain area fraction obtained by iterative deformation and 2 step annealing.

Fig. 4.10. (a) KAM angle distribution (0-2º) and (b) change in dislocation density with different stages of processing.

Fig. 4.11. Comparative analysis of instrumented indentation hardness profile for (a) ED and TD, (b) EDR and TDR, (c) A_1EDR and A_1EDR and (d) A_2EDR and A_2EDR of 18Cr ODS ferritic steel.

Fig. 4.12. Hardness variations for the as-received hot extruded, deformed and annealed specimen in extruded and transverse directions for 18Cr ODS ferritic steel.

Fig. 4.13. (a) Engineering stress-strain tensile curves and (b) yield strength variation with temperature of 18Cr ODS ferritic steel along ED and TD sections.

Fig. 4.14. Overlay image of crystal orientation and grain boundary (5-15º - Gray and >15º - Black) maps of room temperature tensile tested 18Cr ODS ferritic steel along (a) extruded, and (b) transverse direction (c) and (d) inverse pole figure along ED and TD respectively.

Fig. 4.15. Normalized misorientation angle frequency distribution in room temperature tensile tested 18Cr ODS ferritic steel.

Fig. 4.16. KAM (0.5-5º) superimposed with EBSD image quality (IQ) map of room temperature tensile tested 18Cr ODS ferritic steel along (a) extruded and (b)

transverse directions.

Fig. 4.17. EBSD results of (a) overlaid image quality (IQ) and crystal orientation map and (b) inverse pole figure distribution of high temperature (973 K) tensile tested ED specimen of 18Cr ODS ferritic steel.

Fig. 5.1. True stress vs true strain plots of hot extruded 18Cr ferritic steel obtained by hot compression test for strain rates in the range of 0.01 – 10 s^{-1} at temperatures of (a) 1323, (b) 1373, (c) 1423 and (d) 1473 K.

Fig. 5.2. Variation of work hardening rate (ln θ) of 18Cr ODS ferritic steel with strain (ε) at 1373 K (1100 ºC) and strain rate of 0.01 s^{-1}.

Fig. 5.3. Relationship between (a) $\ln\dot{\varepsilon}$ - $\ln\sigma$, (b) $\ln\dot{\varepsilon}$ – σ and (c) $\ln\dot{\varepsilon}$ - $\ln(\sinh(\alpha\sigma)$ of 18Cr ODS ferritic steel in a temperature range of 1323 to 1473 K (1050 to 1200 ºC).

Fig. 5.4. Variation of strain rate sensitivity with temperature and strain rate for 18Cr ODS ferritic steel.

Fig. 5.5. Processing map generated for 18Cr ODS ferritic steel at 0.5 true strain.
(*region marked 1, 2, 3 and 4 are selected for microstructure analysis)

Fig. 5.6. EBSD crystal orientation maps of zone (a) 1, (c) 2, (e) 3 and (f) 4 marked in Fig. 5.5 and corresponding inverse pole figures of zone (b) 1, (d) 2, (f) 3 and (h) 4.

Fig. 5.7. Grain size distribution in zone (marked in Fig. 5.6); (a) 1, (c) 2, (e) 3 and (f) 4.

Fig 5.8. (110) and (111) Pole figures predicted using VPSC-5 during deformation along (a) ED and (b) TD.

Fig. 6.1. Superimposed maps of image quality and grain boundary distribution (colour key: yellow—5-15º (LAGB), green—15-65º (HAGB), red— CSL Σ1-29) map for (a) ED and (b) TD 18Cr ODS ferritic steel.(HAGB-high angle grain boundary and LAGB-low angle grain boundary)

Fig. 6.2. Superimposed maps of image quality and grain boundary distribution (colour key: yellow—5-15º (LAGB-marked Circle), green—15-65º (HAGB-marked arrow), red— CSL Σ1-29) of (a) AEDR and (b) ATDR sections of 18Cr ODS ferrtic steel. (HAGB-high angle grain boundary and LAGB-low angle grain boundary)

Fig. 6.3. Comparison of experimental and theoretical data between ED, TD, AEDR and ATDR 18Cr ODS ferritic steel (a) Misorientation angle distribution and (b) GBCD.

Fig. 6.4. Superposed band contrast and grain boundary map (color key: red—5-15º, black—15-65º) in 9Cr-1Mo steel after (a) IA and (b) IAA treatments.

Fig. 6.5. Misorientation angle distribution for experimental data set for BCC ferrite structure after the isothermal annealing treatments IA and IAA.

Fig. 6.6. Superposed crystal orientation and grain boundary (>5º black line) map of SS 304HCu after annealing treatments at (a) 1073 K (800 ºC, treatment R), (b) 1373 K (1100 ºC, treatment A), and (c) 1573 K (1300 ºC, treatment EA).

Fig. 6.7. Correlated experimental misorientation angle distribution in SS 304HCu subjected to different annealing treatments after cold rolling.

Fig. 6.8. Grain boundary character distribution map (high angle random boundary (>15º) - black, Σ1 low angle (5-15º) boundaries - grey, Σ3 – red, Σ9 – Blue and Σ27 – Green line) map of SS 304HCu after annealing treatments at (a) 1073 K (800 ºC, treatment R), (b) 1373 K (1100 ºC, treatment A), and (c) 1573 K (1300 ºC, treatment EA).

Fig. 6.9. GBCD of cold rolled SS304HCu steel subjected to(a) treatment A and (b) treatment A1; 1 and 2 represent straightened grain boundaries, 3 and 4 represent Σ3 migration, 5 to 9 represent interactions of Σ3 and changes in CSL boundary in the same region; (Random boundary (>5º) - black, Σ3 – red, Σ9 – Blue and Σ27 – Green line).

Fig. 6.10. Schematic representation of two cross section segments used for calculation of polar angle (β) and azimuth angle (γ) where D and d are the distance between grain boundary segment and distance between two sections respectively.

Fig. 6.11. Superposed maps of the grain boundary (red-Section A and blue-Section B) in 9Cr-1Mo steel after (a) IA and (b) IAA treatment. Numbers indicating the analyzed boundary sequence and the alter direction of boundary trace is represented by the arrow marks (black-high angle boundaries and green-sub grain boundaries).

Fig 6.12. Distribution of the misorientation axis of the adjacent crystallites of the analyzed boundary trace in 9Cr-1Mo steel after (a) IA and (b) IAA treatments.

Fig 6.13. Crystallographic depiction of grain boundary interfaces through their normal in 9Cr-1Mo steel after (a) IA and (b) IAA treatment.

Fig. 6.14. Interplanar angle distribution for experimental and random generated data set in 9Cr-1Mo ferritic steel.

Fig 6.15. Variation of misorientation angle between rotation axis and the grain boundary plane normal in 9Cr-1Mo ferritic steel.

Fig. 6.16. Amount of Σ3 type boundaries and deviation angle from ideal Σ3 type boundary in SS304HCu at different annealing temperatures.

Fig. 6.17. Σ3 boundary plane analysis from EBSD single planar section and {1 1 1} pole figure shows the pole distribution of the grains separated by the trace line in extended annealed SS304HCu. (γ and β represents the azimuth (trace of the boundary with +Y-axis), and polar (common pole concentration to the center of pole figure) angles respectively.

Fig. 6.18. Superposed maps of the grain boundary in extended annealed SS304HCu and the analyzed Σ3 boundary (red and green line for section 1 and 2 respectively) traces indicated by arrow marks.

Fig. 6.19. Distribution of (a) deviation angle of grain boundary plane from exact (1 1 1), and (b) angle between adjoining crystallographic planes at the boundary of extended annealed SS304HCu.

List of Table

Table 1.1. Characteristics of 9Cr and high (>12%) Cr ODS steels

Table 1.2. Chronology of development of high (>12%) Cr ODS ferritic steel

Table 1.3. Characteristics studied in various high (>12%) ODS ferritic steel

Table 1.4. Thermo-mechanical processing schedules employed in the manufacturing of 12Cr ODS ferritic steel tubes

Table 2.1. Chemical composition (wt %) of 18Cr ODS ferritic steel powder used in the study

Table 2.2. Chemical composition (wt %) of 9Cr-1Mo steel used in the study

Table 2.3. Chemical composition (wt %) of SS304HCu stainless steel used in the study

Table 2.4. Processing schedules adopted for 18Cr ODS ferritic steel in the present study

Table 3.1. Consolidation parameters of SPS, relative density and average grain size

Table 3.2. Relative density, average grain size, microstructural distribution and texture intensity of 18Cr ODS ferritic steel

Table 3.3. Summary of mechanical properties of 18Cr ODS ferritic steel

Table 4.1. Estimated kinetic parameters for recovery and recrystallization of 50% cold deformed 18Cr ODS ferritic steel

Table 4.2. Microstructural attributes and mechanical properties of 18Cr ODS ferritic steel

Table 5.1. Estimated values of material constants and activation energy for a given strain at peak stress

Table 5.2. Combination of slip systems for cubic bcc crystal is considered for simulation

Table 5.3. Hardening parameters of deformation used for the simulation

Table 5.4. Comparison of α and γ fibre attributes

Table 6.1. Comparison of experimental evaluated and theoretically calculated grain boundary attributes

Table 6.2. Quantitative analysis of grain boundary character distribution

Table 6.3. Predicted SFE of SS 304 and SS304HCu using JMatPro$^{@}$ simulation

Table 6.4. Product of CSL Σ3 type boundary interactions due to multiple twinning

Table 6.5. Comparison of grain boundary attributes of experimental and theoretical data set

List of Abbreviations and General Symbols

A	Annealing
ADXRD	Angle Dispersive X-Ray Diffraction
BCC	Body Centered Cubic
CIP	Cold Isostatic Pressing
CR	Cold Rolling
CRSS	Critical Resolved Shear Stress
CSL	Coincident Site Lattice
DBTT	Ductile to Brittle Transition Temperature
DMM	Dynamic Material Model
DRX	Dynamic Recrystallization
DSC	Differential Scanning Calorimetry
EA	Extended Annealing
EBSD	Electron Backscatter Diffraction
ED	Extrusion Direction
FCC	Face Centered Cubic
GBCD	Grain Boundary Character Distribution
GBE	Grain Boundary Engineering
GND	Geometrical Necessary Dislocation
HAGB	High Engle Grain Boundary
HE	Hot Extrusion
HIP	Hot Isostatic Pressing
HT	Heat Treatment
IA	Isothermal Annealing
IQ	Image Quality
KAM	Kernel Average Misorientation
KJMA	Kolmogorov Johnson Mehl Avrami
LAGB	Low Angle Grain Boundary
MA	Mechanical Alloying
MD	Mackenzie Distribution
ND	Normal Direction
ODS	Oxide Dispersion Strengthened

OIM	Orientation Imaging Microscopy
PM	Powder Metallurgy
R	Recrystallization
ROI	Region of Interest
SEM	Scanning Electron Microscope
SFE	Stacking Fault Energy
SFR	Sodium cooled Fast Reactor
SPS	Spark Plasma Sintering
TD	Transverse Direction
TMP	Thermo-Mechanical Processing
VPSC	Visco Plastic Self Consistent
$\dot{D}$	Rate of Diffusion
$\dot{\varepsilon}$	Strain Rate
2θ	Width of Kikuchi Bands (in Bragg's Difraction)
b	Burgers Vector
d	Separation Distance between Two Sections
D	Apparent Distance between Boundary Line Segments
G	Power Component
$\hat{g}$	Grain Boundary Plane Normal
h	Total Height Travelled by Plunger
h_i	Instantaneous Displacement of Plunger
J	Dissipation of Power Component
k	Arrhenius Rate Constant
m	Multiplicity of Rotation Axis/Strain Rate Sensitivity
m^s	Schmid Tensor
n	Power Law Exponent
P	Applied Pressure/Power Dissipation
$(\phi_1 \Phi \phi_2)$	Eulers Angle
Q	Quaternion/Activation Energy
q	Unit Quaternion Descriptor of Rotations
Q_{eff}	Apparent Activation Energy
q_s	Quaternion of Crystal Symmetry
R	Universal Gas Constant

$\hat{f}$	Rotation Axis
s	Slip System
T	Absolute Temperature
T_m	Melting Temperature
t_r	Time to Rupture
T_s	Transformation Start Temperature
α	Ferrite
β	Polar Angle
γ	Austenite/Azimuth Angle
ε	Strain
η	Efficiency of Power Dissipation
θ	Angle of Rotation (in rotation operations)
θ_0 and θ_1	Initial and Asymmetric Hardening Rate
ξ	Angle Between Rotation Axis and Grain Boundary Normal
$\xi(\dot{\varepsilon})$	Instability Parameter
ρ	Relative Density
ρ_i	Instantaneous Density
σ	Instantaneous Effective Stress
τ	Tolerance Angle
τ^s	Threshold Stress
φ	Shape Factor or Pore Aspect Ratio
ψ	Interplanar Angle
ω	Rotation Angle
ϵ	Strain Rate of Individual Grain

SYNOPSIS

Enhanced properties of structural materials are essential for efficient and economic performance of advanced generation IV reactors for effective nuclear energy utilization [1]. Aggressive service conditions such as high energy neutron irradiation and high temperatures pose a major challenge in selection of materials [1-3]. In this context, nano structured oxide dispersion strengthened (ODS) steels have gained momentum amongst both scientific and industrial community owing to their potentially outstanding properties with respect to high temperature stability, strength and creep resistance [4, 5]. Further, high Cr (>12%) ODS ferritic steels are being considered as candidate materials for core structural application such as 'fuel cladding' in advanced nuclear energy systems due to their enhanced properties such as thermal conductivity and resistance to irradiation induced swelling in contrast to austenitic stainless steel and superalloys [5-8]. The homogeneous ultrafine dispersoid distribution enhances the creep strength and significantly lowers the irradiation induced swelling in conjunction with ferritic (bcc) structures in these steels [9, 10], while the higher Cr content improves the corrosion resistance in service as well during spent nuclear fuel reprocessing [11, 12]. Typically these steels are fabricated through a powder metallurgical route followed by various sequences of cold or warm working and annealing treatments [13]. However, development of anisotropic microstructure during fabrication which induces severe anisotropy in mechanical properties still remains a point of significant concern for their final applications [6, 14, 15]. In view of the above, a systematic experimental and computational study has been carried out in the present thesis and the following themes are addressed.

- Optimization of consolidation conditions for 18% Cr oxide dispersion strengthened (ODS) ferritic steel through evaluation of density, microstructure, microtexture and mechanical properties.

- Design of an optimum thermomechanical treatment (TMT) to minimize anisotropy in 18Cr ODS ferritic steel.
- Description of grain boundary character distribution (GBCD) in 18Cr ODS steel during consolidation, deformation and annealing processes.
- Demonstration of a methodology for describing the interface boundaries based on five parameter characterization in conventional ferritic and austenitic steels with high and low stacking fault energy (SFE) respectively.

This thesis contains seven chapters in all. The organization of the thesis is given below:

Chapter 1: Introduction

This chapter deals with a detailed literature review on the nano structured oxide dispersion strengthened (ODS) steels and its potential requirements for high temperature structural applications in fast reactors vis -a- vis the conventional austenitic and 9Cr ferritic martensitic steels. This is followed by a brief introduction to the development of high Cr (>12%Cr) ODS ferritic steels which includes their historical development, current status and challenges during processing. The high Cr ferritic ODS steels are known to develop directional dependent microstructures during fabrication that lead to severe anisotropy in mechanical properties. The anisotropy of mechanical properties is explained by the combined effect of fine substructure within elongated grains of large aspect ratio and precipitates along the extrusion direction. Strategies to reduce or mitigate anisotropy through an optimum TMT process have also been reported in literature. This chapter also includes a brief discussion on the evolution of the Electron backscatter diffraction (EBSD) technique to characterize various facets of the structure namely morphology, micro-texture and grain boundaries in this study. The broad objective of the work and the scope of the thesis are also outlined.

Chapter 2: Experimental Details

In this chapter, details of the experimental and computational methods employed in this thesis are presented. Brief descriptions on powder synthesis, consolidation methods and annealing treatments are followed by structural characterization techniques namely synchrotron XRD, metallography, scanning electron microscopy, differential scanning calorimetry and EBSD including data analysis are provided. Details of property evaluation using tensile, creep and instrumented hardness is included. The operation conditions, calibration and error analysis for each experimental technique are also described. A brief account on special methods like serial sectioning, quaternion algebra, JMatPro and VPSC modeling used in the thesis are also presented.

Chapter 3: Optimization of consolidation conditions for 18% Cr oxide dispersion strengthened steel through evaluation of microstructure and mechanical properties

This chapter begins with characterization of milled powder using synchrotron X-ray diffraction analysis and electron microscopy techniques for phase identification and morphology. The 18Cr ODS ferritic steel powders have been consolidated by various methods, details of which are as follows:

- Cold isostatic pressing (CIP) and sintering; based on maximum relative density of 92% and microstructural analysis, sintering at 1150 ºC was identified to be optimum;
- Hot isostatic pressing (HIP) of CIP product at 1150 ºC, the optimized temperature and 200MPa pressure which resulted in 97% of theoretical density;
- Spark plasma sintering (SPS) which yielded a density ~ 99%. Sintering temperature of 1323 K (1050 ºC) was found to be optimum based on kinetics of densification and resultant microstructure/microtexture;

Hardness and steady state creep property were evaluated for the consolidated products. The role of dispersoids on microstructure was studied by comparison with the 18Cr

steel powder consolidated by SPS at 1323 K (1050ºC). A signature of (1 1 0) grain cluster and its preferential growth with increase in sintering temperature was observed during consolidation leading to the alignment of the (1 1 0) plane in the direction of applied pressure. Further, systematic Electron Backscatter Diffraction analysis has been carried out to study the grain size distribution and texture as a function of consolidation temperatures. The steel consolidated using hot extrusion (HE) process showed better densification (relative density >99%) and an anisotropic grain size distribution along the axial and transverse direction of extrusion while overall the grain diameters varied within 0.8 - 2 μm.

Comparison of the relative density, morphology, average grain size, texture intensity and mechanical property of the ODS steel consolidated by different methods revealed that despite the morphological anisotropy, which also reflected in the mechanical properties, the hot extruded steel showed a better creep strength and rupture life in contrast to other processes which highlights that density is the crucial parameter that governs the high temperature mechanical properties. Although HE is considered optimum, SPS can be considered as an alternate process for consolidation of 18Cr ODS ferritic steel.

Chapter 4: Study of deformation and recrystallization behavior in ODS 18Cr ferritic steel

This chapter presents the results of an experimental study aimed to obtain an ultrafine equiaxed grain size distribution in 18Cr ODS steel through series of cold working and annealing steps starting with an initial columnar grain structure and a predominant α-fibre texture in a hot extruded product. The salient features of the study are as follows:

- Deformation along the extrusion direction (ED) showed retention of α-fibre texture, while deformation in the transverse direction (TD) showed a shear banded structure with a reduced percentage of α-fibre texture.

- Differential Scanning Calorimetry (DSC) analysis of the deformed steel established the occurrence of two significant events during heating namely recovery and recrystallization, whose temperatures were influenced by the heating rate. The recovery and recrystallization domains have been distinctly observed at 1350 K and 1420 K respectively at a low heating rate of 7 K min^{-1}.
- The microstructure (post DSC) showed very coarse elongated grains interspersed with regions of ultrafine (<1μm) equiaxed grains, due to incomplete recovery.
- The deformed steel was subjected to a two step heat treatment designed based on the recovery and recrystallization domains identified from DSC analysis to reduce the morphological anisotropy in longitudinal direction, which resulted in the randomization of the initial <1 1 0> // ED α-fibre texture, which improved further with repeated deformation and two step heat treatment cycles.
- A gradual increase in hardness during the above cycles was observed reflecting the increase in dislocation density which offered the propensity to achieve an ultrafine grained microstructure.

In addition, tensile tests carried out at 298, 823 and 973 K (25, 550 and 700 ºC) on 18Cr ferritic steel which are directly linked to consolidation process through hot extrusion. Plasticity assessments of tensile tested specimens are carried out to understand the influence of texture on mechanical properties.

Chapter 5: Study of high temperature processing domain in ODS 18Cr ferritic steel

This chapter presents the results of an experimental study aimed to identify hot working domains in 18Cr ODS ferritic steel. The experimental data was obtained by uniaxial compression test using the Gleeble-1500D simulator in a range of temperatures (1323 - 1473 K) and strain rates (0.01 – 10 s^{-1}). An inverse relationship with temperature and positive strain rate sensitivity associated with dynamic recovery and recrystallization, was derived

from the flow stress. Based on the processing map generated at 0.5 true strain using rate dynamic material model (DMM) approach and the calculated instability parameter ($\xi(\dot{\varepsilon})$)>0, the optimum processing domain has been determined for this steel. The most favorable processing parameters are found in the temperature ranges of 1350 - 1450 K with a strain rate of 0.01 s^{-1} as well as 1473 K with a strain rate 0.1s^{-1} with peak efficiency of 30% and 35% respectively.

The material flow behavior was systematically studied by EBSD and the important results are as follows:

- The steel subjected to 1323 K at high strain rate 10 s^{-1} in the low efficiency workability region showed low aspect ratio as compared to the elongated bamboo like initial microstructure;
- Minimum strain rate (0.01 s^{-1}) showed that localized slip/shearing is the key mechanism; Intensity distribution of inverse pole figure showed the presence of significant amount of θ-fibres.
- Dynamic recrystallization dominated at higher efficiency region and γ-fibre texture was evident in the specimen deformed at 1373 and 1473 K with strain rate of 0.01s^{-1} and 0.1s^{-1} respectively;

VPSC constitutive models are used to predict the resultant texture from a distinct initial texture. The resultant texture distribution obtained by the prediction and experimental EBSD analysis has been compared to understand the underlying micromechanism of texture evolution during processing of the steel at high temperatures.

Chapter 6: Analysis of five parameter interface boundaries in advanced steels

The chapter presents the grain boundary character distribution in ODS steel during deformation and annealing process. The ODS steel in consolidated form shows higher low energy coincidence site lattice (CSL) boundaries than theoretically calculated and reduces

during cold working and annealing processes; Further, the frequency of low energy CSL boundaries is found to be reduced due to diffusion assisted grain boundary migration during the annealing process.

In order to understand the micromechanism associated with energy minimization during annealing a methodology for describing interface boundaries has been demonstrated in low and high SFE alloys namely austenitic and ferritic steel respectively. EBSD in conjunction with serial sectioning procedure have been used to obtain a five parameter description of interface boundaries that evolved during annealing in a 9Cr-1Mo steel with polygonal structure and in 304HCu grade austenitic stainless steel.

Chapter 7: Summary and further avenues of research

Chapter 7 presents a summary of the salient features of the experimental and computation studies carried out in this thesis; and also identifies few potential avenues for further research.

References:

1. K. L. Murty, I. Charit, J. Nucl. Mater. 383 (2008) 189–195.
2. Aitkaliyeva, L. He, H. Wen, B. Miller, X.M. Bai, T. Allen, Structural Materials for Generation IV Nuclear Reactors (2017) 253–283.
3. V. de Castro, E. A. Marquis, S. L. Perez, R. Pareja, M. L. Jenkins, Acta Mater. 59 (2011) 3927–3936.
4. R. L. Klueh, Int. Mater. Rev. 50 (2005) 287-312.
5. R. L. Klueh, N. Hashimoto, P. J. Maziasz, Scitpta Mater. 53 (2005) 275-280.
6. S. Ukai, M. Harada, H. Okada, M. Inoue, S. Nomura, S. Shikakura, K. Asabe, T. Nishida, M. Fujiwara, J. Nucl. Mater. 204 (1993) 65–73.
7. S. Ukai, M. Fujiwara, J. Nucl. Mater. 307–311 (2002) 749–757.

8. S. Wurster, R. Pippan, Scitpta Mater. 60 (2009) 1083-1087.
9. C. Cayron, E. Rath, I. Chu, S. Launois, J. Nucl. Mater. 335 (2004) 83–102.
10. H. Hadraba, B. Fournier, L. Stratil, J. Malaplate, A. L. Rouffie, P. Wident, L. Ziolek, J. L. Bechade, J. Nucl. Mater. 411 (2011) 112–118.
11. Z. Oksiuta, J. Mater. Sci. 48 (2013) 4801–4805.
12. R. Novotny, P. Janik, S. Penttila, P. Hahner, J. Macak, J. Siegl, P. Hauˇsild, J. Supercritical Fluids 81 (2013) 147– 156.
13. G. Junceda, M. H. Mayoral, M. Serrano, Mater. Sci. Engg. A 556 (2012) 696–703.
14. S. Ukai, S. Mizuta, T. Yoshitake, T. Okuda, M. Fujiwara, S. Hagi, T. Kobayashi, J. Nucl. Mater. 283-287 (2000) 702-706.
15. M. J. Alinger, G. R. Odette, G. E. Lucas, J. Nucl. Mater. 307 (2002) 484–489.

Introduction

The performance of structural materials is one of the crucial factors that govern the life time and efficiency of nuclear reactors [1]. Aggressive service conditions such as high energy neutron irradiation at high temperatures poses a major challenge in selection of materials for advanced Generation IV reactors [1-5]. In this context, nano structured oxide dispersion strengthened (ODS) steels have gained momentum among the scientific as well industrial community owing to their potentially outstanding properties with respect to high temperature stability, strength and creep resistance [6, 7]. These steels are synthesized by powder metallurgical route and fabricated by various sequences of cold or warm working and annealing treatments [8]. However, formation of anisotropic microstructures during fabrication induces severe anisotropy in mechanical properties and is a point of significant concern for their end applications [9-11]. In the present thesis work an attempt has been made to identify a consolidation method and thermal/thermo-mechanical treatments that can minimize the anisotropy problem based on a systematic experimental study of microstructure, microtexture and grain boundaries in 18Cr ODS ferritic steel. This chapter provides in brief the present status of understanding of these steels based on the review of available literature on topics relevant to the study. This chapter also includes the scope and organization of the thesis.

1.1. Selection of Radiation Resistant High Temperature Materials

Nuclear structural materials are classified based on their usage as "in core" and "out of core" components in fast reactors [12]. In core materials, the thin walled fuel clad tube contains the fuel pellets and experiences operating temperatures up to 973 K (700 ºC) and a neutron flux of the order 10^{15} $ncm^{-2}s^{-1}$ [13]. The fuel pins are housed in a hexagonal wrapper or hexcan and is

termed as a fuel subassembly. The intense irradiation environment results in the production of a high concentration of point defects and leads to change in shape as well as dimensions of the clad and wrapper due to void swelling. The differential swelling across different faces of the hexcan results in bulging and bowing of the fuel subassembly. This catastrophic effect limits the life of the clad tube and wrapper thus disabling efficient utilization of fuel for economic operation of the reactor. Hence, enhanced material properties are sought for core structural materials, which sustain the irradiation resistance up to ~ 180 dpa. Although swelling resistance is a major concern above 50 dpa for austenitic stainless steels, they have been considered as the most preferred materials for core components. Further, swelling resistance has been improvised in these steels by varying content of Ni and Cr [14, 15]; however, it is considerably inferior to ferritic steels with bcc structure with irradiation resistance up to 150 dpa. In addition, ferritic steels possess higher thermal conductivity, low thermal expansion coefficient, better compatibility with liquid metal coolant in comparison to austenitic stainless steels. The variation of coefficient of thermal expansion and thermal conductivity of 18Cr (Fe-18Cr–2W-0.01C–0.2Ti) ferritic and 316LN (Fe-18Cr-10Ni-2Mo-0.03C-0.1N) austenitic stainless steels with temperature were theoretically calculated [16] and compared in Fig. 1.1. It is evident that ferritic steels possess lower coefficient of thermal expansion and better thermal conductivity (Fig. 1.1(a) and (b)). However, high temperature creep resistance of ferritic steels is relatively low, which limits their usage for high temperature applications. The addition of nano dispersoids to the ferrite matrix shows an enhancement of high temperature creep strength and these materials are termed as oxide dispersion strengthened (ODS) ferritic steels [17, 18]. ODS ferritic steels are being considered for ‘cladding’ in advanced nuclear energy systems due to their enhanced thermal conductivity and resistance to irradiation induced void swelling as compared to

austenitic stainless steels and nickel based superalloys [7, 9, 19]. In addition, several reports have also acknowledged the possible use of ODS steels in nuclear fission and fusion reactors, and in ultra super critical steam turbines, owing to their superior high temperature behavior [1, 9, 17, 18, 20-23]. The homogeneous distribution of ultrafine dispersoids imparts the creep strength and significantly lowers the irradiation induced swelling over and above the BCC crystal structure in these steels [24, 25]. Powder metallurgy (PM) route, consisting of mechanical alloying of prealloyed/elemental powders with Y_2O_3 followed by consolidation and thermal/thermo-mechanical treatments is generally adopted for the fabrication of these steels [26, 27].

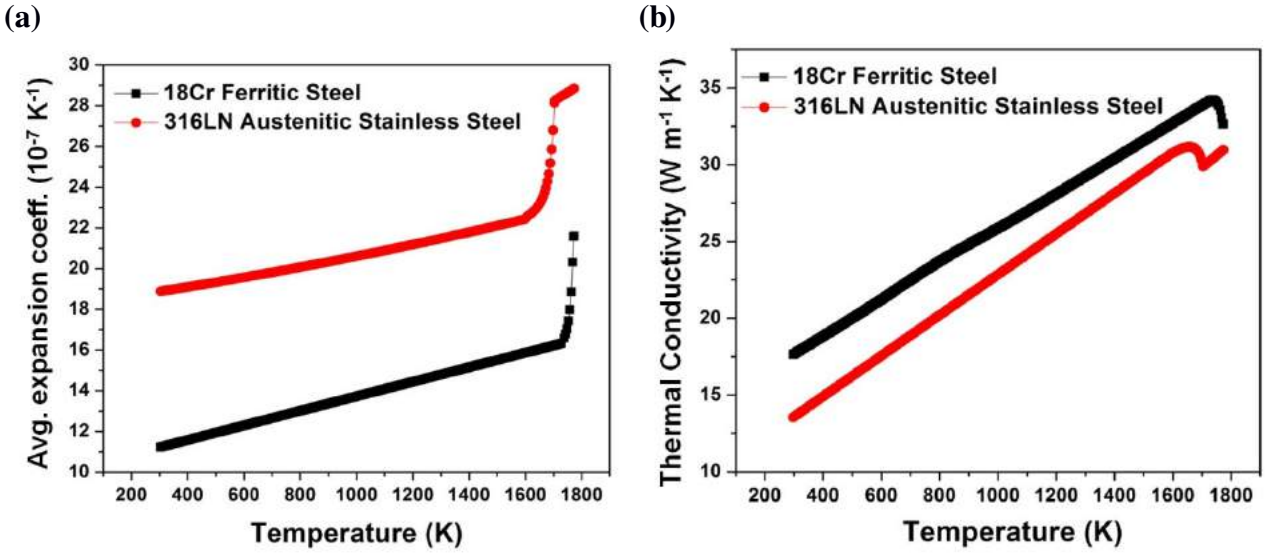

Fig. 1.1. *Comparison of (a) average thermal expansion coefficient and (b) thermal conductivity of ferritic and austenitic steels.*

1.2. Development of ODS Ferritic Steels

The development of ODS steel dates back to 1967 [28, 29], when Huet et al. [28] reported a stable oxide dispersion in a 12Cr ferritic steel using oxides such as Al_2O_3, MgO, ZrO_2, TiO_2 and $ZrSiO_4$. However, interest in ODS ferritic steels gained momentum since 1985 [18, 30] and is witnessing rapid strides since then.

Since 1970s, two classes of ODS steels have been studied for different applications. One is the ferritic/martensitic 9Cr variety and the other is the oxidation resistant fully ferritic (>12%) Cr ODS steels [31]. In 9Cr based ODS steels, the final step of tube production is normalizing and tempering treatment. The ferrite (α) to austenite (γ) transformation while heating during normalizing treatment leads to the nucleation of almost equiaxed grains and hence the elongated grain structure produced during hot extrusion and cold rolling processes are fragmented and recrystallized. A similar observation with a typical homogenous microstructure is reported by Ukai et al. [32] during the fabrication of 9Cr based ODS steel cladding. Further, the homogeneous microstructure in conjunction with minimum shift in ductile to brittle transition temperature (DBTT) in 9Cr based ferritic/martensitic steel makes this class of steel very attractive for high temperature applications. Nevertheless, chromium content of the steel is associated with corrosion resistance in service and fuel clad interaction, and it is therefore desirable to have higher chromium content. Chromium content higher than 12 weight % helps in the formation of Cr rich Cr_2O_3 passive film which is responsible for corrosion resistance [33-35]. The high Cr content in cladding tube imparts good corrosion resistance not only during service, but also during the dissolution of spent fuel in a highly oxidizing medium during nuclear fuel reprocessing [36, 37]. Although ferritic steel with high amount of Cr is known to form sigma (σ) phase, which deteriorates the mechanical properties, the σ phase is unstable in the operating temperature range of the reactor and reverts to a solid solution in the matrix. In general, C, Cr, W, Ti and Y_2O_3 are international alloying additions in ODS ferritic steel, whereas Si, Mn, P, S and Ni are considered as impurity elements. The W content is optimized based on a balance between solid solution strengthening and embrittlement caused by precipitation of Laves phase. The amount of Ti and Y_2O_3 or their ratio plays a vital role in controlling the size as well as

distribution of the dispersoids. Usually the ratio is kept close to 1 which is reported to provide a uniform microstructure [38]. It is also well known that a microstructure with an ultrafine (<1 μm) grain size distribution reduces the DBTT in high (>12%) Cr ODS ferritic steel to around 223 K (-50 °C), which needs to be achieved by employing optimum consolidation and thermo-mechanical treatment methods [38, 39]. Some of the general characteristics of the two classes of ODS steels are compared in Table 1.1.

Table 1.1. Characteristics of 9Cr and high (>12%) Cr ODS steels

Characteristics	**9Cr ODS**	**High (>12%) Cr ODS Steel**
Fabrication	Easy to fabricate	Difficult to remove cold work effect completely with intermediate heat treatment between passes. Two step heat treatment process.
Susceptibility to cracking while cold pilgering	Less	High. Cold pilgering at each pass is carried out for material with increasing hardness.
Means to remove microstructural anisotropy	$\alpha \leftrightarrow \gamma$ phase transformation	No phase transformation; recrystallization heat treatment partially removes the anisotropy.
Microstructure after final heat treatment for fabricated tube product	Tempered Martensite Equiaxed grain structure	Ferritic structure Recrystallized and elongated grains; morphological anisotropy remains.

1.3. Status of Development of High (>12%) Cr ODS Steel

ODS steels with low carbon and high chromium (12–18 weight % Cr) content with dispersion strengthening by titania (TiO_2) and/or yttria (Y_2O_3) particles was introduced to the nuclear industry in the 1970s. These steels had a stable ferrite structure until melting point. The compositions extensively studied were: Fe-13Cr-1.5Mo-2.9Ti-1.8Ti_2O_3 (DT2906) and Fe-13Cr-1.5Mo-2.2Ti0.9Ti_2O_3-0.5Y_2O_3 (DT2203Y05) [29, 40]. Over the last few decades, the advancements in ODS steels have been carried out in Japan [30, 41] and France [42] initially for cladding in the sodium cooled fast reactor programs and then extended to fusion reactor

programs in Japan, Europe and the United States [11, 43, 44]. The development of ODS steels, is one of the innovative technologies in Advanced Fast Reactor Core Technology (FaCT) project, as the most promising material for fuel pin cladding tubes for commercial Sodium Fast Reactor (SFR) cores [45]. Japan Atomic Energy Agency (JAEA) has been developing ODS steels for tubes since 1990 [9]. Table 1.2 shows the chronological development of high (>12%) Cr ODS ferritic steels.

Table 1.2. Chronology of development of high (>12%) Cr ODS ferritic steel

Year	**Development Stages**	**Organization/Country**
1985	Initiation of research and development of ODS ferritic steel [9, 25].	Japan Atomic Energy Agency, Japan
1987	Optimization of alloying elements and mechanical alloying conditions [43].	Power Reactor and Nuclear Fuel Development Corporation, Japan
1989	Trial manufacturing of cladding tubes [9, 18].	
2002	Irradiation campaign of ODS clad tubes [44, 46].	BOR-60 in Russia
2004	Development of two step softening heat treatment for manufacturing of High Cr ODS ferritic steel tubes [31].	Japan Nuclear Cycle Development Institute
2011-2015	Development of 18Cr ODS clad tubes • Finalization of composition • Mechanical milling and consolidation • Optimization of intermediate heat treatment steps in fabrication of rods, characterization of recrystallization and effect of thermo-mechanical processing parameters.	India

Since 1985, there are large number of studies on high (>12%) Cr ODS steels to understand the detrimental effect of chromium on phase transformation, microstructure, and mechanical properties as well as the secondary phase evolution during long term thermal exposure under service conditions. Low Cr ODS ferritic/martensitic steels have insufficient oxidation resistance, which has provided an impetus to develop ODS steels with higher Cr content so as to achieve the advantage of corrosion resistance with minimum impact on the embrittlement phenomena [47, 48]. For fission applications, the Cr content in ODS steels is

usually in the range of 9-18% [49, 50]. Identification and optimization of fabrication route for clad tube is an important step in the development, and Table 1.3 below lists the key issues reported in literature for different high Cr ODS steel systems.

Table 1.3. Characteristics studied in various high (>12%) ODS ferritic steel

Wt. % Cr	Intended Application	Fabrication Route	Characteristics Studied	Reference
12	Nuclear fission and fusion reactors	Mechanical Alloying, Hot Extrusion / hot isostatic pressing, Cold rolling / Pilgering	Microstructure, texture, hardness, tensile, creep properties	[9, 17, 31, 43]
13				[38]
14				[37, 51-54]
16				[55, 56]
18				[38, 53]
20	Supercritical water reactor		Microstructure evolution during service	[57, 58]

1.4. Fabrication of ODS Ferritic Steels

The major challenge in producing ODS steels is to obtain a uniform dispersion of fine refractory oxides [59] with minimum interparticle spacing in the matrix [60, 61]. Conventional melt processing is unsuitable for ODS steel due to density differences between the matrix (heavy) and the refractory oxides (light), which leads to the separation of matrix and dispersoid phase during cooling due to buoyancy [62]. The tendency for agglomeration by nano oxides before introduction and in the melt is also a cause for concern. However, Callejo et al. [63] described an alternative approach to introduce nanoparticles into molten steel. Further, processing paths range from modifications of classical melt and thermo-mechanical practices [63, 64] to few novel techniques such as vacuum casting [65], laser additive manufacturing [66] and selective laser melting [67], which are gaining interest in recent times, although their technology has not matured yet. In general, ODS steels have been processed widely by mechanical alloying (MA) similar to methods used to fabricate particle reinforced composites,

for producing uniform dispersion of nanosized oxides in the metal matrix [68-70]. The MA technique was invented by John S. Benjamin and his colleagues in 1966 with the development of high energy ball mills [71]. Specific to the ODS steel, MA makes possible, the combination of dispersion, solid solution and precipitation strengthening by mixing all the constituents in powder form to produce an intimate mixture of alloy powder with oxides dispersed in the solid solution [72] and the process is well explained in several reports [73-77].

The ODS powder synthesized through MA needs to be compacted in order to produce an engineering component out of it. There are several ways to achieve this, such as Hot Extrusion (HE) [11, 78-80], Hot Isostatic Pressing (HIP) [59, 81] and Spark Plasma Sintering (SPS) [82-84]; all of which employ simultaneous application of high pressure and high temperature to achieve density. Processing technologies such as HE, HIP and SPS are well established techniques and can be adapted from laboratory to industrial scale for ODS steels with suitable optimization trials. HE is a very viable process for consolidation more so when the final product is required in rod or tube form. A high density product and very fine structure is obtained by HE as compared to other methods. Further, it is reported by Alamo et al. that in case of hot extruded and unrecrystallized steel with a very fine microstructure, the DBTT can be similar to that of a martensitic steel (around 223 K (-50 °C)) [39] even with higher Cr (>12%) content. However, the issue linked to the ODS steels is their pronounced anisotropy resulting from the consolidation route. Alinger et al. [11] reported that ODS steels typically contains grains elongated with a factor 1:10 in the extrusion direction. A similar observation has also been reported by Hadraba et al. [85] that the microstructure of as-extruded ODM401 (13Cr-0.29Mo-0.85Ti-0.25Y2O3-Fe bal.) steel has grains elongated in the uniaxial direction by ratio about 1:5–1:10.

Thus, the grain structure must be modified by post extrusion thermo-mechanical treatments, typically involving sequences of cold or warm working followed by softening or recrystallization treatments, which are also needed to manufacture product forms such as thin walled clad tubes. The problem associated with the microstructure that evolves during hot extrusion is described in the next section.

1.5. Anisotropy in High (>12%) Cr ODS Ferritic Steel

ODS ferritic steels with chromium content Cr > 12% possess a ferritic structure and the high temperature strength is determined by several parameters like dispersoid distribution, grain size and texture. The anisotropic behavior was first reported by Ukai et al. [43] for a low carbon 13Cr-3W-(0.2-0.3)Y_2O_3 ferritic steels during manufacturing of clad tubes. A bamboo like grain structure and strong deformation texture along the extruded direction, resulting in poor bi-axial creep properties is reported. Serrano et al. [86, 87] studied the anisotropy in ferritic ODS steels of the 12 – 14 Cr variety, and have reported the deformation induced anisotropy that forms due to successive unidirectional cold deformation during fabrication of clad tubes. The elongated α grains that form during the hot extrusion process remain throughout the subsequent cold working and heat treatments due to absence of $\alpha \leftrightarrow \gamma$ phase transformation unlike 9Cr based ODS steels [31, 32].

1.5.1. Cause of Anisotropy in Hot Extruded High (>12%) Cr Ferritic Steel

Anisotropic mechanical properties of the deformed high Cr (≥12%) ODS ferritic steel is basically attributed to the following microstructural features [25, 31]:

i) Preferred crystallographic orientation

ii) Elongated fine grains with a high aspect ratio

iii) Clusters of fine grains with presence of segregation/precipitation/inclusions along the extrusion direction.

Directionality during recrystallization with the elongated grains aligned along the extruded direction was first reported by Chou et al. [78]. Extensive efforts to engineer the microstructure through recrystallization were made by Narita et al. [31] and Baloch et al. [88]. A columnar or directionally recrystallized grain structure is suitable for elevated temperature applications, where creep resistance is important. However, in a tubular product, the resistance to hoop stresses is far lower than desirable. Though different processing conditions are known to influence the degree of anisotropy, fully equiaxed microstructure has not been achieved yet. The deformation texture that exists in the tube products [10, 11, 43] is another important point of concern that needs to be addressed for the end application.

1.5.2. Methods to Overcome Anisotropy

The best possible way to remove/reduce the anisotropy of high Cr (≥12%) ODS steel is to produce a fully recrystallized structure, which is known to improve the strength and ductility in hoop direction [10]. Hence, design of appropriate thermo-mechanical processing sequence to effect recrystallization during the final heat treatment is the need. Narita et al. [31] have examined the effect of intermediate heat treatment in the process of four pass cold rolling. Three different thermo-mechanical processing (TMP) schedules (Process A, B and C) were employed in the manufacturing of 12Cr ODS ferritic steel tubes (Table 1.4). This consisted of successive cold working to an extent of 50% followed by annealing for different time durations at different temperatures in the range of 1323 to 1423 K (1050 to 1150°C). The processes and the resultant microstructures are summarised in Table 1.4. The first heat treatment for all the processes was annealing at 1373 K (1100°C) for 30 minutes in order to reduce the residual stress in the

deformed tube. In process A, tubes were heated at 1423 K (1150°C) for 30 minutes to get recrystallization with lower hardness after the second heat treatment, and then the heat treatment after the third cold rolling was omitted. In processes B and C, a lower temperature of 1323 K (1050°C) for 120 minutes was used for the second heat treatment to inhibit recrystallization. Then the third heat treatment was given at the same temperature for process B (i.e. 1323 K (1050°C) for 10 min.). However, similar to process A, third heat treatment was omitted for process C as well. The final heat treatment was conducted at 1423 K (1150°C) for all the three processes (i.e. Process A, B and C).

Table 1.4. Thermo-mechanical processing schedules employed in the manufacturing of 12Cr ODS ferritic steel tubes [31]

Processing Schedule	1st treatment		2nd treatment		3rd treatment		4th treatment		Final Microstructure
	CR (%)	HT (K)	CR (%)	HT (K)	CR (%)	HT (K)	CR (%)	HT (K)	
Process A	50	1373/ 0.5 h	50	1423/ 0.5 h	50	---	50	1423/ 0.5 h	Elongated fine grains
Process B	50	1373/ 0.5 h	50	1323/ 2h	50	---	50	1423/ 0.5 h	Partially recrystallized grain
Process C	50	1373/ 0.5 h	50	1323/ 2 h	50	1323/ 0.1 h	50	1423/ 0.5 h	Uniform recrystallized grain

*Note: CR-Cold rolling, HT-Heat Treatment

The reported OIM (orientation image microscopy) images revealed a typical recrystallized texture [{110} <111>] achieved in the process A [31, 89] after the second heat treatment, whereas third and fourth cold rolling induced the rolling texture (Fig. 1.2). On the other hand, in process B, the rolling texture was produced at the second and third heat treatments, which caused only recovery, whereas the recrystallized texture was achieved only after the final heat treatment. It is known that {111} <110> texture gives rise to recrystallization texture by heat treatment in bcc alloys. Therefore, recrystallization in process B is attributed to

the presence of the strong rolling texture of {111} <110> prior to the final heat treatment, whereas the random orientation produced by cold rolling of the already recrystallized structure did not induce further recrystallization in the process A. Another important observation made by Narita et al. [31] was that accumulated strain energy could cause recrystallization even at lower temperatures. Hence, it is necessary to maintain the recovered structure, at the same time reduce the hardness to less than 400 HV, which is achieved by intermediate heat treatments at lower temperatures. It is reported that a two step heat treatment of longer duration of 2h at 1323 K (1050 °C) followed by a shorter duration at the higher temperature of 1423 K (1150°C) resulted in a uniform recrystallized grain structure as compared to the other processes [31]. The above description provides the basic philosophy of the two step heat treatment adopted in the industry for fabrication of clad tubes.

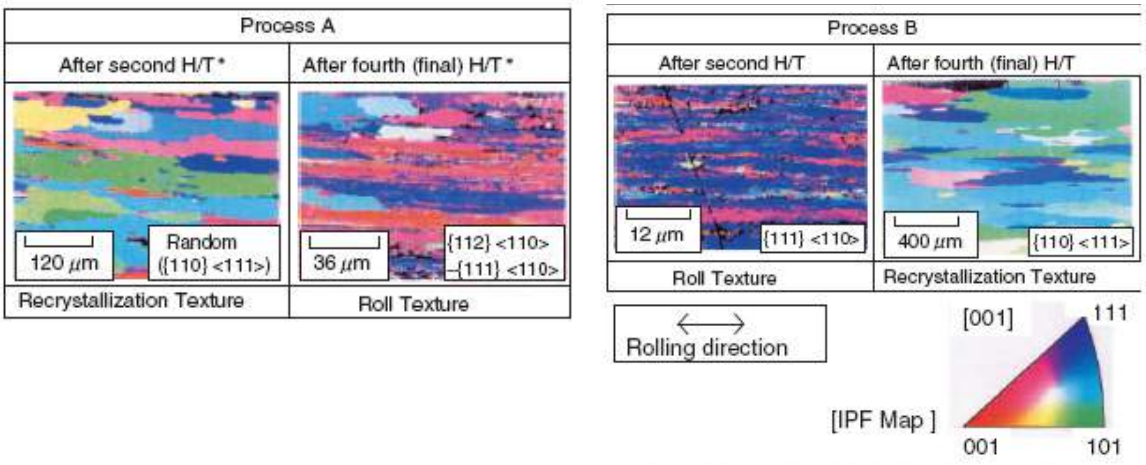

Fig. 1.2. *Texture evolved during various stages of processing [31].*

It is known that tube drawing in 12Cr ODS ferritic steel is more susceptible to cracking as the intermediate heat treatments do not reduce the hardness appreciably as compared to martensitic 9Cr ODS steel [90], In this context the two step heat treatment gains significance to reduce the anisotropy along with reduction in hardness to decrease the susceptibility to cracking .

Recently Narita et al. [89] have also investigated the recrystallization behavior of 15Cr ODS ferritic steel and have reported that the two step heat treatment reduces the driving force for recrystallization by structural recovery and is effective for producing a stable recrystallized structure, which is a very useful input for the fabrication of ODS ferritic steel cladding. Chou et al. [78, 79] have reported that grain intercept along the transverse direction tends to be insensitive to the heat treatment, and is probably controlled by the number of sites for initiation of recrystallization. Thus a more isotropic grain structure could in principle be produced by reducing the grain growth velocity. This can be achieved by reducing the stored energy, via recovery process before recrystallization. The schematic of recrystallization growth front, dependent on stored energy is shown in Fig. 1.3 [79]. The combined effect of annealing at lower temperature to effect partial recrystallization and this treatment leads to enhanced nucleation and limited growth, which facilitates enhanced isotropic mechanical properties (Fig. 1.3) [79].

(a)

(b)

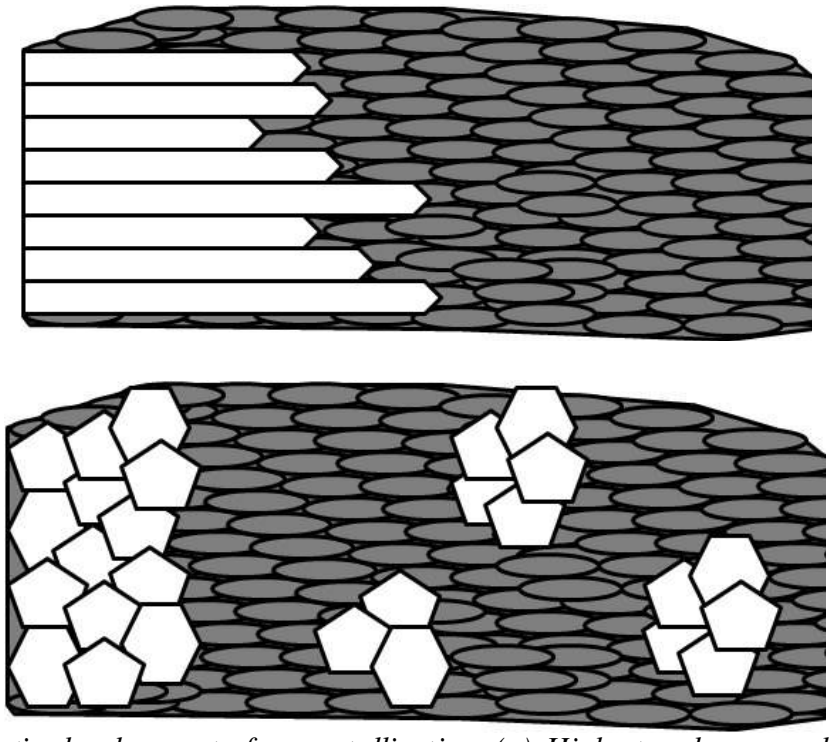

Fig. 1.3. *Schematic development of recrystallization, (a) High stored energy, high anisotropic grain growth velocity, (b) Low stored energy, low anisotropic growth velocity [79].*

1.6. Electron Backscatter Diffraction (EBSD) Characterization of ODS Steels

In literature, few studies on microstructure and microtexture characterization of high (>12%) Cr ODS steels [8, 54, 92-98], through electron backscatter diffraction (EBSD) is reported to assess:

- Nano structural aggregates of grains, bimodal distribution, and aspect ratio of grains.
- Role of oxide particles on deformation microstructure.
- Dynamic recrystallization during thermo mechanical processing
- Secondary recrystallization upon high temperature heat treatments
- Grain boundary analysis and their migration

The evolution of recrystallization microstructures in oxide dispersion strengthened alloys has been investigated by a number of researchers, but the precise mechanism of secondary recrystallization still remains ambiguous. A quantitative description of the dynamic or secondary recrystallization to correlate with the thermo mechanical treatment is also not documented yet, to the best of my knowledge. EBSD is a very effective tool to characterize such changes, which involves determination of grain orientations, grain boundary misorientation angles, grain boundary character distribution etc.

EBSD technique has been extensively used in this thesis to analyse the resultant microstructures after consolidation of powders, deformation and annealing treatments and has been judiciously employed to identify the micromechanisms governing the evolution of texture and anisotropy in ODS steels. In addition, a better understanding of texture heterogeneities at the substructure level has enabled the optimization of thermo-mechanical treatments to minimize anisotropy effects. Further, the grain boundary character distribution in ODS steels during deformation and annealing process have been evaluated using EBSD misorientation data. EBSD

analysis together with serial sectioning procedures has also enabled the five parameter description of interface boundaries to obtain an insight into the micromechanisms associated with energy minimization during annealing.

1.7. Scope of the Thesis

Typically high (>12%) Cr ODS ferritic steels are fabricated through a powder metallurgical route followed by various sequences of cold or warm working and annealing treatments. However, development of anisotropic microstructure during fabrication, which induces severe anisotropy in mechanical properties, still remains a point of significant concern for their final applications. In view of the above, a systematic experimental and computational study has been carried out in the present thesis and the following themes have been addressed.

- Optimization of consolidation conditions for 18% Cr oxide dispersion strengthened (ODS) ferritic steel through evaluation of density, microstructure, microtexture and mechanical properties.
- Design of an optimum thermo-mechanical treatment (TMT) to minimize anisotropy in 18Cr ODS ferritic steel.
- Description of grain boundary character distribution (GBCD) in 18Cr ODS ferrtic steel during consolidation, deformation and annealing processes.
- Demonstration of a methodology for describing the interface boundaries based on five parameter characterization in ferritic and austenitic steels with high and low stacking fault energy (SFE) respectively.

1.8 Organization of the Thesis

This thesis contains seven chapters in all. The organization of the thesis is given below:

Chapter 1 deals with a detailed literature review on the nano structured oxide dispersion strengthened (ODS) steels and its potential requirements for high temperature structural applications in fast reactors vis -a- vis the conventional austenitic and 9Cr ferritic/martensitic steels. This is followed by a brief introduction to the development of high Cr (>12%Cr) ODS ferritic steels which includes their historical development, current status and challenges during processing. The high (<12%) Cr ferritic ODS steels are known to develop directional dependent microstructures during fabrication that lead to severe anisotropy in mechanical properties. The anisotropy of mechanical properties is explained by the combined effect of fine substructure within elongated grains of large aspect ratio and precipitates along the extrusion direction. Strategies to reduce or mitigate anisotropy through an optimum thermo-mechanical process have also been reported in literature. This chapter also includes a brief discussion on the evolution of the Electron backscatter diffraction (EBSD) technique to characterize various facets of the structure namely morphology, micro-texture and grain boundaries in this study. The broad objective of the work and the scope of the thesis are also outlined.

The second chapter titled " Experimental Details" gives a brief descriptions on powder synthesis, consolidation methods and annealing treatments followed by structural characterization techniques namely synchrotron XRD, metallography, Scanning Electron Microscopy (SEM), Differential Scanning Calorimetry (DSC) and EBSD including data analysis. Details of property evaluation using tensile, creep and instrumented hardness is included. The operation conditions, calibration and error analysis for each experimental technique are also described. A brief account on special methods like serial sectioning, quaternion algebra, JMatPro and VPSC modeling used in the thesis are also presented.

The third chapter titled "Optimization of consolidation conditions for 18% Cr oxide dispersion strengthened steel through evaluation of microstructure and mechanical properties" presents a systematic study to understand the densification behavior and microstructural evolution of Fe-18Cr-2W-0.25Ti-0.1C-0.35Y_2O_3 ferritic steel (18Cr ODS ferritic Steel) during consolidation by different powder metallurgy routes. The steel powders were consolidated by cold isostatic pressing (CIP) and sintering, CIP and hot isostatic pressing (HIP), spark plasma sintering (SPS) and hot extrusion (HE) processes. The effective process parameters of consolidation have been arrived at based on measurement of relative density, microstructural and microtexture analysis. The room temperature hardness and high temperature creep properties have been evaluated for comparison of the consolidation methods and an optimum process has been identified.

In the fourth chapter titled "Study of deformation and recrystallization behavior in ODS 18Cr ferritic steel", the strategies for effective heat treatments have been identified to reduce anisotropy during unidirectional cold rolling of hot extruded 18Cr ODS ferritic steel. DSC analysis was carried out on deformed 18Cr ODS ferritic steel to identify the regime of recovery and recrystallization based on stored energy release during the heating cycle. Also, microstructural analysis using SEM based EBSD studies has been made to assess the effectiveness of the designed heat treatments. Further, repeated cold working followed by two step heat treatment has been carried out to achieve an ultra-fine grained microstructure and randomization of texture. Hardness measurements have been carried out to support the microstructural features and correlate with the mechanical properties of the steel after the above treatments.

The fifth chapter on "Study of high temperature processing domain in ODS 18Cr ferritic steel", the processing map of an 18Cr ODS ferritic steel is generated by hot compression tests using Gleeble simulator and the hot working parameters have been identified. The evolution of microstructure and microtexture in the processing domains has been studied using EBSD analysis. In addition, VPSC constitutive models are used to predict the resultant texture from a distinct initial texture. The resultant texture distribution obtained by the prediction and experimental EBSD analysis has been compared to understand the underlying micromechanism of texture evolution during processing of the steel at high temperatures.

In the sixth chapter titled "Analysis of five parameter interface boundaries in advanced steels", the grain boundary character distribution in 18Cr ODS ferritic steel during deformation and annealing process is presented. 18Cr ODS ferritic steel in consolidated form shows high fraction of low energy coincidence site lattice (CSL) boundaries than the theoretically calculated values, which reduces during cold working and annealing processes. Further, the frequency of low energy CSL boundaries is found to reduce during the annealing process due to diffusion assisted grain boundary migration. In order to understand the mechanism driving the energy minimization during annealing, a methodology for describing the interface boundaries in low and high SFE alloys namely austenitic and ferritic steels respectively has been developed. EBSD in conjunction with serial sectioning procedure has been used to demonstrate a five parameter description of interface boundaries in annealed 9Cr-1Mo steel and 304HCu austenitic stainless steel.

The last chapter summarizes the important findings of the thesis, and suggests additional research work for further study.

Experimental Details

This chapter describes the details of the experimental and computational methods employed in the present study. The chemical composition of the three steels namely 18Cr Oxide Dispersion Strengthened (ODS) ferritic steel, 9Cr-1Mo ferritic martensitic steel and 304HCu austenitic stainless steel (SS 304HCu) used in this study are tabulated in Tables 2.1, 2.2 and 2.3. The steels were subjected to several thermo-mechanical treatments and systematically characterized for microstructure, microtexture and mechanical properties, the details of which are elaborated in this chapter. Brief descriptions on powder synthesis, consolidation methods and annealing treatments, followed by structural and microstructural characterization techniques namely synchrotron X-ray Diffraction (XRD), metallography, Scanning Electron Microscopy (SEM), Electron Backscattered Diffraction (EBSD) and including data analysis are presented sequentially. Details of mechanical property evaluation using tensile, creep and instrumented hardness techniques and thermal property evaluation by Differential Scanning Calorimetry (DSC) are also provided. The operating conditions, calibration and error analysis for each experimental technique are also included. A brief account on special methodologies like quaternion algebra, JMatPro and VPSC modeling used in the thesis are also presented.

Table 2.1. Chemical composition (wt %) of 18Cr ODS ferritic steel powder used in the study

C	Cr	W	Mn	Si	Ti	S	P	Y_2O_3	Fe
0.016	18.14	2.30	0.12	0.09	0.25	0.001	0.008	0.35	Bal.

Table 2.2. Chemical composition (wt %) of 9Cr-1Mo steel used in the study

C	Cr	Mo	Si	Mn	Ni	S	P	Fe
0.10	9.27	1.05	0.75	0.63	1.12	0.001	0.02	Bal.

Table 2.3. Chemical composition (wt %) of SS304HCu stainless steel used in the study

C	Cr	Ni	Cu	Nb	Si	Mn	S	P	Fe
0.1	18	9	3	0.5	0.75	0.63	0.001	0.02	Bal.

2.1. Powder Synthesis and Consolidation

2.1.1. Mechanical Alloying

The argon gas atomized pre-alloyed Fe-18Cr-2W-0.25Ti steel powder was blended mechanically with $0.35Y_2O_3$ (wt%) with particle size of 30 to 50 nm. Milling was carried out at Institute of Minerals and Materials Technology, Bhubaneswar, in planetary ball mill (Model: In-Smart, India) with grade 440C stainless steel vial and balls of hardness of 832 HV. The milling mechanism involves frequent high energy impact of balls resulting in milling of the powder. In addition, the rotation of the base plate provides the centrifugal force to the grinding balls. Independent rotation of vials, in opposite directions, makes the balls collide on the inner wall of the vial [71, 99-101]. Due to the rotation of the vials in the opposite direction, grinding to a major extent is by friction. In the present work, the base plate rotation is fixed at 300 RPM, whereas the vial rotates at 150 RPM with the ball to powder weight ratio of 10:1 and a milling duration of six hours. Post milling, the powder was collected from the vial inside a glove box maintained under argon atmosphere and preserved in a sealed container to avoid oxygen pickup.

2.1.2. Cold Isostatic Pressing (CIP) Followed by Sintering

Isostatic pressing at room temperature (CIP) followed by sintering of metallic and ceramic powders is an important powder metallurgy route, which imparts uniform pressure distribution within the compact and consequently, more uniform density at a given compaction pressure and relatively defect free compacts when applied to brittle or fine powders [102]. The milled powders are sealed in a flexible cylindrical rubber mould (neoprene rubber) and assembly was immersed in the fluid. The rubber mould helps in transmitting the pressure during pressurization of hydrostatic liquid (water) during the process. Figure 2.1 shows the press and a schematic of the cross-section of the mould assembly. Compared to die compaction, CIP

provides more uniform pressure distribution within the compact due to absence of die wall friction and greater area over which pressure is applied. It produces compacts of practically uniform grain structure and density, independent of length-to-diameter ratio.

In the present study, mechanically alloyed powder of 18 Cr ODS steel was compacted by CIP by gradual increase of applied pressures in the range of 0-100 MPa in 3-4 minutes, held for 2 minutes, increase to 100-200 MPa, held for 2 minutes, and then increased to 200-300 MPa in 3-4 minutes, and then held for 15 minutes. The powder is rammed inside the flexible mould and the sealed mould is pressurized in a vessel filled with hydrostatic fluid (water). During pressurization, care has to be taken that all seals must be under compression to prevent leakage of the pressurization fluid into the powder. Cylindrical rubber mould is used for easy transmission of pressure to the powder particles from all the directions. Further, in order to establish the metallurgical bond and achieve good densification, the compact was sintered at different temperatures between 1323 to 1523 K (1050 to 1250 ℃) at 50 K intervals in hydrogen (reducing) atmosphere. Near cylindrical shaped specimens of ~ 25 mm diameter and 40 mm length were obtained by CIP and sintering process.

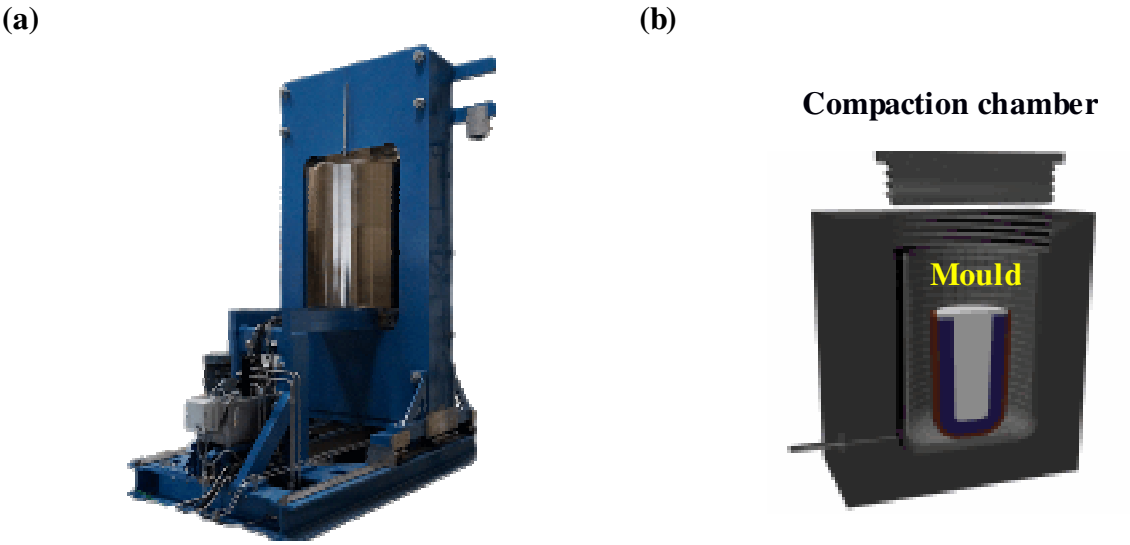

Fig. 2.1. *(a) Cold isostatic pressing equipment used in the present study and (b) schematic showing the compaction chamber and mould.*

2.1.3. CIP Followed by Hot Isostatic Pressing (HIP)

Sintering occurs when heat is applied to powder or to a body containing pores. The driving force for sintering is the reduction in surface area associated with pores. Further, surface diffusion takes place at the contact point of particles with high strain due to dislocation bonding during CIP. However, HIP results in a better densification in comparison to CIP/sintering due to further application of compaction pressure at high temperature. The combination of pressure and temperature is used to achieve a higher density at a lower temperature and pressure than would be attained by sintering or CIP alone [103]. The lower temperature is beneficial to control grain growth. In the present study, the CIP product was processed by HIP at 1423 K (1150 ℃) and isostatic pressure of ~200 MPa in argon atmosphere to avoid chemical reactions.

2.1.4. Spark Plasma Sintering (SPS)

Applicability of a powder depends on the ability to reach near theoretical density through a suitable method. In this respect, SPS of powders is a relatively new sintering based technique having specific advantages for ODS steel production. Compared to other conventional techniques such as HE and HIP, which has a ramp rate of 50 - 80 K/min and a few hours of holding time, SPS has the advantage that it is characterized by very fast heating (up to 2000 $Kmin^{-1}$) and cooling rates and short holding times (minutes) to achieve near theoretical density [104-107]. In addition to that, SPS works at a lower temperature of compaction and relatively low applied pressure [104-107]. During the SPS process, the powder to be consolidated is loaded into an electrically and thermally conductive graphite mould and a large DC pulsed current (1000–5000 A) is applied under a uni-axial pressure. The heat in SPS rapidly generates internally, which is very different to pressure less or hot press sintering [108-112]. When current passes through the graphite mould the powder is heated from both outside and inside owing to

the Joule heating from the intrinsic electrical resistance of the powder material, resulting in a consolidated specimen [108-112]. The schematic representation of an SPS unit is shown in Fig. 2.2. The SPS unit consists of a pressure device with upper and lower water-cooled hydraulic rams, a DC generator that generates high current pulses and a computer based process controller. The shrinkage, pressure, average voltage and current are recorded during the process. The powder is filled inside the conductive graphite die for sintering with optical pyrometer or thermocouple as temperature detector [113]. The high densification of the product in SPS due to rapid heating and cooling rates is responsible for the retained intrinsic properties of nano dispersoids [114].

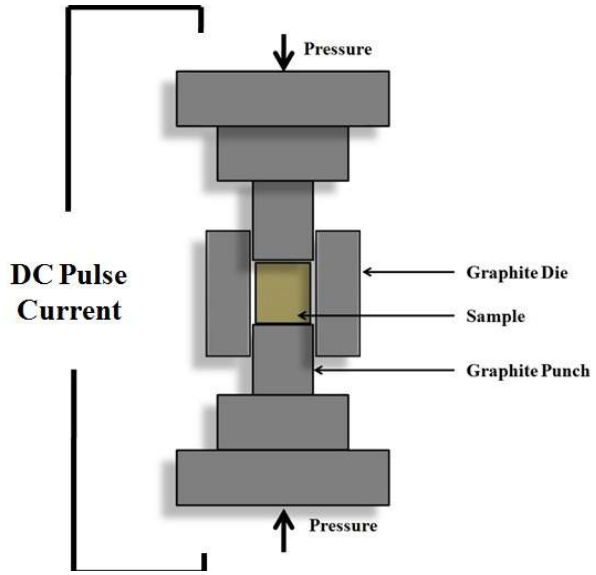

Fig. 2.2. *Schematic diagram of an SPS unit containing an assembled graphite die and punches.*

In this study, the milled ODS powders were consolidated using SPS (Dr. Sinter SPS-625, Fuji Electronic Industrial Co., Ltd., Japan) by a gradual increase of applied axial pressure from 0 to 40 MPa using a cylindrical graphite die and plunger (30 mm outer diameter) for transmitting the pressure. The temperature was simultaneously raised from room temperature to the selected range of 1273 to 1423 K (1000 to 1150 ℃), which was attained within 10 minutes, followed by a soaking time of 5 minutes before cooling to room temperature. The temperature was measured

by a K type thermocouple attached to the die. The progressive movement of the plunger with time, temperature and pressure was monitored. Specimens with diameter and thickness of 30 mm and 15 mm respectively were produced by SPS at different temperatures.

2.1.5. Hot Extrusion (HE)

In the present study, consolidation using hot extrusion (HE) process was carried out in collaboration with Nuclear Fuel Complex (NFC), Hyderabad. Details of consolidation are as follows [115]:

- The pre-alloyed steel powder with nominal composition of Fe-18Cr–2W-0.01C–0.2Ti and average particle size of ~ 100 μm was produced by inert gas atomization in collaboration with International Advanced Research Centre for Powder Metallurgy (ARCI), Hyderabad**.** The steel powder was blended with 0.35 weight % Y_2O_3 powder of 30-50 nm size under argon atmosphere in a high-energy horizontal attritor mill (Simoloyer CM-20) with a rotational speed of 550 rpm for duration of ~ 6 h using a ball to powder ratio of 7.5:1. The blended powders were packed in mild steel cans of 72 mm diameter and hot upset forged at 1323 K (1050 ℃) under a pressure of 800 MPa to produce forged billets.
- The forged billets were extruded at 1423 K (1150 ℃) with extrusion speed 25-30 ms^{-1} at a pressure of 620 MPa into rods of diameter 24 mm with extrusion ratio about 20.

2.2. Processing Treatments

Several treatments were carried out on the three steels with an aim to obtain fine grain microstructures and random microtexture in a muffle furnace which is well calibrated with a temperature accuracy of ±5 K and the details of the treatments are given below:

18Cr ODS ferritic steel:

In order to study the mechanism of recovery and recrystallization in deformed steel, specimens from the extruded rod were sectioned using a precision cutting machine along two perpendicular directions namely along the direction of hot-extrusion termed as ED and the perpendicular or transverse direction termed TD section. A set of specimens cut along ED and TD sections were cold rolled by 50% and annealed for one hour at 1420 K (1147 °C) for recrystallization of ferrite grains. In addition, the deformed ED section of the cold rolled steel was subjected to a double step heat treatment consisting of annealing at (a) 1350 K (1077 °C) for 2 h followed by (b) 1420 K (1147 °C) for 0.5 h. The first annealing at low temperature is intended to reduce the stored energy, while the second annealing for short duration at high temperature is aimed to achieve a fine recrystallized microstructure and restrict grain growth. Further, repeated rolling and two step heat treatment was carried out on ED specimens to systematically assess the evolution of microstructure at each step. A uniform heating rate of 7 $Kmin^{-1}$ was maintained for all heat treatments. Above treatments are summarized in Table 2.4.

9Cr-1Mo steel:

Samples of typical dimensions 10 mm x 10 mm x 5 mm were used for carrying out the heat treatment namely, 'Isothermal Annealing' (IA), which consisted of austenitizing for 1h at 1323 K (1050 °C) followed by isothermal annealing for 4 h at 1023 K (750 °C), and air cooling to room temperature. This austenitizing treatment is aimed at producing homogeneous γ-grains, and the isothermal annealing at a temperature close to nose of C-curve of TTT diagram was designed to complete the diffusional mode of transformation in a short time to obtain a polygonal ferrite grain structure [116]. The IA specimen was further annealed for 50 h at 1093 K (820 °C) which is designated as IAA. The additional annealing was intended to induce grain growth of

ferrite and to allow the microstructures to adopt potential low energy boundary configurations. A higher annealing temperature (< Ac_1 ~1113 K (840 ℃)) was adopted to accelerate the diffusion kinetics and stimulate significant changes in grain boundary character distribution (GBCD).

Table 2.4. Processing schedules adopted for 18Cr ODS ferritic steel in the present study

Initial condition	Processing			Specimen Code
	Deformation	Heat Treatment		
		Temperature (K)	Time (h)	
Hot Extruded	----	----	----	ED
	----	----	----	TD
ED	50%	----	----	EDR
TD	50%	----	----	TDR
EDR	----	1420	----	AEDR
TDR	----	1420	----	ATDR
EDR	----	1350	2	A_1EDR
		1420	0.5	
A_1EDR	50%	1350	2	A_2EDR
		1420	0.5	
A_2EDR	50%	1350	2	A_3EDR
		1420	0.5	

*Note: ED, TD stands for extrusion and transverse directions respectively; R stands for rolling.

304HCu austenitic stainless steel:

Three sets of heat treatment namely, 'Recrystallization' (R), 'Annealing' (A and A1) and 'Extended Annealing' (EA) were carried out after 20% cold deformation of the steel. Treatment 'R' consisted of annealing for 1h at 1073 K (800 ℃) to attain fully recrystallized fine grain microstructure; treatment 'A' corresponds to annealing at 1373 K (1100 ℃) for 1h to get a homogeneous equiaxed microstructure [117, 118]. Treatment A1 corresponds to further annealing of the specimen subjected to treatment 'A' at the same temperature (1373 K (1100 ℃)) for an additional 1h to identify grain boundary migration. The treatment 'A1' was carried out in a high vacuum furnace (10^{-6} bar) to protect the specimen surface for repeated analysis of the same region before and after annealing. Further high-temperature annealing at 1573 K (1300 ℃)

(treatment 'EA') was carried out to induce grain growth and allow the microstructure to adopt possible low energy boundary configurations to stimulate significant changes in GBCD.

2.3. Characterization

The steels were characterized by employing a variety of techniques, which included optical microscopy, Scanning Electron Microscopy (SEM), Electron backscattered diffraction (EBSD) and Synchrotron XRD. The recovery and recrystallization domains were measured by Differential Scanning Calorimetry (DSC). The specimen preparation, operating conditions and procedure adopted for analysis for the techniques employed in the present study are given in the subsequent sections.

2.3.1. Specimen Preparation

Standard metallographic specimen preparation methods were employed for Scanning Electron Microscopy, synchrotron XRD studies, and Hardness measurements. Flat surface was obtained by successive grinding with SiC abrasive discs. Further, a mirror finish of the surface was obtained by polishing with 1 micron diamond paste with kerosene as the lubricant / coolant. In addition, a final electropolishing step (20% acetic acid in methanol electrolyte, 283 K, 15 V, 20 sec) was used to obtain strain-free surface suitable for EBSD examination.

2.3.2. Scanning Electron Microscopy (SEM)

SEM analysis was carried out using Philips XL-30 ESEM and Helios Nanolab 600i Field Emission Scanning Electron Microscope (FE-SEM) at 20 kV in the Secondary Electron (SE) imaging modes. The various SEM operation tasks such as: restart/shut down of system, control/monitoring of operating parameters, adjusting and optimizing imaging conditions and storage of output image data were performed through the computer console. The metallographic

specimen was firmly pasted on aluminum stub, and introduced into the stage holder of the SEM chamber. A vacuum level better than $6X10^{-5}$ bar was achieved using a turbo molecular pump backed by primary pumping system before switching 'ON' the high voltage. Focusing and beam raster conditions were adjusted to optimize image quality, and brightness/contrast settings were further tuned to obtain SE and BSE images of good clarity.

2.3.3. Electron Backscatter Diffraction (EBSD)

EBSD is a powerful technique that captures electron diffraction patterns from crystals, constituents of material [119, 120]. The raw data of an EBSD scan consists of identification of crystal type, and its orientation represented using Euler's angle, as a function of spatial co-ordinates in the region of interest [121, 122]. Captured patterns can then be used to determine the crystallographic orientation or texture of materials, which is strongly correlated to both properties and performance of materials. A complete and quantitative representation of sample microstructure can thus be established with EBSD [123].

The 70° pre-tilt specimen holder aids in obtaining higher intensity, which is effectively collected by the EBSD detector positioned at the horizontal position. A stationary electron beam interacts with a tilted crystalline specimen (~70^{o} with the horizontal) and the diffracted electrons form a pattern that is detected on a fluorescent screen, as shown schematically in Fig. 2.3. A working distance of about 10 mm was found optimum. Based on a number of trial scans, image grabbing by 4X4 binning and an exposure time of ≅ 40 ms was found to be optimum to obtain well resolved band patterns (for good indexing). EBSD detector signal averaged over the region of interest was used to find the central halo distribution of diffracted BSE signals, which was then used for background subtraction to get an EBSD band pattern with good contrast. Appropriate magnifications were chosen for the SEM/EBSD scans to include reasonable number

of grains with a scan step (0.06-1) μm and optimized settings were used to obtain good angular resolution of about 0.1º [124]. Crystal orientation data was obtained by post-processing and analyzing the microtexture scan data using TSL-OIM™ software.

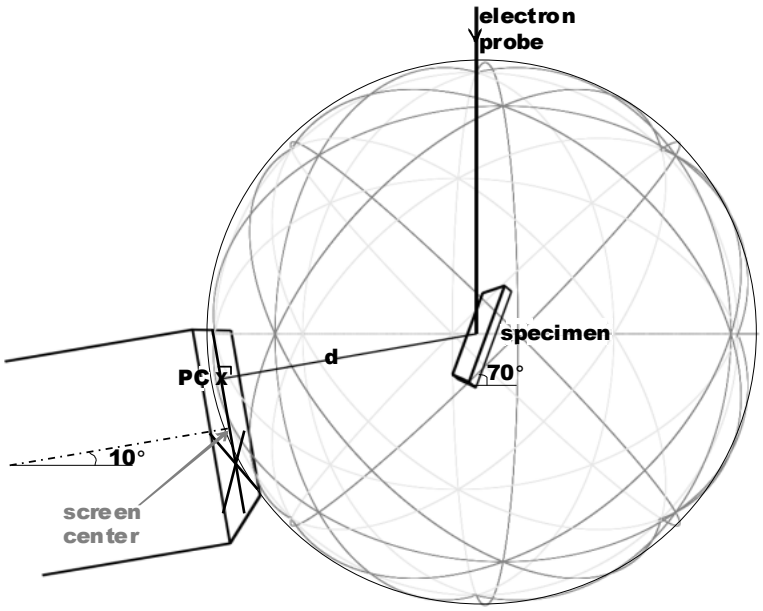

Fig. 2.3. *Illustration of specimen and detector geometry, spherical Kikuchi map construction of crystal plane trace and its gnomonic projection as straight lines collected over a small solid angle covered by the detector screen.*

The intercept method (length of the average of horizontal and vertical intercept) is used to measure the grain size from EBSD crystal orientation map. A misorientation criterion of low angle (5-15°) (LAGB) and high angle (>15°) (HAGB) grain boundary between neighboring pixels was used to classify the grain boundaries [125, 126] and Σ3 twin boundaries (60º @ <111>) were evaluated using Brandon's criterion [127]. The data was found to vary within ±1% and standard deviation for GBCD and grain size was found to be within 0.8%. The extent of local deformation was evaluated by calculation of the average misorientation angle between a given pixel and its surrounding pixels. Several neighboring domains were considered for defining the Kernel average misorientation (KAM) through local misorientation angles < 2º

[128, 129]. Misorientation angle above 2° between adjacent pixels were ignored, so as to exclude the misorientations associated with discrete sub-grain and grain boundaries. The intensity distribution in pole figures and inverse pole figures were analyzed in this study and approximated by harmonic series expansion with a tolerance angle criterion of 5° to determine the extent of preferred orientation for each specimen [130].

2.3.4. Synchrotron XRD

Synchrotron XRD experiments on ball milled 18Cr steel powder before and after mechanical alloying with Y_2O_3 were carried out using angle dispersive x-ray diffraction (ADXRD) beamline (BL-11) at Indian Synchrotron Source (Indus 2), at RRCAT Indore . The high brilliance of synchrotron source as compared to conventional source enabled the identification of minor phases of very low volume fraction. A monochromatic X-ray beam (λ = 0.44917 Å) was used to record the diffraction pattern in reflection geometry using the image plate detector setup. FIT2D software was used to transform the image plate data into intensity vs. 2θ data.

2.3.5. Differential Scanning Calorimetry (DSC)

DSC studies on extruded (ED) and 50% cold worked extruded (EDR) rods were carried out in a Setaram Setsys 1600 heat flux differential scanning calorimeter under flowing high pure Ar-gas atmosphere (50 $mlmin^{-1}$) at heating rates of 7, 15 and 30 $Kmin^{-1}$. Small specimens of about 2x2x2 mm^3 with mass in the range of 80 -100 mg and flat surfaces were used for DSC experiments to minimize the thermal gradient and noise. Care was taken to ensure uniformity in mass and good surface flatness, for a reliable and reproducible measurement of stored energy.

Detailed procedures for baseline, temperature and heat flow calibration during the DSC experiments are reported by Raju et al. [131, 132].

In the present study, an empty cylindrical alumina crucible with a volume of 100 µL is taken as reference and the sample is loaded into an identical crucible. Before starting the experiment, the experimental chamber consisting of DSC probe and the furnace is evacuated and purged with pure argon gas with a flow rate of about 50 ml per minute. The flow rate is maintained by means of electronic mass flow controller (MFC) throughout the experiment. An argon pressure of about 1300 mbar is maintained in the graphite furnace chamber. In the first step of the experimental schedule, the furnace temperature is gradually raised to 473 K (200 ºC) at a heating rate of 5 or 10 $Kmin^{-1}$ and is allowed to stabilize at this temperature for about 15 minutes. This leads to a smooth baseline, which ensures the attainment of thermal equilibrium of the system before starting any measurement that is essential for quantitative DSC experiments. Following this step, suitable heating and cooling programs are adopted. Fresh samples were employed for each run and a few runs were also repeated for select heating rates (10 and 100 K min^{-1}) in order to ensure the reproducibility.

2.4. Evaluation of Mechanical Properties

2.4.1. Instrumented Hardness

Hardness measurements were carried out using a Zwick Roell instrumented hardness tester (Model No.: BH10.ZHN.001) with a Vickers indenter with 500 mN force in constant displacement mode with a holding period of 20 s. The fast hardness module conforming to ISO 14577 was used to carry out the measurements. The function at the instant of measurement gives the hardness for the material with elastic moduli (related to stiffness) and dynamic

viscoelastic properties such as penetration rate during the application of constant load [133]. The average experimental values were calculated based on 20 tests.

2.4.2. Compression Test (Gleeble Simulator)

The hot compression tests were carried out using a Gleeble simulator (Model No.: 1500D). Supplementary thermocouples and infrared pyrometer were attached for precise feedback control of specimen temperatures. The Gleeble systems run thermal tests typically 3 to 10 times faster as compared to conventional furnace equipped machines, because of the unique high speed heating method. The grips that hold the specimen possess high thermal conductivity, which enables high cooling rates in Gleeble 1500D. An additional water quench system was also provided to attain further high cooling rates for the specimen and to avoid temperature gradients. Further, the mainframe controller in the system keeps a constant true strain rate during deformation. The axisymmetric compression test is carried out by compressing the cylindrical sample between two parallel platens and the displacements of the platens impose the axial compression. In this study, cylindrical specimens of 9±0.1 mm height and 6±0.1 mm diameter were fabricated from the extruded rod for the hot compression tests. During compression testing at high temperatures, it is reported that the contact surface experiences a higher stress than the center [134]. This means a higher possibility of sticking to the die, which could lead to high strain level and increase in the friction coefficient as well. Application of lubricant helps in reducing the friction. Hence, the flat faces of the cylindrical samples were grooved lightly with concentric circles upto 0.5 mm depth for holding the lubricant to reduce the effect of friction [135]. The thermocouple was welded to specimen surface for precise temperature measurement during testing. Specimens were held for 5 minutes at the testing temperature prior to the deformation process to attain equilibrium. The specimens were

deformed to a maximum strain of 50% at a constant true strain rate in the range 0.01 s^{-1} to 10 s^{-1} in the temperature range of 1323 K (1050 ℃) to 1473 K (1250 ℃) at intervals of 50 K, followed by immediate cooling to suppress any diffusional transformation during cooling. A total of 16 specimens were used for each of the four strain rates and four temperature conditions.

2.4.3. Tensile Test

Tensile tests were carried out on plate specimens cut out from the hot extruded 18Cr ODS ferritic steel rod. Specimens were fabricated from the two perpendicular directions of the extruded rod as per the specimen geometry shown in Fig. 2.4. The loading axes are parallel and normal to the direction of extrusion for 'ED' and 'TD' specimens respectively. Tensile tests were conducted using Hung Ta-2402 universal tensile testing machine at a strain rate of 10^{-3} s^{-1}. The total length of the specimen was 20 mm and gauge dimensions were 10 mm in length 2 mm in width and 1.5 mm in thickness. The gauge length of 10 mm (five times of diameter) as per ASTM E8M standard was maintained for calculating strain and stress was estimated by dividing the load value by initial area [136]. Selected test temperatures were 298, 823 and 973 K (25, 550 and 700 ℃).

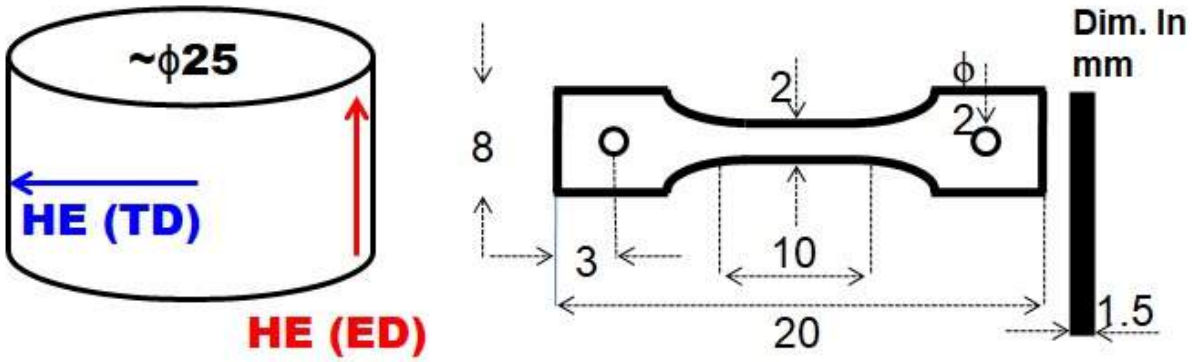

Fig. 2.4. *Schematic of tensile specimen of 18Cr ODS ferritic steel after consolidation by hot extrusion (HE) (all dimensions are in mm).*
**Note: ED and TD are parallel and perpendicular to extrusion direction respectively.*

2.4.4. Creep Test

The creep behavior of consolidated 18Cr ODS ferritic steel was studied on miniature specimens using conventional creep testing method. Flat creep specimens of 2 mm gauge width and 10 mm gauge length were used for the measurement, since a ratio of 1:5 is known to give higher accuracy in strain measurement (Fig. 2.5) [137]. The thicknesses of the specimens were 1.5 mm. Creep tests were carried out under atmospheric conditions at a constant stress of 300 MPa, at 873, 923 and 973 K (600, 650 and 700 ℃). The temperature was maintained within ±1 K and the elongation of the specimen was monitored using an extensometer and digital dial gauge attachment.

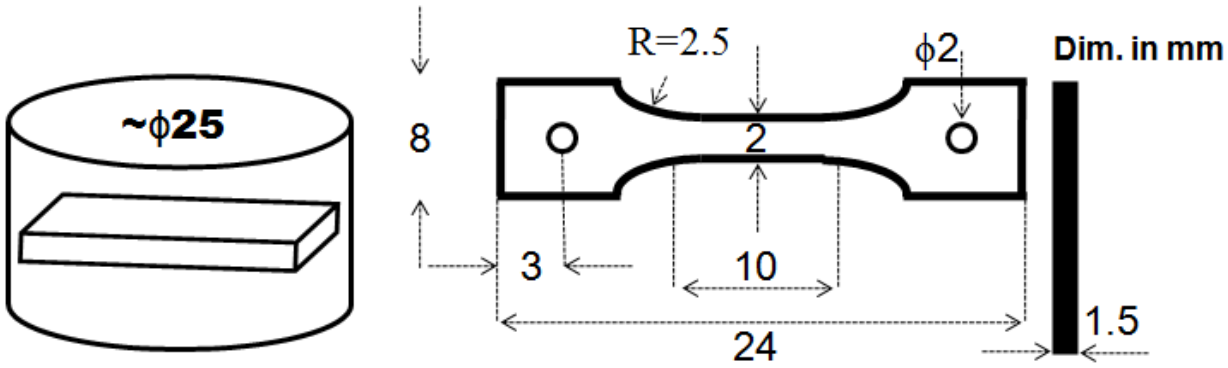

Fig. 2.5. *Schematic of creep specimen of 18Cr ODS ferritic steel after consolidation (all dimensions are in mm).*

2.5. Serial Sectioning Method and Quaternions

The serial sectioning procedure offers a method to measure two parameters [azimuth (γ) and polar angles (β)] in addition to rotation angle ω – rotation axis r̂ pair from the shift in grain boundary trace between two successive overlay images. These parameters define the grain boundary plane inclination with respect to specimen X-Y reference frame, from which the information about grain boundary interface plane can be derived.

The serial sectioning method has been used to study the interface plane of grain boundaries. This method involves the following steps:

- Marking of the region of interest (ROI) using four fiducial marks made by Vickers hardness indentation using square shaped diamond pyramid indenter with a dihedral angle of 136° to locate and align the specimen before each EBSD scan
- EBSD characterization of ROI
- Controlled removal of material from the surface by mechanical polishing
- EBSD characterization of the serially sectioned surface
- Comparison of the EBSD scans from two consecutive sections.

This method minimizes the experimental inaccuracy due to remounting by the parallel mounting of the specimen using EBSD 70° pre-tilt stub edge, and careful uniform mechanical polishing maintaining the parallelism between the two sections. The serially sectioned image was translated horizontally along the x and y-axes with respect to the EBSD image from the previous surface to coincide with the indentation center, followed by rotation to align the diagonals. Further, the indentation made by the pyramidal indenter is correlated with depth of the indentation, i.e., depth = diagonal length / 7 [138, 139], and the exact separation between two sections is calculated to determine the shift in grain boundary trace.

In addition, calculations based on quaternion algebra have been adopted to arrive at orientation distribution of interface boundaries (Chapter-6). Quaternions are a number system analogous to complex numbers and can be used to represent orientation in three dimensions. The qaternion can be represented as,

$$Q = (a, b, c, d) = a + bi + cj + dk \quad (2.1)$$

where a, b, c and d are real numbers and i, j and k are imaginary numbers. A unit quaternion has its norm equal to 1, and it provides a convenient mathematical notation for representing orientation and rotations of objects in three dimensions. A rotation by angle θ (anti-clockwise) about a unit rotation axis can be denoted by quaternion unit quaternion q:

$$q(\theta,\hat{n}) = q\left(\theta, n_1\hat{\imath} + n_2\hat{\jmath} + n_2\hat{k}\right) = cos\left(\theta/2\right) + sin\left(\theta/2\right)\left[n_1\hat{\imath} + n_2\hat{\jmath} + n_2\hat{k}\right] \quad (2.2)$$

For a unit quaternion the square root of the sum of squares of the four scalar components of the quaternion is 1. The quaternion denotes the basic orientation descriptor linking the crystal orientation with the reference sample axis. The function relating the parameters of single step rotation by quaternion and the Euler angles can be express as,

$$\boldsymbol{q}(\omega,\hat{r}) = cos\left(\frac{\Phi}{2}\right)cos\left(\frac{\varphi_1+\varphi_2}{2}\right) + sin\left(\frac{\Phi}{2}\right)\left[cos\left(\frac{\varphi_1-\varphi_2}{2}\right)i + sin\left(\frac{\varphi_1-\varphi_2}{2}\right)j\right] + cos\left(\frac{\Phi}{2}\right)sin\left(\frac{\varphi_1+\varphi_2}{2}\right)k \quad (2.3)$$

The mean orientation $\bar{q}$ can be obtained by quaternion averaging method [140, 141] and $\bar{q}$ derived as,

$$\bar{q} = \frac{\boldsymbol{q^1+q^2+q^3....+q^n}}{\left\|\boldsymbol{q^1+q^2+q^3....+q^n}\right\|} \quad (2.4)$$

Detailed calculations to arrive at 5-parameters of grain boundary are included in Chapter-6.

2.6. JMatPro® Simulation

JMatPro® is used to predict the change in phase constitution as a function of temperature. In addition, JMatPro® based simulation has been used to predict the creep properties of 18Cr ferritic steel as a function of stress and temperature to correlate with the experimental results. JMatPro® uses a CALPHAD based internal database for the calculation of thermodynamic properties [142, 143]. The 'Stainless steel and General steel' module available in JMatPro® version 7 has been used in this study. Thermodynamic properties such as stability regime of

phases, phase fraction and its size variation at different temperature domains were evaluated through equilibrium calculations.

2.7. Simulation with VPSC5 Code

VPSC constitutive models have been used to predict the resultant texture from a distinct initial texture. The resultant texture distribution obtained by the prediction and experimental EBSD analysis has been compared to understand the underlying micromechanisms of texture evolution during processing of the 18Cr ODS ferritic steel at high temperatures.

The following inputs are required for the code:

- Initial crystallographic texture (grain orientations and weights).
- Single crystal properties (active slip and twinning systems, their critical resolved shear stresses, and the associated hardening parameters).
- Initial morphological texture (initial grain shapes and shape orientations).
- Parameters controlling convergence, precision and type of run.
- Optional input: strain history, rolling components, previous state of grains (POSTMORT.IN).

The output of the code is:

- Final (optionally intermediate) crystallographic and morphologic textures of each phase after deformation.
- Evolution of the stress and strain components during deformation.
- Statistics of slip and twinning systems activity during deformation.
- Statistics of average magnitudes during deformation: stress and strain-rate components and their standard deviations, average grain shape, average grain rotation, etc.

- Optional output: texture morphology of each phase, rolling components, PCYS scan, Lankford scan, Cauchy stresses, state of grains and polycrystal (POSTMORT.OUT)

2.8. Summary

To summarize, this chapter covered a comprehensive description of alloy synthesis, heat treatments, microstructure and microtexture characterizations and evaluation of mechanical properties. Brief descriptions of the techniques used in the present thesis, their principle, procedure and calibration wherever required have been provided. The experimental results analyses are also supported by computational/theoretical methods, the details of which have also been included in this chapter.

Microstructure and Mechanical Properties of Oxide Dispersion Strengthened 18Cr Ferritic Steel Consolidated by Various Methods

This chapter presents the results of a systematic study to understand the densification behavior and microstructural evolution of Fe-18Cr-2W-0.25Ti-0.01C-0.35Y_2O_3 ferritic steel (18Cr ODS ferritic Steel) during consolidation by different powder metallurgy routes. The steel powders were consolidated by cold isostatic pressing (CIP) and sintering, CIP and hot isostatic pressing (HIP), spark plasma sintering (SPS) and hot extrusion (HE) processes. The effective process parameters of consolidation have been arrived at based on measurement of relative density, microstructural and microtexture analysis. The room temperature hardness and high temperature creep properties have been evaluated for comparison of the consolidation methods and an optimum process has been identified.

3.1. Characterization of Milled Powders

Pre-alloyed powder of Fe-18Cr-2W-0.25Ti-0.01C steel was mechanically milled with 0.35 weight % of Y_2O_3. Figure 3.1(a-b) shows the SEM micrograph of the powder before and after mechanical alloying. The powder particles are observed to be spherical in shape (Fig. 3.1(a)) which is typical of the gas atomization process for powder synthesis and found to change into a flaky morphology after milling, with few large agglomerates of particles. The particles are found to be in the size range of 10-30 and 8-14 μm before and after milling respectively (Fig. 3.1(c)). Synchrotron XRD spectra of 18Cr ferritic steel and after mechanical alloying with Y_2O_3 in Fig. 3.2, shows the presence of only ferrite in both the cases and no evidence was obtained for the presence of any other phase from the XRD profiles. After milling with Y_2O_3, the ferrite peaks showed trends of shifting to lower 2θ values in addition to peak broadening of the full width at half maxima.

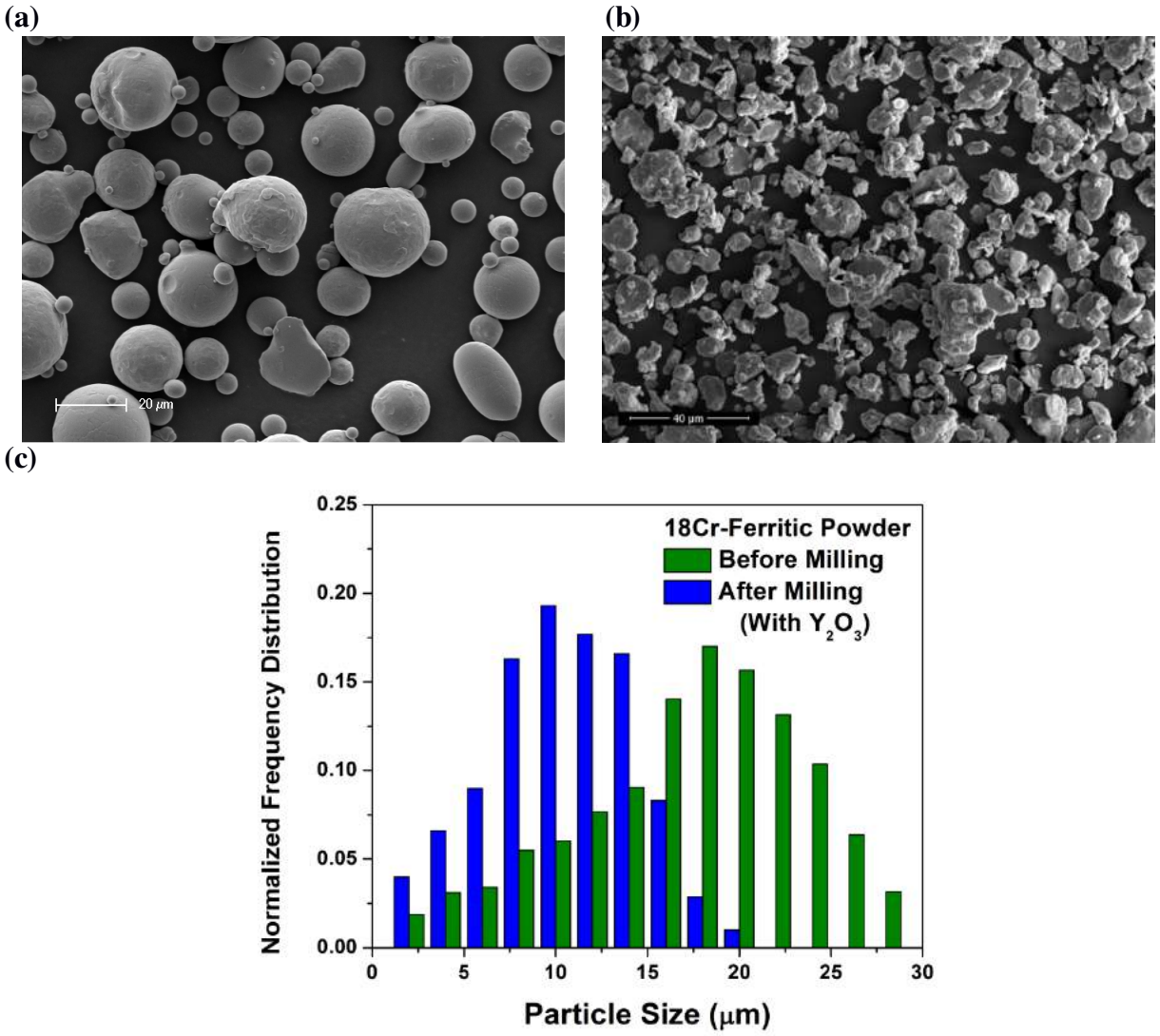

Fig. 3.1. *SE micrograph of (a) pre-alloyed 18Cr ferritic steel powder (b) mechanically alloyed 18Cr ferritic steel powder and Y_2O_3 and (c) particle size distribution before and after milling.*

The observed peak broadening is attributed to the increase in strain and decrease in crystallite size during high energy ball milling (Fig. 3.2) [108]. Although the particle size was found to be substantially large (~ 14 μm) due to repeated flattening, cold welding, fracture and re-welding during high energy ball milling, the average crystallite size estimated using Debye Scherrer analysis [109] is about 32 nm in contrast to crystallite size about 68 nm of the initial powder. Another important observation made from Fig. 3.2 is the increase in intensity of (1 1 0)

peak due to impact deformation, which indicates a particular systematic growth of $(110)_{bcc}$ crystal faces [110]. It is reported that in Fe-24Cr-15 wt% Y_2O_3 the oxide powder fragments into fine size particles and become nearly amorphous in the metal matrix during mechanical milling [104]; and nucleate into fine crystals during the subsequent processing [114]. It is reported that diffusion of Fe atom into the Y_2O_3 lattice during the course of mechanical milling causes distortion of the lattice that helps in amorphization of Y_2O_3 [115]. However, amorphization of Y_2O_3 could not be established by XRD analysis in the present study due to its low amount (~0.35 wt.%) [106, 107].

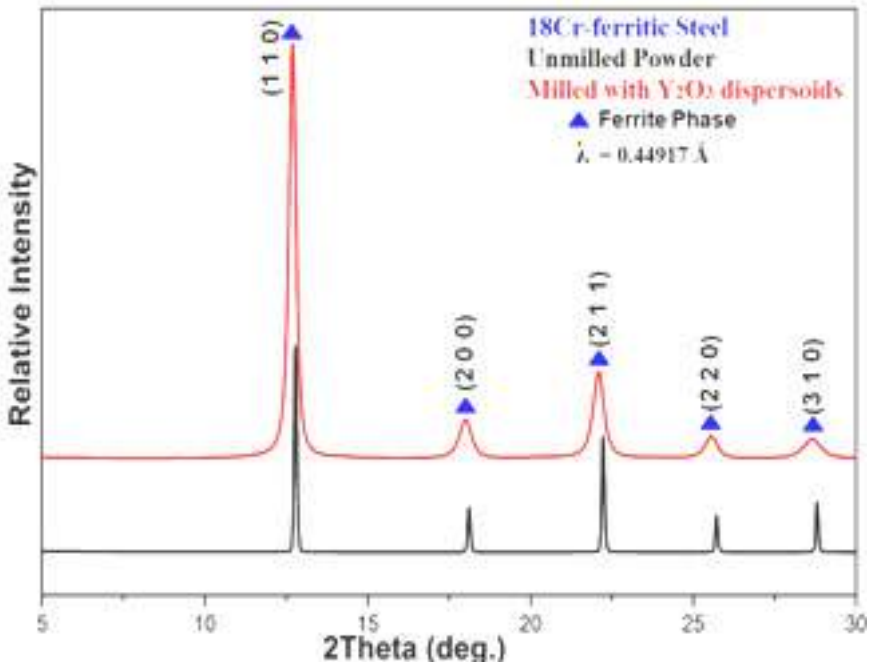

Fig. 3.2. *Synchrotron X-ray diffraction pattern of 18Cr-ferritic steel powder with and without Y_2O_3 dispersoids.*

3.2. Consolidation of Steel by Cold Isostatic Pressing (CIP) and Sintering

3.2.1. Microstructural Analysis

18Cr ODS ferritic steel powder consolidated by CIP yielded ~63% green compact density suggesting that CIP is an effective method for nearly uniform densification. Figure 3.3 shows a

typical SE image after CIP, revealing the incomplete nature of powder packing with gaps and large fraction of pores. However, in some regions (marked in Fig. 3.3) the particles were found to be more compactly packed. The morphology of particles was found to be altered due to deformation of individual powder particles, which helped in holding and packing neighboring particles.

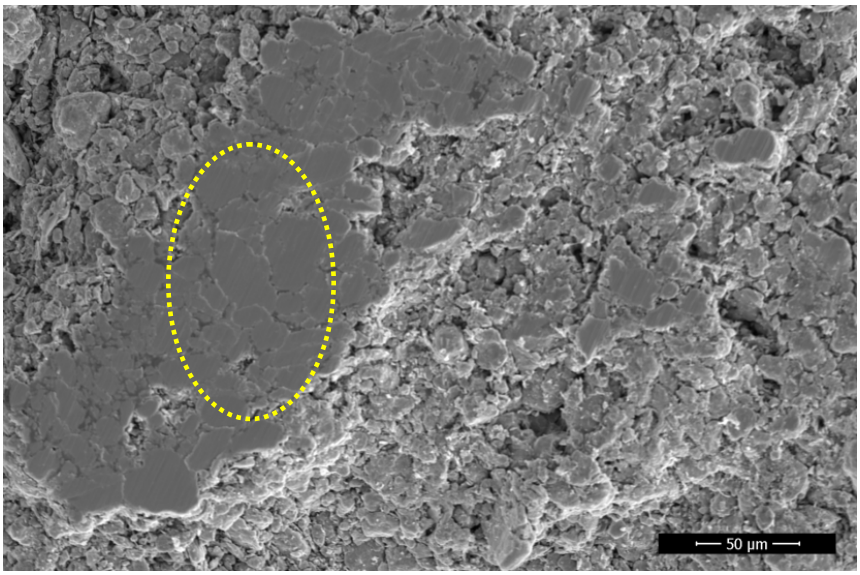

Fig. 3.3. *SE micrograph of cold isostatic pressed (green compact) 18Cr ODS ferritic steel (more compactly packed region is circled)*

3.2.2. Optimization of Sintering Temperature

In powder metallurgical processing, the densification during consolidation is strongly influenced by sintering temperature. Figure 3.4(a) shows relative density of the sintered specimens as a function of sintering temperature in the range of 1273 to 1523 K (1000 to 1250 ℃). The relative density systematically increased with sintering temperature, and saturates beyond 1423 K (1150 ℃). The increase in relative density is also reflected in the correspondingly decreasing amount of porosity (Fig. 3.4(b)), which also shows saturation of compaction beyond 1423 K (1150 ℃). The maximum density attained after sintering was 92% in comparison with starting green compact density of 63% after CIP process. It is well known that

formation of interparticle bonds is the dominant process during sintering, which provides strength to the compact, and manifests itself in the microstructure as change in morphology and size distribution of grains and pores, leading to grain growth, decrease of net porosity/pore density and increase in average pore size. Consolidation of green compact into a single unified structure requires long range diffusion of atoms and formation of metallic bonds between neighboring powder particles. The above results can be understood in terms of diffusion being aided by the high temperature of sintering and subsequent densification due to coalescence of neighboring particles.

During sintering, grain boundaries sweep the pores with them and the pores are found to be congregated along the grain boundaries. The pores are reported [145] to slow down the grain growth, but they become less effective in stopping rapid grain growth during high temperature sintering. This is attributed to the equal rate of migration of pores and grain boundaries up to 1423 K (1150 ℃), which enhances densification with minimal grain growth. However, above 1423 K (1150 ℃) the boundaries migrate at a higher rate leading to a saturation of pore fraction with negligible change in density. Thus, sintering at 1423 K (1150 ℃) was found to be optimum for obtaining a homogeneous sintered microstructure with small grain size and low porosity.

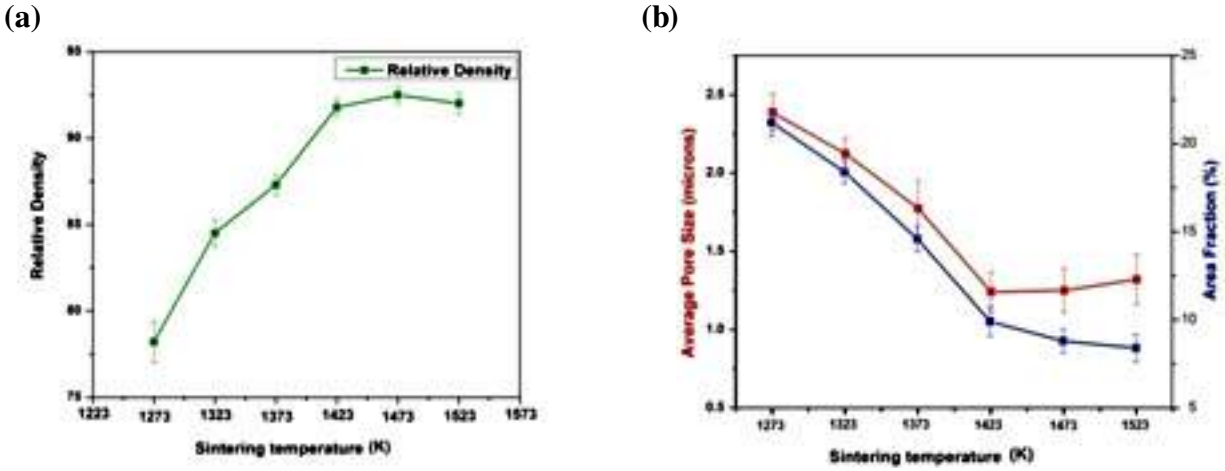

Fig. 3.4. *Change in (a) relative density and (b) size and area fraction of pores as a function of sintering temperature during consolidation of 18Cr ODS ferritic steel by CIP*

Figure 3.5(a) shows the EBSD crystal orientation map of compacted steel powder sintered at 1423 K (1150 °C) after the standard post processing (to assign average orientation to non-indexed points based on its surrounding pixels), which reveals an equiaxed microstructure with an average grain size of 24μm. Figure 3.5(b) shows the corresponding texture intensity variation obtained from the inverse pole figure map with respect to the perpendicular axis of the cylindrical specimen. Although a signature of <1 1 1> fiber texture is evident from the figure, the intensity of concentrated data points is found to be only ~1.5 times higher than random and hence can be considered as random texture that evolved during this process.

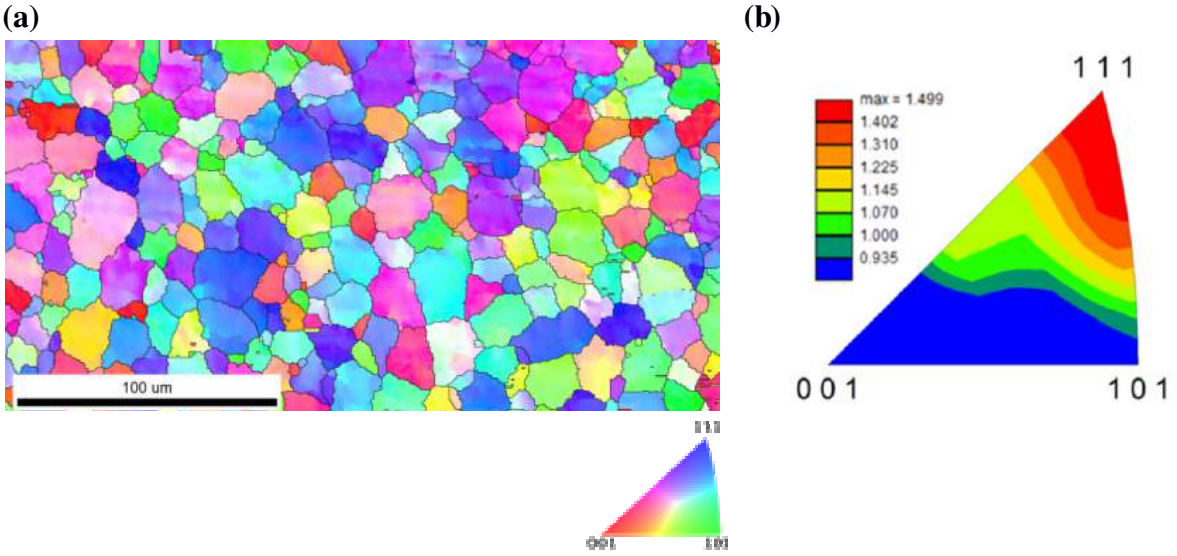

Fig. 3.5. *(a) EBSD crystal orientation map and (b) inverse pole figure along the axial direction of cylindrical specimen of 18Cr ODS ferritic steel after CIP and sintering at 1423 K (1150 ºC).*

3.3. Characterization of Steel Consolidated by CIP and HIP

The CIP product was subjected to HIP at the optimized temperature of 14223 K (1150 ℃) and pressure of 200MPa, which resulted in 97% of theoretical density. EBSD crystal orientation map of the above specimen is shown in Fig. 3.6(a). The figure reveals equiaxed

polygonal grains and the grain size is distinctly lower (16μm ± 4) after HIP than the sintered specimen after CIP (Fig. 3.5(a)).

Figure 3.6(b) shows the inverse pole figure with respect to the perpendicular axis of the cylindrical specimen from the EBSD microtexture data. The data points concentrated 5.5 times higher than random at (1 1 1) in this case in comparison with the CIP product sintered at 1423 K (1150 ℃) (1.5 times). During CIP, an increase in strain energy and dislocation bonding is expected due to the necking of particle interface, which leads to recrystallization (static phenomena) with a γ-fiber texture. However, HIP provides a material flow due to further compaction under a pressure of 200 MPa at 1423 K (1150 ℃), which results in dynamic recrystallization with a higher extent of γ-fiber texture.

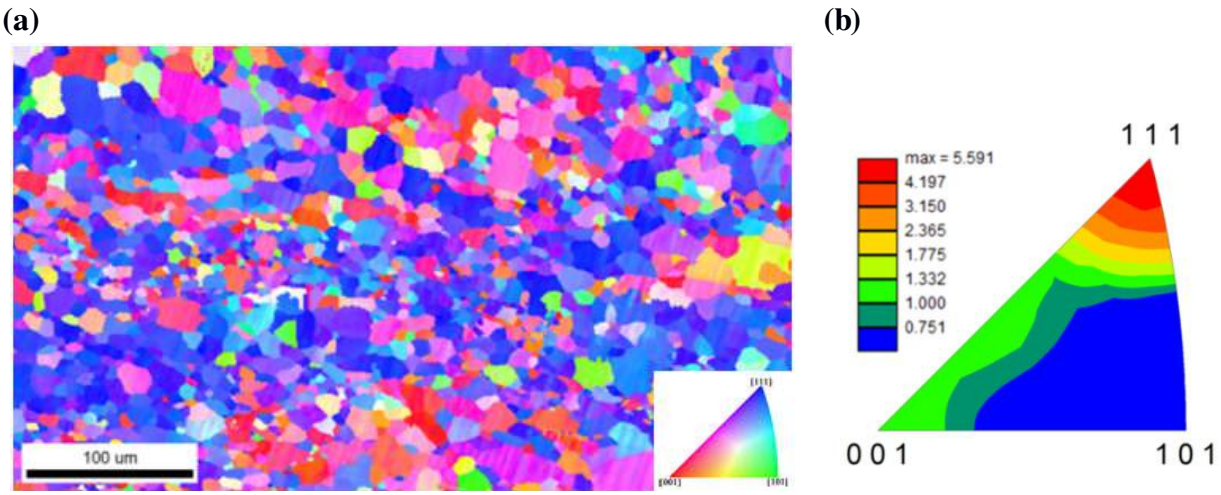

Fig. 3.6. *EBSD (a) crystal orientation map and (b) inverse pole figure of HIP product.*

3.4. Consolidation of 18Cr ODS Ferritic Steel by Spark Plasma Sintering

Consolidation using spark plasma sintering (SPS) technique, which is a relatively modern sintering method, is gaining significant momentum in the scientific as well industrial community as a potentially outstanding processing method. It enables rapid metallurgical bonding (up to 99% relative density) at comparatively lower temperatures and durations in contrast to HIP

[104-107] in a variety of materials including metals, ceramics, and composites [105, 106]. In SPS, a graphite die is designed to provide an instantaneous pulsed direct current, which leads to surface activation of the particles due to self heating, thus facilitating rapid heat and mass transfer [148-152]. The high densification of the product achieved due to rapid heating and cooling rates in SPS is responsible for the retained intrinsic properties of nano dispersoids [153].

3.4.1. Consolidation and Densification Characteristics

In this study, the milled powders were consolidated by SPS in the temperature range of 1273 to 1423 K (1000 to 1150 ℃) at an interval of 50 K. The applied pressure and temperature during SPS provide the driving force for densification, which involves processes such as plastic yielding of particles, their arrangement, surface diffusion etc. [154, 155] and the density is expressed by the following equation:

$$\rho_i = \left(\frac{h_i}{h}\right) * \rho_r \tag{3.1}$$

where ρ_i and h_i is the instantaneous density and displacement of plunger respectively, and h is the total height travelled by the plunger and ρ_r is the relative density of the specimen. ρ_r is obtained from ratio between density of consolidated product and theoretically calculated density of reference material. The instantaneous pulse current flow in SPS assists the plasma formation during sintering due to the building up of particle surface charge/discharge phenomena which leads to heating/melting of the particle surface and the simultaneously applied pressure facilitates the densification by both grain rotation and sliding [109]. There are several reports on densification mechanisms based on creep theory, and power law creep is reported to make a dominant contribution to the viscoelastic behavior of crystalline solids [146-149], which is expressed by the following equation [148, 149]:

$$\dot{\varepsilon} = \frac{C}{T}\sigma^{n} exp\ (-\frac{Q}{RT}) \tag{3.2}$$

where ε̇ is the strain rate, C is a constant, σ is the instantaneous effective stress acting on the porous body, n is the power law exponent, and a value of ~6.9 for α-Fe is employed for the calculation [106, 150], Q is the activation energy for the deformation process, R is the universal gas constant (8.314 $Jmol^{-1}K^{-1}$), and T is the absolute temperature. Further, ε̇ strain rate associated with densification is expressed by the following relationship [148, 151]:

$$\dot{\varepsilon} = \frac{1}{(1-\rho_r)} * \left(\frac{1}{\rho_r}\frac{d\rho}{dt}\right) \tag{3.3}$$

where ρ_r is the relative density of the specimen. In addition, the instantaneous effective stress (σ), which depends on the shape factor or pore aspect ratio (φ) and applied pressure is expressed as:

$$\sigma = \varphi * P \tag{3.4}$$

where P is the applied pressure. It has been reported that the increase in density leads to reduction in pore size and spherical finer pore shape distribution [152]. Further, 'φ' which associated with the aspect ratio of the porosity decreases with the increase in relative density attributed to the decrease with the amount of porosity; and hence, can be related to density by the relationship:

$$\varphi = \frac{1}{\rho_r} \tag{3.5}$$

Substituting the constitutive equation (3.5) in equation (3.2) gives

$$ln\left(\frac{T*\left(\frac{1}{(1-\rho_r)}*\left(\frac{1}{\rho_r}\frac{d\rho}{dt}\right)\right)}{\left(\frac{p}{\rho_r}\right)^{n}}\right) = lnC - \frac{Q}{RT} \tag{3.6}$$

$$D = \left(\frac{T * \left(\frac{1}{(1-\rho r)} * \left(\frac{1}{\rho r} \frac{d\rho}{dt} \right) \right)}{\left(\frac{p}{\rho r} \right)^{n}} \right) \quad (3.7)$$

where, D is the rate of diffusion for a given temperature T and pressure P. Further, Equation (3.6) represents a line and from the plot of D as a function of reciprocal of the absolute temperature for the highest rate of densification during consolidation, activation energy Q is determined experimentally.

Figure 3.7(a) shows the instantaneous relative density obtained during SPS process. It is evident that the densification rate increased with temperature from 1273 to 1323 K (1000 to 1050 ℃). Although higher temperature aids faster diffusion and sintering, for increased compaction and density, no significant increase in the rate of densification is observed beyond 1323 K (1050 ℃). It is also observed from Fig. 3.7(a) that at each temperature, densification attains saturation beyond ~ 600 s. This trend can be explained based on the fine grain size (~30 nm) and higher surface energies in the initial stages, which accelerates the rate of diffusion and grain boundary migration resulting in high densification rates [153]. However, with time the increase in grain size leads to reduced grain boundary migration. Subsequently, the time dependent grain boundary and lattice diffusion dominate in the hold time region [148, 153], thus resulting in sluggish densification. Figure 3.7(b) shows the densification rate as a function of time during the heating cycle. Region (1) marked in the figure indicates a small peak, which is attributed to the arrangement of particles in the powder and their local deformation during initial stage of consolidation (~573 K (300 ℃)). Region (2) marked in Fig. 3.7(b) corresponds to a higher rate of densification indicating effective consolidation. However, an additional peak (3) marked in Fig. 3.7(b) is observed during holding beyond 600 s duration, which is associated with

an observable densification rate due to mass transport phenomena [154], wherein maximum density is attained; further hold time shows no observable change in densification rate.

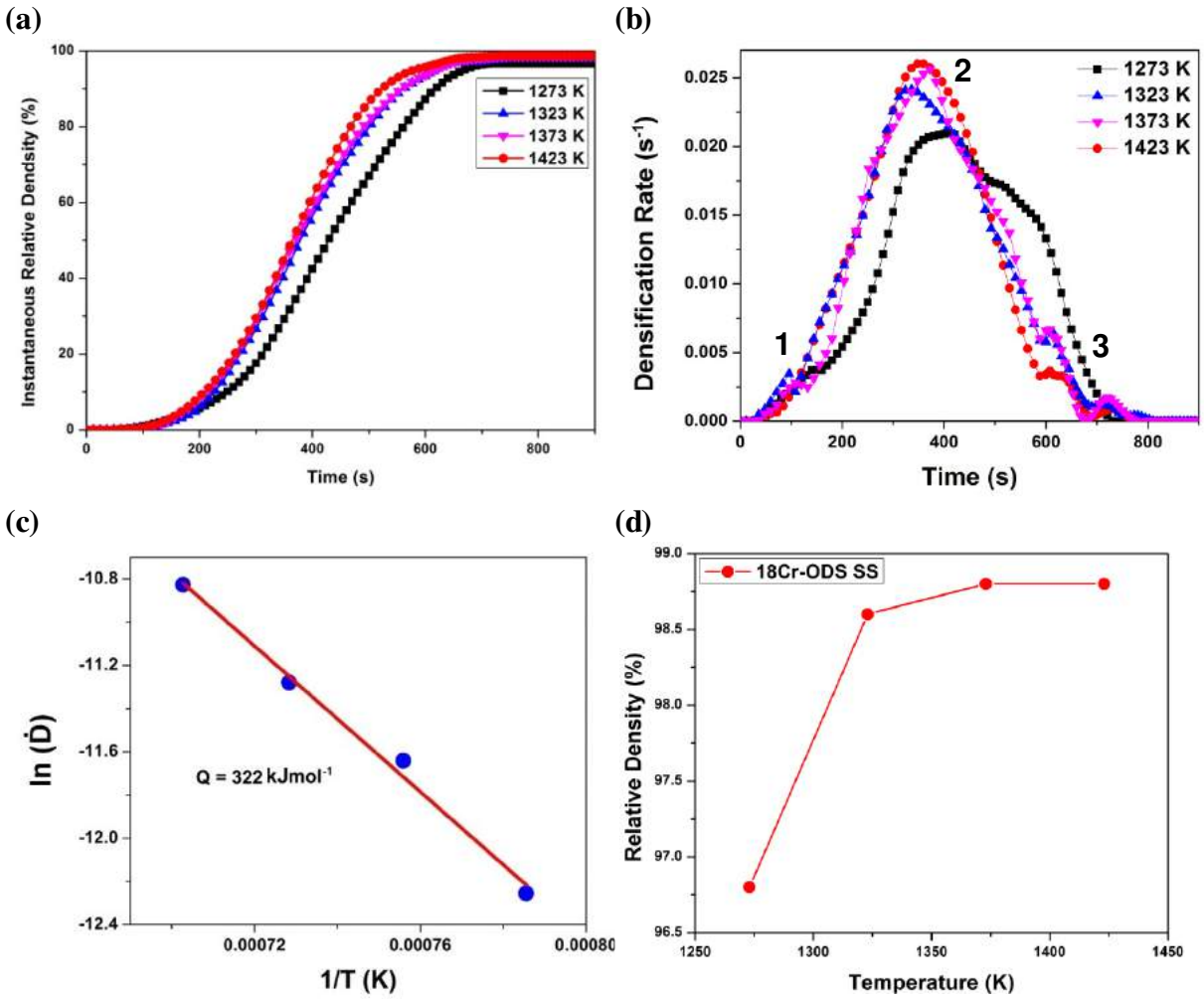

Fig. 3.7. *Relative variation of (a) density and (b) densification rate (Marked regions indicate 1- localized deformation, 2- bulk deformation, 3-mass transport phenomena) as a function of time, (c) plot of ln(D) with respect to 1/T and (d) density variation with temperature during consolidation by SPS.*

The rate of diffusion (D) is calculated from the sintering parameters and has been plotted with respect to 1/T (Fig. 3.7(c)). The activation energy of densification calculated from the slope of the line from the plot is estimated as ~322 kJmol^{-1}, suggesting that the densification is diffusion aided during the sintering process. This is understood in the light of dislocation glide/climb and volume diffusion which operate in this temperature domain in region 2 (local

deformation) and 3 (hold time) respectively [155]. Figure 3.7(d) shows the relative density of the sintered specimens as a function of temperature. The maximum attainable density is ~99%, which remains almost constant above 1323 K (1050 ºC) within a range of 50 K. The coalescence of micropores driven by grain boundary migration is reported as the first temperature dependent step during consolidation [145]. The point of inflection in Fig. 3.7(d) indicates the equal rate of migration of pores and grain boundaries at 1323 K (1050 ºC), which enhances densification; however, just above 1323 K (1050 ºC) the boundaries migrate at a higher rate leading to a saturation of the pore fraction without significant change in densification.

3.4.2. Effect of Sintering Temperature on Microstructure

Figure 3.8(a-d) shows the EBSD inverse pole figure-maps superimposed with grain boundary maps. The corresponding grain size distribution is shown in Fig. 3.8(e). The average grain sizes are listed in Table 3.1. The specimen sintered at 1273 K (1000 ºC) exhibits (Fig. 3.8(a)) a bimodal grain size distribution consisting of ultra-fine grains (0.3 μm) at interfaces of fine grains (~1.5 μm). Above 1323 K (1050 ºC) an equiaxed grain structure of 1-2 μm grain size is observed. From the inverse pole figure maps, no strong texturing effect is observed at any sintering temperature. However, small clusters of fine grains with a (1 1 0) orientation (circled in Fig. 3.8(b-d)) with respect to sample normal (direction of applied pressure in SPS) are observed in the microstructure. The above observation can be further augmented with the results of grain boundary distribution within the clusters (Fig. 3.8(b-d)), where an increase in the concentration of low angle boundary trace among the commonly observed (1 1 0) oriented grain clusters is observed with increase in sintering temperature. Figure 3.9 shows the texture intensity variation obtained from the inverse pole figures with respect to the applied pressure axis. It is found to be 2.4 to 2.8 times higher than that corresponding to a random orientation.

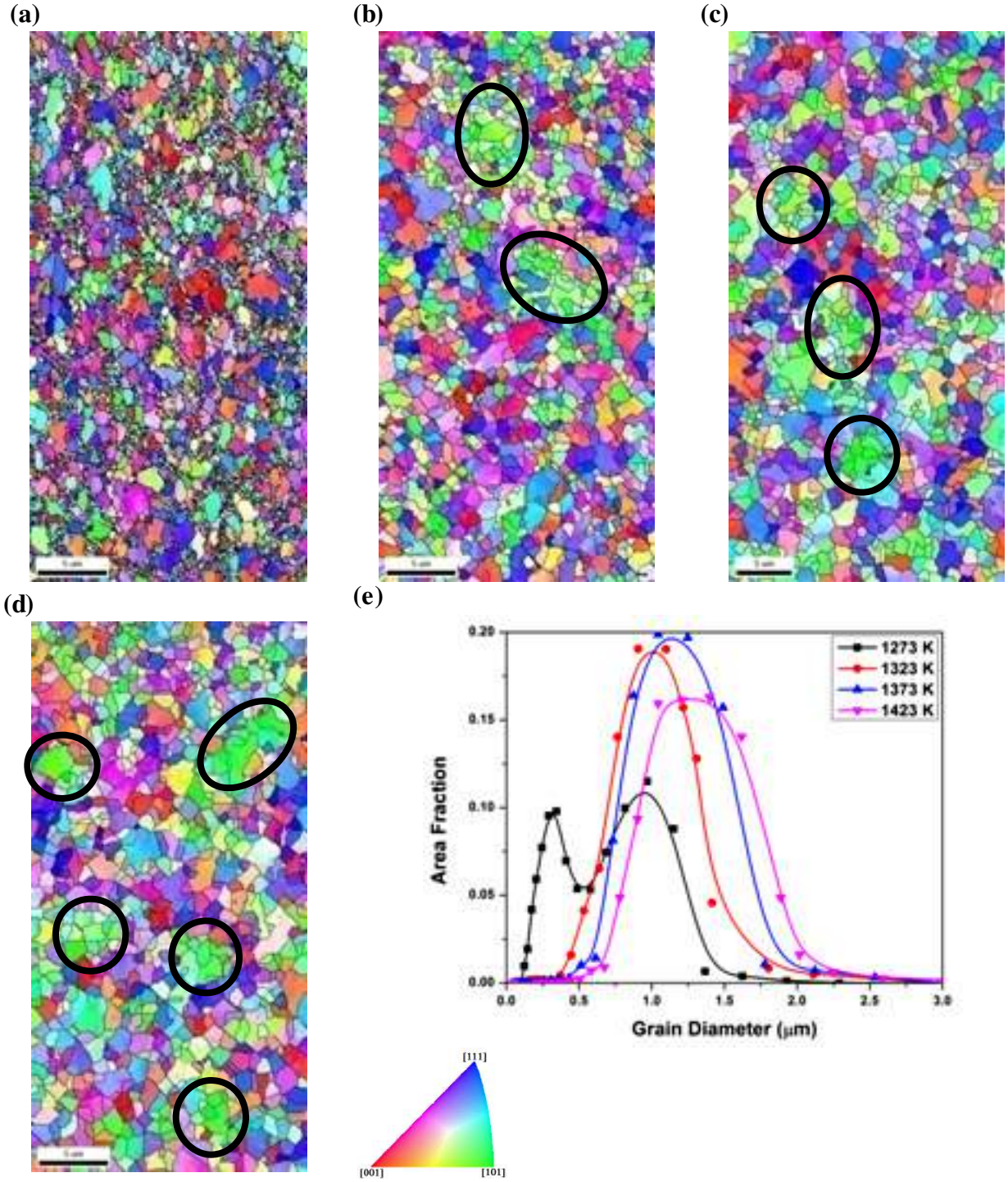

Fig. 3.8. *EBSD crystal orientation maps superimposed with grain boundary (misorientation angle 5-15º- Gray and >15º - Black) of 18Cr-ODS ferritic steel powder consolidated by SPS at (a) 1273 K (1000 °C),(b) 1323 K (1050 °C), (c) 1373 K (1100 °C), (d) 1423 K (1150 °C) and the clustering of grains with [110] orientation are circled in (b-d) and (e) grain size distribution at different sintering temperatures.*

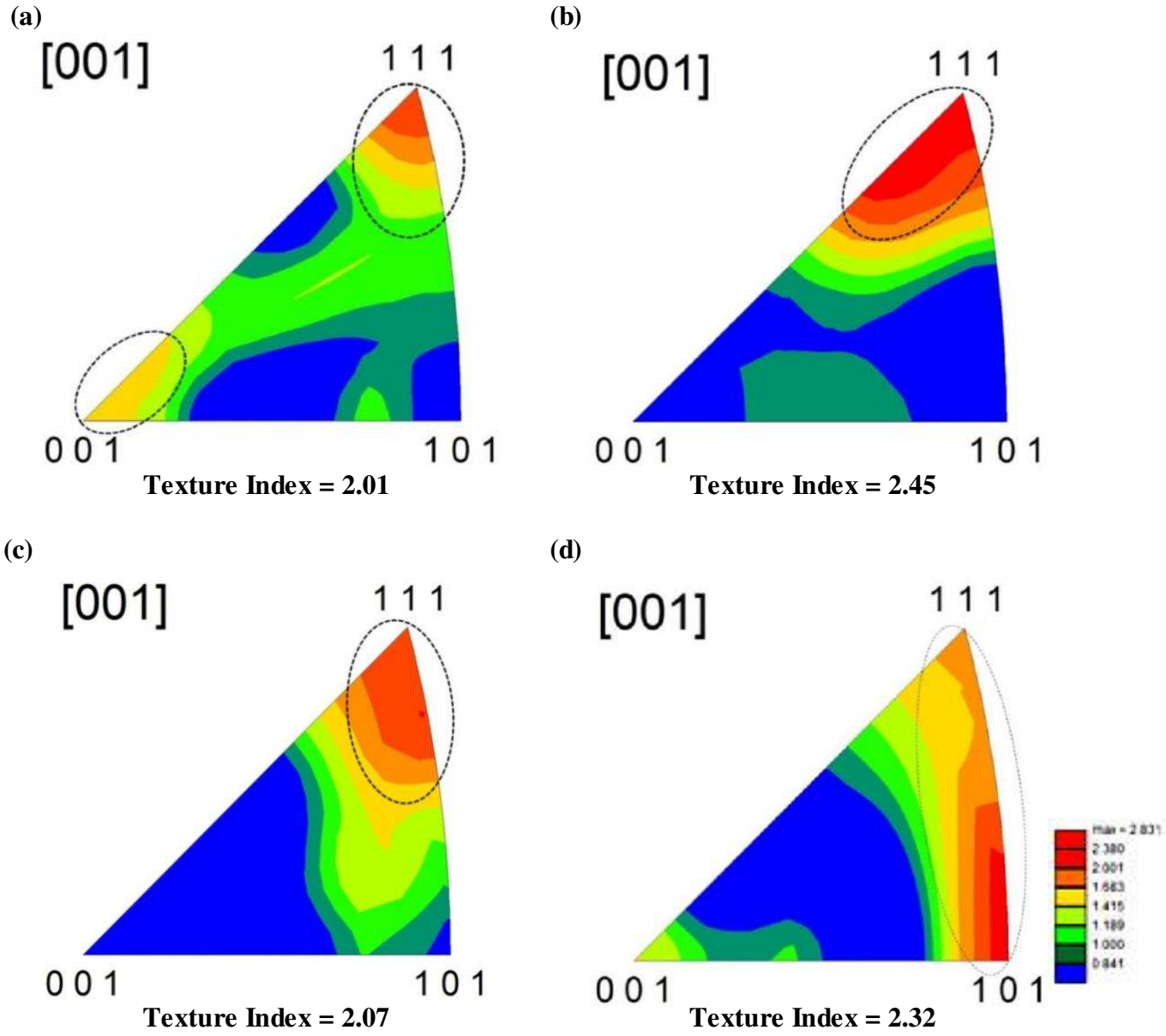

Fig. 3.9. *Inverse pole figure (with contour intensity level better than random: 2.4 to 2.8) with respect to applied direction of pressure during consolidation (denoted as [001]) of 18Cr ODS ferritic steel by SPS at (a) 1273 K (1000 °C),(b) 1323 K (1050 °C), (c) 1373 K (1100 °C), (d) 1423 K (1150 °C). (encircled region shows the alignment of crystallographic plane with respect to crystal coordinate axis)*

A signature of (1 1 1) and (1 0 0) planes aligned along the direction of applied pressure is evident from Fig. 3.9(a) at 1273 K (1000 ℃), while at 1323 K (1050 ℃) the (1 1 1) plane orientation (Fig. 3.9(b)) is evident. However, it is apparent that the (1 1 0) planes tend to be

parallel towards the direction of applied pressure ((Fig. 3.9(c-d)) with increase in sintering temperature to 1373 K (1100 ℃). It is also reported that formation of fine grains is due to recovery and recrystallization process during sintering process [156]. While a partially recrystallized microstructure is observed at 1273 K (1000 ℃), it changes to a fully recrystallized structure at 1323 K (1050 ℃).

It is well known that density is of prime concern for high temperature mechanical properties such as creep. It may be recalled that relative density was found to saturate above 1323 K (1050 ℃) and beyond 1373 K (1100 ℃) no further increase in density has been observed. Hence, based on densification characteristics and microstructures, temperature in the range of 1323 + 50 K (1050 + 50 ℃) is identified to be optimum for sintering by SPS.

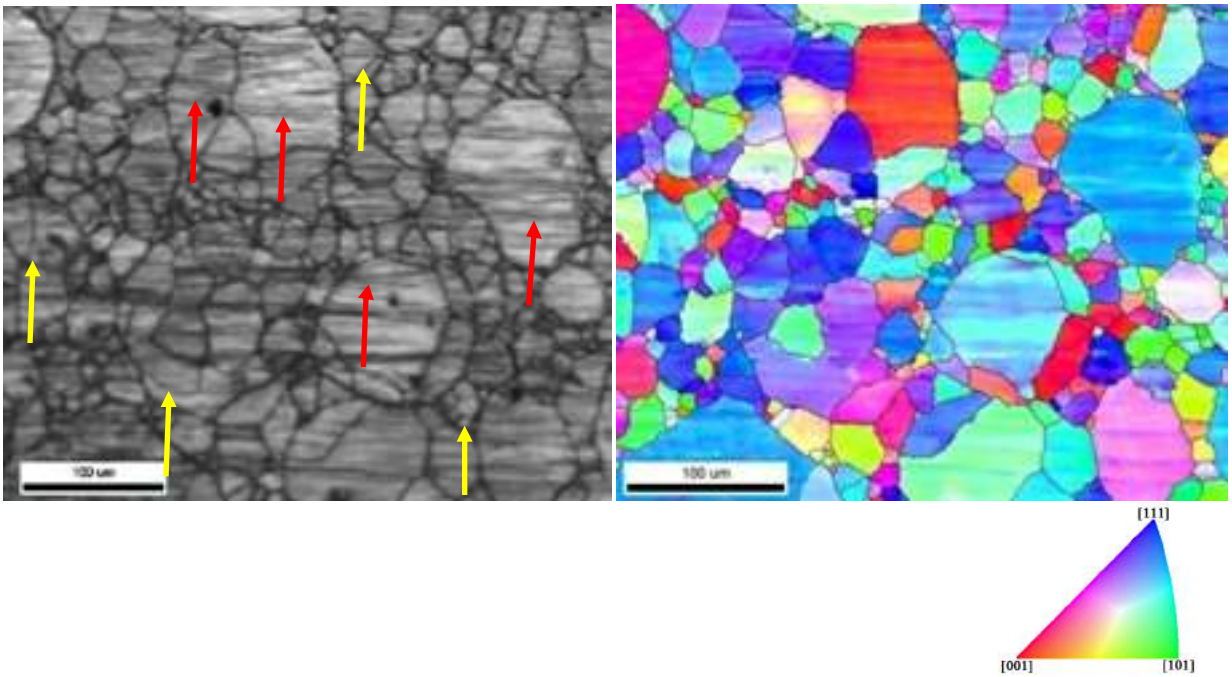

Fig. 3.10. *EBSD (a) image quality and (b) crystal orientation map of 18Cr ferritic steel powder consolidated by SPS at 1323 K (1050 °C) showing deformation bands (yellow arrows) and subgrains (red arrows)*

In order to understand the role of dispersoids, the pre-alloyed 18 Cr steel powder was consolidated by SPS under similar condition at 1323 K (1050 ℃). Image quality map of the

sintered steel given in Figure 3.10(a) shows large variation in grain size and the presence of deformation bands (yellow arrows) and subgrains (red arrows). EBSD analysis has been repeated at several regions on a fresh sample under identical conditions. However, similar features were observed, which indicate that the lines observed are intrinsic features of the specimen, due to high temperature and pressure that prevail during consolidation. Further, Figure 3.10(b) shows the EBSD inverse pole figure map of the sintered steel specimen, which shows a bimodal grain distribution. The microstructure reveals a large variation in grain size with coarse (~100 μm) grains encircled by small (~20 μm) grains (Table 3.1). This is attributed to the rapid grain growth due to grain boundary migration associated with strain energy reduction in the absence of "Zener pinning" effect [157] of the dispersoids, even for short sintering durations. This clearly establishes that nanosized dispersoids are responsible for grain refinement in ODS steels even at temperatures of 1423K (1150 ℃) [158], which in turn has profound influence on the mechanical properties, which is discussed in the next section.

Table 3.1. Consolidation parameters of SPS, relative density and average grain size

Steel	SPS Parameters		Relative Density (%)	Average Grain Size (μm)	Grain Size distribution
	Pressure (MPa)	Temperature (K)			
18Cr ODS ferritic steel	40	1273	96.8	0.5±0.2, 1±0.5	Bimodal
	40	1323	98.6	1.2±0.5	Equiaxed
	40	1373	98.8	1.5±0.6	Equiaxed
	40	1423	98.8	2±0.6	Equiaxed
18Cr ferritic steel	40	1323	99.2	20±4, 100±16	Bimodal

3.4.3. Evaluation of Mechanical Property

Figure 3.11(a) presents the indentation load-displacement curves for steels consolidated by SPS at 1323 K (1050 ℃) with and without dispersoids. The hardness of 18Cr ODS ferritic steel consolidated by SPS was 396±4 and 402±4 HV in axial and transverse directiona

respectively with respect to direction of applied pressure, in contrast to an average value of 146±6 HV for the steel without dispersoids.

(a)

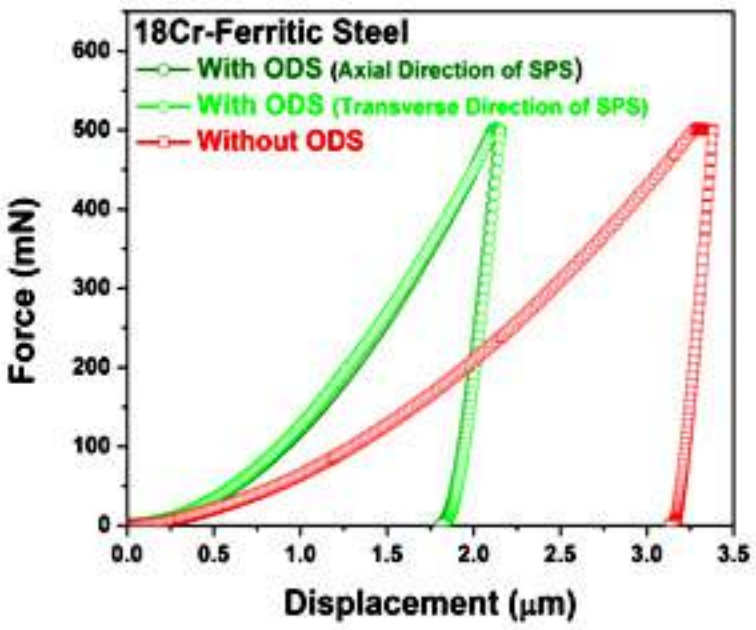

(b)

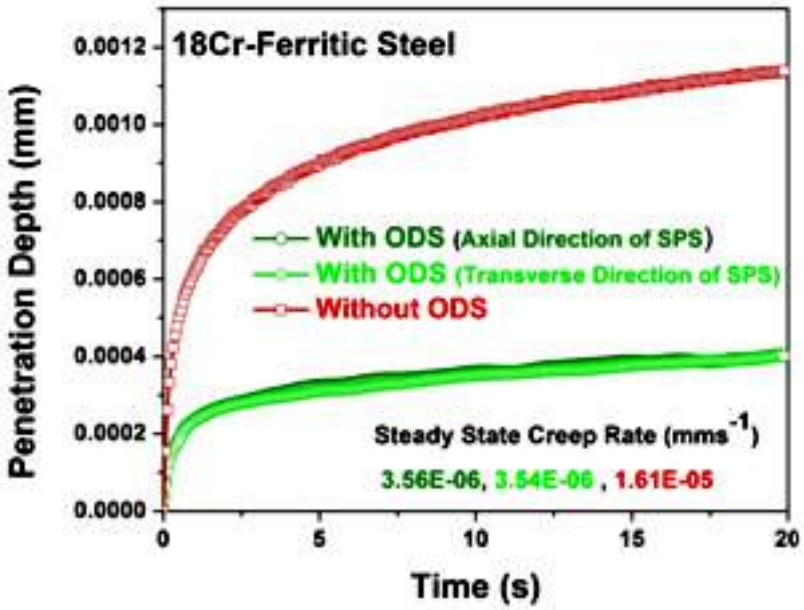

Fig. 3.11. *Instrumented indentation hardness profile of 18Cr ferritic steel with (along axial and transverse direction of applied pressure in SPS) and without dispersoid consolidated at 1323 K (1050 °C)(a) load-displacement curves and (b) penetration profile.*

Further, the slope of initial region of the unloading curve is a characteristic of elastic modulus (related to stiffness) [133], and the dispersoid added steel exhibited a higher elastic modulus of ~262 GPa in both axial and transverse direction, in comparison to the steel without Y_2O_3 addition (228 GPa). The similar hardness and elasticity modulus in both axial and transverse direction to the applied pressure after SPS suggests the absence of any directional properties, due to recrystallization, which is also supported by the rescrystallized microstructure obtained at this temperature (Fig. 3.8(b)). Further, the combined effect of dispersion strengthening and grain refinement manifests itself as high hardness along with a higher elastic modulus. Dynamic properties as a function of time such as penetration rate derived from the penetration profile during the dwell time of indentation for both the steels are shown in Fig. 3.11(b). The rate of penetration for the consolidated steel with and without dispersoids was $3.5x10^{-6}$ s^{-1} and $1.6x10^{-5}$ s^{-1} respectively. The decrease in penetration rate in 18Cr ODS ferritic steel by about an order of magnitude reflects the high resistance to deformation offered due to the presence of dispersoids. The deformation behavior of 18Cr ODS ferritic steel consolidated by SPS based on creep studies are described below.

Figure 3.12(a) shows the typical creep curves tested at 873, 923 and 973 K (600, 650 and 700 ºC) of 18Cr ODS ferritic steel consolidated by SPS at 1323 K (1050 ºC). The creep curves exhibited a short primary creep stage followed by a secondary creep stage where strain increased linearly with time. However, the tertiary stage in the creep curve is found to be minimal and abrupt fracture is found to be apparent at very low deformation of about >1% which is consistent with the creep study reported by B. Fournier et al [53]. The change in creep rate with time at different temperature regimes are shown in Fig. 3.12(b). The minimum creep rate of the steel tested at 873, 923 and 973 K (600, 650 and 700 ºC) was estimated as $5x10^{-7}$ h^{-1}, $1 x10^{-5}$ h^{-1} and

$1x10^{-4}$ h^{-1} respectively (Fig. 3.12(b)). The results show a linear relationship with inverse of test temperature (Fig. 3.12(c)). It has been reported that the creep rupture time in hot extruded ODS steel is far lower along the transverse direction as compared to the extruded direction [10]. However, the present study on the transverse direction of SPS consolidated specimen shows a much higher creep life than that reported for extruded direction of HE product [10, 51, 53, 159]. This clearly suggests good biaxial creep properties and less anisotropy, which is attributed to the ultra-fine (~ 1 μm) equiaxed grain microstructure in the transverse direction for the rod shaped product consolidated by SPS.

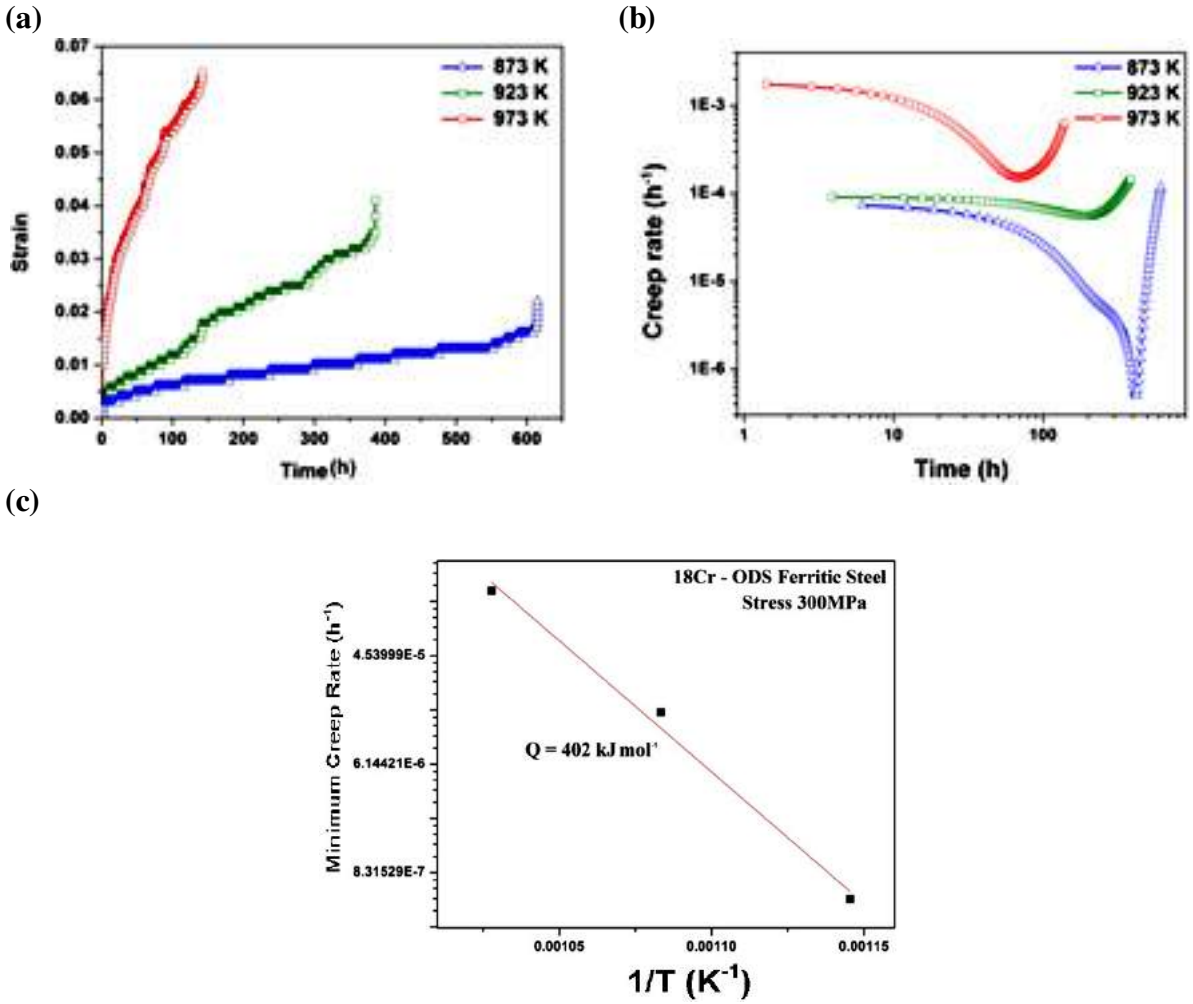

Fig. 3.12. *Creep analysis of 18Cr-ODS steel consolidated by SPS at 1323 K (1050 ºC) tested at 300MPa stress, (a) Creep curves at various temperatures, (b) creep rate variation with time, and (c) Arrhenius type relationship between minimum creep rate (h^{-1}) and temperature.*

In order to assess the influence of dispersoids on the creep behavior of the steel, creep rate of 18Cr ferritic steel (without dispersoids) as a function of stress and temperature was computed using 'JMatPro®' and compared with experimental results of both the steels. The resultant predicted/experimental creep rates and corresponding rupture life with respect of temperature are compared in Fig. 3.13(a) and (b) respectively. The predicted creep rate and rupture life was found to be similar to that of experimentally determined values for 18Cr ferritic steel without dispersoids. However, the creep rate was observed to be higher by about two to three orders of magnitude than 18Cr ferritic steel with dispersoids.

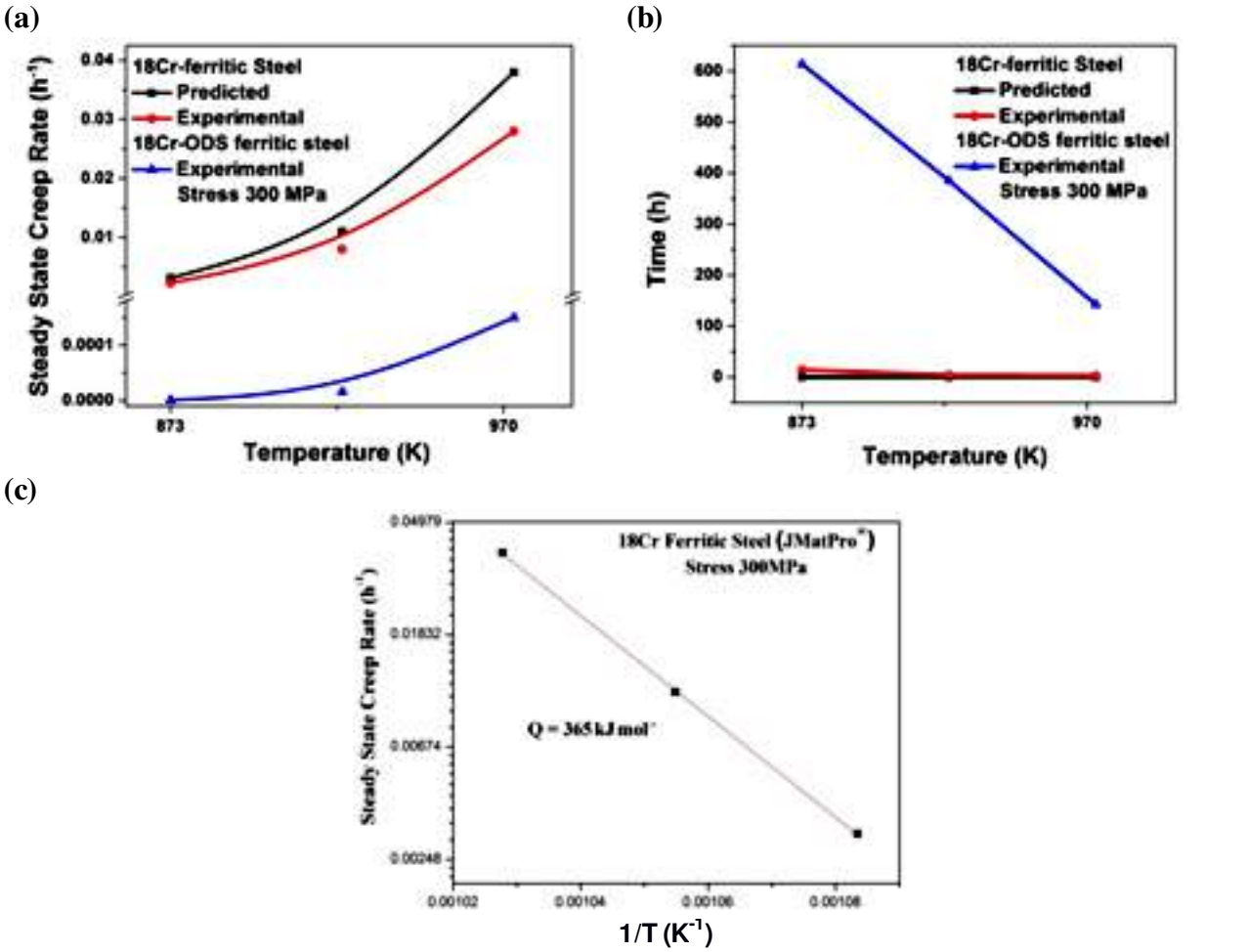

Fig. 3.13. *Prediction of creep properties in 18Cr ferritic steel, calculated using 'JMatPro®'; predicted and experimentally determined variation of (a) steady state creep rate, (b) rupture life with temperature and (c) Arrhenius type relationship between minimum creep rate in steady state region and temperature.*

The minimal rupture life was about 3-14 h in the temperature range 873 to 973 K (600 to 700 ℃) and 300MPa stress in contrast to about 600 h in 18Cr ODS ferritic steel. The minimum creep rate of the material depends on the stress and temperature. For a given stress, the dependence of creep rate on temperature follows the Arrhenius rate equation [160],

$$\dot{\varepsilon} = A\sigma^{n} \exp(-{}^{Q}/_{RT}) \quad (3.8)$$

where $\dot{\varepsilon}$ is the minimum creep rate, which depends on the stress and temperature, A is a constant, Q is the apparent activation energy for the deformation process, R is the universal gas constant (8.314 $Jmol^{-1}K^{-1}$), and T is the absolute temperature. In Fig. 3.12(c) and 3.13(c), the minimum creep rate of the SPS consolidated 18Cr ODS ferritic steel is plotted against the reciprocal of the absolute temperature.

The activation energy Q calculated from the slope of the best-fit lines was about 402 $kJmol^{-1}$ and 365 $kJmol^{-1}$ for the steel with and without dispersoids respectively. The activation energy for lattice self-diffusion in α-Fe is reported as 225 $kJmol^{-1}$ (activation energy of diffusion creep) [161]. The higher Q value for the 18Cr ferritic steel is attributed to the presence of solid solution strengthening alloying elements such as Cr and W in the matrix (365 $kJmol^{-1}$), which is further higher by about ~40 $kJmol^{-1}$ in the presence of dispersoids. Thus the creep deformation mechanism in the steel is inferred to be by lattice diffusion assisted climb of dislocations [162] over the barriers such as dispersoids.

The fractographs of SPS consolidated 18 Cr ODS ferritic steel creep tested at 873 and 973 K are presented in Fig. 3.14(a, b). Radially aligned fine dimples observed at higher magnifications were more prominent at lower test temperatures (Fig. 3.14(a)). It is reported that the dispersoids impede the dislocation motion in the initial stages of the test leading to increase in stress concentration and cavitations [162]. At higher temperatures of 973 K (700 ℃), the signatures of

pull-out and void coalescence strikingly evident in (Fig. 3.14(b)) suggest that the microcavities due to coalescence or impingement cause failure. The above results from the fracture surface show a ductile mode of fracture under creep test conditions.

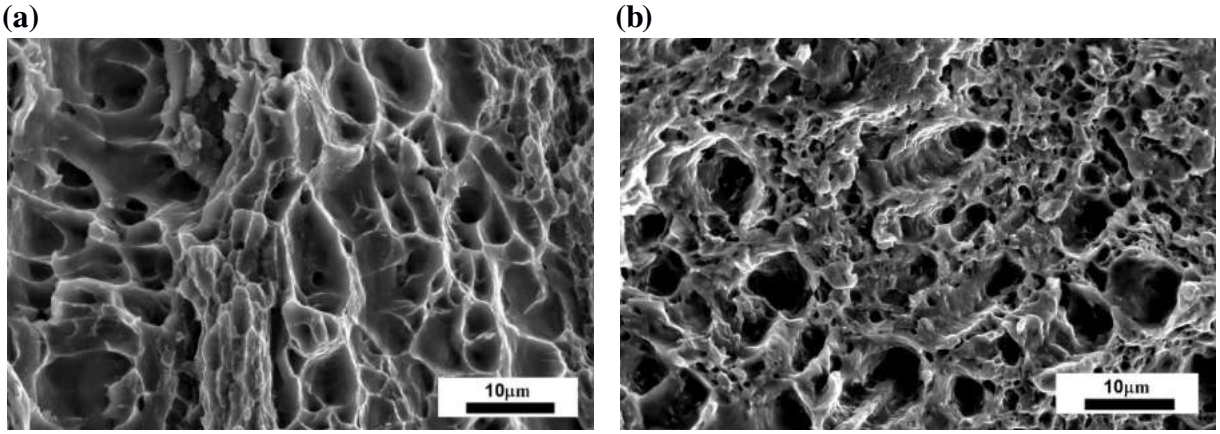

Fig. 3.14. *SEM fractographs of SPS consolidated 18Cr ODS ferritic steel creep tested at (a) 873 K (600 ºC) and (b) 973 K (700 ºC) showing ductile failure.*

3.5. Characterization of Steel Consolidated by Hot Extrusion

18Cr ODS ferritic steel powder was also consolidated by hot extrusion at 1423 K (1150 ºC). The EBSD crystal orientation maps along extruded direction (ED) and transverse direction (TD) superimposed with grain boundary distribution map is shown in Fig. 3.15(a) and (b). It is evident from the figures that the grains are elongated along ED in contrast to equiaxed grains along TD (Fig. 3.15(a) and (b)).

The microstructure exhibits elongated grains along ED. The average aspect ratio of the elongated grains along ED is 1.6 and the maximum dimensions of the grains are ~0.8 ± 0.2 and ~2 ± 0.5 μm in the transverse and extruded directions respectively. The black and grey lines in the microstructure represent the low (5-15º) and high (>15º) angle boundaries respectively. A close look shows a network of low-angle boundaries contained within the high angle boundaries. The low angle boundary networks indicate an intragrain rotation in the partially recovered

microstructure, which is attributed to dynamic recovery during the extrusion process, which are the most common deformation and annealing mechanisms at high temperatures [94, 163].

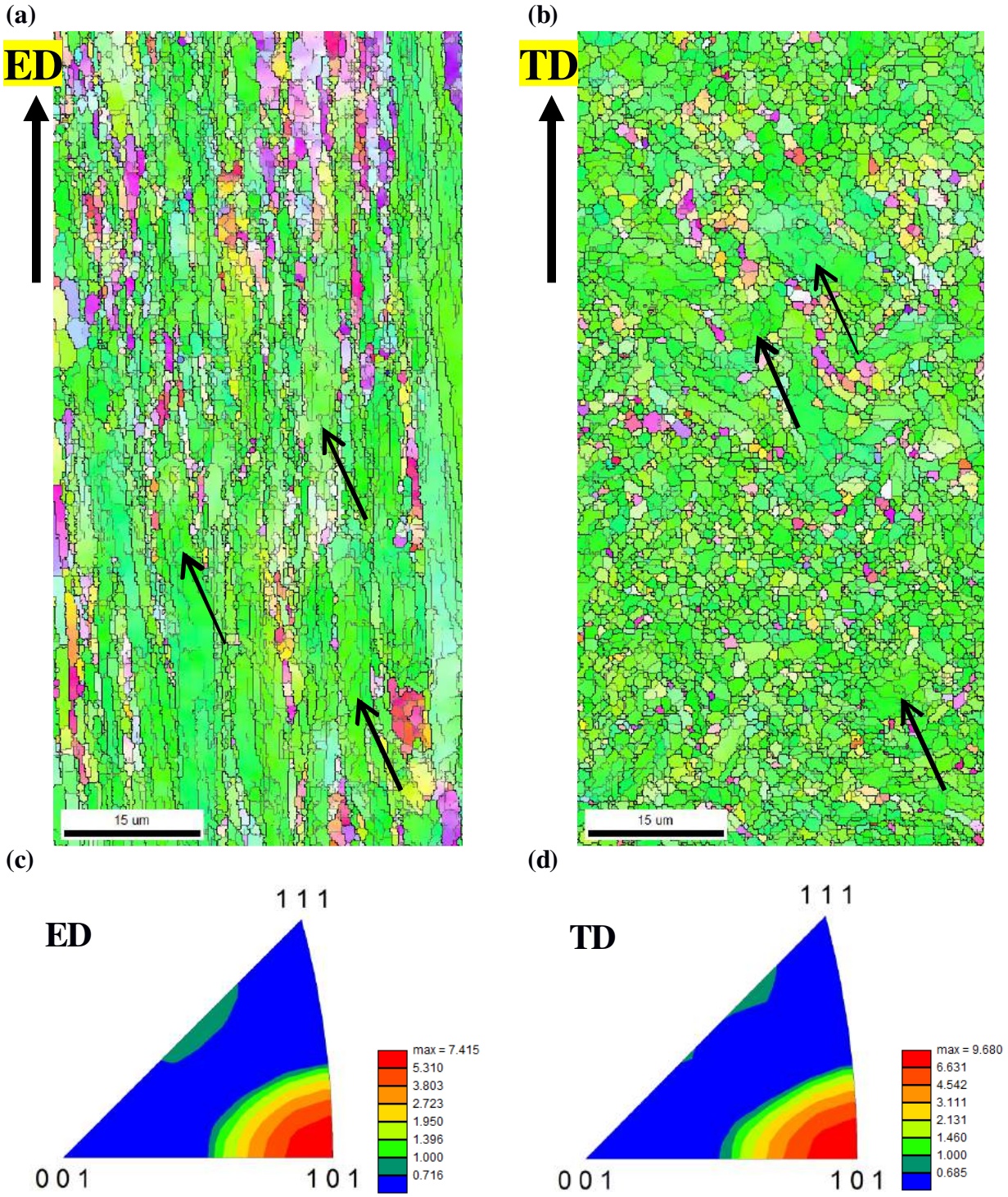

Fig. 3.15. *Overlay image of inverse pole figure and image quality maps obtained by EBSD along (a) extruded, and (b) transverse directions of hot extruded 18Cr ODS ferritic steel and (c) and (d) inverse pole figures along ED and TD respectively showing a strong (110) or α-fiber texture.*

Further, the orientation map suggests the existence of a preferential texture of <1 1 0> plane normal along the extrusion direction, which has been confirmed by the analysis of the inverse pole figure (IPF) (Fig. 3.15(c) and (d)). The intensity of pole concentration is found to be about seven and nine times higher than random distribution in ED and TD respectively. This is a strong indication of texture and is a matter of concern with respect to anisotropy in mechanical properties [52, 97]. The existence of preferential texture is attributed to the deformation induced α-fiber texture introduced during extrusion. This is in agreement with the observed microstructural features, and is also reported in ODS ferritic steel [97, 164] unlike the ODS ferritic martensitic steels.

3.5.1. Mechanical Properties

Figure 3.16 represents the variation in indentation load-displacement curves of hot extruded 18Cr ODS ferritic steel along ED and TD. The average hardness of the steel along ED and TD is measured as 464±6 and 476±6 HV respectively. This high value of hardness is due to the combined effect of fine grain structure (< 2 μm) and dispersoid strengthening. The difference in hardness between ED and TD is a reflection of the initial morphological anisotropy discussed earlier (Fig. 3.15(a) and (b)). Figure 3.17(a) and (b) shows the creep plots of the specimens extracted from the extruded (ED) and transverse (TD) direction of the hot extruded steel and tested at 873, 923 and 973 K (600, 650 and 700 ℃). The creep curves exhibit similar characteristics to those obtained from the SPS consolidation (Fig. 3.12(a)). The change in minimum creep rate and rupture life with temperature at different temperature regimes are shown in Fig. 3.17(c) and (d) respectively. Both the parameters show a linear relationship with test temperature.

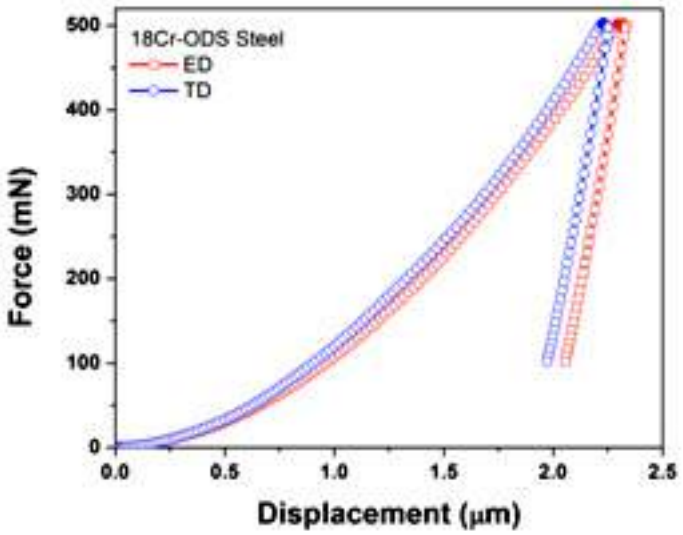

Fig. 3.16. *Comparative analysis of instrumented indentation hardness profile of ED and TD sections of hot extruded 18Cr ODS ferritic steel.*

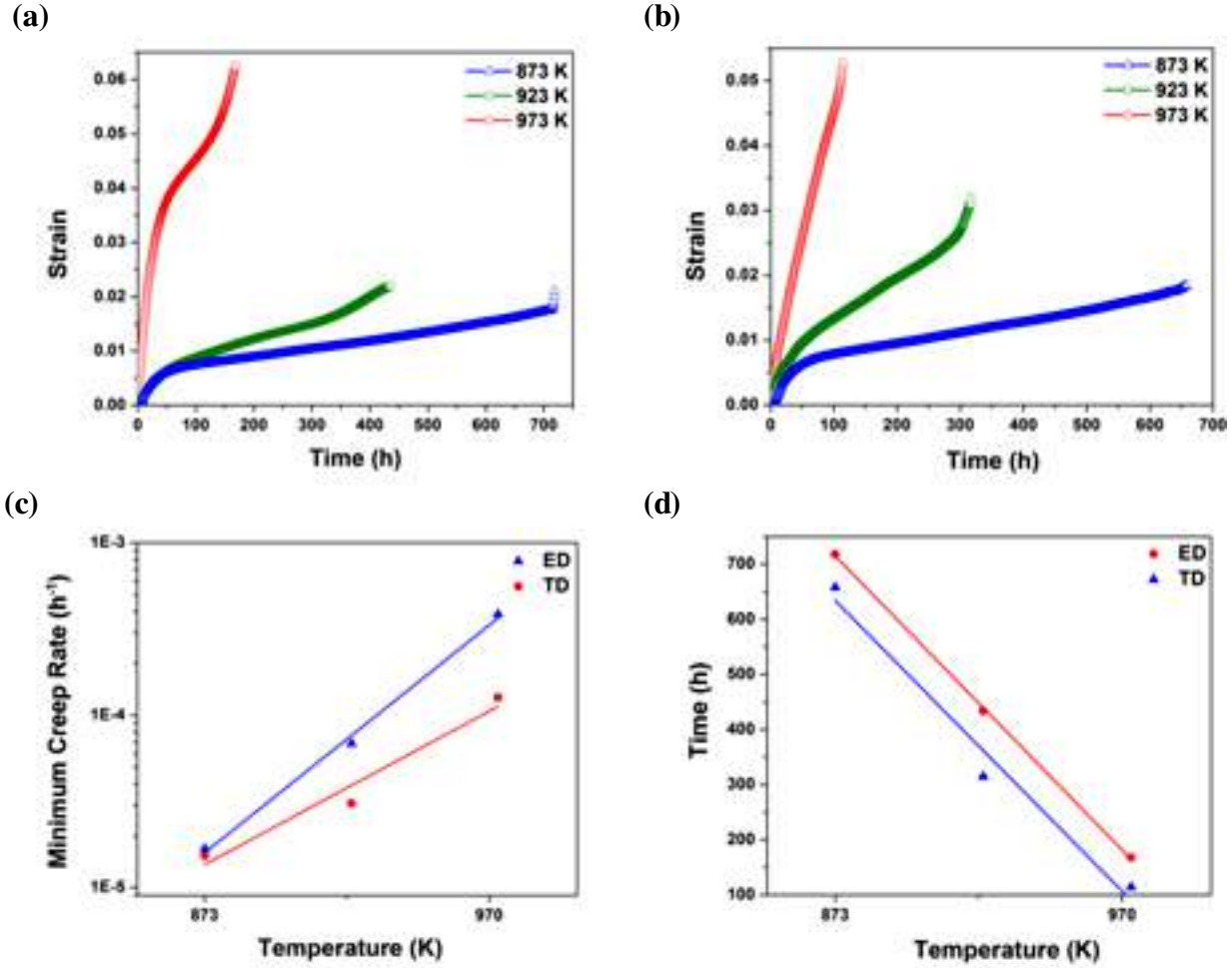

Fig. 3.17. *Creep curves of hot extruded 18Cr ODS ferritic steel at a stress of 300MPa along (a) ED, (b) TD , variation of (c) creep rate and (d) rupture life with temperature.*

It is evident from Fig. 3.17(c) that there is a variation of one order of magnitude in creep rate between the two directions in the temperature range 873 to 973 K (600 to 700 ℃); however, a small divergence is also observed with temperature. Further, the rupture time is observed to be higher along ED than TD. This clearly establishes that the steel has high strength along ED as compared to TD despite the persistence of anisotropy in mechanical properties during hot extrusion, which is also in agreement with the reported literature [10, 51, 53, 159].

(a)

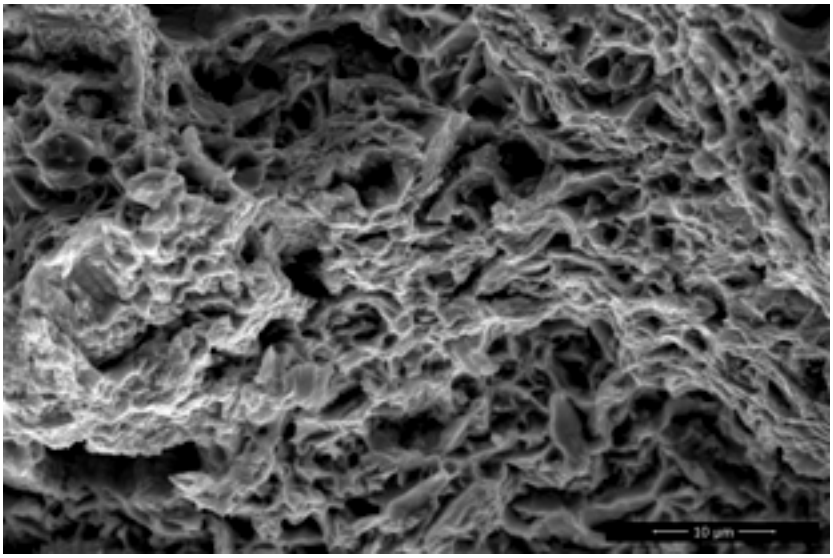

(b)

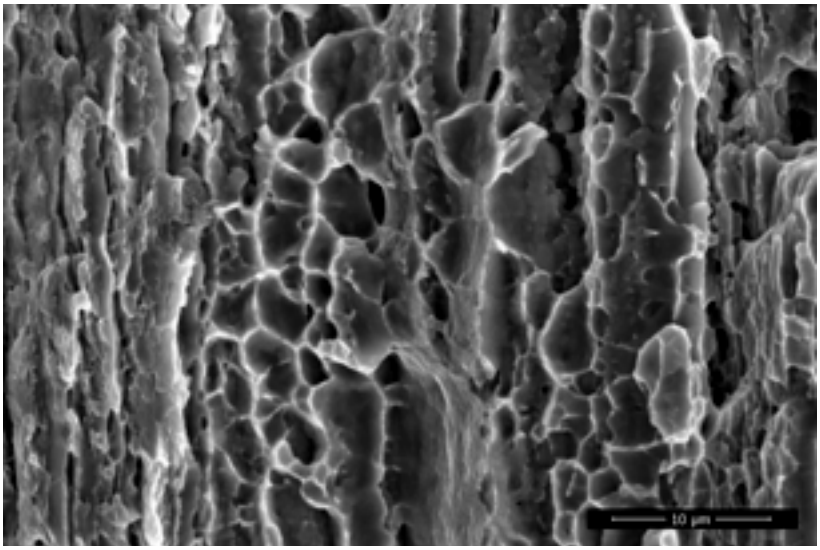

Fig. 3.18. *SEM fractographs from (a) ED and (b) TD surfaces of hot extruded 18Cr ODS ferritic steel and creep tested at 973 K (700 ºC).*

Figure 3.18 shows the SEM fractograph of the creep tested steel after hot extrusion. The fracture surface along TD exhibits shallow dimple type fracture and blunt fracture facets, while that along ED exhibits elongated features. These features correspond to the relatively isotropic small grains in TD and fine elongated structures in ED, which are in agreement with the EBSD results (Fig. 3.15(a) and (b). This characteristic fracture surface explains the lower ductility along TD, while the fracture surface along ED shows relatively uniform dimples and a fibrous structure due to grain boundary sliding.

3.6. Comparison of Various Consolidation Methods

Detailed analysis of the relative density, average grain size, microstructure and texture of 18Cr ODS ferritic steel after consolidation by different methods is listed in Table 3.2. As described earlier, the relative density of 92% for CIP, which saturated after sintering above 1423 K (1150 ℃) and showed an increasing relative density with ~ 97% for HIP, ~ 99% for SPS, and >99% for HE methods. As a consequence, equiaxed fine (~1.2 μm) grain distribution is observed after SPS. Although HE shows an anisotropic grain size distribution along the two perpendicular axes of extrusion, microstructural features vary within 0.8 to 2 μm and are comparable to SPS specimens. The relevant texture components which evolve during the consolidation are <1 1 1>, <1 1 0> fibers [41]. The <1 1 1> fibers in CIP and sintering, CIP and HIP, and SPS is observed to be about 1.5, 5.5 and 2 times higher respectively than the random texture due to the static and dynamic recrystallization processes during consolidation; however, HE specimen showed a strong <0 1 1> fiber about 7-9 times higher than random texture due to the deformation induced during the consolidation process.

The steel consolidated by SPS and HE showed better mechanical properties in contrast to CIP - sintered, and CIP - HIP process due to higher density as well as fine grained (0.8-2 μm)

structure (Table 3.3). However, anisotropy in mechanical properties is displayed by the HE steel, which is basically attributed to the crystallographic texture [165]. However, HE steel showed a better creep strength and rupture life than SPS, which clearly establishes that density is a crucial parameter for high temperature mechanical properties such as creep.

Based on the above comparison, HE is considered to be an optimum consolidation process for 18Cr ODS ferritic steel and SPS an alternate one. The cause for ‘‘anisotropy’’ in hot-extruded ODS ferritic steels is established to be:

(1) preferred crystallographic orientation and

(2) elongated fine grains with a high aspect ratio along ED.

However, the first reason is insignificant during plate or sheet fabrication as the longitudinal and transverse directions have same equivalent (1 1 0) orientation [166]. The second factor explains for the anisotropy through grain boundary sliding of the elongated grains that are oriented parallel to the hot-extrusion direction [166]. Hence, the elimination or reduction of anisotropy in mechanical properties of ODS ferritic steels is possible during subsequent product fabrication processes by adopting a suitable manufacturing process with well designed intermediate heat treatments.

Table 3.2. Relative density, average grain size, microstructural distribution and texture intensity of 18Cr ferritic ODS steel

Parameter	CIP and Sintering	CIP and HIP	SPS	HE	
				ED	TD
Relative Density (%)	92	96.6	98.6	>99	
Grain Size (μm)	24±5	16±3	1.2±0.5	0.8±0.2	2±0.5
Microstructure	Equiaxed	Equiaxed	Equiaxed	Equiaxed	Elongated
Texture intensity	~1.5	~5.5	~2.5	~7.5	~9.5

Table 3.3. Summary of mechanical properties of 18Cr ferritic ODS steel

Consolidation method			Avg. Hardness (HV_{20})	Creep test at 300MPa					
				873 K		923 K		973 K	
				t_r (h)	Elongation (%)	t_r (h)	Elongation (%)	t_r (h)	Elongation (%)
CIP and Sintering			268±5	--	--	--	--	4	<1
CIP and HIP			290±5	--	--	--	--	7	<1
SPS	ODS Steel	Transverse Direction	393±4	614	2.4	386	4.7	142	6.5
		Axial Direction	402±4	--	--	--	--	--	--
	Steel		146±6	14	0.6	4	1.2	3	1.4
HE	Transverse Direction		464±6	658	1.8	315	2.2	114	5.3
	Extruded (Axial) Direction		476±6	718	2.1	434	3.2	168	6.3

3.7. Summary

18Cr ODS ferritic steel powder was consolidated by various powder metallurgical processes like CIP, HIP, SPS and HE. The influence of sintering temperature on the relative density and microstructure has been elucidated. The following are the salient conclusions drawn from this study:

- Cold isostatic pressing (CIP) and sintering at 1423 K (1150 ℃) was identified to be optimum for achieving good compaction (92% density), which increases to 97% with CIP followed by HIP at 1423 K (1150 ℃). An equiaxed ferrite grain microstructure was observed in both cases, though the average grain size reduced from 24μm to 16μm from CIP/sintering to CIP/HIP treatment.
- EBSD characterization of CIP and sintering at 1423 K (1150 ℃) specimen revealed predominantly random texture. However, signature of preferential texture towards (1 1 1) and a nearly 5.5 times higher intensity than random is seen for the CIP and HIP processes.
- Consolidation using Spark Plasma Sintering was found to be very effective to achieve a density about 99% and a temperature range of 1323 to 1373 K (1050 to 1100 ℃) was found to be optimum for sintering by SPS.
- Consolidation temperature for a given stress plays a significant role in SPS on the densification behavior up to 1323 K (1050 ℃) and then saturates at slightly higher temperature, whereas hold time shows a negligible effect on the density. The microstructure changes from bimodal to uniform distribution of fine equiaxed recrystallized grains above 1323K (1050 ℃) with increase in sintering temperature.

- Consolidation temperature also influences the evolution microtexture; partially recrystallized microstructure observed at 1273 K (1000 ℃) changes to fully recrystallized structure at 1323 K (1050 ℃) during the sintering process by SPS. High temperature sintering favors the growth of (1 1 0) type clusters.
- The mechanism of creep deformation is established as lattice diffusion assisted by climb of dislocations over the dispersoids. The apparent activation energy is estimated as ~402 $kJmol^{-1}$ for stress level of 300MPa in the range of 873 to 973 K (600 to 700 ℃).
- The creep rate varied between one-two orders at 300 MPa between 873 to 973 K (600 to 700 ℃) and SEM investigation indicated ductile mode of failure.
- The anisotropy in mechanical properties, such as hardness and creep properties, of the 18Cr ODS ferritic steels consolidated by hot extrusion was investigated with special emphasis on microstructure and fractographic features.
- The <1 1 0> fiber texture along the ED was confirmed for the hot-extruded ODS steel. The cause for anisotropy of mechanical properties is the combined effect of preferred orientation and the distribution of elongated grain along ED.
- Size of the dimples and the presence of blunt fracture facets after HE support the lower creep strength in the transverse direction than in the longitudinal direction.
- Based on densification characteristics and microstructure, HE is considered to be optimum and SPS can be considered as an alternate consolidation process for 18Cr ODS ferritic steel.

Study of Deformation and Recrystallization Behavior in Oxide Dispersion Strengthened 18Cr Ferritic Steel

It has been established in Chapter 3 that consolidation of steel powder by hot extrusion results in high density with fine grained microstructure with enhanced mechanical properties as compared to other methods like hot isostatic pressing and spark plasma sintering. However, the unidirectional processing in hot extrusion results in a columnar grain structure, which leads to directional growth of grains with a high aspect ratio during further axial deformation for tube drawing and other downstream processes [78, 79]. Suppression of austenite to martensite phase transformation in these steels due to high chromium content is another challenge to control the microstructure through thermal treatments. Further, the high hardness obtained during the processing steps requires softening through intermediate annealing, which induces recovery and recrystallization in these steels [31].

The persistent morphological anisotropy during cold working manifests itself as non-uniform mechanical properties in the axial and transverse directions of the tube product [79]. Besides, the oxide dispersoids stabilize the microstructure through Zener pinning and contribute to the enhanced anisotropy during further processing. Although recrystallized grains enhance the ductility and high-temperature strength in hoop direction in the final tube/cladding product [31, 167], there are difficulties in achieving a stable equiaxed recrystallized fine grain structure by various intermediate heat treatments [89, 168]. It is well known that the stored energy in deformed alloys can be exploited to obtain equiaxed grains by recrystallization, despite the extreme directionality of initial microstructure [79]. Further, the role of oxide dispersoids on the softening mechanism, reduction of stored energy during intermediate annealing and incubation period for the substructural changes during heat treatment is not well understood. In this chapter,

the strategies for effective heat treatments have been identified to reduce or suppress anisotropy during unidirectional cold rolling of hot extruded 18Cr ODS ferritic steel. Differential Scanning Calorimetry (DSC) analysis has been carried out on deformed 18Cr ODS ferritic steel to identify the regime of recovery and recrystallization based on stored energy release during the heating cycle. Also, microstructural analysis using EBSD studies has been made to assess the effectiveness of the designed heat treatments. Further, repeated cold working followed by two step heat treatment has been carried out to achieve an ultra fine grained microstructure and randomization of texture. Hardness measurements have been carried out to support the microstructural observations and correlate with the mechanical properties of the steel after the above treatments.

4.1. Microstructure and Microtexture Characterization

4.1.1. EBSD Characterization of As-Received Steel

The microstructure of the hot extruded 18Cr ODS ferritic as decribed in detail in section 3.5, showed the presence of elongated grains along ED and equiaxed grains along TD (Fig. 3.15). The pole figures (Fig. 4.1(a) and (b)) reveal the predominance of (1 1 0) planes aligned in the perpendicular direction to ED and parallel to TD respectively. The intensity of pole concentration is found to be about seven and nine times higher than the random distribution in ED and TD respectively. This is a strong indication of texture and is a matter of concern with respect to anisotropy in mechanical properties [52, 97]. Apart from the above the intensity contours with intensity ~3 observed in Fig. 4.1(b) correspond to (1 1 0) [1 1 1] and (1 1 2) [1 1 1] components of α-fiber. The existence of preferential texture is attributed to the deformation induced α-fiber texture introduced during extrusion, which is in agreement with literature [97, 169].

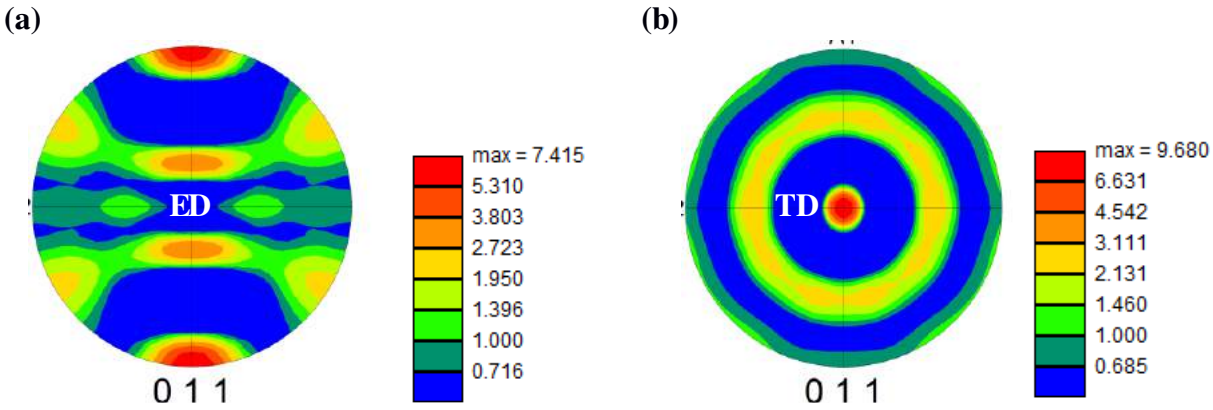

Fig. 4.1. *(011) pole figure of hot-extruded 18Cr ODS ferritic steel for (a) ED and (b) TD sections.*

4.1.2. EBSD Characterization of Deformed Steel

In order to study the effect of plastic deformation on the mechanism of recovery and recrystallization, the hot extruded steel along both ED and TD sections was subjected to cold rolling (uniaxial), which are termed as EDR and TDR sections respectively, which is illustrated as a schematic in Fig. 4.2.

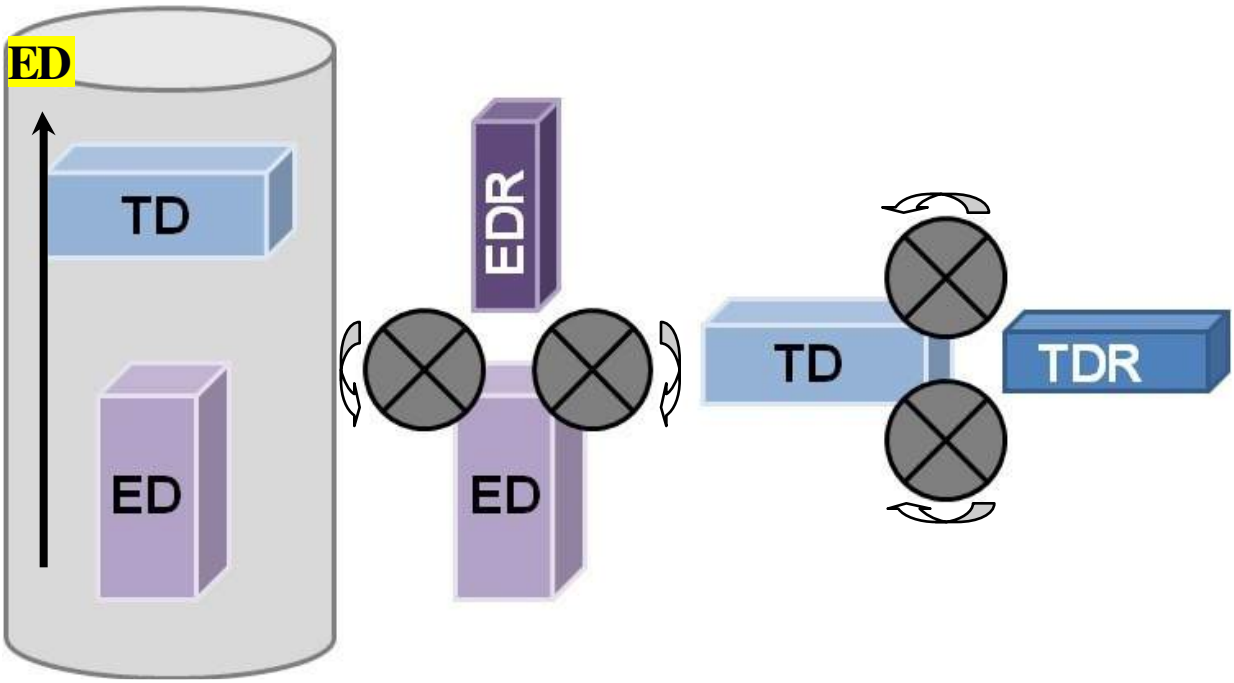

Fig. 4.2. *Schematic of sampling and direction of rolling from hot extruded 18Cr ODS ferritic steel.*
**Note: ED, TD and R stands for extrusion, transverse and rolling direction respectively.*

EBSD IQ and crystal orientation maps of EDR and TDR sections obtained by 50% cold rolling along the two directions are presented in Fig. 4.3(a) and (b). The microstructure exhibits distinct deformation bands and intensity gradients within a grain in contrast to Fig. 3.15 (Chapter-3, Section 3.5). This can be understood as follows: In a deformed material the increased dislocation density causes diffuse diffraction patterns which is indicative of slip activity or substructure modifications; further the color gradient within individual grains is a signature of minor change in orientation due to substructure formation. Figure 4.3 clearly indicates the differences in deformation substructure along ED and TD despite similar type and extent of deformation, which is caused by the grain morphology and preferential texture observed in Fig. 3.15 (section 3.5). The crystal orientation map of EDR shows the retention of a directional microstructure along with localized microstructural variations marked in Fig. 4.3(a). The region marked (1) in Fig. 4.3(a) indicates ultrafine banded structure (width <0.5μm) parallel to the rolling direction, which is typical of compression of the initial band and additional unidirectional flow of material during rolling, while regions marked 2 and 3 show a coarse deformation bands possibly due to coalescence of grains with similar orientations. Further, the presence of a grain with a cell structure with directional alignment in the rolling direction is observed, which is a signature of strain gradient and signifies the formation of geometrically necessary dislocations (GNDs). The GNDs and fine grain size promote toughness and ensure strain compatibility during rolling [170].

Figure 4.3(b) shows the microstructure of TDR specimen. The presence of shear bands along with ultra-fine (<0.5 μm) grains surrounding the shear bands (Fig. 4.3(b)) is clearly revealed. The formation of shear bands during deformation over (0 1 1) planes in TD suggests that the material flow is higher in the ED direction or in <0 1 1> direction.

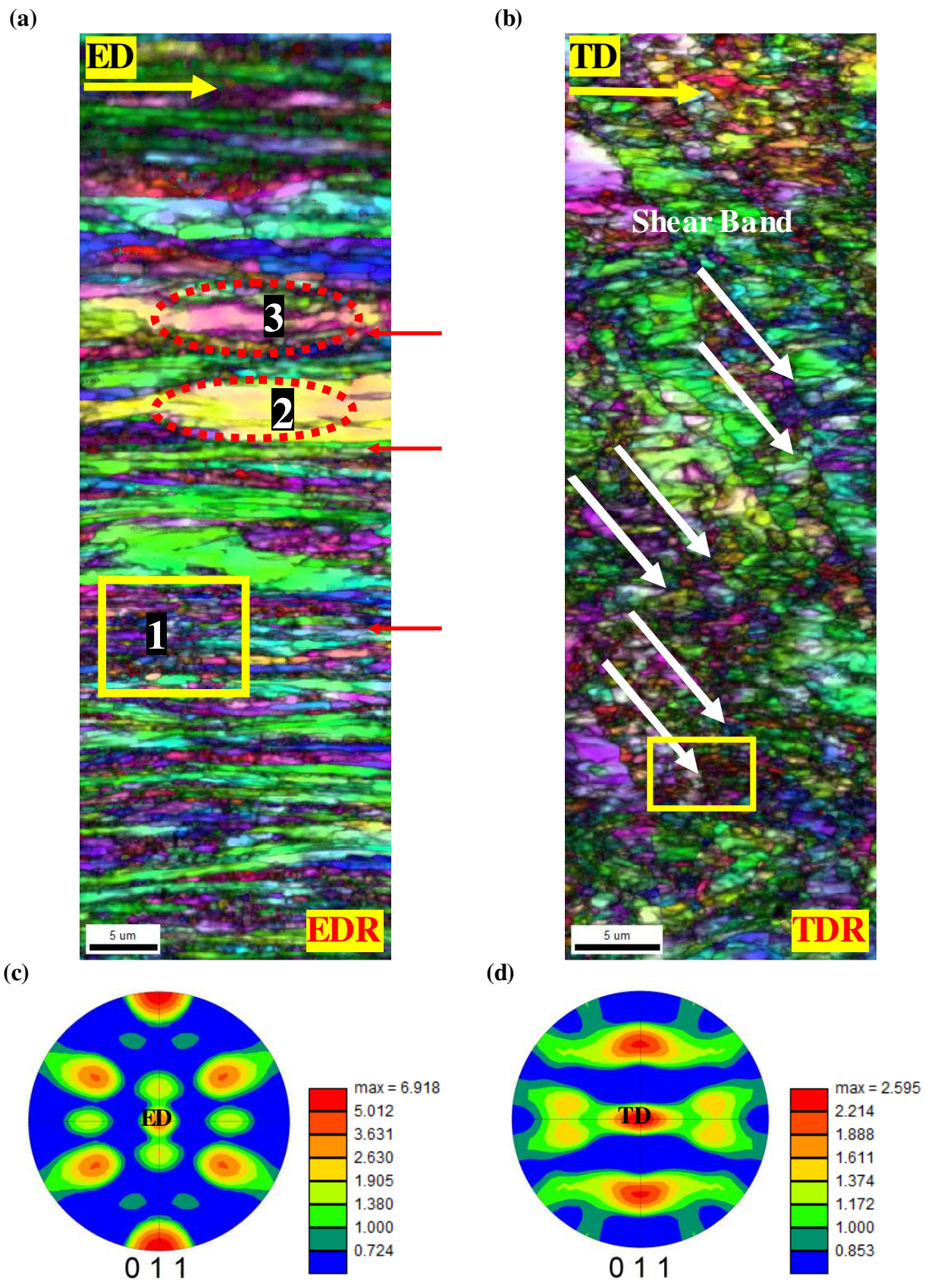
(a)
ED
3
2
1
5 um
EDR
(b)
TD
Shear Band
5 um
TDR
(c)
ED
0 1 1
max = 6.918
5.012
3.631
2.630
1.905
1.380
1.000
0.724
(d)
TD
0 1 1
max = 2.595
2.214
1.888
1.611
1.374
1.172
1.000
0.853

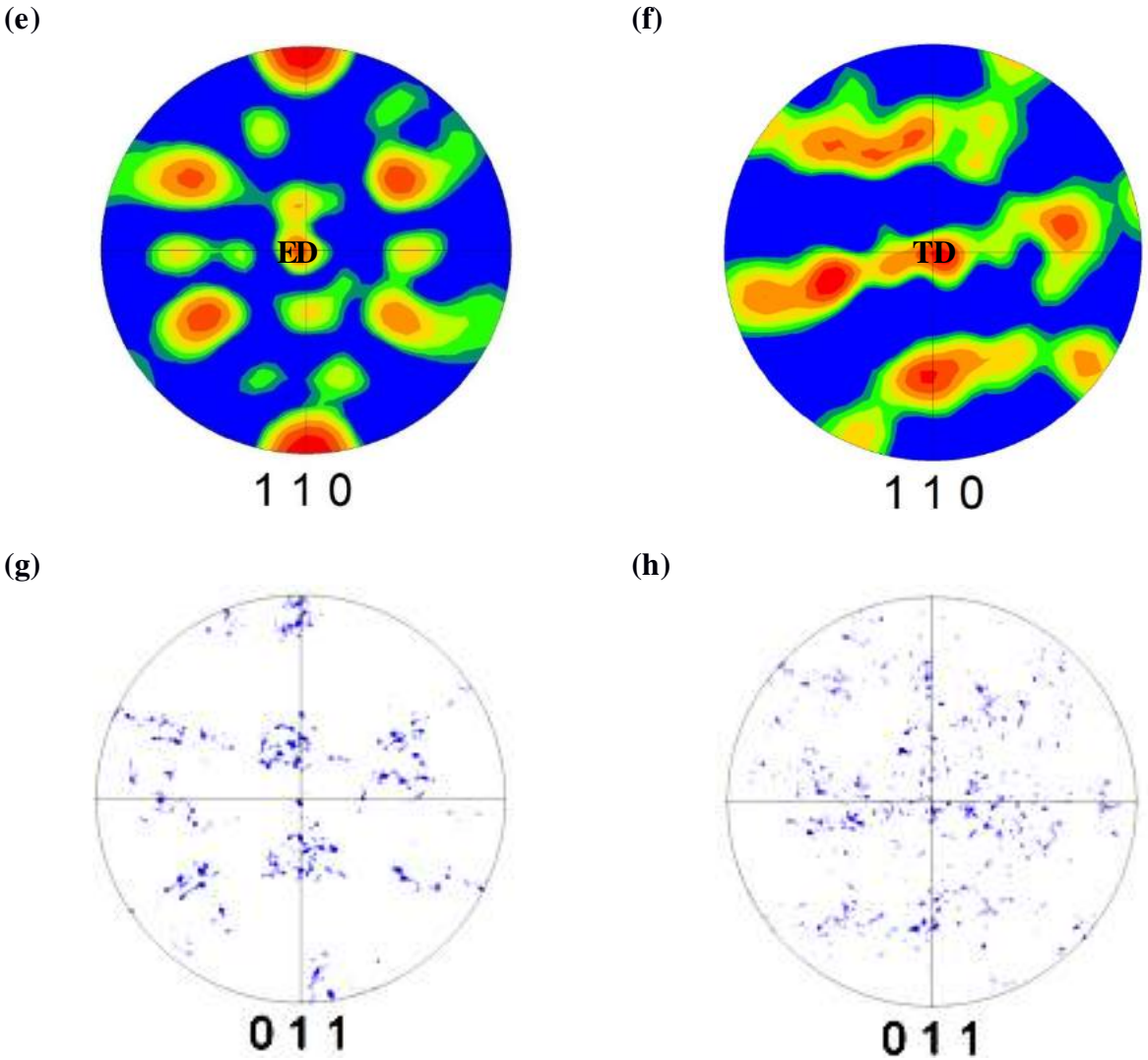

Fig. 4.3. *Overlay image of EBSD inverse pole figure and image quality maps of hot-extruded 18 Cr ODS ferritic steel obtained after 50% cold rolling along the (a) extruded, and (b) transverse direction; (c,d) (011) pole figure after rolling along ED and TD respectively and discrete {0 1 1} pole figure distribution of (d) retained cellular structure of matrix region (marked red square box in Fig. 4.3(b)) and (e) cellular structure in shear band (marked blue square box in Fig. 4.3(b)) after deformation*

Figures 4.3(c)/(e) and (d)/(f) show the corresponding pole figures with and without imposing rolling symmetry, revealing the resultant texture distribution during rolling. A similar distribution of (1 1 0) [1 1 1] fiber texture and intensity is observed for EDR as that of ED. However, the development of (1 1 0) [0 0 1] component in EDR is attributed to the deformation induced α-fiber texture during rolling as discussed earlier (Chapter-3, Section 3.5). The texture

intensity is found to be reduced in TDR specimen to ~3 as compared to its original extent of ~9 in TD section. The initial (1 1 0) [0 0 1] fiber texture in TD section is found to change to (1 1 2) [1 1 1] fiber texture in TDR due to simple shearing mechanism [171], which clearly shows the dependence of direction of applied load on the resultant texture. Further, EBSD analysis of a typical region in the microstructure (marked – yellow square box in Fig. 4.3 (a) and (b)) reveals that the cellular structure within the shear bands in an individual grain is again of similar crystallographic orientation after this level of strain in EDR, as shown in the pole figure of Fig. 4.3(g). Preferred orientation of shear bands is identified to be identical with the initial texture of ED specimen with about 5º deviation and with similar texture intensity (Fig 4.3(g)). However, rolling along TD specimen shows nearly random distribution (Fig. 4.3(h)) for the fragmented grain within the shear bands and an overall texture intensity (~3) of TDR is found to be decreased unlike rolling along ED.

4.2. Study of Recovery and Recrystallization Kinetics by Differential Scanning Calorimetry (DSC) Analysis

4.2.1. Identification of Recovery and Recrystallization Temperature Domain

Figure 4.4 shows the baseline corrected DSC thermograms for the heating cycle of the hot extruded, 50% cold rolled (Run#1) and repeat run (Run#2) of post DSC steel. The first sharp endothermic peak seen at 934 K in all the three thermograms corresponds to the Curie transition from ferro to paramagnetic [172]; however, two sequential secondary peaks have been observed for the 50% cold rolled specimen (Run#1). However, the repeat run (Run#2) of this same specimen does not show the two peaks. These observations can be explained as follows: when a metal is cold worked by plastic deformation, a small portion of the mechanical energy expended in deforming the metal is stored in the specimen. This stored energy resides in the crystals in the

form of point defects (vacancies and interstitials), dislocations, and stacking faults in various forms and combinations in the metal. Therefore, a cold-worked specimen, being in a state of higher energy, is thermodynamically unstable. With thermal activation, such as provided by annealing, the cold-worked sample tends to transform to states of lower energies through a sequence of processes with microstructural changes.

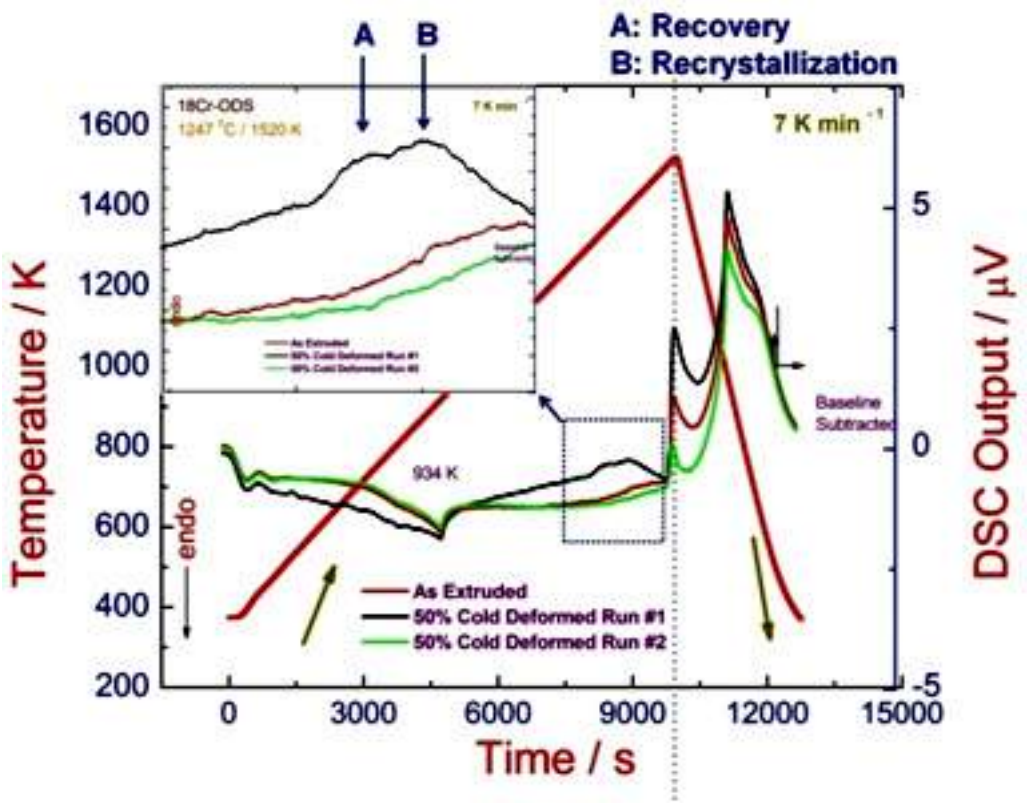

Fig. 4.4. *Comparison of three DSC traces: as-received hot extruded steel, Run#1 on 50% cold worked and Run#2 is successive of Run#1 under identical experimental conditions; inset corresponds to the marked region in the on heating DSC thermogram showing distinct thermal arrests due to recovery and recrystallization.*

The secondary peaks in Run#1 indicate the release of stored energy due to deformation during rolling, in the form of thermal activated restoration processes which results in the rearrangement of dislocations via recovery and recrystallization [163, 173]. Hence, the two distinct peaks at temperatures of about 1350 and 1420 K (1177 and 1147 °C) signify the

occurrence of recovery and recrystallization respectively. However, the observed recovery and recrystallization peaks are about 400 to 500 K (127 to 227 ℃) higher than the reported temperatures of 815 and 1070 K (542 and 797 ℃) respectively for 70-80% deformed austenitic stainless steel [174]. The higher recovery and recrystallisation temperature in the present study provides evidence for the strong pinning effect offered by the dispersoids. However, the repeat run (Run#2) of the same specimen does not show the two peaks, which indicates that the peaks resolved in the previous DSC thermogram arise from the release of stored energy due to defect relaxation.

4.2.2. Kinetics of Recovery and Recrystallization

The fraction of recovery and recrystallization rate at different heating rates is illustrated in Fig. 4.5. It is clearly observed that both recovery and recrystallization occur at lower temperatures at lower heating rate (7 $Kmin^{-1}$) suggesting higher rate of transformation, than at higher heating rates (15 and 30 $Kmin^{-1}$). The start and finish temperatures of both recovery and recrystallization are found to increase with rate of heating, though it saturates at higher heating rates (15 and 30 $Kmin^{-1}$), due to lower rate of stored energy release. The stored energy release in recovery and recrystallization has been understood using the non-isothermal Kolmogorov–Johnson–Mehl–Avrami (KJMA) formalism with the approximation of site saturation during the microstructural changes for a given heating rate [175-178]. The kinetic expression can be mathematically expressed as follows [179]:

$$f(T) = 1 - \exp\left[-k_0^n . \exp\left\{-\frac{nQ_{eff}}{RT_p}\right\} \times \{R(T - T_s)^2/\beta Q_{eff}\}^n\right] \quad (4.1)$$

where, 'k_0' is the rate constant which shows the approximate number of atomic species diffusing from a suitable site to take part in volume diffusion, 'n' is the Avrami growth exponents, T_s is the

transformation start temperature and β is the heating rate. Further, the apparent activation energy 'Q_{eff}' for the overall transformation process including recovery and recrystallization can be determined by using the following Arrhenius rate expression:

$$k = k_0 . \exp\left(\frac{-Q_{\text{eff}}}{RT_p}\right) \tag{4.2}$$

where k is the Arrhenius rate constant, R is the universal gas constant (8.314 $Jmol^{-1}K^{-1}$) and T_p is the absolute transformation temperature. Q_{eff} derived by the Kissinger linearization approximation procedure [174] is illustrated in Fig. 4.6 (a) and (b) and kept constant for fitting in the model. It is seen that the KJMA model shows a reasonably good fitting for both the recovery and recrystallization curves represented by the line passing through the experimental data points in Fig. 4.5. The kinetic parameters calculated based on the model are listed in Table 4.1.

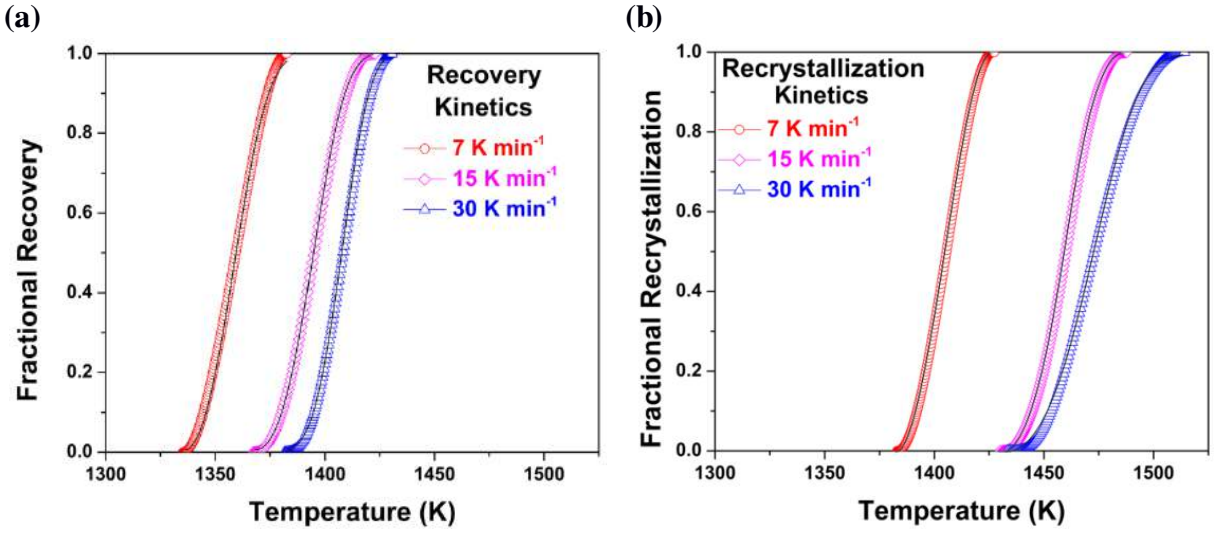

Fig. 4.5. *Fractional (a) recovery and (b) recrystallization as a function of temperature under different heating rates for 50% cold worked 18Cr ODS ferritic steel.*

The apparent activation energy, Q_{eff}, is estimated as ~ 266 and 358 $kJmol^{-1}$ for the recovery and recrystallization processes respectively. These values are higher than the reported value of ~225 $kJmol^{-1}$ for lattice self diffusion in α-Fe [180]. This clearly establishes the role of dispersoids,

which act as diffusion barriers although the mechanisms of recovery and recrystallization are similar. The estimated activation energy value of 358 $kJmol^{-1}$ for recrystallization suggests that activated bulk diffusion is the predominant mechanism for recrystallization of the deformed steel. This value is close to that reported for TWIP steel (Fe–25 Mn–1 Al (wt%)) [181] which is about 330 $kJmol^{-1}$, where bulk diffusion is the operative mechanism for recrystallization.

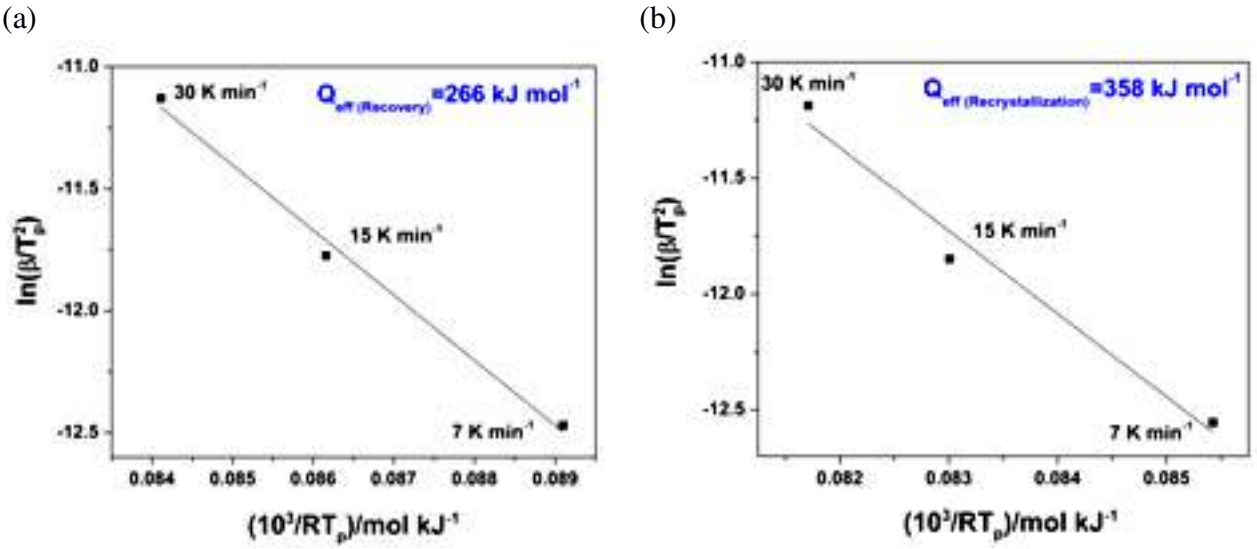

Fig. 4.6. *Plot showing the Arrhenius type relationships for the steady state (a) recovery and (b) recrystallization.*

Table 4.1. Estimated kinetic parameters for recovery and recrystallization of 50% cold deformed 18Cr ODS ferritic steel

Heating rate (β) [$Kmin^{-1}$]	n	Q [$kJmol^{-1}$]	K_0 [s^{-1}]	R^2 value for the fit
Recovery				
7	0.95	266	1.32×10^{10}	0.97
15	1.10	266	6.62×10^{10}	0.99
30	1.22	266	1.18×10^{11}	0.99
Recrystallization				
7	0.96	358	1.39×10^{14}	0.99
15	1.10	358	5.52×10^{13}	0.99
30	0.97	358	4.45×10^{13}	0.98

Since it is well established that the recrystallization temperature for most ferritic steels is in the temperature range of 0.5-0.6 T_m (T_m – melting temperature in K) [182], the observed high

activation energy and temperatures for recovery and recrystallization in the present steel is clearly a consequence of the presence of fine dispersoids. The effective kinetic exponent 'n' estimated from Equation 4.1 is in the range of 0.9 to 1.2 for various heating rates for both recovery and recrystallization process. Further, 'k_0', which is a measure of the number of equivalent sites for diffusional process shows an increasing value for recovery with increase in heating rate (Table 4.1). On the other hand, lower heating rates show a higher k_0 value for recrystallization, which indicates near equilibrium diffusion assisted phenomena.

4.3. Design of Heat Treatment to Minimize Anisotropy

DSC studies have clearly established the effect of heating rate on the kinetics of recovery and recrystallization phenomena, and the two processes are clearly delineated at low heating rate. Hence it is expected that lower heating rate would provide higher driving force for recrystallization resulting in a fine, equiaxed grain structure. Hence, the microstructure of the steel recrystallised during DSC experiment has been simulated, wherein the EDR and TDR samples were subjected to two types of heat treatments: (a) single step heat treatment consisting of heating at a rate of 7 $Kmin^{-1}$ to 1420 K, holding for 1h followed by air cooling to room temperature, which are designated as AEDR and ATDR respectively, (b) series of two step heat treatments with intermediate rolling as illustrated in Table 2.2 (Section 2.2). The changes in microstructure and microtexture are discussed in the following sections to identify the optimum treatment.

4.3.1. Conventional Recrystallization Treatment

EBSD crystal orientation map superimposed with IQ map of AEDR and ATDR are shown in Fig. 4.7. The figure reveals significant growth of the recrystallized grains. The AEDR

specimen exhibited an increase in the aspect ratio up to 8 in contrast to 3 in ATDR. The rapid growth of elongated grains is attributed to grain boundary migration associated with strain energy reduction. The large strain energy provides the driving force for rapid migration of boundaries at this high temperature far exceeding the 'Zener pinning' effect of the dispersoids [79, 183].

Figure 4.7 shows regions (marked) consisting of distribution of ultrafine (<0.5 μm) equiaxed grains interspersed between the coarse elongated grains. In general, the heterogeneous nature of deformation is attributed to individual grain orientation and morphology that evolved during rolling [184].

The cell structure in regions marked 2 and 3 in Fig. 4.3(a) that formed during the deformation process in EDR treatment leads to a larger reduction in the stored energy unlike in region 1, the deformation shear band in Fig. 4.3 during the process of annealing. This observation also establishes the initiation of recovery during slow heating leading to annihilation or rearrangement of dislocations, which reduces the stored energy considerably to levels where the Zener pinning effect is manifested thus limiting the grain growth. This is supported by the presence of the small peak corresponding to the recovery phenomena at 1320 K in the DSC profile. The combined influence of the dispersoid pinning and the driving force for grain boundary migration at high temperatures is essentially controlled by the amount of stored energy. The low stored energy due to recovery does not assist the advancement of the boundary front despite the high temperature, resulting in small and equiaxed grains. However, the duration in the recovery regime is not adequate for complete recovery which results in a bimodal distribution at localized regions in the microstructure. Although randomization of texture was observed in both AEDR and ATDR, the anisotropy in grain morphology in the ED section as compared to

TD is of major concern. Hence, further studies focus on the EDR specimen where different thermo-mechanical treatments have been attempted with an aim of obtaining a uniform grain size distribution and texture.

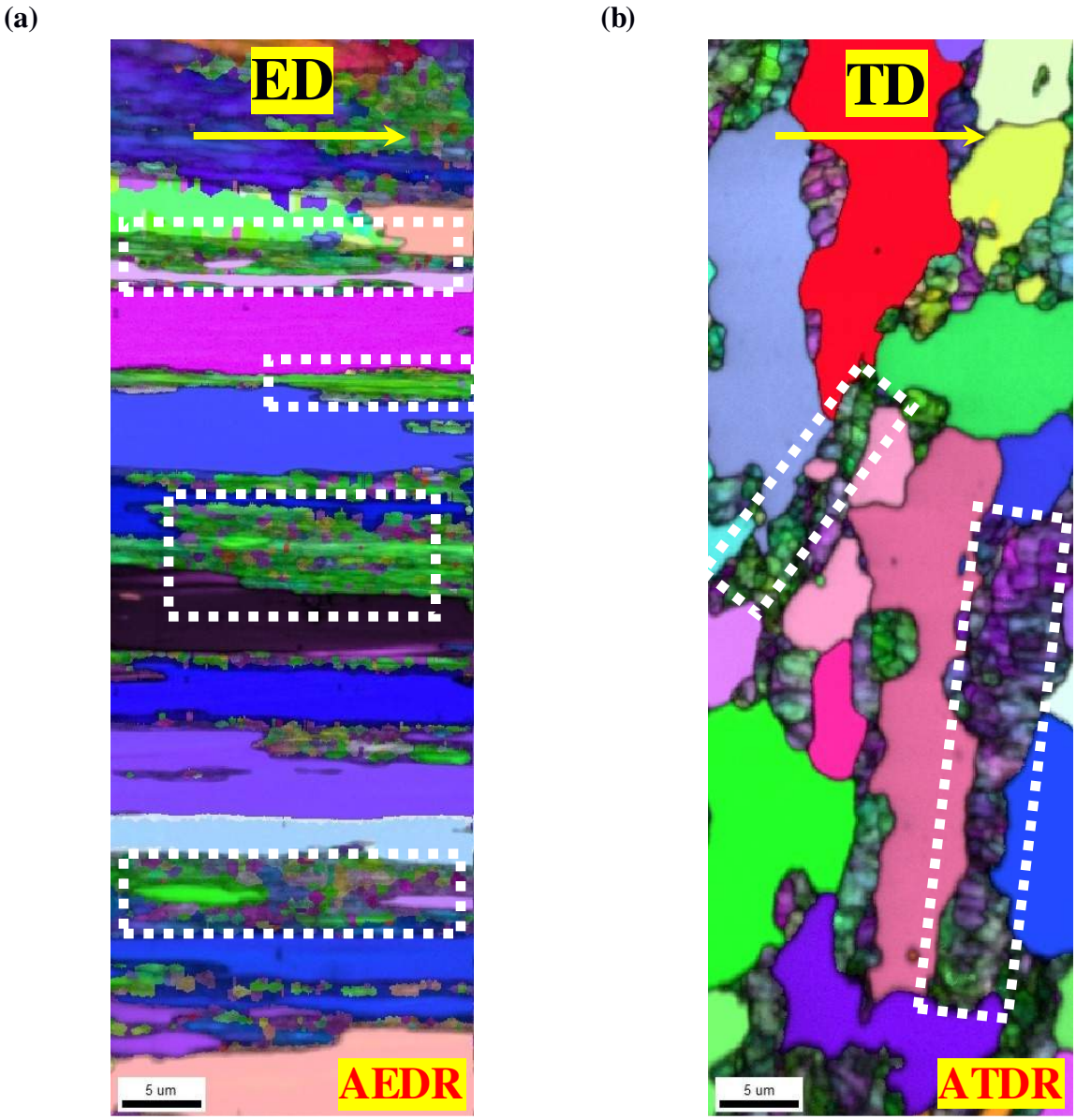

Fig. 4.7. *Overlaid EBSD crystal orientation and IQ maps of (a) AEDR and (b) ATDR steel. (Fine grain region marked)*

4.3.2. Two Step Heat Treatment

Based on the inputs from DSC analysis a two step heat treatment has been designed simulating the recovery and recrystallization phenomena. The EDR specimen was heated at a

constant rate of 7 $Kmin^{-1}$ to 1350 K held for 2 h followed by raising the temperature to 1420 K held for 0.5 h and air cooled, and the sample is designated as A_1EDR. The duration at 1350 K is kept higher (2 h) to achieve a higher extent of recovery and a shorter duration at 1420 K to restrict grain growth. An iterative process of deformation (50% cold rolling) and two step annealing has been carried out on the steel subjected to treatment A_1EDR to generate a uniform equiaxed ultrafine grain microstructure and the samples are designated as A_2EDR and A_3EDR respectively and characterized in detail, which is described in the next section. The above treatments that have been chosen in the present study are summarized in Table 2.4 (Section 2.2).

4.3.3. Characterization of Microstructure after Two Step Heat Treatment

The EBSD superimposed crystal orientation and IQ maps for the A_1EDR, A_2EDR and A_3EDR are shown in Fig. 4.8. The presence of ultrafine (average size ~ 0.5 μm) equiaxed grains is observed from the figure (marked with black arrow). In addition, the microstructure also shows the presence of few regions with elongated grains (marked with white arrow), whose fraction progressively decreases from A_1EDR to A_3EDR (0.3 to 0.1) and is far lower than in EDR (0.8) (Fig. 4.3(a)). This is possibly due to the retention of the substructure that formed due to deformation in EDR discussed earlier (Fig. 4.3(a), region marked 2 and 3). Further, the respective (110) pole figures of Fig. 4.8(a-c) are presented in Fig. 4.8(d-e), which shows an increasing extent of random orientations.

The (1 1 0) [1 1 1] fiber is generated during the process and the (1 1 2) [1 1 1] fiber generated due to shear (Fig. 4.3(a)) is found to be reduced; however, the intensity shows a tendency towards randomization (intensity about 1-2). The grain size distribution after the above thermo-mechanical treatments is shown in Fig. 4.9. The figure reveals a distinct bimodal grain size distribution; which tends to become more uniform from A_1EDR to A_3EDR. This is

attributed to the fragmentation of elongated grains during the deformation process of 50% cold rolling and two step heat treatment which helps in nucleating fine grains.

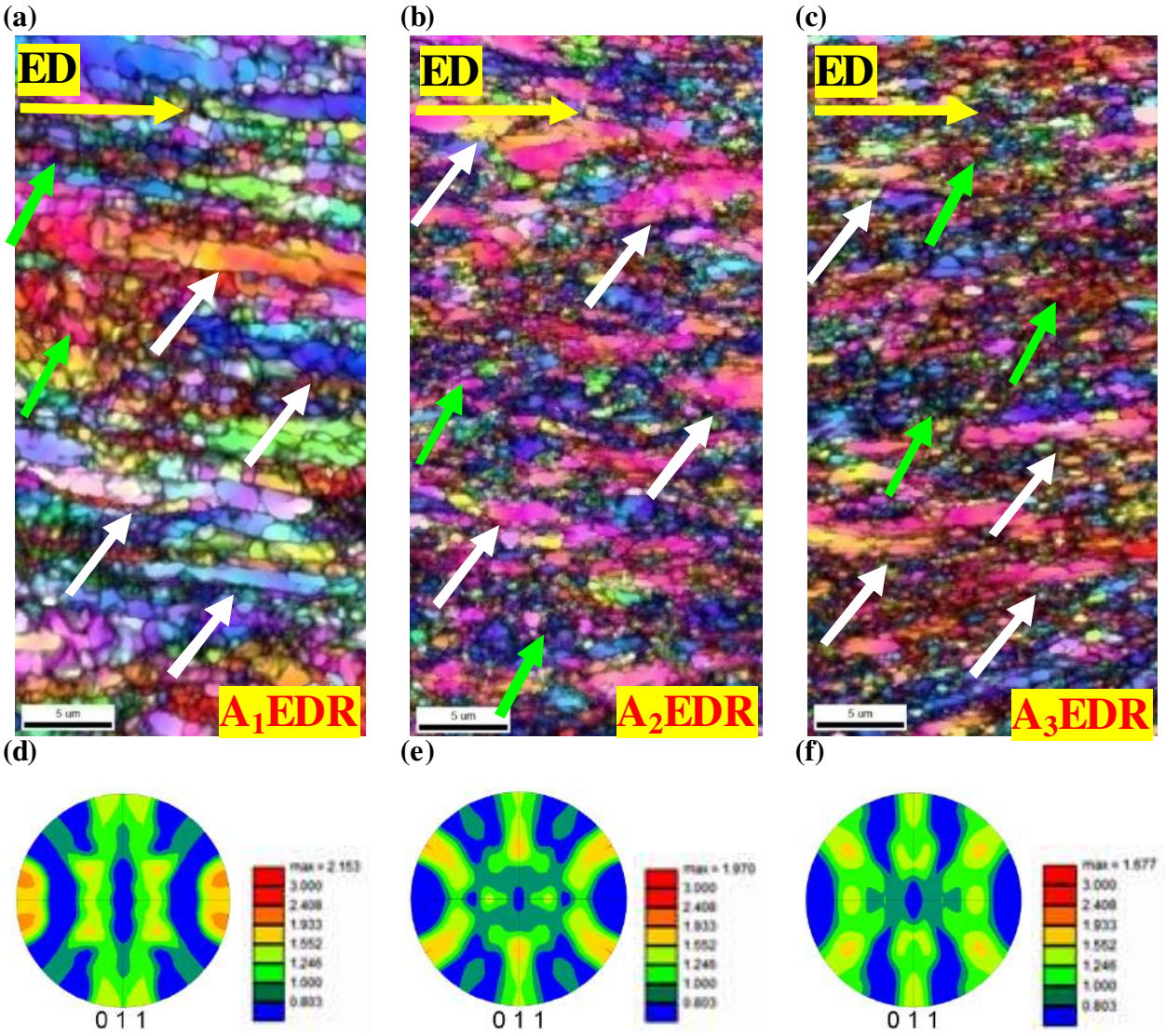

Fig. 4.8. *Overlay image of EBSD crystal orientation and image quality maps of 50% cold rolled 18Cr ODS ferritic steel followed by two step heat treatment (a) A_1EDR (1^{st}), (b) A_2EDR (2^{nd}) and (c) A_3EDR (3^{rd}) iteration of deformation followed by 2 step heat treatment and (c), (d) and (e) relevant (011) pole figures. (ED- Extruded direction, Marked region: fine grain structure- green arrow, elongated deformation band- white arrow).*
*(*Note: A uniform legend (intensity value from 0-3) has been used for ease of interpretation)*

Further insight into the substructure is obtained by analysis of intragranular misorientation data (< 2° misorientation) using Kernel Average Misorientation (KAM) angle

distribution. The dislocation densities that are related to GNDs have been measured using the average KAM value. The KAM distribution shown in Fig. 4.10(a) establishes the lower extent of local misorientation in ED as compared to EDR.

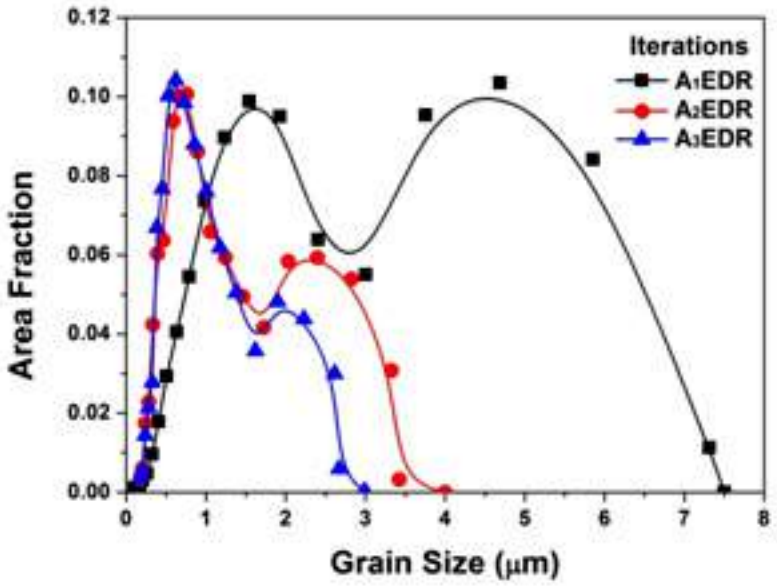

Fig. 4.9. *Comparison of variation of grain area fraction obtained by iterative deformation and 2 step annealing.*

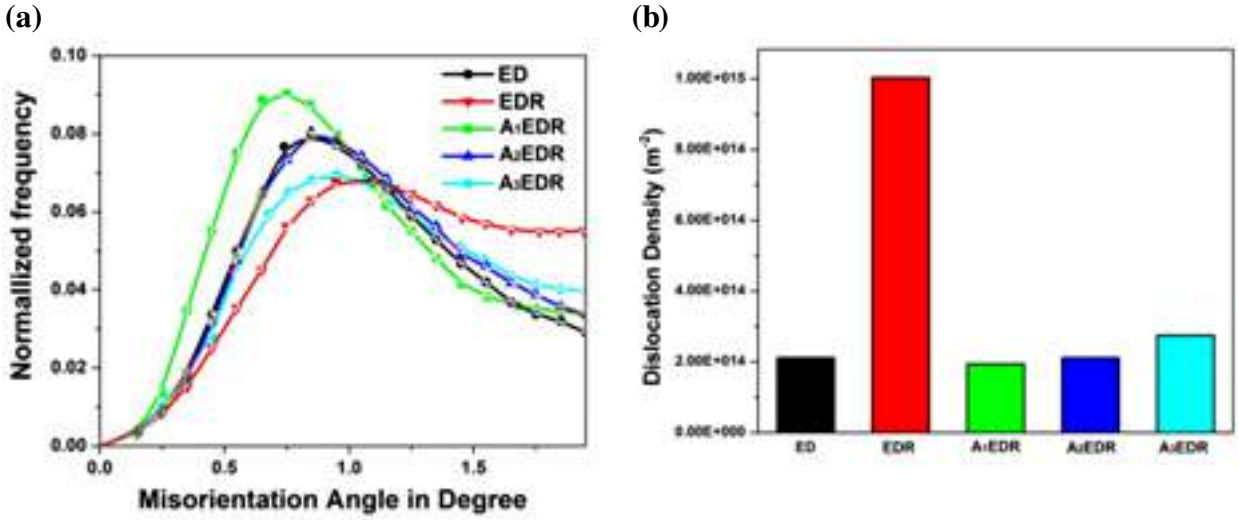

Fig. 4.10. *(a) KAM angle distribution (0-2°) and (b) change in dislocation density with different stages of processing.*

Although minimum KAM value is observed in A_1EDR, further treatments shift the peak of KAM distribution to a higher value, which can be correlated to the dislocation density after these treatments as follows [185, 186]:

$$\rho_{GND} = \frac{\theta_{KAM(avg)}}{2b} r_{avg} \quad (4.3)$$

where GND respresent the Geometrically Necessary Dislocations, θ is average KAM angle in radians, b is the Burgers vector (2.48×10^{-10} m) and r_{avg} is ratio of surface area and volume of substructure (within misorientation of 2º). Table 4.2 shows the variation in average local misorientation and dislocation density for the different treatments. Figure 4.10(b) shows the variation in density of GND for the different treatments including the reference ED condition. It is evident from the plot that density of GND for ED, A_1EDR, A_2EDR and A_3EDR are about one order lower in contrast to EDR, which indicates the annihilation of dislocations during annealing treatments. Further, A_1EDR shows the lowest GND, which is comparable to that of ED condition. The rearrangement of dislocations generated during progressive deformation and annealing manifests as ultrafine equiaxed grain distribution in the microstructure (Fig. 4.8(a-c)). The retention or increased dislocation density as observed in Fig. 4.10(b) despite repeated treatments is attributed to the pinning effect of dispersoids, which is also responsible for the progressive reduction in average grain size (Table 4.3) than achievable in conventional ferritic steels [187, 188].

4.3.4. Evaluation of Mechanical Properties using Instrumented Hardness

Figure 4.11 represents the variation in indentation load-displacement curves for ED, TD, EDR, TDR, A_1EDR and A_2EDR specimens of 18Cr ODS ferritic steel. The average hardness for the ED and TD specimens is measured as 464±6 and 476±6 HV respectively. This high value of

hardness is due to the combined effect of fine grain structure (<2 μm) and dispersoid strengthening. The difference in hardness values across the two directions is given in Fig. 4.12(a). A variation of about 40 HV between ED and TD is a reflection of the initial morphological anisotropy discussed earlier (Chapter-3, Section 3.5). An increase in average hardness to 515±8 HV and 568±8 HV was observed in EDR and TDR respectively due to the deformation. Further hardness measurements were carried out on two perpendicular surfaces ED and TD sections of the A_1EDR and A_2EDR samples.

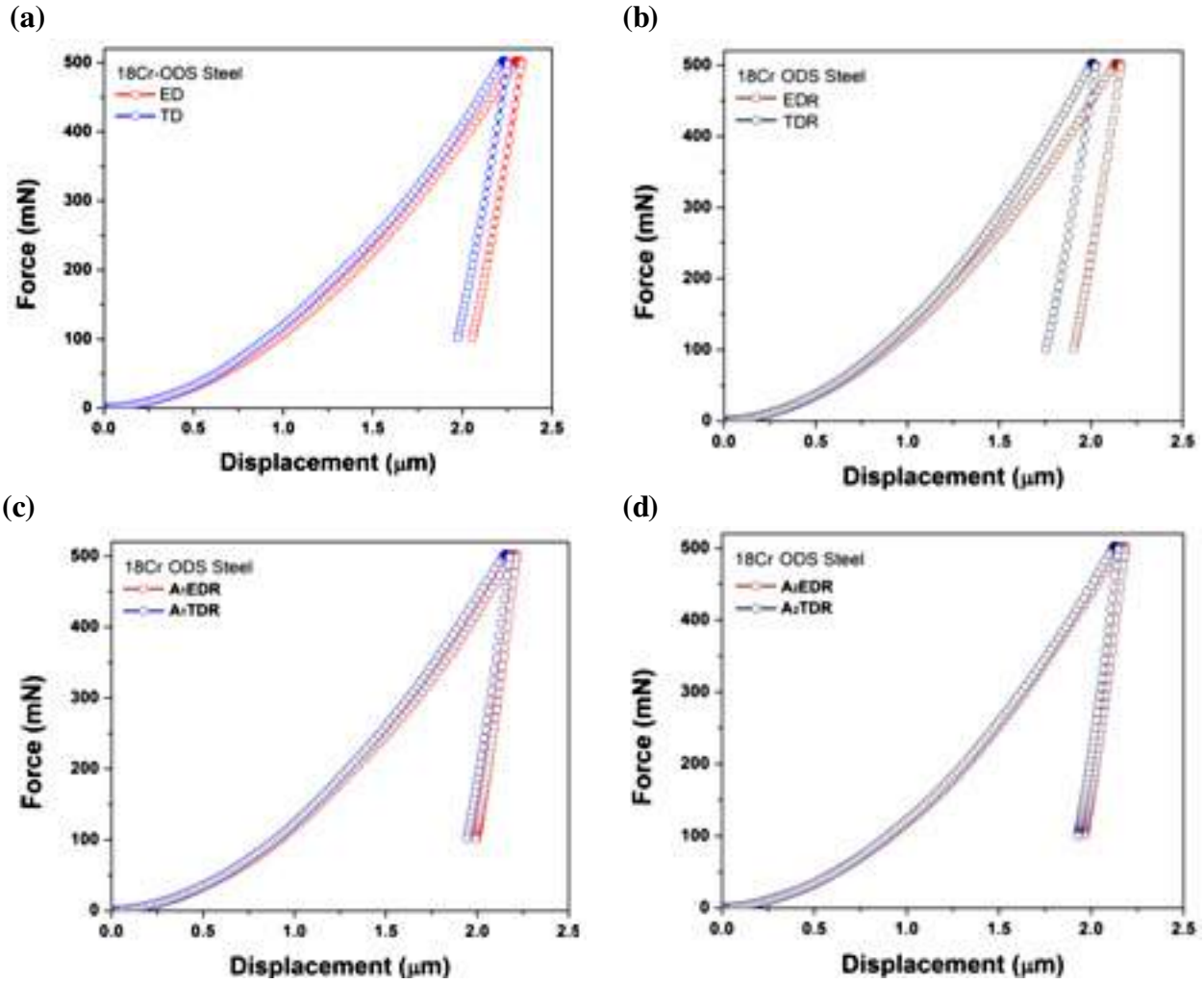

Fig. 4.11. *Comparative analysis of instrumented indentation hardness profile for (a) ED and TD, (b) EDR and TDR, (c)* A_1EDR *and* A_1EDR *and (d)* A_2EDR *and* A_2EDR *of 18Cr ODS ferritic steel.*

The hardness of A_1EDR sample along ED and TD directions was determined to be 475±4 and 495±4 respectively. Similarly the hardness of A_2EDR sample along ED and TD directions was determined to be 489±4 and 505±4 respectively. These observations suggest that the difference in hardness between the ED and TD sections decreases with repetitive deformation and annealing treatments. Further, the slope of initial region of the unloading curves in Fig. 4.11 is a characteristic of elastic modulus (related to stiffness) [133]. The elastic modulus of ED and TD samples was estimated to be 146 and 148 GPa respectively, which is nearly same. The elastic modulus in EDR and TDR also showed an increase to 177 and 187 GPa respectively, due to the strain during rolling. A high value of elastic moduli ~ 200 GPa is obtained for A_1EDR and A_2EDR, which suggests that repeated deformation and annealing process has resulted in grain refinement as well as isotropic mechanical properties (Table 4.2). A near two fold increase in the difference to about 60 HV is observed between EDR and TDR. Further, the difference in hardness value after rolling is found to manifest more in TD than in ED specimen, which indicates the higher rate of strain hardening and dislocation pile-up during rolling along [1 1 0]. This difference gradually decreases after the two step heat treatment due to formation of fine grains thus reducing the anisotropy in the steel. Though, addition of Al is reported [189] to reduce the microstructural anisotropy during hot processing, anisotropy in mechanical properties upon recrystallization remains a major concern for high Cr ODS ferritic steel [189]. However, nearly similar hardness and elastic moduli in ED and TD after repeated treatments supports the observed ultra-fine grain distribution and randomization of texture attributes (Fig. 4.8). Figure 4.12(b) shows the penetration profiles obtained during indentation of the specimen to derive the dynamic properties as a function of time.

Table 4.2. Microstructural attributes and mechanical properties of 18Cr ODS ferritic steel

Specimen code	Grain size (μm)	Fraction of equiaxed grain (Aspect ratio ~1)	Maximum texture intensity	Average KAM (degree)	GND ($10^{14}m^{-2}$)	Hardness (HV)	Elastic modulus (GPa)
ED	5±0.1	<0.1	~7.5	0.85	2.11	448±6	145
TD	1±0.3	0.8-0.9	~9.5	-	-	487±6	148
EDR	10±1	>0.9	~7.0	1.2	10.02	515±8	176
TDR	0.8±0.4	0.6-0.7	~2.5	-	-	568±8	186
AEDR	Min:0.5±0.1 Max:80±15 (Bimodal)	0.4-0.5	-	-	-	-	-
ATDR	Min:0.5±0.1 Max:22±6 (Bimodal)	0.2-0.3	-	-	-	-	-
A_1EDR	Min:2±0.5 Max:5±0.5 (Bimodal)	0.6-0.7	~2.1	0.75	1.93	475±4	199
A_1TDR	-	-	-	-	-	495±4	197
A_2EDR	Min:0.5±0.1 Max:2.5±0.5 (Bimodal)	0.8-0.9	~1.9	0.84	2.11	489±4	204
A_2EDR	-	-	-	-	-	505±4	203
A_3EDR	Min:0.5±0.1 Max:2±0.5 (Bimodal)	>0.9	~1.6	0.95	2.74	518±4	206

*Note: Average of maximum diameter has been provided for grain size measurement.

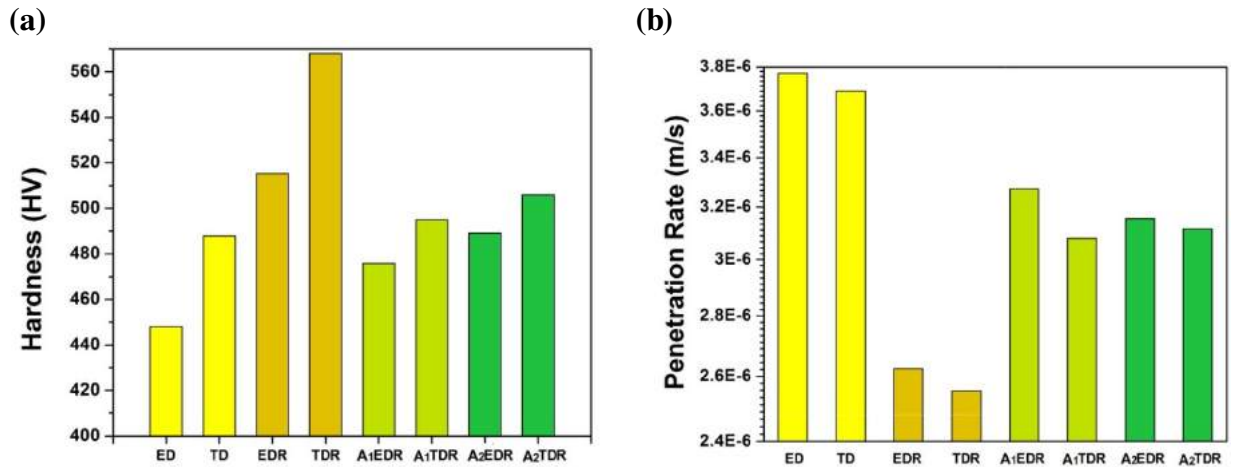

Fig. 4.12. *Hardness variations for the as-received hot extruded, deformed and annealed specimen in extruded and transverse directions for 18Cr ODS ferritic steel.*

The penetration rates for ED and TD specimen are higher in contrast to EDR and TDR suggesting the higher accumulation of dislocations during rolling. However, heat treatment A_1EDR shows an increase in the rate of penetration due to recrystallisation and softening. Further treatments did not show significant differences in the penetration rate.

4.4. Plasticity Assessment of Tensile Tested Specimen

4.4.1. Tensile Test

Figure 4.13(a) shows the tensile curves of hot extruded steel 18Cr ODS ferritic steel obtained at 298 K (25 ℃), 823 K (550 ℃) and 973 K (700 ℃) along two perpendicular loading directions namely ED and TD. From the Fig. 4.13(a) it is evident that the anisotropic behavior of this steel influences the yield stress, ultimate stress and total strain. Powder metallurgy route made materials tensile specimens are preferred in the case of smallest sub-size specimens. Further, according to ASTM [136], the smallest sub-size round specimens are 2.5 mm diameter, with a 10 mm (L/D=4) or 12.5 mm (L/D=5) gage length, width=1 cm; and the specimens dimensions are well within the dimensional tolerance limit in agreement with ASTM standard.

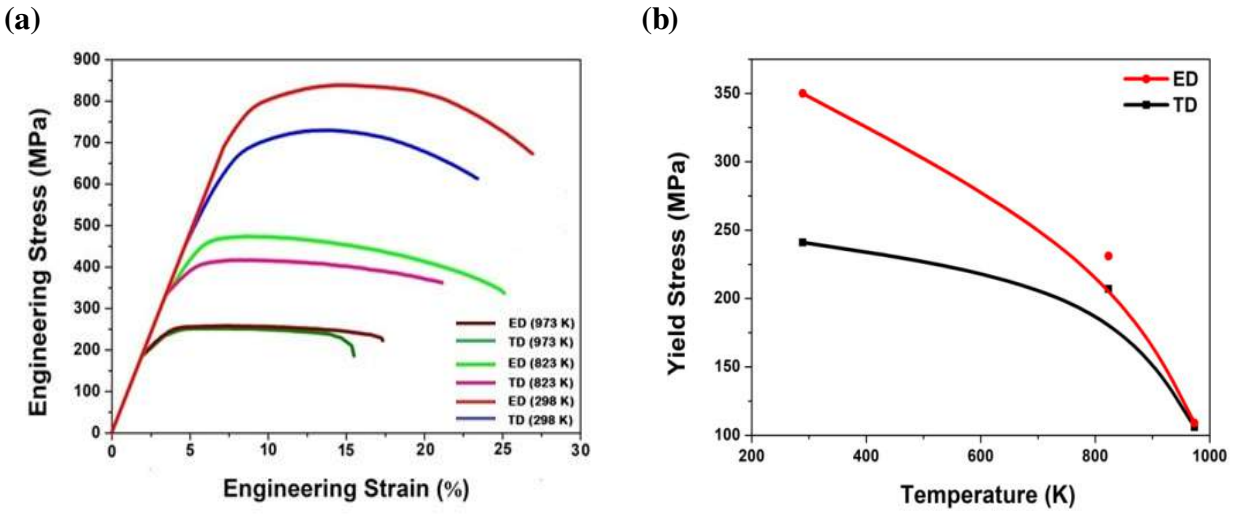

Fig. 4.13. *(a) Engineering stress-strain tensile curves and (b) yield strength variation with temperature of 18Cr ODS ferritic steel along ED and TD sections.*

Hence, the results show that the use of smaller specimens does not affect the evaluation of the total plastic strain. The maximum value of the plastic strain, which is a measure of ductility, is observed higher for ED specimen irrespective of temperature. Further, the yield strength with respect to temperature is shown in Fig. 4.13(b) for the different specimen orientations. For the loading direction along ED, a maximum of yield strength about 350 MPa is observed at 298 K (25 ºC). Tensile data obtained using different specimen geometry are already reported [190]; similar tensile properties have been obtained in both the directions at 973 K (700 ºC) and the relative difference decreases as temperature increases. The influence of microstructure and microtexture on orientation dependent anisotropic behavior in this steel is address in subsequent sections.

4.4.2. Microtexture Distribution in Room Temperature Tensile Tested Specimen

Figure 4.14 shows the superposed grain boundary and crystal orientation maps and their corresponding inverse pole figures of hot extruded 18Cr ODS ferritic steel subjected to room temperature tensile testing. A near single orientation with a uniform color gradient is observed within individual grains of TD in contrast to ED specimen (Fig. 4.14(a) and (b)), which suggests a stronger texture effects during deformation along TD than ED. The color gradient within individual grains observed in crystal orientation map of deformed specimen is a signature of presence of substructure, which could be attributed to deformation induced intra-grain rotation [191, 192]. The resultant substructures of dislocation cell in the microstructure showed directional alignment towards the loading direction and is found to be markedly different for ED and TD specimen. Further, shear band activity (marked Fig. 4.14(a) and (b)) are found to be at

30º and 45° for ED and TD respectively, with respect to the loading direction, which indicates the favorable direction of material flow. Due to the restriction to deformation imposed by neighboring grains, resulted in a lower inclination angle of the banded structure with respect to the loading direction in ED specimen (Fig. 4.1(a)) than TD specimen.

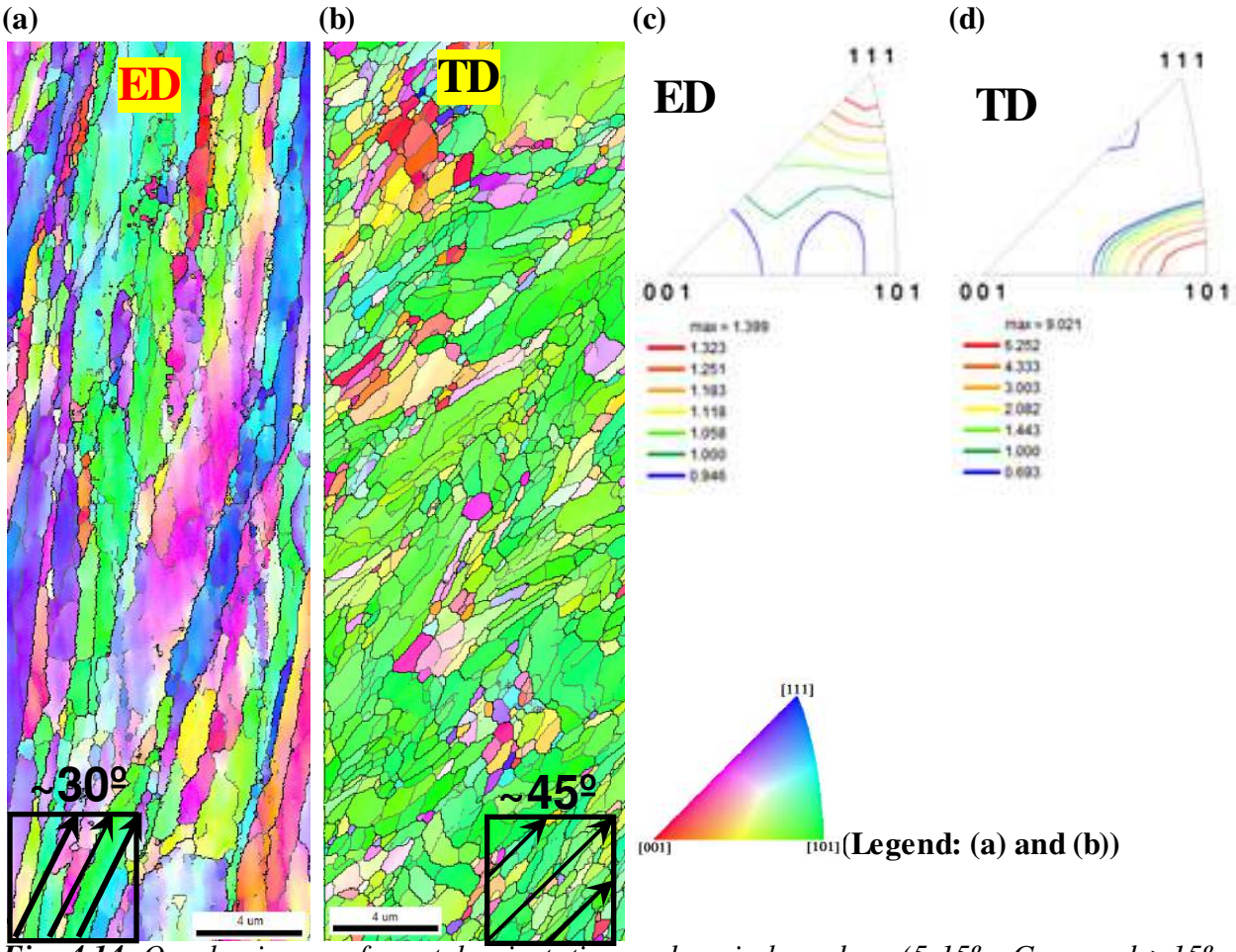

Fig. 4.14. *Overlay image of crystal orientation and grain boundary (5-15º - Gray and >15º - Black) maps of room temperature tensile tested 18Cr ODS ferritic steel along (a) extruded, and (b) transverse direction (c) and (d) inverse pole figure along ED and TD respectively*

Also, the fragmented low angle boundaries within the continuous network of high angle boundaries in Fig. 4.14(a) along ED indicate coalescence of subgrains. However, the equiaxed morphology in TD section changes to an elongated and faceted morphology with straight boundary contours after tensile deformation (Fig. 4.14(b)). However, a retention of <1 1 0> fiber (maximum intensity ~8 times better than random) is observed for TD specimen (Fig. 4.14(d)).

This suggests that the deformation during loading in ED allows the material to flow in <1 1 1> direction, which is corroborated with the banded structure tending towards ~ 30º to the extrusion axis (Fig. 4.14(a)), which assist the randomization of the texture component by grain rotation. However, deformation during loading along <1 1 0> fiber such as in TD specimen does not lead to any slip activity according to Schmid's law [193, 194].

As observed in pole figures, the (1 1 0) slip plane normal are parallel to TD, which brings the Schmid factor to a low level, making its activation unlikely. This is consistent with the dislocation structures reported in deformed materials [195]. The highly textured structure of the extruded steel as seen from the crystal orientation map (Fig. 4.1(b)) of TD specimen assists the deformation in each grain in a similar manner. Though, the grains appear to behave as if they were single crystals, unlike a single crystal the activation of secondary slip planes occurs only at the grain boundaries without any significant intragrain rotation due to slip activity. Figure 4.15 shows the misorientation angle distribution across neighboring pair of pixels, and a higher density of low angle (0.5º–10º) misorientation is revealed in the tensile tested ED specimens.

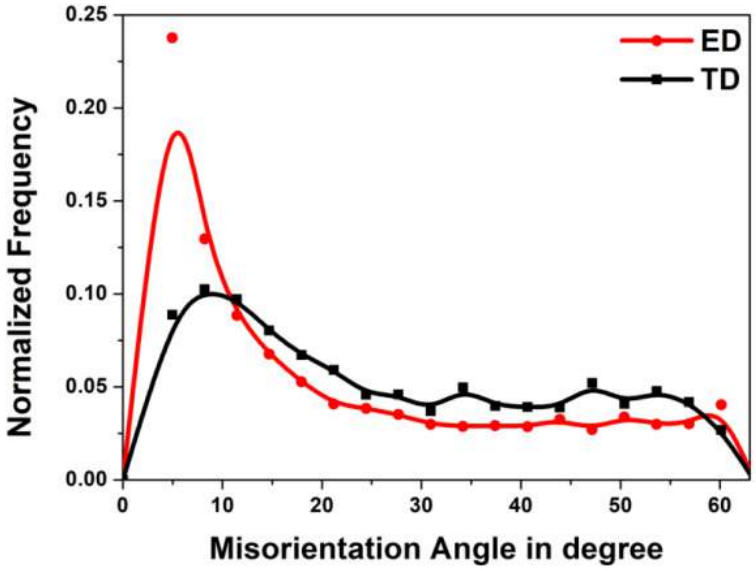

Fig. 4.15. *Normalized misorientation angle frequency distribution of room temperature tensile tested 18Cr ODS ferritic steel.*

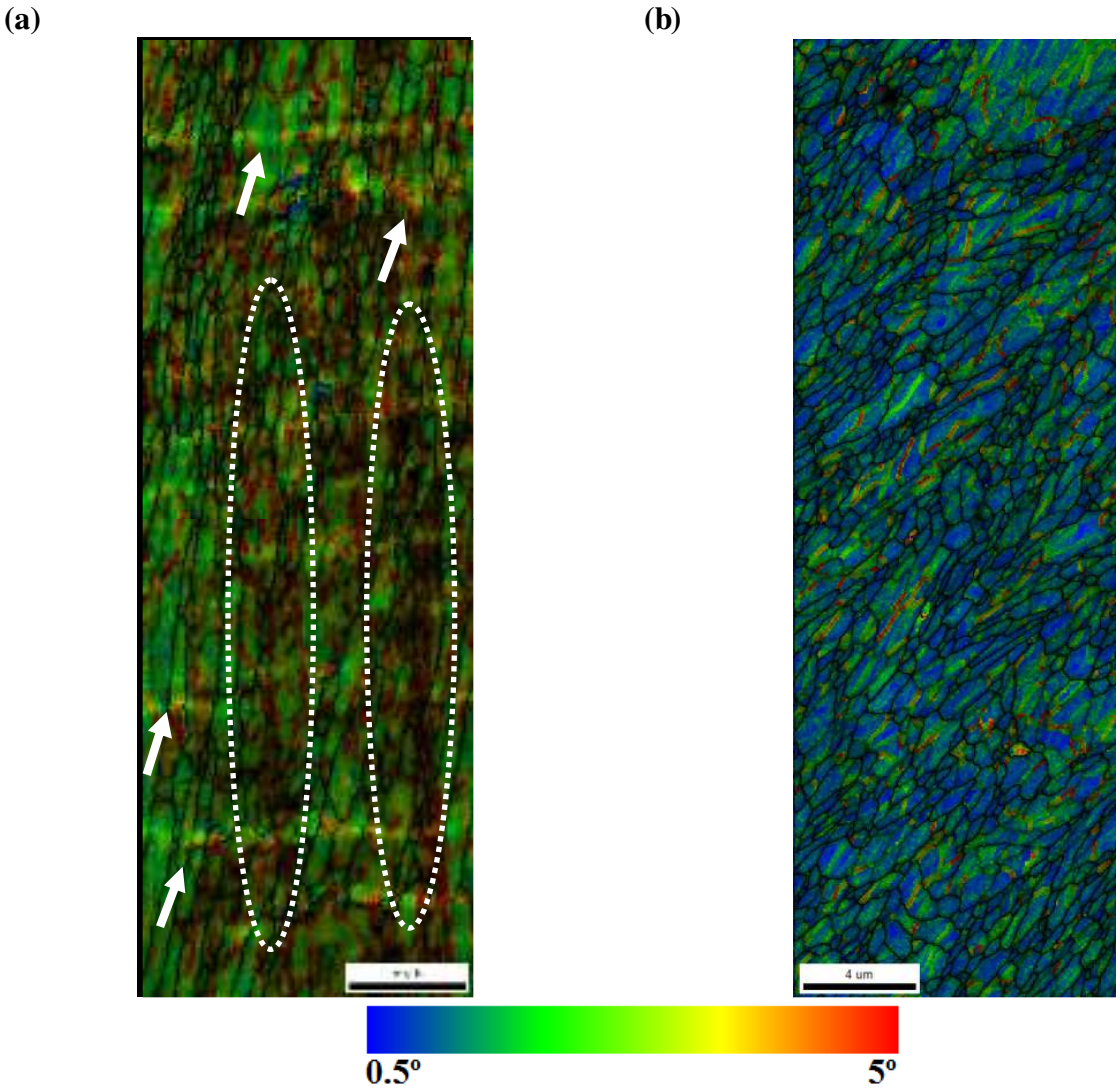

Fig. 4.16. *KAM (0.5-5º) superimposed with EBSD image quality (IQ) map of room temperature tensile tested 18Cr ODS ferritic steel along (a) extruded and (b) transverse directions.*

Misorientation angle distribution corroborates the formation of substructure cells after deformation. The KAM is more effective in resolving deformed regions to assess the localization of plastic strain in the microstructure.

Figure 4.16(a) and (b) show the overlay image of KAM and IQ maps of room temperature tensile tested steel along ED and TD respectively; the color of individual pixel represents the severity of KAM angle between 0.5° to 5º. A non-uniform KAM angle distribution is identified in the ED specimen, which is attributed to the heterogeneous nature of grain

deformation. Also, deformation bands aligned along the loading direction across several neighboring ferrite grains are observed irrespective of material flow as discussed earlier (Fig. 4.14(a)). In addition, the banded structure follows a wavy morphology (marked white arrow in Fig. 4.16(a)) which is probably due to restriction on the material flow during loading and this pattern seems to form, when slip lines are twisted across the grain boundaries [196], and is responsible for the higher strength when the applied load is normal to the <1 1 0>.

However, the TD specimen shows a nearly uniform KAM value of ~1.5º for the most of the region in the microstructure, irrespective of the shape/size and orientation of the grains. The grain boundaries are the regions of strain gradients, which shows that strain was preferentially accommodated in the proximity of boundary network. During tensile loading along TD with <1 1 0> fiber texture, the slip activity at the grain boundary in the direction of material flow enables rapid strain hardening and further straining leads to boundary decohesion and low strength in contrast to loading along ED.

4.4.3. Microtexture Distribution in High Temperature Tensile Tested Specimen

In view of the similarity of the tensile deformation curves along ED and TD sections at a high temperature of 973 K (700 °C), microtexture analysis of the ED section is presented in this section. Figure 4.17(a) shows the image quality (IQ) map obtained from 18Cr ODS ferritic tensile tested at a high temperature of 973 K (700 °C) along ED, close to fracture surface. A fine micro-banded (~1µm width) feature (marked in white arrow) similar to the one observed in the room temperature tensile tested specimen is evident (Fig. 4.16(a)). In addition, clusters of ultra fine grains (~0.4µm) within elongated regions (marked with red arrow in Fig. 4.17(a)) are also observed, markedly different from the initial microstructure (Fig. 3.15, Section 3.5). A similar

behavior has also been reported by Watanabe [197] for Fe-0.8at%Sn alloy creep tested at 973 K (700 °C). An equiaxed grain distribution observed is probably a consequence of dynamic recrystallization of the strong substructure within the elongated grains. High temperature deformation in ODS ferritic steel is reported to consist of grain deformation though shearing mechanism and high temperature promotes the grain boundary sliding [196, 198].

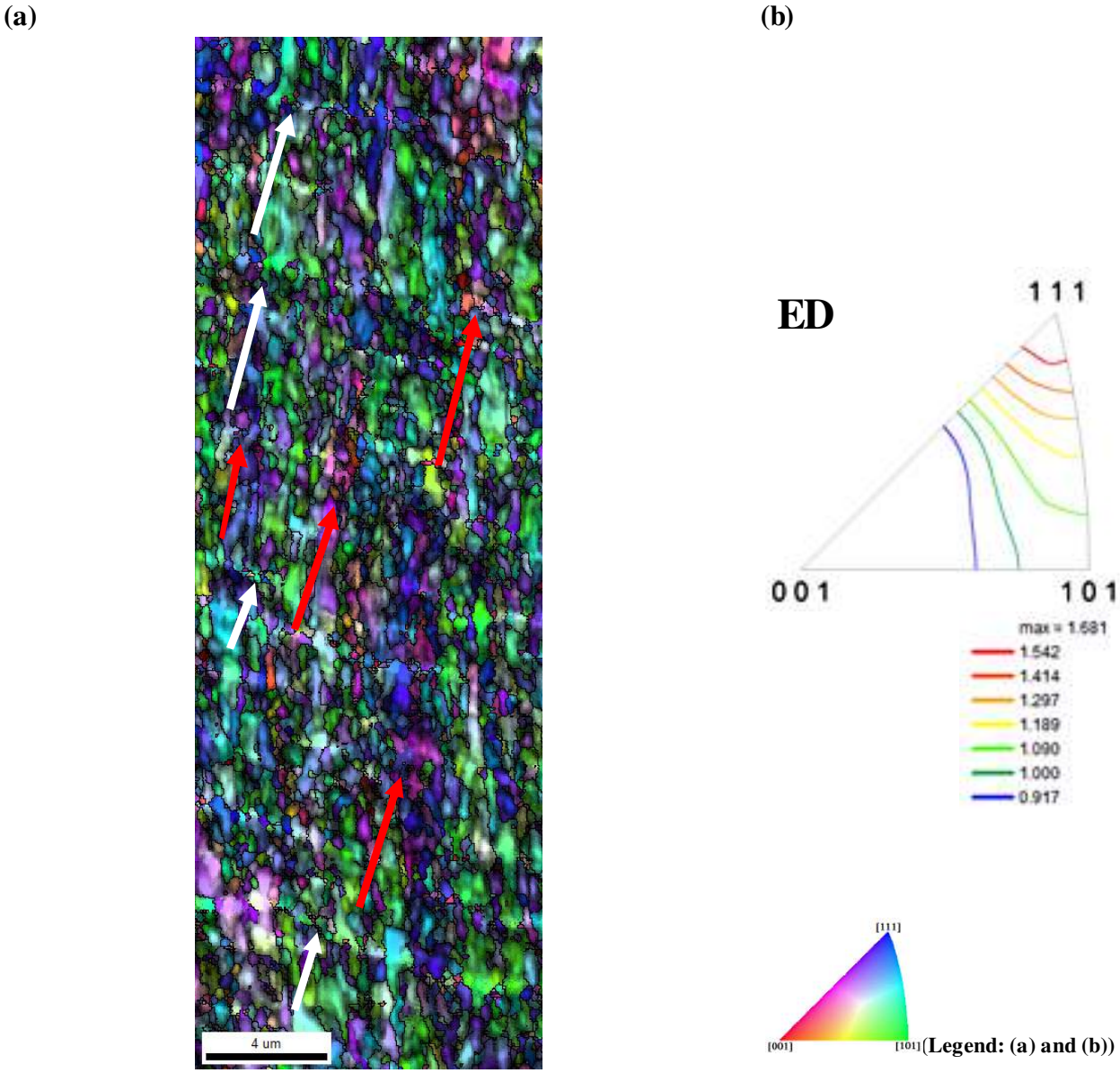

Fig. 4.17. *EBSD results of (a) overlaid image quality (IQ) and crystal orientation map and (b) inverse pole figure distribution of high temperature (973 K) tensile tested ED specimen of 18Cr ODS ferritic steel.*

Hence, the results in the present study can be understood as follows: (1) shearing mechanism as a part of material flow during deformation produced banded structure during uniaxial loading; (2) temperature assists the grain boundary sliding and nucleation of fine grains through dynamic recrystallization. Okada et al. [166] have first reported grain boundary sliding in a Fe–13Cr–3W ODS ferritic steel compression tested at 923 K (650 ℃). They observed that the sliding mechanism was promoted along grain boundaries with large tilt angles and that fracture occurred by nucleation, growth and coalescence of grain boundaries. This suggest at high temperatures (at 973 K (700 ℃)) grain boundary sliding is more likely to be promoted, and mechanical properties at ED and TD are similar. Analysis of the inverse pole figure distributions reveals a nearly random (intensity about 1-2) texture; however, a preferential increase in intensity of clustering towards (111) planes parallel to the loading direction (Fig. 4.17(b)) with increase in the extent of recrystallization is observed as compared to room temperature tensile tested ED specimen.

From the above studies it can therefore be concluded that the tube drawing process at high temperature (> 973 K (700 ℃)) and low strain rate ($<10^{-3}$ s^{-1}) is possibly an alternate fabrication process to achieve fine equiaxed grain structure along the extruded direction of 18Cr ODS ferritic steel. Further, identification of hot working domains for a given temperature and strain rate in 18Cr ODS ferritic steel is described in the next chapter.

4.5. Summary

Various deformation and heat treatment processes have been carried in oxide dispersion strengthened (ODS) 18Cr ferritic steel in order to obtain an ultrafine equiaxed grain distribution. The following conclusions have been drawn from this study:

- The characteristic elongated grains structure obtained by hot extrusion is retained during further cold rolling along ED.
- Recovery and recrystallization temperature domains have been identified as 1350 and 1420 K (1077 and 1147 ℃) when a heating rate of 7 $Kmin^{-1}$ is employed based on DSC thermograms.
- The apparent activation energy for recovery and recrystallization are estimated at 266 and 358 $kJmol^{-1}$ respectively, which are attributed to lattice diffusion and diffusion assisted climb during recovery and recrystallization respectively.
- Higher incubation period at recovery region for lowering the stored energy preceding recrystallization is found to be beneficial to attain a fine grain size distribution and reduces microstructural anisotropy in the steel, which is achieved by the two step heat treatment.
- The fraction of ultrafine equiaxed grains is observed to increase progressively with repetitive deformation and two step treatments, resulting in a high extent of texture randomization.
- The hardness trends reflect the combined effect of grain refinement and increase in dislocation density during repeated deformation and annealing treatments.
- Tensile tests carried out at 298, 823 and 973 K (25, 550 and 700 ℃) on ODS 18Cr ferritic steel along ED and TD sections showed (1) A strong anisotropy of elongation , with transverse ductility lower as compared to the axial ductility; (2) Yield stress anisotropy (mechanical strength anisotropy) was found to be temperature dependent.
- Application of load along extruded direction during tensile test allows the material to flow in <1 1 1> direction; however, (1 1 0) slip plane normal are parallel to the direction

of loading for transverse direction and brings the Schmid factor to a lower level, which makes slip activation unlikely.

- Deformation bands are observed to be aligned with the loading direction in ED specimen across several neighboring ferrite grains irrespective of material flow. Grain boundaries being strain gradient regions show that strain was preferentially accommodated in proximity to the boundary network for TD specimen.
- High temperature (973 K (700 ℃)) tensile test in ED found to promote nucleation of fine grains within the elongated bands by dynamic recrystallization and inverse pole figure distribution shows a preferential increase in intensity of clustering towards (111) planes parallel to the loading direction.

Although fraction of ultrafine equiaxed grains is observed to increase progressively with repetitive deformation and two step treatments, tube drawing process at high temperature (> 973K (700 ℃)) and low strain rate ($<10^{-3}s^{-1}$) can be considered as an alternate possible fabrication process to achieve fine equiaxed grain structure in extruded direction of 18Cr ODS ferritic steel.

Study of High Temperature Processing Domain in Oxide Dispersion Strengthened 18Cr Ferritic Steel

Thermo-mechanical treatments induce a variety of metallurgical changes like dynamic recovery and recrystallization as well as work hardening and flow instability of materials [199, 200]. Since the mechanical properties and performance of the final product during service exposure are influenced by the resultant microstructure, it is necessary to optimize the high temperature deformation domains. In this context the dynamic material models (DMMs) are useful for the generation of processing maps [201, 202]. Several studies are reported on processing parameters for various materials such as austenitic stainless steels [203-205] and 9Cr-1Mo/9Cr ODS steels [206, 207] based on their high-temperature deformation behavior, and the mechanisms have also been reported. Few studies are available on high (>12%) Cr ODS ferritic steels, wherein the microstructural modification is achieved through various thermo-mechanical treatments [31, 208]. Further, various deformation and heat treatment processes have been carried in oxide dispersion strengthened (ODS) 18Cr ferritic steel in order to obtain an ultrafine equiaxed grain distribution, which have been described in Chapter 4.

In the present chapter, the processing map of an 18Cr ODS ferritic steel is generated by hot compression tests using Gleeble simulator and the hot working parameters have been identified. The evolution of microstructure and microtexture in the processing domains has been studied using EBSD technique. In addition, VPSC constitutive models are used to predict the resultant texture from a distinct initial texture. The resultant texture distribution obtained by the prediction and experimental EBSD analysis has been compared to understand the underlying micromechanism of texture evolution during processing of the steel at high temperatures.

5.1. Effect of Temperature and Strain Rate on Flow Stress

Figure 5.1 shows the experimental flow curves of the 18Cr ODS ferritic steel compression tested in a range of 1323 to 1473 K (1050 to 1200 °C) and strain rates from 0.01 s^{-1} to 10 s^{-1}. The direction of compression is parallel to the extruded direction (ED). As the dimensional changes of the specimens after the compression tests were found to be uniform in radial direction, deformation is considered to be homogeneous. The flow stress characteristics are observed to vary with test temperature and strain rate. A sharp increase in flow stress is observed at all temperatures and strain rates in the initial stages of deformation due to strain hardening. However, beyond a true strain value of 0.2, saturation or decrease in flow stress was observed, which is attributed to softening due to dynamic recovery and recrystallization [207]. At 1323 K (1050 °C), at strain rate ≥ 0.1 s^{-1} a mild increase in flow stress with strain is observed (Fig. 5.1(a)). This is attributed to higher work hardening rate due to deformation at low temperature and high strain rate. Flow stress curves show a dominant softening behavior at low strain rates of ≤ 0.1 s^{-1} and high temperatures of 1373 to 1473 K (1100 to 1200 °C), suggesting recovery process. A steady state behavior of the flow stress curves implies a balance between work hardening and thermal softening. This behavior is attributed to dynamic recovery, which is characteristic of materials with high Stacking Fault Energy (SFE). The flow curve determined in the temperature range of 1323 to 1473 K (1050 to 1200 °C), at a strain rate of 0.01 s^{-1} suggests occurrence of dynamic recrystallization, characteristic of high temperature of deformation [209].

Although the characteristics of true stress–strain curves qualitatively indicate dynamic recrystallization [210], Poliak et al. [209] have reported a point of inflection in the relationship of work hardening rate (θ) with stress (σ). Since, $d\theta/d\sigma = d(\ln\theta)/d\varepsilon$, an inflection point is also expected in the plot of $\ln(\theta)$ as a function of ε, which is a signature of dynamic recrystallization

[211-213]. The plot of ln(θ) vs ε at 1373 K (1100 ℃) with strain rate of 0.01 s^{-1} is shown in Fig. 5.2. A sharp point of inflection in Fig. 5.2 thus substantiates the event of dynamic recrystallization above the >1373 K (1100 ℃) in this steel, which is in agreement with the observations from Fig. 5.1. However, the experimental true stress-strain curves reflect the complex interplay of concurrently operating phenomena of work hardening and softening processes during high temperature deformation and annealing. The identification of various workability regimes from the predicted flow stress using constitutive equations is explained in the subsequent section.

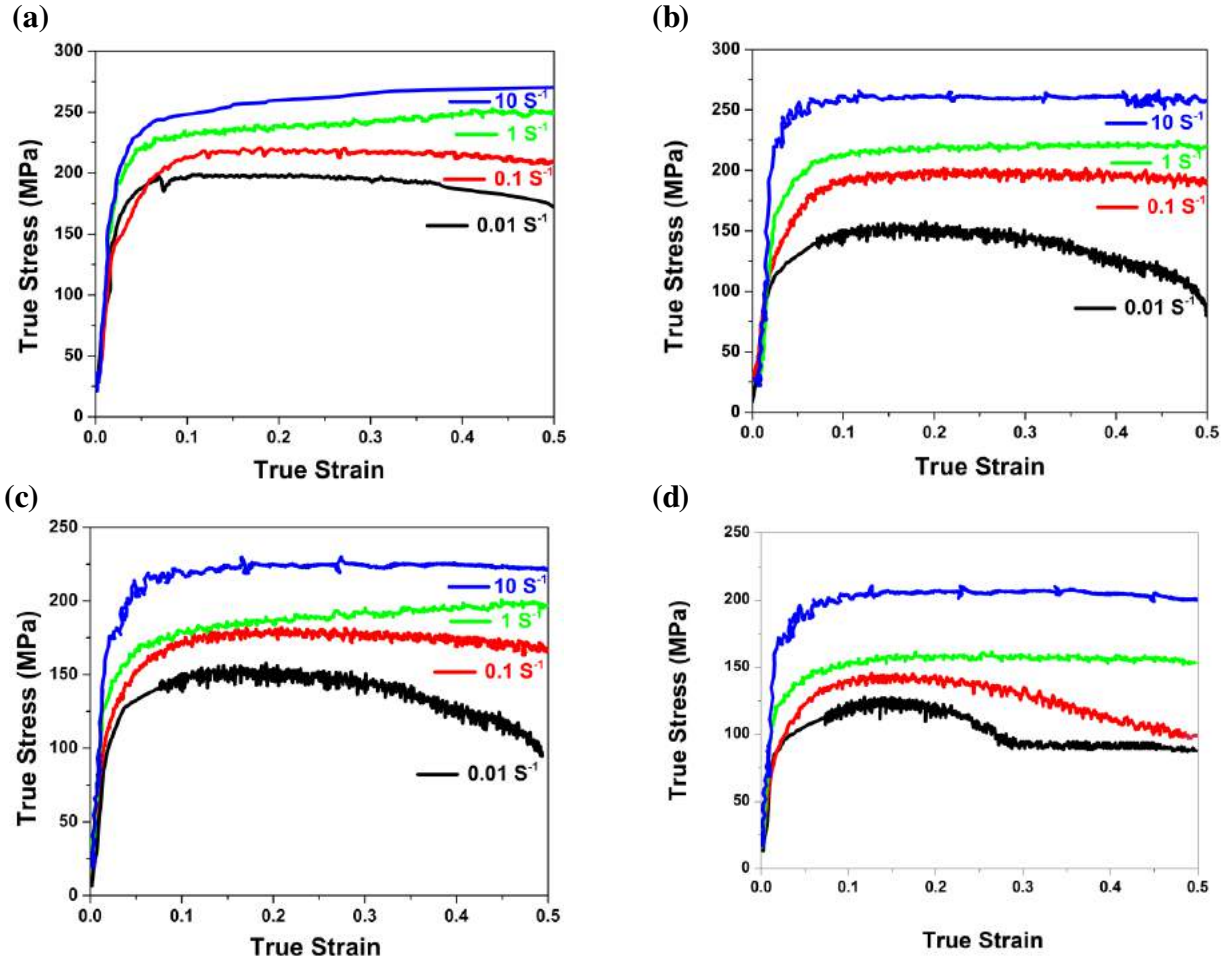

Fig. 5.1. *True stress vs true strain plots of hot extruded 18Cr ferritic steel obtained by hot compression test for strain rates in the range of 0.01 – 10* s^{-1} *at temperatures of (a) 1323, (b) 1373, (c) 1423 and (d) 1473 K.*

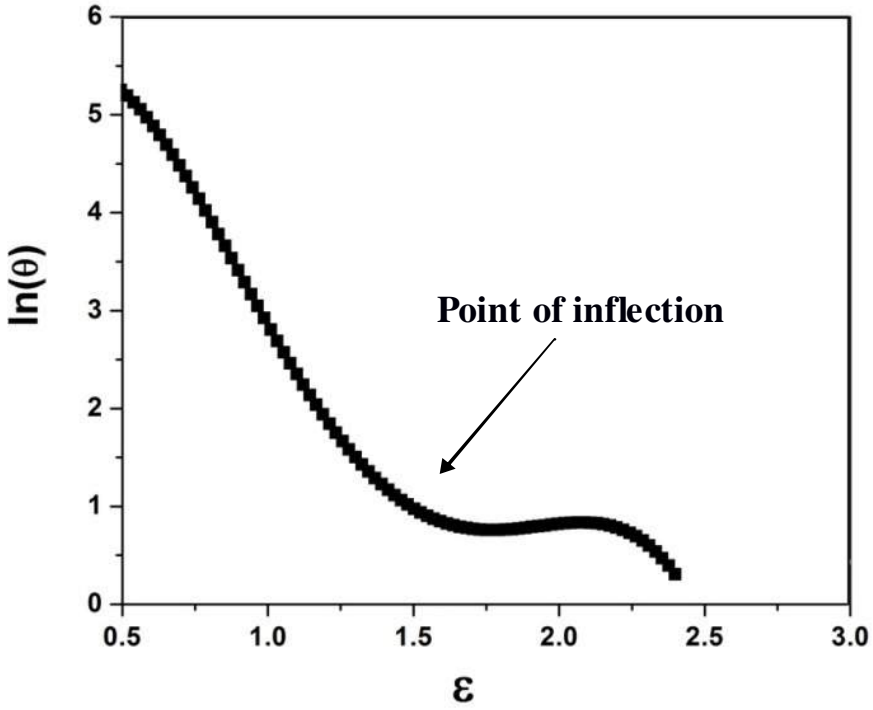

Fig. 5.2. *Variation of work hardening rate (ln θ) of 18Cr ODS ferritic steel with strain (ε) at 1373 K (1100 ℃) and strain rate of 0.01 s^{-1}.*

5.2. Hot Deformation Constitutive Equations

The analysis of the flow behavior of the steel under study can be predicted and simulated using constitutive equations. The Arrhenius equation is used to derive the correlation between flow stress and strain rate during high temperature deformation [214] and the constitutive behavior can be explained as follows [207, 215-218]:

$$\dot{\varepsilon} = A_1 \sigma^{n_1} \exp\left[-\frac{Q}{RT}\right] \quad (5.1)$$

$$\dot{\varepsilon} = A_2 \exp(\beta\sigma) \exp\left[-\frac{Q}{RT}\right] \quad (5.2)$$

$$\dot{\varepsilon} = A \left[\sinh(\alpha\sigma)\right]^n \exp\left[-\frac{Q}{RT}\right] \quad (5.3)$$

where, equation (5.1), and (5.2) correspond to the power exponent relationship in the low and high stress conditions respectively, whereas equation (5.3) represents hyperbolic sine

relationship for all stress conditions, and therein $\dot{\varepsilon}$ is the strain rate, σ is the flow stress, T and Q are the temperature and activation energy during deformation respectively, R is the gas constant (8.31 J mol^{-1} K^{-1}) and A1, A2, A, n1, n, α, and β are material constants. Further, equations (5.1) to (5.3) can be rewritten in the following way:

$$ln\ \dot{\varepsilon} = n_1 ln\ \sigma + \ln A_1 - Q/(RT) \quad (5.4)$$

$$ln\ \dot{\varepsilon} = \beta\sigma + \ln A_2 - Q/(RT) \quad (5.5)$$

$$ln\ \dot{\varepsilon} = n \ln [\sinh(\alpha\sigma)] + \ln A - Q/(RT) \quad (5.6)$$

The peak stress, which is a function of the deformation condition signifies the highest load during high temperature compression and is selected for estimating the corresponding strain [207]. Equations (5.4) to (5.6) represent linear relationships between $\ln\dot{\varepsilon}$ - lnσ, $\ln\dot{\varepsilon}$ – σ and $\ln\dot{\varepsilon}$ - ln(sinh(ασ)), and the values n_1, β, and n are derived from the slope of the fitted lines of the above plots in the temperature range of 1323 to 1473 K (1050 to 1200 ℃) (Fig. 5.3). Further, α can be calculated from the relationship $\alpha = \beta/n_1$ and the average value of α and n are considered as optimum for a given strain [219]. Estimated values of material constants and activation energy are given in Table 5.1.

Further, the correlation of flow stress and the strain rate is presented based on linear regression corresponding to the hyperbolic sine relationship as follows:

$$ln\dot{\varepsilon} = 6.64\ \ln[\sinh(0.00418\,\sigma)] - 4.1494\ \ for\ T = 1323\ K$$

$$ln\dot{\varepsilon} = 6.49\ \ln[\sinh(0.00493\,\sigma)] - 2.7013\ \ for\ T = 1373\ K$$

$$ln\dot{\varepsilon} = 7.22\ \ln[\sinh(0.00541\sigma)] - 1.8078\ \ for\ T = 1423\ K$$

$$ln\dot{\varepsilon} = 6.95\ \ln[\sinh(0.00616\,\sigma)] - 0.43846\ \ for\ T = 1473\ K$$

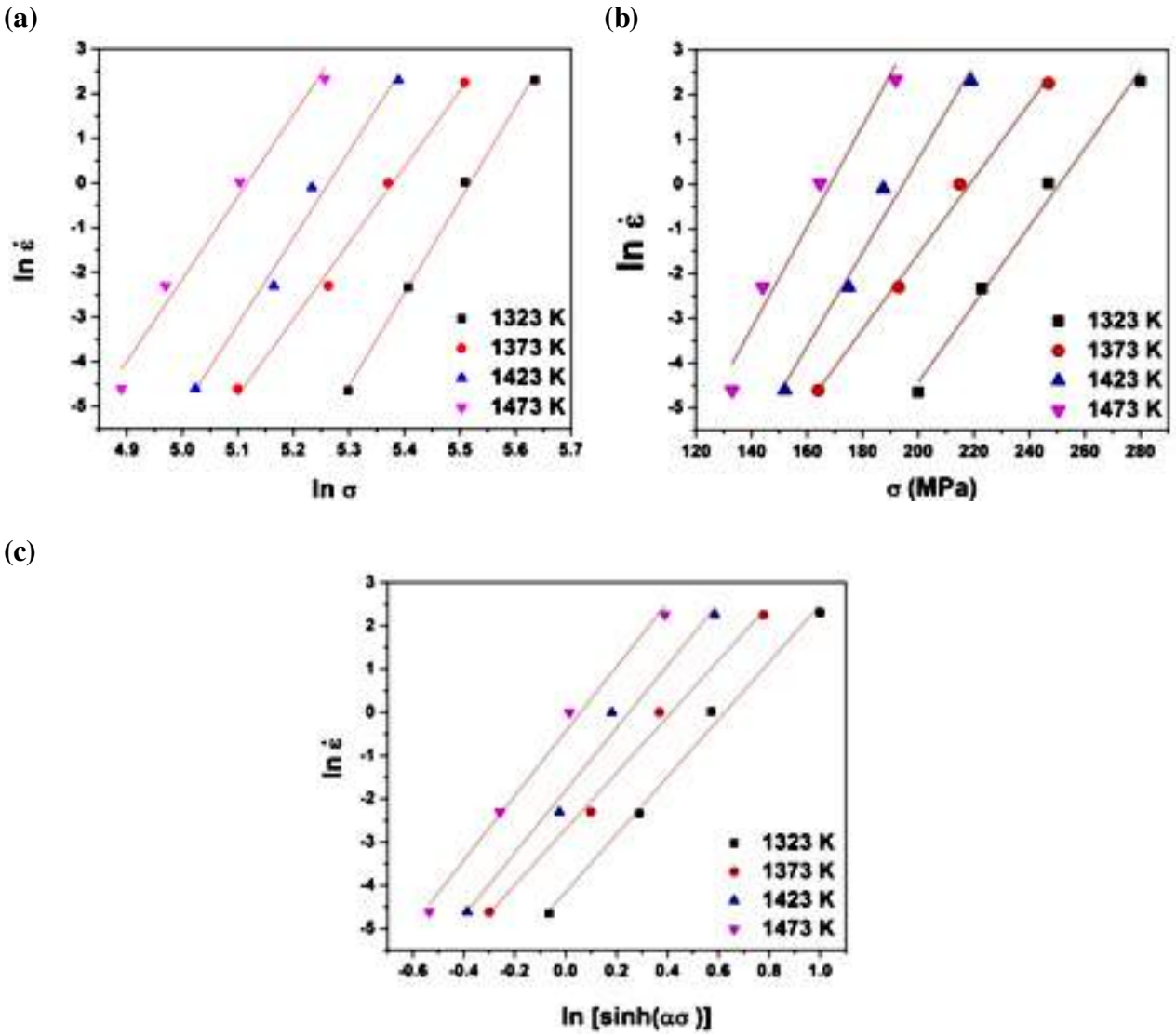

Fig. 5.3. *Relationship between (a) $ln\dot{\varepsilon}$ - $ln\sigma$, (b) $ln\dot{\varepsilon} - \sigma$ and (c) $ln\dot{\varepsilon}$ - $ln(sinh(\alpha\sigma)$ of 18Cr ODS ferritic steel in a temperature range of 1323 to 1473 K (1050 to 1200 ºC).*

The activation energy for hot deformation is assumed to remain constant for small temperature ranges in which the strain rate is constant [215, 219]. Further, equation (5.6) can be rearranged for all the stress levels as follows:

$$n \ln [\sinh(\alpha\sigma)] = ln\ \dot{\varepsilon} + \mathrm{Q}/(\mathrm{RT}) - \ln A \qquad (5.7)$$

The activation energy (Q) is then calculated from the slope of the plot that is derived from the intercept of nln(sinh(ασ)) vs. ln ε̇ as a function of 1/T; further, the intercept gives the

value of lnA [215, 219]. The estimated Q value and lnA for the 18Cr ODS ferritic steel are ~ 624 $kJmol^{-1}$ and 34 respectively in the temperature range of 1323 to 1473 K (1050 to 1200 ℃) in the strain rate range of 0.001 to 1 s^{-1} (Table 5.1). The estimated Q value is higher than that reported for T24 ferritic steel (515 $kJmol^{-1}$) [215]. The higher values are attributed to the dislocation pinning by the dispersoids, which introduces a threshold stress for deformation.

Table 5.1. Estimated values of material constants and activation energy for a given strain at peak stress

α (MPa^{-1})	β (MPa^{-1})	n_1	n	Q (kJ/mol)	ln *A*
0.0051	0.0977	18.9227	6.9557	624	34.70

During the initial stage of deformation, the dispersoids induce elastic stress through lattice mismatch within the matrix that restricts dislocation motion. The movement of dislocations is also restricted through the pinning effect, which causes dislocation gliding and climbing with increase in strain energy; increases in strain energy influences the process of dynamic recovery [207]. In addition, the dispersoids also delay recrystallization by obstructing the formation of grain boundary and their advancement. Besides, the reduction of grain boundary strength at high temperature helps the material to deform easily, which outweighs the recrystallization phenomena.

Taking into account the values of α, Q, A, and n into Eq. (5.3), the constitutive equation of 18Cr ODS ferritic steel can be expressed as:

$$\dot{\varepsilon} = [\sinh(0.00517\sigma)]^{6.955}\exp(34.70) \bullet \exp\,(-624/RT) \qquad (5.8)$$

5.3. Generation of Processing Maps

A dynamic material model (DMM), which considers the basic concepts for a large plastic flow with the conjunction of both continuum mechanics [220] and irreversible thermodynamics

reliably predicts [221-223] the various workability regimes for a given material and processing map can be arrived at. According to the governing principle, the power dissipation (P) from the work piece during hot working is harmonized by two complementary components G and J as per the following equation:

$$P = \sigma \bullet \dot{\varepsilon} = \int_0^{\dot{\varepsilon}} \sigma \bullet d\dot{\varepsilon} + \int_0^{\sigma} \dot{\varepsilon} \bullet d\sigma = G + J \tag{5.9}$$

where, σ is the flow stress and $\dot{\varepsilon}$ is the strain rate. Further, G corresponds to power component, which is dissipated during plastic deformation and J signifies the dissipation of power component that leads to evolution of microstructure via dynamic recovery/recrystallization [200, 207]. The order of strain rate at a given temperature influences power dissipation, which can be described by the constitutive material flow properties and strain rate sensitivity *m* [207].

$$m = \left(\frac{d(ln\sigma)}{d(ln\dot{\varepsilon})}\right) = \frac{dJ}{dG} \tag{5.10}$$

Further, the efficiency of power dissipation (η), which specifies the workability of the material at different domains of temperature and strain rate can be defined by [207]:

$$\eta = \frac{J}{J_{max}} = \frac{2m}{m+1} \tag{5.11}$$

where J_{max} corresponds to maximum dissipation of power component.

In addition, the instability parameter ($\xi(\dot{\varepsilon})$), which represents the unstable region can be related to strain rate and strain rate sensitivity by the relationship [207]:

$$\xi(\dot{\varepsilon}) = \frac{d\left(ln\frac{m}{m+1}\right)}{d\,(ln\dot{\varepsilon})} + m \tag{5.12}$$

The processing domain falls in the instability region if ($\xi(\dot{\varepsilon})$) < 0 [207, 223] and the instability map is obtained from the plot of change in efficiency of power dissipation at different

temperatures and strain rates. The workability regimes are separated with a contour value ($\xi(\dot{\varepsilon})$) =0. The flow stress at a finer step size has been calculated through the cubic spline interpolation to improve reliability and for each step size, strain rate sensitivity (m), efficiency of power dissipation (η) and instability parameter ($\xi(\dot{\varepsilon})$) were determined from Eq. (5.10), (5.11) and (5.12) respectively.

Figure 5.4 shows the strain rate sensitivity (m) map with respect to temperature and strain rate. The variation of m in the entire range of temperatures and strain rate domains employed in this study is found to be in the range of 0.06 to 0.25. Similarly η and ($\xi(\dot{\varepsilon})$) contour maps were also generated for all temperatures and strain rates. The processing map of 18Cr ODS ferritic steel is generated by superimposing the η and ($\xi(\dot{\varepsilon})$) contour maps and is shown in Fig. 5.5, which reveals a limited safe workability regime (marked yellow) for processing this material.

It is also observed that an instability domain exists in the temperature range of 1300 to 1473 K (1023 to 1200 ºC) with strain rate >1 s^{-1} and 1330 to 1423 K (1057 to 1150 ºC) with a strain rate > 0.1 s^{-1}. The stored energy increases during deformation at high strain rate, since it is not rapidly distributed throughout the matrix due to localized deformed regions. This leads to thermoplastic/flow instability domain at higher (>1) strain rates for this steel [224]. The safe temperature and strain rate domains of processing the steel are identified to lie between 0.01 to 1 s^{-1} at 1323 K (1050 ºC) and 1473 K (1200 ºC) (encircled in Fig. 5.5), which is also evident from the strain rate sensitivity map (Fig. 5.4) where the m values are very high. A change in the dominant mechanism for material flow from dynamic recovery at 1323 K (1050 ºC) to dynamic recrystallization at 1423 K (1150 ºC) is also observed at low strain rate of 0.01 s^{-1}. These results are in agreement with the reported temperatures of 1323 and > 1423 K (1050 and > 1150 ºC) for

the recovery and recrystallization respectively [31] in ODS ferritic steels, where the dispersoid distribution favors higher dislocation pining during deformation.

Though the processing map indicates a safe domain at 1323 K (1050 ℃) at a strain rate 10 s^{-1}, the η contour value is low and also the domain size is small, suggesting that it is not energy efficient. Hence, the most favorable processing parameters are found to be in the temperature range of 1323 to 1423 K (1050 to 1150 ℃) with a strain rate of 0.01 s^{-1} and 1473 K (1200 ℃) with a strain rate 0.1 s^{-1}, based on high values of peak efficiency (η) up to 30-35% in the safe workability domain.

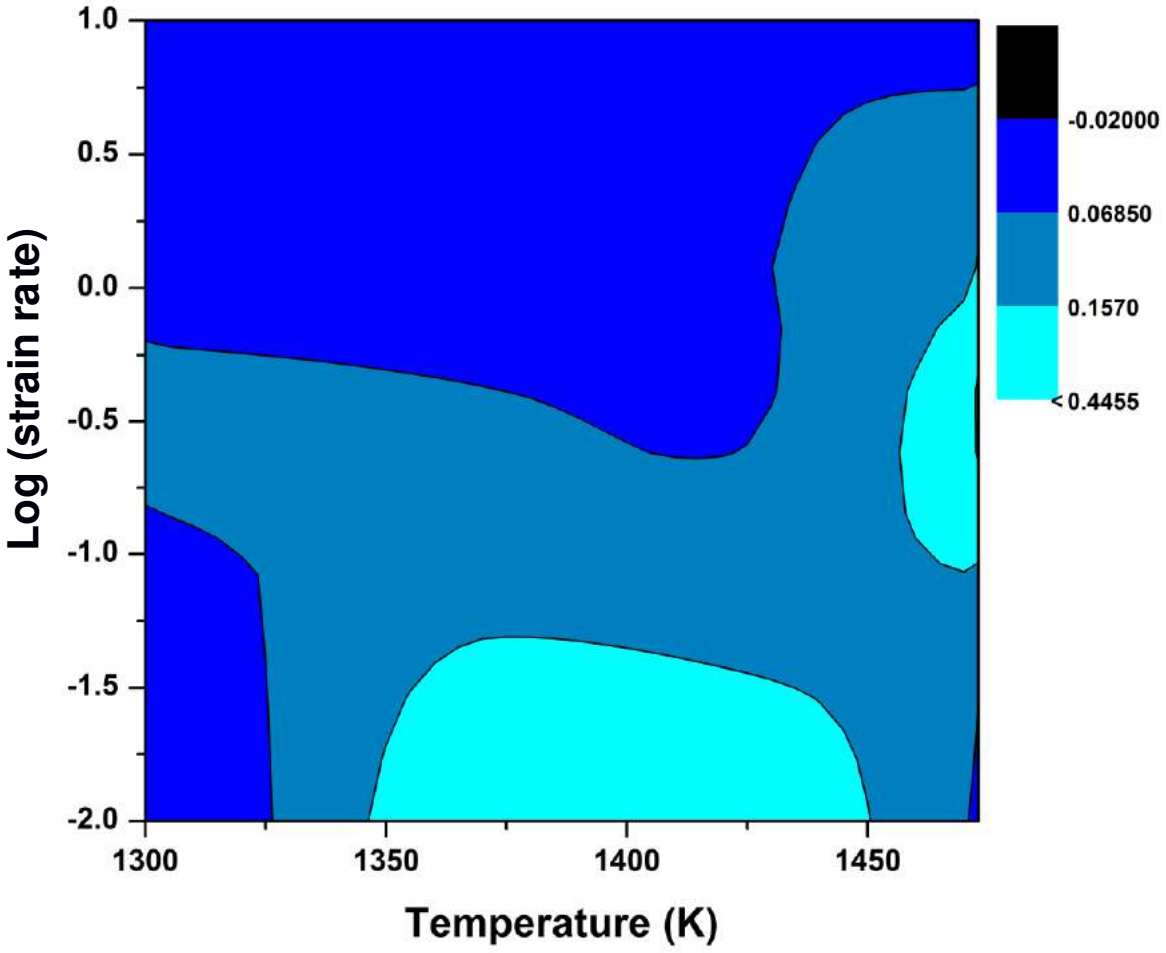

Fig. 5.4. *Variation of strain rate sensitivity with temperature and strain rate for 18Cr ODS ferritic steel.*

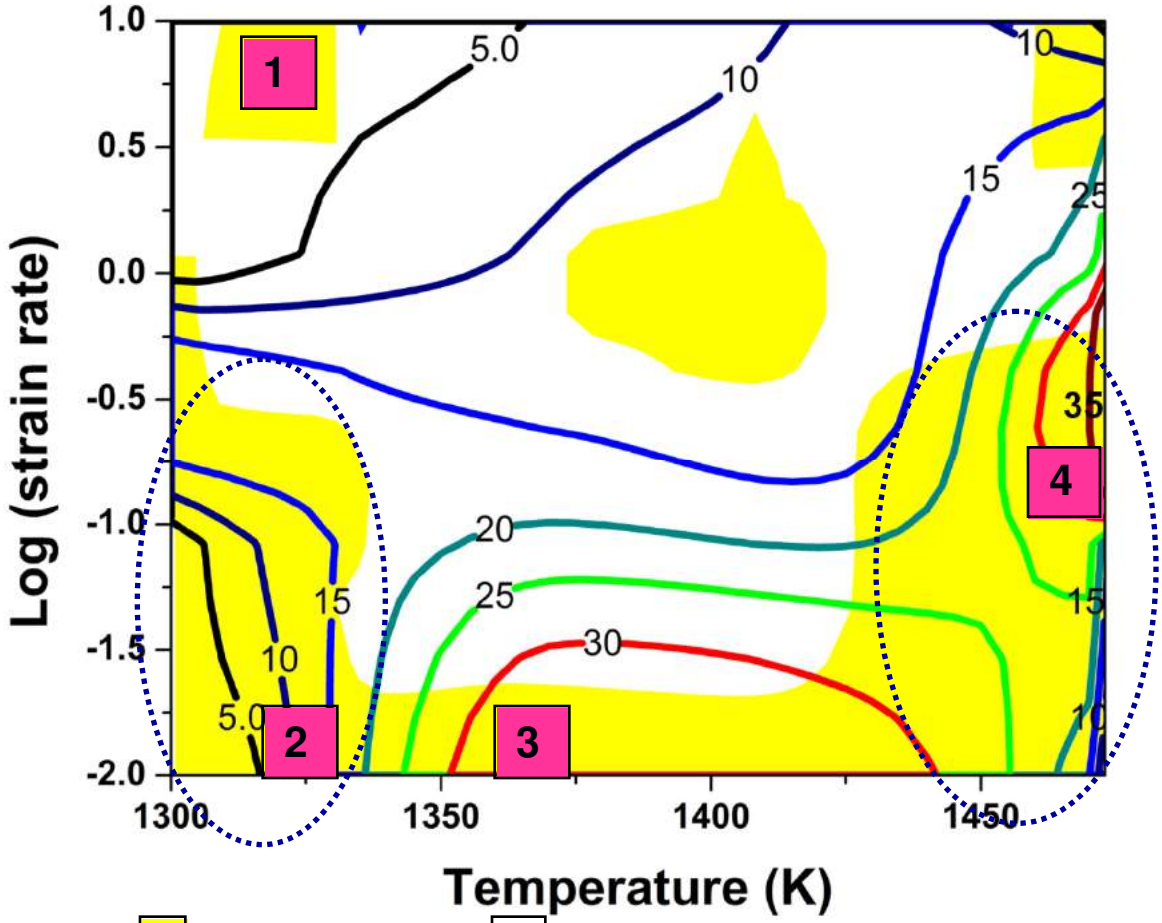

Stable Domain: *Unstable Domain:*

Fig. 5.5. *Processing map generated for 18Cr ODS ferritic steel at 0.5 true strain. (*region marked 1, 2, 3 and 4 are selected for microstructure analysis)*

5.4. Evolution of Microstructure and Microtexture during Hot Compression Testing

The safe zone in processing map with respect to temperature and strain rate has been identified. However, this needs to be validated in conjunction with a detailed microstructure analysis. Hence 4 regions in the safe zone (marked in Fig. 5.5) of the processing map have been selected for detailed analysis. Region 1 corresponds to high strain rate and low temperature zone, Region 2 corresponds to low strain rate and temperature zone, while regions 3 and 4 lie in the high efficiency safe zones. The resultant room temperature microstructures from these four regions are shown in Fig. 5.6(a, c, e and g). Significant differences are observed in Fig. 5.6 from

the initial extruded microstructure of elongated grains along ED (Fig. 3.15 in Section 3.5). Fig. 5.6(a) shows the microstructure from region 1 corresponding to the steel deformed at 1323 K (1050 ºC) with strain rate of 10 s^{-1}. Elongated grains typical of a deformation induced microstructure are evident from the figure. A closer look at Fig. 5.6(a)) indicates the coalescence of the initial fine bamboo-like structure of the extruded steel. Low angle boundaries between the grains have been marked to indicate the retention of the deformed microstructure. Low ductility and low efficiency (~5%) during deformation in this region is also evident from the lower strain rate sensitivity. The microstructure of the steel tested at 1323 K (1050 ºC) with strain rate of 0.01 s^{-1} from the safe domain (region 2) is shown in Fig. 5.6(c). The microstructure reveals shear bands developed during deformation and initiation of fine recrystallized microstructure at the periphery of shear bands. Hence, it can be concluded that deformation at low temperatures and low strain rates leads to dynamic recovery, which softens the material and average efficiency of up to 15% is achieved. Since the temperature is not high enough to compensate for the strengthening effect due to dislocation pinning by the dispersoids this region is prone to develop shear bands [79]. With further increase in temperature from 1323 to 1423 K (1050 to 1150 ºC) with strain rate 0.01 s^{-1} (region 3) the average efficiency and strain rate sensitivity increases from 5 to 30% and 0.068 to >0.157 respectively. The microstructure corresponding to this region is given in Fig 5.6(e) which shows equiaxed grain morphology, suggesting that dynamic recrystallization is the key mechanism associated with deformation in this domain. A similar workability region is also observed at 1473 K (1200 ºC) with strain rate of 0.1 s^{-1} and the corresponding microstructure is shown in Fig. 5.6(g). This microstructure also reveals an equiaxed microstructure with slightly coarser grains due to higher temperature and strain rate in contrast to the specimen deformed at a strain rate of 0.01 s^{-1} at 1373 K (1100 ºC).

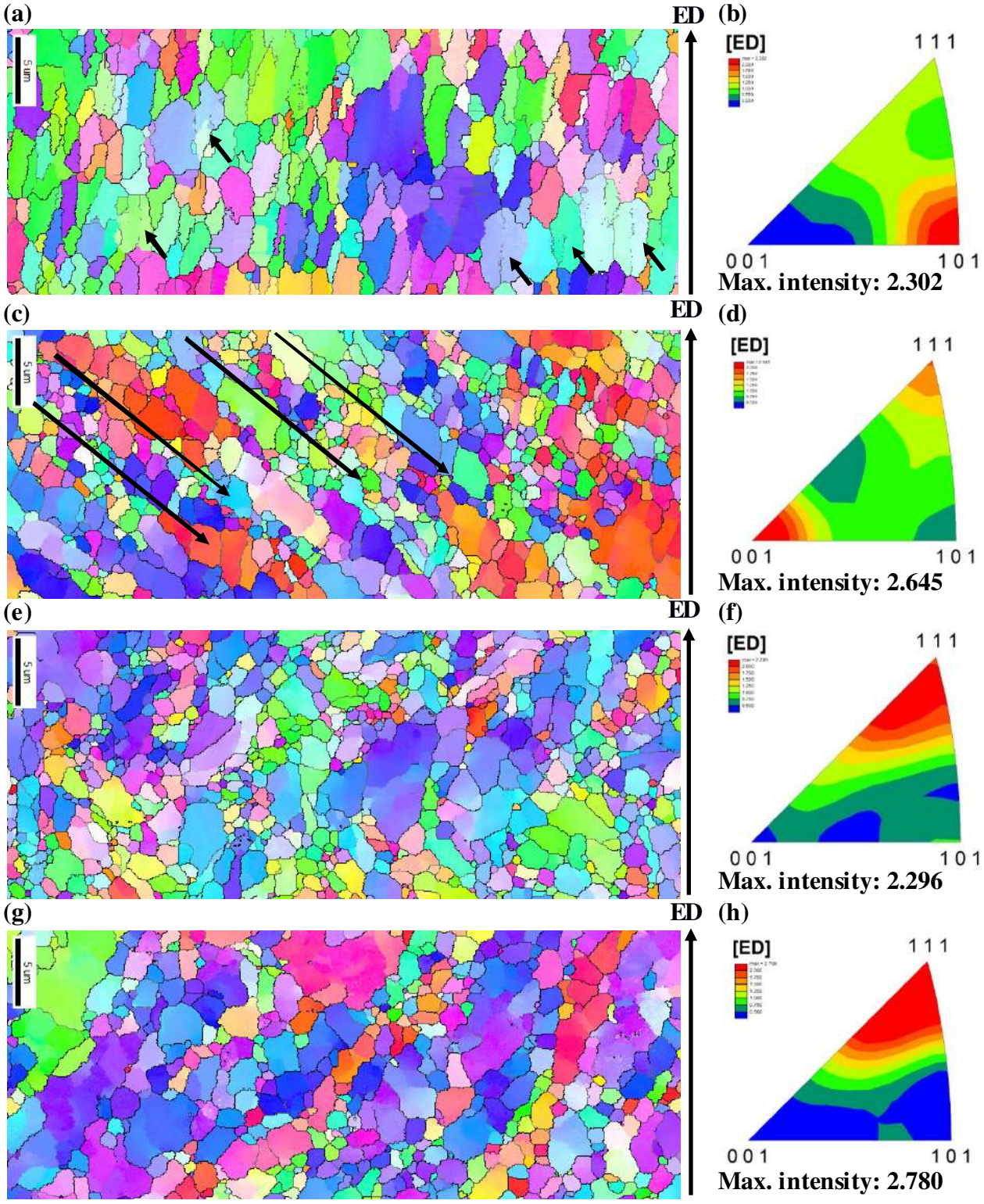

Fig. 5.6. *EBSD crystal orientation maps of zone (a) 1, (c) 2, (e) 3 and (f) 4 marked in Fig. 5.5 and corresponding inverse pole figures of zone (b) 1, (d) 2, (f) 3 and (h) 4.*

This shows that dynamic recrystallization with partial grain growth is dominant during deformation in this domain. Figure 5.7 compares the frequency distribution of grain size in these four regions. The analysis shows a large variation in grain size distribution at low temperatures, due to coalescence of grains during the deformation process. Dynamic recrystallization is favored during deformation at temperatures around 1373 K (1100 ℃) for strain rates below rate 10^{-2} s^{-1}, while at temperatures >1423 K (>1150 ℃), dynamic recrystallization is observed even at a high strain rate of 10^{-1} s^{-1}. The resultant microstructure consists of nearly uniform fine sized (2-3 μm) grains where the pinning effect of the dispersoids effectively restricts grain growth despite high temperatures. Figure 5.6(b, d, f and h) shows the inverse pole figure maps corresponding to the same 4 regions discussed above, showing the evolution of texture during hot compression. During uniaxial deformation, the fiber texture is typically represented using inverse pole figures to truly represent the tendency for preferred crystallographic directions with respect to particular sample axis.

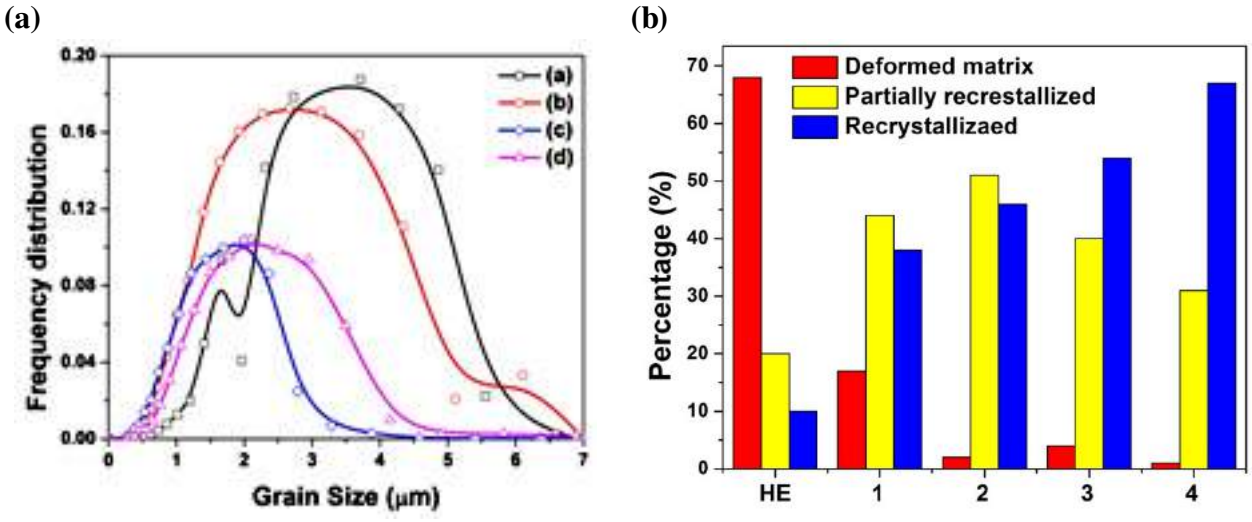

Fig. 5.7. *(a) Grain size distribution in zone (marked in Fig. 5.6); (a) 1, (c) 2, (e) 3 and (f) 4.and (b) distribution of extent of recrystallisation (*Note: HE, Z-1, Z-2, Z-3 and Z-4 marked in X-axis in (b) are as extruded (Fig. 3.15(a) and 1 to 4 (Fig. 5.5) respectively).*

Further, Fig. 5.7(b) shows the distribution of recrystallisation extent comparison for as-extruded and four regions marked in Fig. 5.5. The recrystallization grains are identified about 10% in the as-extruded specimen Fig. 5.7(b), which is attributed to the heterogeneous nature of strain localization at the grain boundaries and within the grains. However, the percentage of recrystalization is found to be enhanced during high temperature deformation and exhibits about 40-70% in contrast to as-extruded specimen. This could be associated with the material flow during deformation process at high temrpature and resulted in dynamic recrystallization. Further, the extent of recrystallization is in corroborated with the efficiency of processing map (Fig. 5.5).

It is observed that there is significant reduction of <1 1 0> fiber texture intensity from 8.1(Fig. 3.15 in Section 3.5) in the hot extruded steel to 2.3 after deformation at 1323 K (1150 ℃) at strain rate of 10 s^{-1} (fig. 5.6(b)). The retention of directional microstructure at this temperature reflects efficient pinning effect of dispersoids, which also restrict boundary migration [79]. Also, the decrease in <1 1 0> fiber texture during hot deformation through uniaxial compression of metals, can be understood based on grain coalescence due to the reversal in direction of deformation [225]. However, at the same temperature of 1323 K (1050 ℃), when the strain rate is reduced from 10 to 0.01 s^{-1}, α-fiber texture along <1 1 0> changes to predominantly θ-fiber texture <1 0 0> with small contribution from <1 1 1> as seen from Fig. 5.6(d).

Shearing as well as partial recrystallization is responsible for the development of a double fiber texture during plastic deformation at 1323 K (1050 ℃) at low strain rate of 0.01 s^{-1}, which is reported as characteristic of bcc alloys [226]. Figure 5.6(f) shows the IPF maps corresponding to region 3 subjected to deformation at 1373 K (1100 ℃) at a low strain rate 0.01 s^{-1}, which reveals the development of <1 1 1> fiber without any signature of <1 1 0>. It is also observed

from Fig. 5.6(h) that there is no appreciable change in texture intensity, when the compressive deformation temperature and strain rate are increased to 1473 K (1200 ℃) and 0.1 s^{-1} respectively. This clearly indicates that the preferential <1 1 1> texture along the deformation direction is responsible for the dynamic recrystallization during deformation in both these cases. However, dynamic recrystallization occurs through progressive subgrain rotation at 1373 K (1100 ℃) with strain rate of 0.01 s^{-1}. Both cases involve strain-induced phenomenon with limited or no movement of high-angle boundaries at 1473 K (1200 ℃) [33]. The relevant texture components, which evolve during high-temperature deformation of ferritic steels are often reported to be α-fibers ({110}//RD), γ-fibers (<111>//ND) and θ-fibers <100>//ND [227]. Hence, comparison of the IPFs in the present study confirms the following:

a) Formation of θ-fiber during deformation at 1323 K (1050 ℃) with strain rate of 0.01 s^{-1} due to shearing mechanism , and
b) Formation of γ-fiber during deformation at 1373 K (1100 ℃) with strain rate of 0.01 s^{-1} and 1473 K (1200 ℃) with strain rate < 0.1 s^{-1} due to dynamic recrystallization.

5.5. Prediction of Texture Using VPSC-5 Constitutive Model

5.5.1. Model Description

Visco plastic self consistent (VPSC) simulation [228] was carried out using the VPSC-5 to predict the texture evolution during uniaxial deformation of steel in the plastic range. It is true that Taylor type simulation is not applicable to capture dynamic recrystallisation (DRx) associated with unrestricted dislocation motion. However, the presence of dispersoids, influence the work hardening mechanism in DRx domain. Hence VPSC simulations have been carried out in this study to capture hot deformation texture. The crystal plasticity mechanism is considered based on slip activity during deformation with respect to resolved shear stress. The details of the

model developed for deformed single phase material are reported [229, 230]. The response of the single crystal is expressed with the help of rate sensitive constitutive law [231]:

$$\epsilon_{ij}(\bar{X}) = \Sigma_s m_{ij}^s \gamma^s(\bar{X}) = \gamma_0 \Sigma_s m_{ij}^s \left(\frac{m_{kl}^s \sigma_{kl}(\bar{X})}{\tau_0^s}\right)^n \quad (5.13)$$

where 'ϵ' is the strain rate of the individual grain, 'm^s' is Schmid tensor, 's' is the given slip system, 'τ^s' is the threshold stress, which controls the activation of the slip system and 'n' denotes the rate sensitivity. The activation of slip system leads to self or latent hardening of it due to the activation of same slip system or any other slip system respectively. This is outlined by the empirical Voce law given as [231]:

$$\hat{\tau}^s = \tau_0^s + (\tau_1^s + \theta_1^s \Gamma)\left(1\exp\left(-\Gamma\left|\frac{\theta_0^s}{\tau_1^s}\right|\right)\right) \quad (5.14)$$

where $\Gamma = \Sigma_s \Delta\gamma^s$ depicts the accumulated shear in the grain; τ_0 and (τ_0+τ_1) are the initial and extrapolated CRSS value respectively; θ_0 and θ_1 are the initial and asymmetric hardening rate respectively. In the VPSC model, a polycrystalline aggregate is assumed to be represented by a number of crystals with individual orientation, shape and volume fraction. Plasticity of the material is accommodated by the activation of slip in each grain. Since the specimens are largely deformed, only the plasticity is calculated and the elasticity part is neglected in the VPSC model. The crystallographic texture after deformation of the steel has been generated using VPSC-5 code using the following inputs:

(1) Initial crystallographic texture, individual grain orientations and their volume fraction from EBSD data,

(2) Deformation mode associated with hardening from experimental flow curve, and

(3) Active slip/twinning systems form the BCC crystal structure (Table 5.2) [232].

Further, during modeling the deformation texture using VPSC code, the intermediate n_{eff} = 10 approach was considered. In order to simulate the texture development during compression deformation, nearly 1000 random orientations were taken. The simulation was carried out till ε = 0.5 for compression deformation using velocity gradient:

$$\begin{pmatrix} 0.5 & 0 & 0 \\ 0 & 0.5 & 0 \\ 0 & 0 & -1 \end{pmatrix}$$

Simulated stress strain curves with the activation of the above slip systems were compared with experimentally obtained stress strain curve. The values of the hardening parameters for the best fit of the deformation through compression are given in Table 5.3.

Table 5.2. Combination of slip systems for cubic bcc crystal is considered for simulation

{110}<111> SLIP						**{112}<111> SLIP**						**{123}<111> SLIP**					
0	1	1	1	1	-1	-2	1	-1	-1	-1	1	1	2	3	1	1	-1
												-1	3	2	1	1	-1
1	0	1	1	1	-1	1	-2	-1	-1	-1	1	2	1	3	1	1	-1
												-2	3	1	1	1	-1
1	-1	0	1	1	-1	1	1	2	-1	-1	1	3	-1	2	1	1	-1
												3	-2	1	1	1	-1
0	1	-1	1	-1	-1	-2	-1	-1	-1	1	1	-1	2	-3	1	-1	-1
												1	3	-2	1	-1	-1
1	0	1	1	-1	-1	1	2	-1	-1	1	1	2	-1	3	1	-1	-1
												2	3	-1	1	-1	-1
1	1	0	1	-1	-1	1	-1	2	-1	1	1	3	1	2	1	-1	-1
												3	2	1	1	-1	-1
0	1	1	1	-1	1	2	1	-1	1	-1	1	1	-2	-3	1	-1	1
												1	3	2	1	-1	1
1	0	-1	1	-1	1	-1	-2	-1	1	-1	1	2	-1	-3	1	-1	1
												2	3	1	1	-1	1
1	1	0	1	-1	1	-1	1	2	1	-1	1	3	1	-2	1	-1	1
												3	2	-1	1	-1	1
0	1	-1	1	1	1	2	-1	-1	1	1	1	1	2	-3	1	1	1
												1	-3	2	1	1	1
1	0	-1	1	1	1	-1	2	-1	1	1	1	2	1	-3	1	1	1
												2	-3	1	1	1	1
1	-1	0	1	1	1	-1	-1	2	1	1	1	-3	1	2	1	1	1
												-3	2	1	1	1	1

Table 5.3. Hardening parameters of deformation used for the simulation

Slip	τ_0 (MPa)	τ_1 (MPa)	θ_0 (MPa)	θ_1 (MPa)
{1 1 0}	180	110	800	140
{1 1 2}	120	110	600	100
{1 2 3}	130	110	500	80

5.5.2. Simulated Texture Distribution

Figure 5.8 shows the predicted pole figures for the deformation of the steel in the directions parallel to ED (Fig. 5.8(a)) and TD (Fig. 5.8(b)). The figure reveals the variation in the texture components evolved in contrast to the initial texture. The deformation along ED resulted in <1 1 1>//ED; however, <1 1 0> fiber texture gives way to the formation of <1 1 0> and <1 1 1> // ED component during deformation along TD. Table 5.4 shows the relevant texture components that evolved during the deformation namely α-fibers ({110}//TD) and γ-fibers (<111>//ED). An enhancement in γ-fiber component is observed in both experimental and predicted texture, which is attributed to dynamic crystallization assisted high temperature deformation. However, the deformation along ED offers more dominant γ-fiber texture in contrast to TD. This suggests that the reduction ratio of diameter to thickness should be higher during high temperature processing for tube fabrication to assist the preferential growth of γ-fibers in contrast to α-fiber.

Table 5.4. Comparison of α and γ fiber attributes

Fiber Texture (%)	Initial Texture		High-temperature Deformation (0.5 strain)		
	ED	TD	Experimental (ED)	Predicted (ED)	Predicted (TD)
α	8	10	7	5	25
γ	5	3	18	42	18

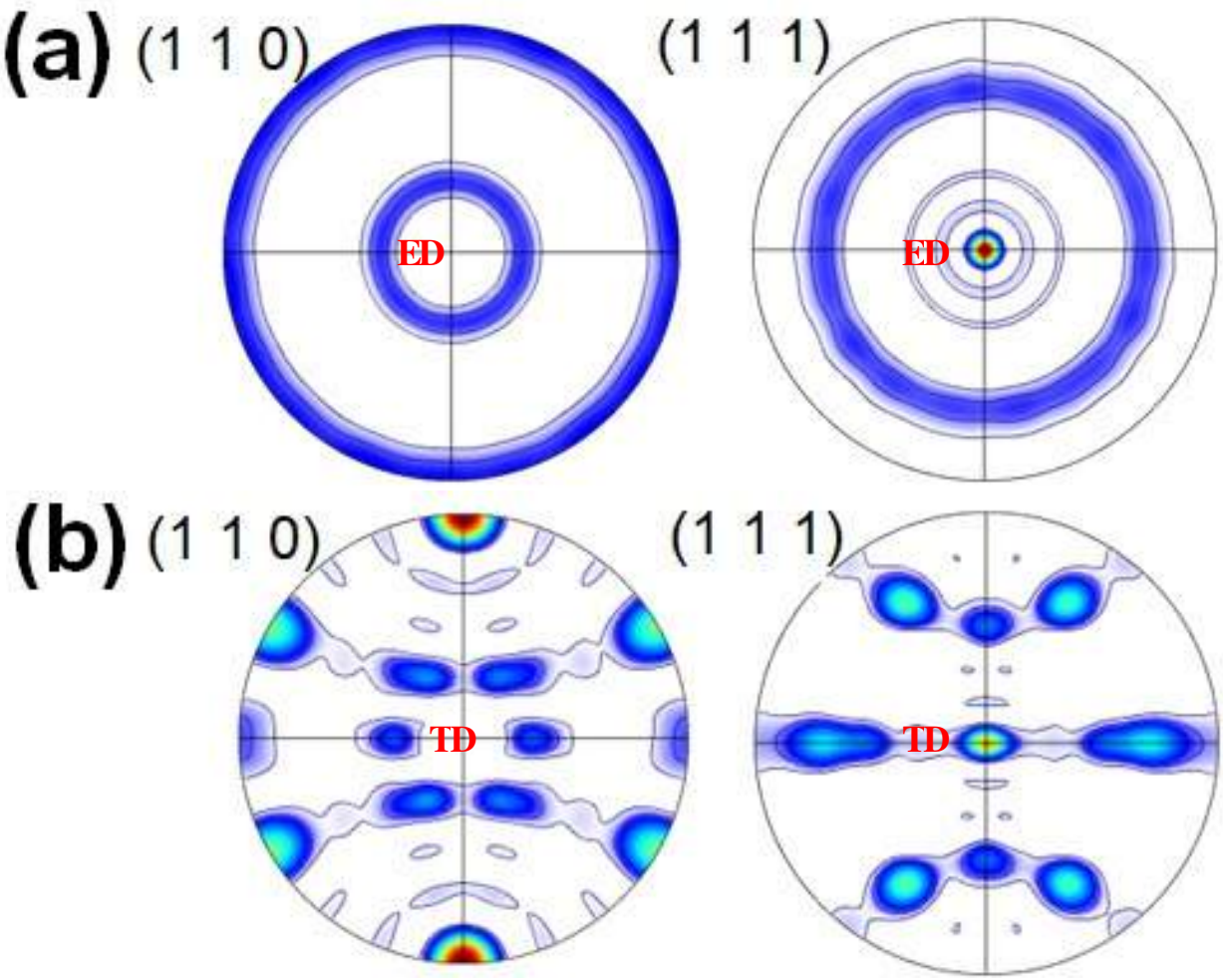

Fig 5.8. *(110) and (111) Pole figures predicted using VPSC-5 during deformation along (a) ED and (b) TD.*

5.6. Summary

The optimum high temperature workability region has been identified for 18Cr Cr oxide dispersion strengthened ferritic steel based on dynamic material model approach from the analysis of the results of hot isothermal compression tests in a wide range of temperatures (1323 to1473 K) and strain rates (0.01 to 10 s^{-1}). The variation in microstructure and microtexture in different safe domains of processing map are analyzed. The following important conclusions are drawn from this investigation.

- Limited safe processing domains have been identified based on the influence of strain rate sensitivity (m), efficiency of power dissipation (η) and instability parameter ($\xi(\dot{\varepsilon})$) parameters.
- Instability domains have been identified in the temperature range of 1323 to 1423 K (1050 to 1150 ℃) with strain rate > 0.1 s^{-1}.
- Based on superior workability region with peak efficiency up to 30-35%, the most favorable processing parameters have been optimized in the range of 1350 to 1450 K (1077 to 1177 ℃) at a strain rate of 0.01 s^{-1} and 1473 K (1200 ℃) at a strain rate 0.1 s^{-1}.
- Low efficiency parameter in the safe processing domain resulted in shearing and retention of deformed microstructure, at high strain rate (10 s^{-1}) and low strain rates (0.01 s^{-1}) respectively and a coarse grain size distribution is attributed to coalescence of grains during deformation.
- High temperature compression minimizes the <1 1 0> fiber texture. At 1373 K (1100 ℃) with strain rate < 0.01 s^{-1} and at 1473 K (1200 ℃) with a strain rate of < 0.1 s^{-1} <1 1 1> fiber texture is obtained.
- Intensity of γ-fiber is found to be dependent on the direction of applied stress to the initial texture and the reduction ratio of diameter to thickness should be higher during high temperature processing of tube from hot extruded product to assist the preferential growth of γ-fibers in contrast to α-fiber.

Characterization of Interface Boundaries in Advanced Steels using 5-Parameter Description

Microtexture analysis by EBSD technique enables the characterization of grain boundaries in a material, based on misorientation across neighboring grains. The change in crystal orientation between a pair of adjacent grains can be described using the rotation angle (ω) and rotation axis ($\hat{f}$) pair or relative Euler angles, and have three degrees of freedom. It is further possible to extend the characterization of microstructure in the third dimension and evaluate the grain boundary plane inclination [233, 234]. Thus, five parameters are available for macroscopic description of the grain boundary namely, three parameters associated with rotational alignment of unit cells of adjacent grains, and two parameters [azimuth (γ) and polar (β) angles] for defining the grain boundary plane inclination [235-237].

It is well known that grain boundaries in steels can be engineered with respect to their nature and distribution, to design a microstructure with desirable properties through Grain Boundary Engineering (GBE). The microstructure is designed so as to enhance the amount of $\Sigma 3^n$ Coincident Site Lattice (CSL) boundaries, generally by recovery and recrystallization processes in systems associated with low stacking fault energy (SFE) as in FCC alloys [238]. Twinning related GBE aims to increase the fraction of $\Sigma 3$ boundaries due to their low energy in contrast to other CSLs ($< \Sigma 29$). However, recrystallization induces a completely polygonal ferrite grain structure with high angle boundary interfaces, which are generally non CSL in character. Twinning related grain boundary engineering concepts are not applicable to ferritic steel with high SFE.

In the present chapter, the grain boundary character distribution (GBCD) in high SFE steels of two types, namely 18Cr ODS and 9Cr-1Mo ferritic steels have been studied by planar

sectioning method and compared with GBCD in annealed 304HCu austenitic stainless steel (SS304HCu) with low SFE. GBCD analysis provides interface characteristics like rotation axis and misorientation angle, which does not define the grain boundary plane inclination. This shortcoming has been addressed by developing a methodology of five parameter description of interface boundaries using serial sectioning method in conjunction with EBSD data. This methodology provides information on rotation axis ($\hat{r}$), misorientation (ω), azimuth (γ) and polar (β) angles and has been demonstrated in high SFE 9Cr-1Mo ferritic steel and low SFE SS304HCu, which is useful to understand the mechanism of energy minimization during diffusional transformations in these steels. In order to establish the influence of SFE on grain boundary characteristics, a comparison has been made between 9Cr-1Mo ferritic and 304HCu austenitic stainless steels, which have been subjected to deformation and annealing treatments.

6.1. Evaluation of Grain Boundary Character Distribution in 18Cr ODS Ferritic Steel

EBSD data was processed by neighboring 0.1 confidence index value for extrapolation for identification of grains and evaluation of grain boundary types (low angle, high angle, CSL). Misorientations greater than 5° across neighboring pair of pixels were considered as grain boundaries, CSL boundaries were evaluated using Brandon's criterion [127] and the relative amounts of CSL (Σ1-29) boundaries were calculated based on the length fraction.

6.1.1. Characterization of Grain Morphology and Boundary Network

Figure 6.1 shows a representative superimposed EBSD image quality (IQ) and grain boundary distribution map from two perpendicular surfaces namely ED and TD of extruded steel. The IQ map in the background exhibited fine grain morphology with size of 1-2 μm. However, the microstructure of ED specimen shows retention of elongated grains (Fig. 6.1(a))

with an average aspect ratio of ~1:5, in contrast to near equiaxed structure in TD specimen (Fig. 6.1(b)). A close look shows variation in contrast within the network of high angle boundaries in ED specimen (arrow marked in Fig. 6.1(a)) indicating an intragrain rotation during the extrusion process as discussed in Chapter 3 (Section 3.5). The grain boundary network does not show any preferential distribution of low angle, high angle or CSL boundaries along both ED and TD.

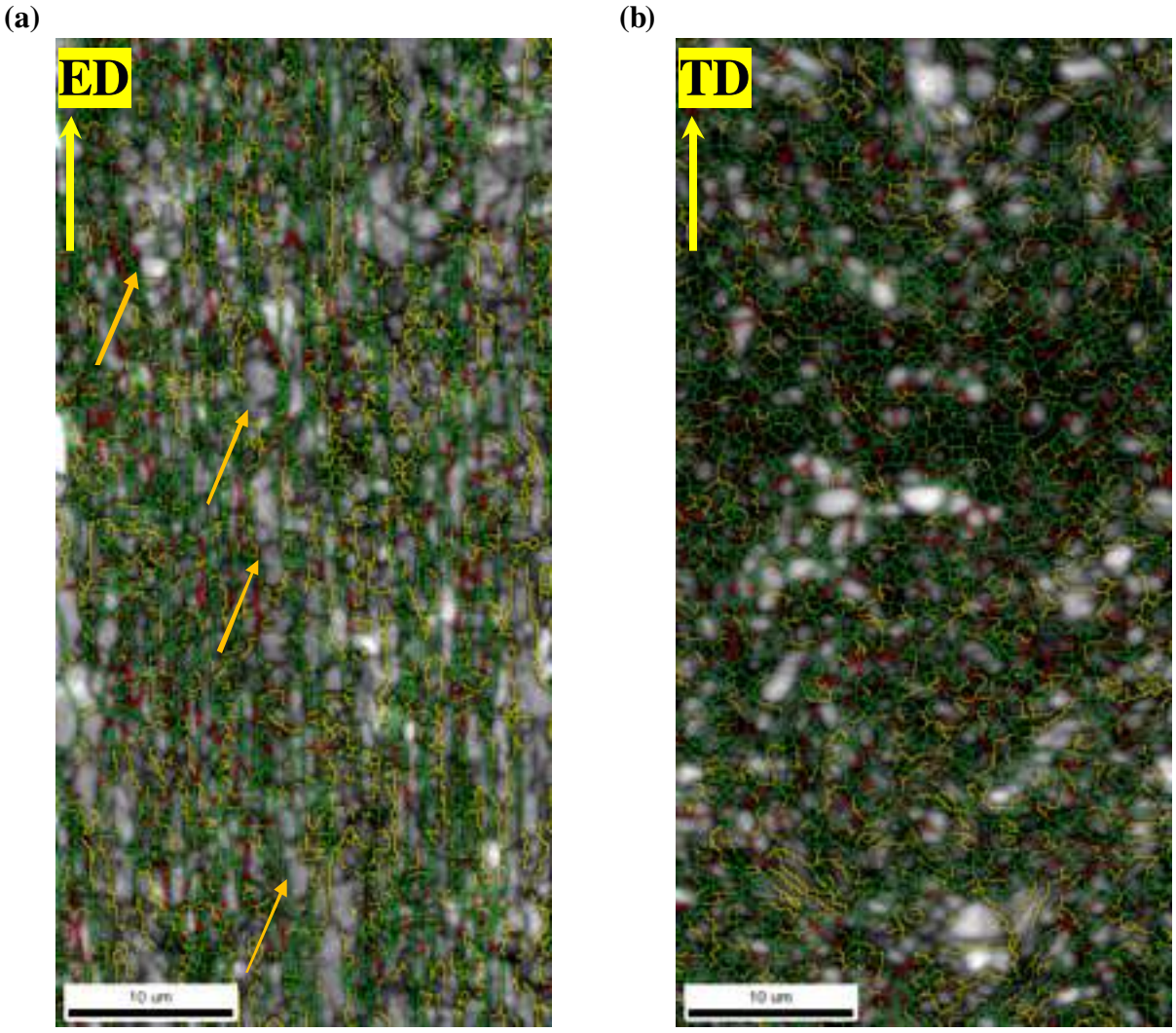

Fig. 6.1. *Superimposed maps of image quality and grain boundary distribution (colour key: yellow—5-15º (LAGB), green—15-65º (HAGB), red— CSL Σ1-29) map for (a) ED and (b) TD 18Cr ODS ferritic steel.(HAGB-high angle grain boundary and LAGB-low angle grain boundary)*

The extruded steel was cold worked to 50% thickness along ED and TD directions and the specimens are designated as EDR and TDR. These specimens were heated at a rate of 7 $Kmin^{-1}$ to 1420 K (1147 ℃), held for 1 h and air cooled to room temperature and the specimens are designated as AEDR and ATDR respectively (Table 2.4, Section 2.2). The IQ map with an overlay of grain boundary distribution map in Fig. 6.2(a) and (b) from the AEDR and ATDR specimens reveal a mixed structure of recrystallized grains (substructure free ferrite grains) due to thermally activated diffusional transformation and substantial recovery of the deformation substructure.

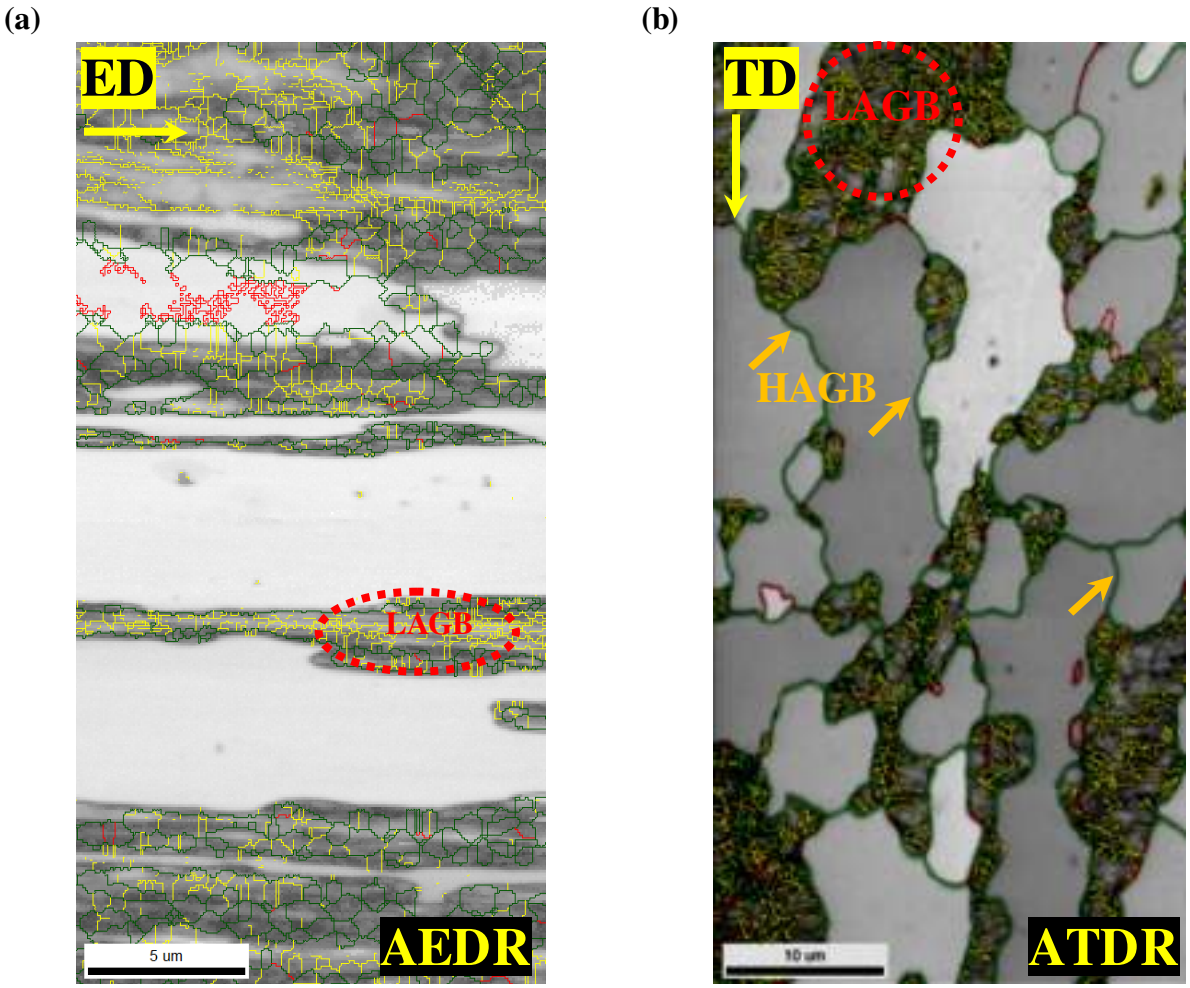

Fig. 6.2. *Superimposed maps of image quality and grain boundary distribution (colour key: yellow—5-15º (LAGB-marked Circle), green—15-65º (HAGB-marked arrow), red— CSL Σ1-29) of (a) AEDR and (b) ATDR sections of 18Cr ODS ferrtic steel. (HAGB-high angle grain boundary and LAGB-low angle grain boundary)*

The AEDR and ATDR specimens show larger grain size (14 - 15 μm) as well as a higher fraction of low angle boundaries as compared to ED and TD, due to grain growth during the additional deformation and annealing. The observed jagged boundaries on the growth front are attributed to the pinning effect of the dispersoids, which also restrict grain growth.

6.1.2. Grain Boundary Character Distribution (GBCD)

Misorientation angle is a single parametric description of GBCD between neighboring grains for a given microtexture. The probability of misorientation angle close to CSL can be evaluated from the uncorrelated random orientations [239], by the following expression:

$$p_{\Sigma n} = \left(\frac{24}{\pi}\right) m\left(\tau - \sin\tau\right) \tag{6.1}$$

where, m is the multiplicity of the rotation axis of ideal CSL boundary and τ is the tolerance angle given by Brandon's criteria [127]. The theoretical CSL boundary fraction was estimated as ~13% considering a misorientation angle > 5° between grain boundaries.

Figure 6.3 depicts the frequency distribution of misorientation angles between grain boundaries and the theoretical Mackenzie distribution [240]. The experimental data for ED, TD, AEDR and ATDR follow a similar behavior, which is markedly different from the Mackenzie distribution. The fraction of boundaries with misorientation angle between 10° to 20° was marginally higher than the boundaries with high misorientation angle between 55° to 60° as seen in Fig. 6.3(a). Peak 1 at ~10° in Fig. 6.3(a) indicates an intragrain rotation in ED and TD specimens. The higher frequency of low angle boundaries in AEDR and ATDR is attributed to the partially recovered microstructure during deformation and annealing. Peak 2 represents the fraction of boundaries with misorientation angle between 55° to 60° and also includes the Σ3 CSL boundaries ((111) at 60°) following the Brandon criteria [127].

(a)

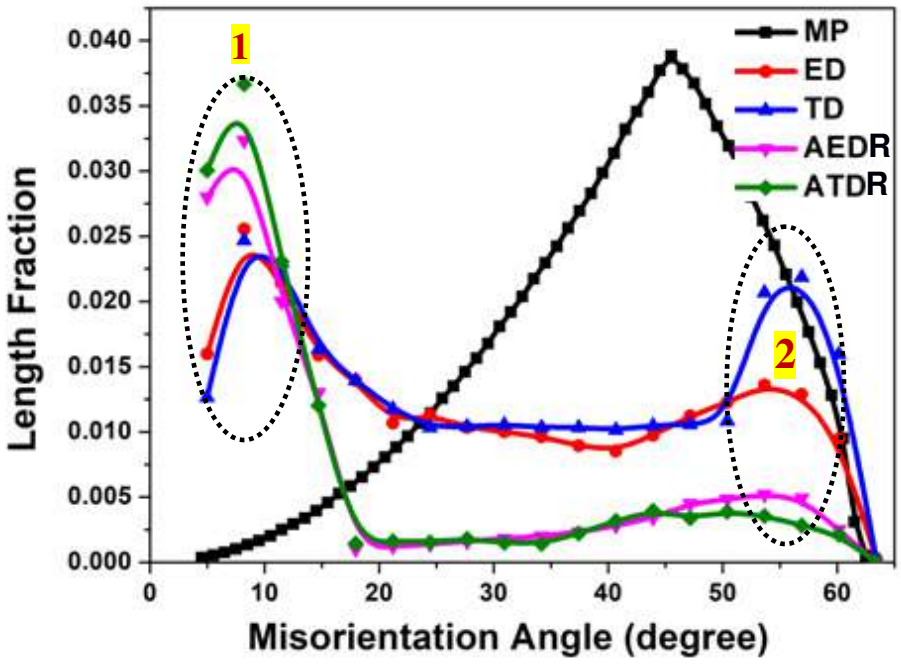

(b)

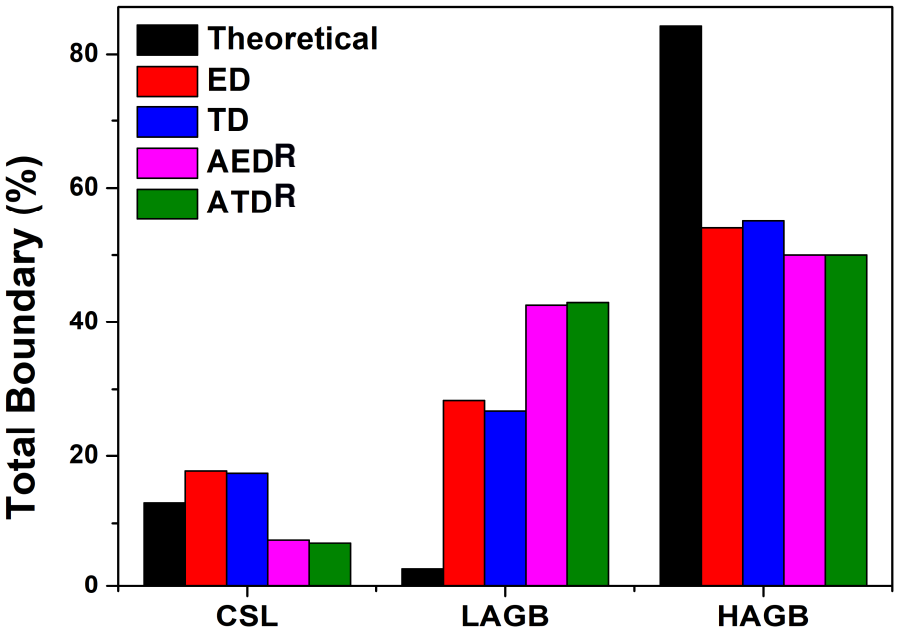

Fig. 6.3. *Comparison of experimental and theoretical data between ED, TD, AEDR and ATDR 18Cr ODS ferritic steel (a) Misorientation angle distribution and (b) GBCD.*

Figure 6.3(b) shows the GBCD of various types of boundaries (CSL, low and high angle boundaries) evaluated from ED, TD, AEDR and ATDR specimens. Table 6.1 lists the average

grain size and various GBCD attributes determined by EBSD analysis for the four specimens, which are compared with the theoretical values. The amount of low angle grain boundaries in ED, TD, AEDR and ATDR specimens is 28, 27, 48 and 43% respectively. The CSL fraction in AEDR and ATDR specimens are lower than in ED and TD specimens, which is attributed to the diffusion assisted recrystallization phenomena leading to predominantly random boundaries (Fig. 6.3 (a) and (b)). The diffusion assisted recrystallization phenomena induced a complete polygonal ferrite grain structure with high angle boundaries within the neighboring grains, which were generally non CSL in character. The high SFE in ferritic steels prohibits twinning during deformation and annealing. This is in contrast to the high amount of $\Sigma 3^n$ boundaries due to recovery and recrystallization in deformed and annealed FCC alloys with low SFE [238, 239].

Table 6.1. Comparison of experimental evaluated and theoretically calculated grain boundary attributes

Particulars	ED	TD	AEDR	ATDR	Theoretical
Grain Size (μm)	2±0.5	1±0.5	0.5±0.1and >40	0.5±0.1 and 6±2	----
Grain Morphology	Elongated	Equiaxed	Bimodal	Bimodal	----
CSL Boundary	18	17	6	7	13
LAGB	28	27	48	43	3
HAGB	54	56	46	50	84

In order to understand the role of grain size on GBCD, the study was extended to well annealed 9Cr-1Mo ferritic steel with an average grain size of 40 μm in contrast to grain size of 1 μm in 18Cr ODS ferritic steel. The polygonal ferrite grain structure in 9Cr-1Mo steel was obtained by (a) isothermal annealing (IA) treatment (austenitizing at 1323 K (1050 ºC) for 1h followed by isothermal annealing at 1023 K (750 ºC) for 4h and air cooling to room temperature) and (b) additional annealing (IAA) (IA + 50h at 1093 K (820 ºC)) for grain growth. GBCD in both the specimens have been evaluated and the results are discussed in the following section.

6.2. Evaluation of Grain Boundary Character Distribution in 9Cr-1Mo steel

6.2.1. Characterization of Grain Morphology and Boundary Network

Figure 6.4 shows the band contrast microstructure map and the distribution of low (5º to 15º) and high angle (>15º) boundaries after IA and IAA treatments. The microstructure consists of ferrite grains with statistical variation in grain size and shape in both the specimens. Similar microstructures have been reported by EBSD analysis of iron [233]. During the IA treatment, diffusional phase transformation of austenite to ferrite and carbides takes place with nucleation of ferrite grains at prior-austenite boundaries along with precipitation of carbides. The observed irregular grain boundary contours in the final microstructure is a synergistic effect of the pinning effect of the carbides and impingement of growing ferrite grains [240-243]. The surface tension effects of curved boundaries leads to non-uniform mobility of grain boundaries [244, 245]. Even after extended annealing (IAA), due to pinning effect of the carbides, grains with irregular boundaries persisted (Fig. 6.4(b)). Thus, the expected enhancement of boundaries with straight contours or formation of low energy boundaries was not achieved even after prolonged annealing.

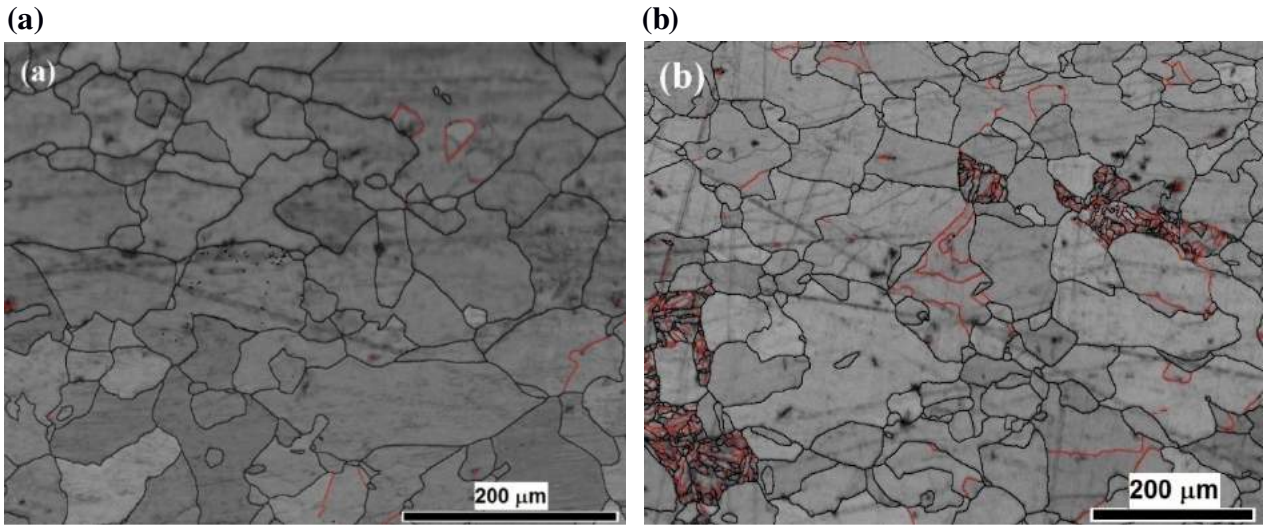

Fig. 6.4. *Superposed band contrast and grain boundary map (color key: red—5-15º, black—15-65º) in 9Cr-1Mo steel after (a) IA and (b) IAA treatments.*

Presence of large grains is due to thermally activated diffusional transformation with a significantly rapid reconstructive growth of interfaces during isothermal annealing. This is in sharp contrast to 18Cr ODS ferritic steel, where the presence of nano dispersoids restricted the grain growth. The IAA treatment resulted in coarse grains (average diameter ~ 58 μm) as compared to IA (average diameter ~ 46 μm), due to grain growth during the additional annealing. A higher fraction of low angle boundaries were observed in IAA (6.8%) as compared to IA specimen (2.8%), which is understood as follows: High angle boundaries exhibit higher mobility, and promote the growth of large grains (and annihilation of fine grains), whereas, low angle boundaries with low energy are less mobile and tend to persist. Also at triple junctions, two meeting random high angle boundaries connected by a low angle grain boundary would tend to migrate away, leading to extension of LAGB resulting in higher length fraction.

6.2.2. Grain Boundary Character Distribution (GBCD)

Figure 6.5 depicts the relative frequency distribution of misorientation angle of grain boundaries as compared to the theoretical Mackenzie distribution [240]. The experimental data set was found to be in agreement with the theoretical distribution for both the specimens. The experimental plots followed the theoretical trend. In an earlier study, the amount of CSL (Σ1 to Σ29) boundaries in isothermally annealed specimens (16%) was similar to the theoretical value (13%) of random and un-correlated orientation ensemble of grains [239]. Thus, the diffusional transformation of lath martensite to polygonal ferrite is seen to result in grain boundaries of random character, while the low angle boundaries persist during grain growth process during extended annealing. GBCD analysis of 18Cr ODS and 9Cr-1Mo ferrrtic steels discussed above clearly showed the effect of recrystallisation and annealing on enhancing the fraction of LAGB than calculated theoretically. The above results also show that the grain size or dispersoids do not

significantly influence the GBCD in the two types of ferritic steels and the low amount of CSL boundaries is due to the high SFE of BCC structure. In an FCC system $\Sigma 3^n$ (n=1, 2, 3….) type boundaries are formed during deformation and subsequent annealing processes [246] in contrast to BCC ferritic steels. Hence, a systematic study has been carried out to highlight the differences in GBCD after cold rolling and annealing in an austenitic stainless steel (SS304HCu), which is described below.

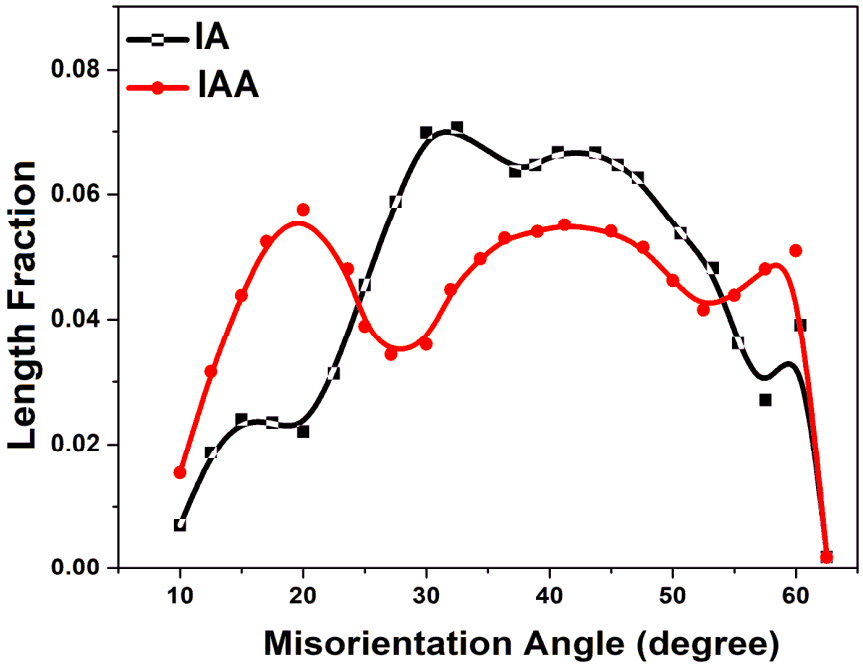

Fig. 6.5. *Misorientation angle distribution for experimental data set for BCC ferrite structure after the isothermal annealing treatments IA and IAA.*

6.3. Evaluation of Grain Boundary Character Distribution in 304HCu Austenitic Stainless Steel (SS304HCu)

6.3.1. Microstructural Evolution during Annealing Treatments

Crystal orientation maps superimposed on grain boundary (with misorientation angle: >5º) of the steel after different annealing treatments (recrystallization 'R', annealing 'A' and extended annealing 'EA') are shown in Fig. 6.6, which shows an equiaxed grain microstructure.

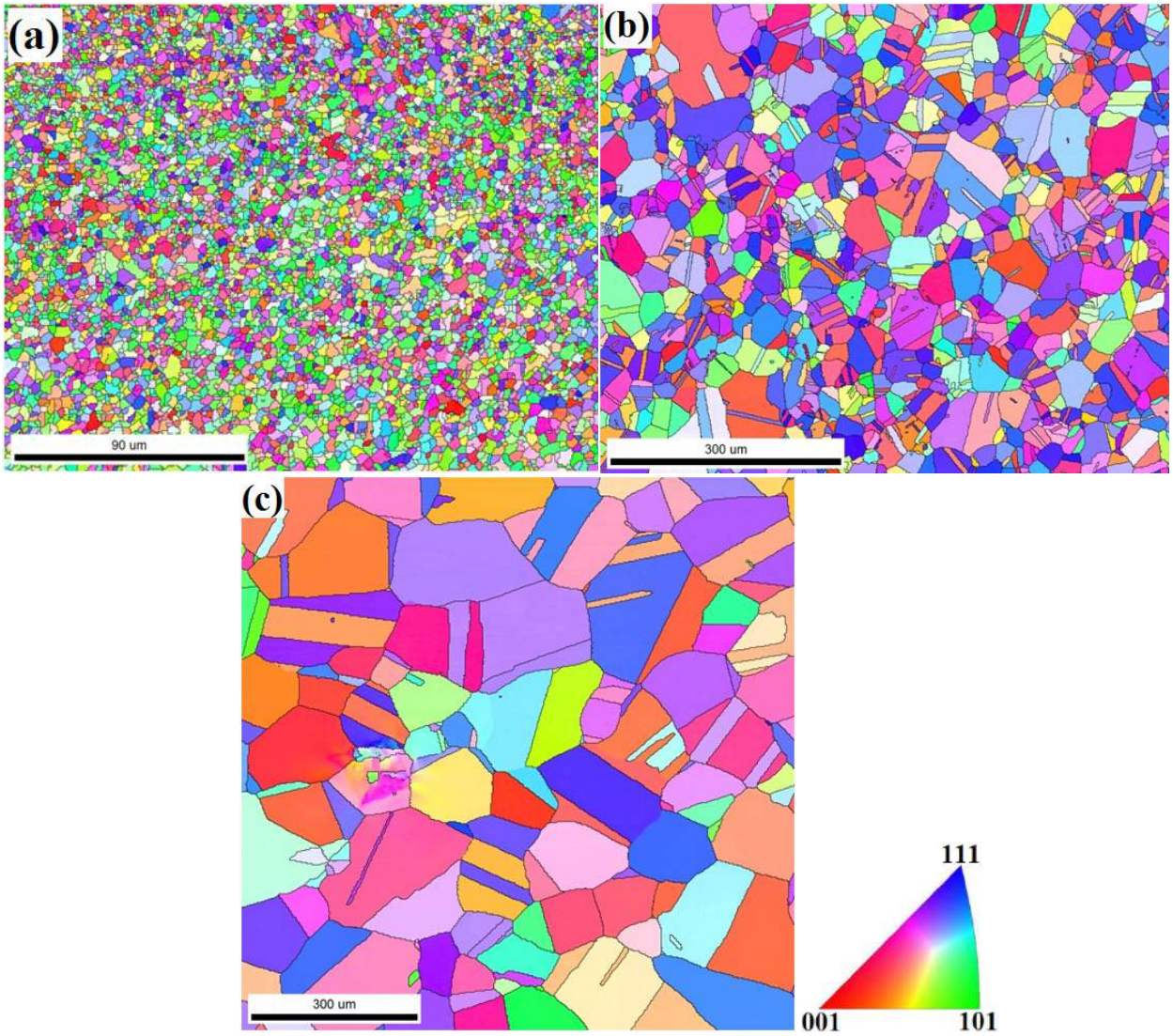

Fig. 6.6. *Superposed crystal orientation and grain boundary (>5º black line) map of SS 304HCu after annealing treatments at (a) 1073 K (800 ºC, treatment R), (b) 1373 K (1100 ºC, treatment A), and (c) 1573 K (1300 ºC, treatment EA).*

The average grain size was measured as 8 ± 2 μm after recrystallization treatment 'R' at 1073 K (800 ℃); but pronounced grain growth to 36 ± 4 μm and 72 ± 9 μm was observed for the treatments 'A' at 1373 K (1100 ℃) and 'EA' at 1573 K (1300 ℃) respectively. Treatment 'A1', with an additional exposure of specimen 'A' at 1373 K (1100 ℃) for 1 h did not show a significant increase in grain size. The presence of large grains in 'EA' is attributed to the enhanced kinetics of grain growth at a high temperature of 1573 K (1300 º). The observed planar grain boundaries after treatment 'EA' at 1573 K suggests a preferential reduction of surface

tension of curved boundaries [247]. In addition to the above, a number of annealing twins of single orientation were observed within a grain in the 'A' and 'EA' specimens, which provides evidence for similar stacking fault sequences occurring within a grain of distinct orientation.

6.3.2. Description of Grain Boundary Character

The single parametric description using the correlated experimental data on misorientation angles is a straightforward approach to identify the grain boundary distribution. Figure 6.7 represents the relative frequency distribution of misorientation angles at all annealing temperatures, which shows a considerable deviation from the general Mackenzie distribution [240]. The frequency distribution also showed a systematic variation in the misorientation angle with annealing temperature. Frequency distribution of misorientation in the range of 30°- 40° and 50°- 60° is observed to decrease and increase respectively with annealing temperature. It suggests the decrease in Σ9/Σ27 boundaries and increases in Σ3 boundaries qualitatively.

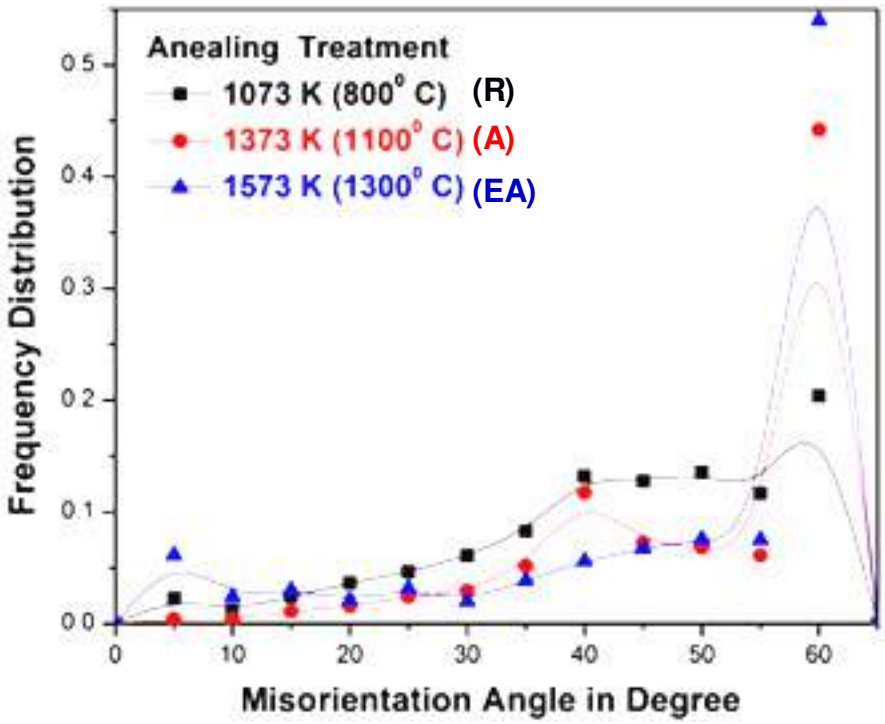

Fig. 6.7. *Correlated experimental misorientation angle distribution in SS 304HCu subjected to different annealing treatments after cold rolling.*

The low angle boundaries (5-15º) are found to be higher in 'EA' treatment at 1573 K (1300 ºC) compared to 'R' and 'A' treatments at 1073 (800 ºC) and 1373K (1100 ºC) respectively, which implies the persistence of Σ1 boundaries during grain growth.

Figure 6.8 shows the GBCD map of the steel after different annealing treatments. The amount of high angle random boundaries after treatment 'R' was 65% with a noticeable decrease to 40% and 33% after treatments 'A' and 'EA' respectively. However, the fraction of 'Σ1' low angle boundaries in 'EA' was higher (6.5%) than in 'R' (3%) (Fig. 6.8(c)).

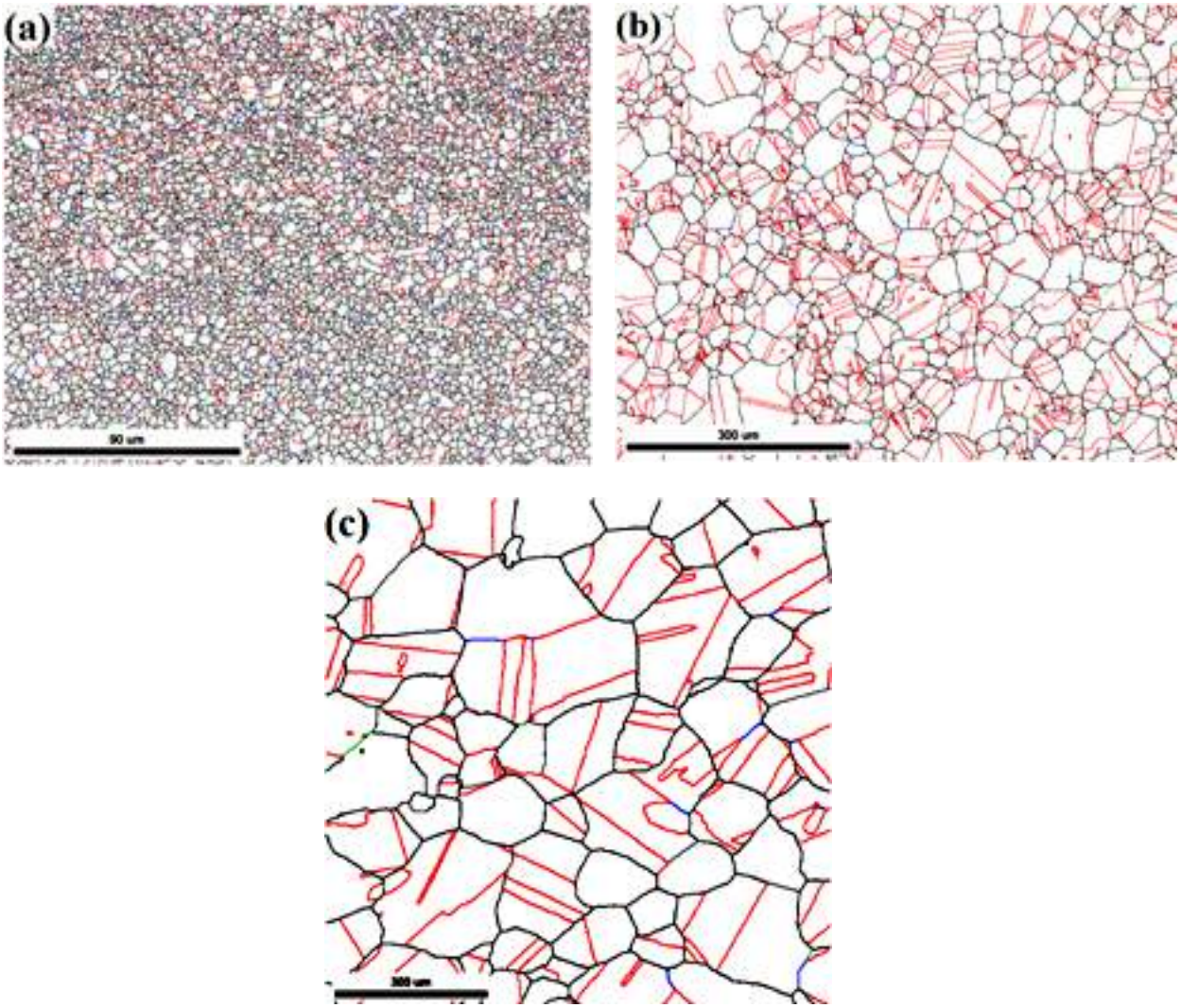

Fig. 6.8. *Grain boundary character distribution map (high angle random boundary (>15º) - black, Σ1 low angle (5-15º) boundaries - grey, Σ3 – red, Σ9 – Blue and Σ27 – Green line) map of SS 304HCu after annealing treatments at (a) 1073 K (800 ºC, treatment R), (b) 1373 K (1100 ºC, treatment A), and (c) 1573 K (1300 ºC, treatment EA).*

This increase in the fraction is attributed to the higher mobility of the high angle random boundaries that annihilate during grain growth, in contrast to low angle boundaries, which are less mobile and tend to persist. Fresh interface planes can form due to the annihilation of (intermediate) fine grains, but are less likely to exhibit a LAGB character [248]. However, the observed increase in LAGB is attributed to the stretching of LAGB boundaries at triple junctions, since the random boundaries migrate away from the triple junction, as discussed in section 6.2. The length fraction of Σ1-Σ29 CSL boundaries in 'R' was 32% as compared to 13% in the ideal random case [239] and increased to 56 to 59% in the 'A' and 'EA' specimens (Table 6.2). The CSL boundaries are predominantly of Σ3 type, reaching a maximum of about 86% and consist of mainly annealing twins introduced during recrystallization. A network of Σ3-Σ9-Σ27 has also been observed, which is due to the Σ3-Σ3 and Σ3-Σ9 interaction.

Table 6.2. Quantitative analysis of grain boundary character distribution

Particulars	LAGB (Σ1) (%)	HAGB (Random)	Total CSL (Σ1-Σ29) (%)	Individual $\Sigma 3^n$ Contribution (%)		
				Σ3	Σ9	Σ27
'R'	3	65	32	60	13	6
'A'	4	40	56	83	9	2
'EA'	6.5	34.5	59	86	1	0.2
Theoretical	1.6	85	13	20	4	0.1

It is reported [249] that in deformed and annealed (grain boundary engineered) SS304, a maximum of about 60% of low 'Σ' CSL boundary population, of which the contribution of Σ3 twin boundaries is about 67%. In contrast, though the low 'Σ' CSL boundary population remains the same in SS304HCu, Σ3 twin boundary contribution shows a maximum of about 86% (Table 6.3). This high value of twin boundary fraction in SS304HCu is attributed to its low SFE, which is evaluated as 10.6 mJm^{-2} as compared to 18.2 mJm^{-2} for SS304 (Table 6.3). This clearly

establishes the role of Cu in decreasing the SFE and hence enhancing the fraction of Σ3 CSL boundaries in SS304HCu.

Table 6.3. Predicted SFE of SS 304 and SS304HCu using JMATPro@ simulation

Steel	Chemical Composition (wt %)						Phase Included		SFE (mJm^{-2})
	Cr	Ni	C	Cu	Nb	Fe			
SS 304	18	8.5	0.06	---	---	Bal.	$M_{23}C_6$		18.2
SS304HCu	18	9	0.1	3	0.5	Bal.	$M_{23}C_6$	Cu-Rich	10.6

The high CSL fraction is mostly composed of Σ3, Σ9, and Σ27 in treatment 'R' at 1073 K (800 ℃), which is considerably higher than the theoretical values. However, a significant decrease in fraction of Σ9 and Σ27 boundaries is observed in the 'A' and 'EA' specimens and the values are similar to the random case. Increase in fraction of Σ3 type boundaries is attributed to the impingement effects caused due to the growing grains [239] and faults on (1 1 1) plane [250] or nucleation through stacking faults [251]. These phenomena were found to be more significant at 1073 K (800 ℃), than at 1373 K (1100 ℃) due to the high number density of fine grains. However, annealing at a higher temperature of 1573 K (1300 ℃) showed a negligible effect on Σ3 boundary fraction. Further, several studies report a fivefold decrease in Σ9 boundary fraction as compared to Σ3 type, and the fraction of Σ27 type is similar to the theoretical distribution in low SFE materials [252, 253]. A similar distribution is observed at 1073 K (800 ℃) in contrast to treatments 'A' (1373 K (1100 ℃)) and 'EA' (1573 K (1300 ℃)), which show a nearly theoretical distribution for the $\Sigma 3^n$ type boundary (Table 6.2).

6.3.3. Σ3 Type Boundary and Its Interaction

The CSL boundaries encountered during processing of austenitic stainless steel are predominantly either Σ3 or $\Sigma 3^n$ based on Grain Boundary Engineering considerations. It is possible to represent 'n' up to 9 [254]; however, based on the relevant $\Sigma < 29$ for cubic systems

'n' is considered up to 3 (Σ27) [238]. The Σ3 boundary consisting of 60° misorientation about (111) axis is coherent and low-energy type. However, during migration of grain boundaries, Σ3 interacts to generate Σ9/ Σ27 [255], and the geometrical structure correlation is equivalent to one of the orientations satisfied by multiplication of Σ3 type. The results of multiple twining have been calculated using quaternion algebra [247]. The coherent Σ3 axis are (1 1 1)/(1 -1 1)/(1 1 -1)/(-1 1 1) with misorientation angle of 60º. The Σ3 type interface plane orientation $q_{\Sigma 3n\ (n=1\ to\ 4)}$ can then be represented as,

$$q_{\Sigma 3n}(\theta, \hat{n}) = cos\left(\frac{\theta}{2}\right) + sin\left(\frac{\theta}{2}\right)(n_1 i + n_2 j + n_3 k) \quad (6.2)$$

where, θ is the misorientation angle 60º, and n̂ is the unit vector of interface plane normal. Also quaternion $q(\theta, \hat{n})$ resulting due to multiplication of Σ3 type boundary can be calculated as,

$$q(\theta, \hat{n}) = q^{-1}_{\Sigma 3n\ (n=1\ to\ 4)} \bullet q_{\Sigma 3n\ (n=1\ to\ 4)} \bullet q_s \quad (6.3)$$

where q_s are 24 quaternions associated with rotational symmetries of the cubic crystal. Among the 24 values of θ calculated from 24 q_s in Eq. (6.3), the minimum angle represents the misorientation angle (ω), and the corresponding n̂ vector denotes misorientation axis (r̂). Similar steps can be followed for the calculation of Σ3 interaction with Σ9, Σ27a, Σ27b and the resultant twins, which are summarized in Table 6. 4.

Table 6.4. Product of CSL Σ3 type boundary interactions due to multiple twinning

Twin Multiplication	h	k	l	ω (in degree)	Resulted Twin
CSL 'Σ3 X Σ3'	1	1	0	38.94	CSL Σ9
CSL 'Σ3 X Σ9'	1	1	1	60	CSL Σ3
	2	1	0	35.43	CSL Σ27a
	1	1	0	31.58	CSL Σ27b
CSL 'Σ3 X Σ27'	1	1	0	38.94	CSL Σ9
	5	3	1	38.37	CSL Σ81a
	4	1	1	38.94	CSL Σ81b
	3	2	2	54.52	CSL Σ81c

The probabilities of formation of Σ3, Σ9, Σ27 and Σ81 boundaries due to interactions are calculated as 0.098, 0.20, 0.058 and 0.052 respectively. At a triple junction of two intersecting Σ3 boundaries (60°<1 1 1> misorientation), a Σ9 boundary (39.0°<1 1 0> misorientation) is observed at the third boundary. Similarly, Σ3 and Σ9 boundaries interacted at triple junctions to form another Σ3, or Σ27a (35.4°<2 1 0> misorientation) / Σ27b (31.5°<1 1 0> misorientation) boundary. Along similar lines Σ3 and Σ27a/ Σ27b interaction forms Σ3 or Σ81a/ Σ81b/ Σ81c boundaries. As compared to other interactions, formation of Σ9 boundaries is possible only as a resultant of Σ3-Σ3 interactions. However, the boundary interactions are found to reduce with annealing temperature (Table 6.2). As per reported literature, the CSL of Σ81 type boundary energy is similar to that of high angle random boundary and has not been considered in the present study. The migration of $\Sigma 3^n$ type boundary during annealing is analyzed by EBSD and the results are presented in the following section.

6.3.4. $\Sigma 3^n$ Boundary Migration

To study the migration of $\Sigma 3^n$ type boundary the specimen was subjected to treatment 'A1' at 1373 K (1100 °C) subsequent to treatment 'A'. Figure 6.9 shows the GBCD map with significant changes marked in the figure. Additional annealing treatment showed negligible difference in grain size. However, a closer look shows the higher migration of Σ9 and Σ27 boundaries in comparison to Σ3 type, which is due to their higher energy. These boundaries are found to become straight and shorter during annealing. Although it has been suggested by Wang et al. [256], that very high shear stress facilitates twin boundary migration, the twins were found to be advancing along the length of the twin rather than along the width during annealing. Also, a shortening of Σ9 and Σ27 boundaries by closure of triple points has been observed in comparison to Σ3 boundaries. This causes the reduction in contribution of Σ9 and Σ27 boundaries to total

CSL boundaries (Table 6.2). These observations show that energy minimization resulted in the reduction of Σ3 interacted (Σ9 and Σ27) boundaries, in contrast to the increase in fraction and continuous network of Σ3 boundary during annealing. Although annealing is expected to bring about more linear and planar grain boundaries, the presence of corrugated boundaries are observed in this study, whose fraction increases with duration of annealing ('A' to 'A1' treatment in Fig. 6.9).

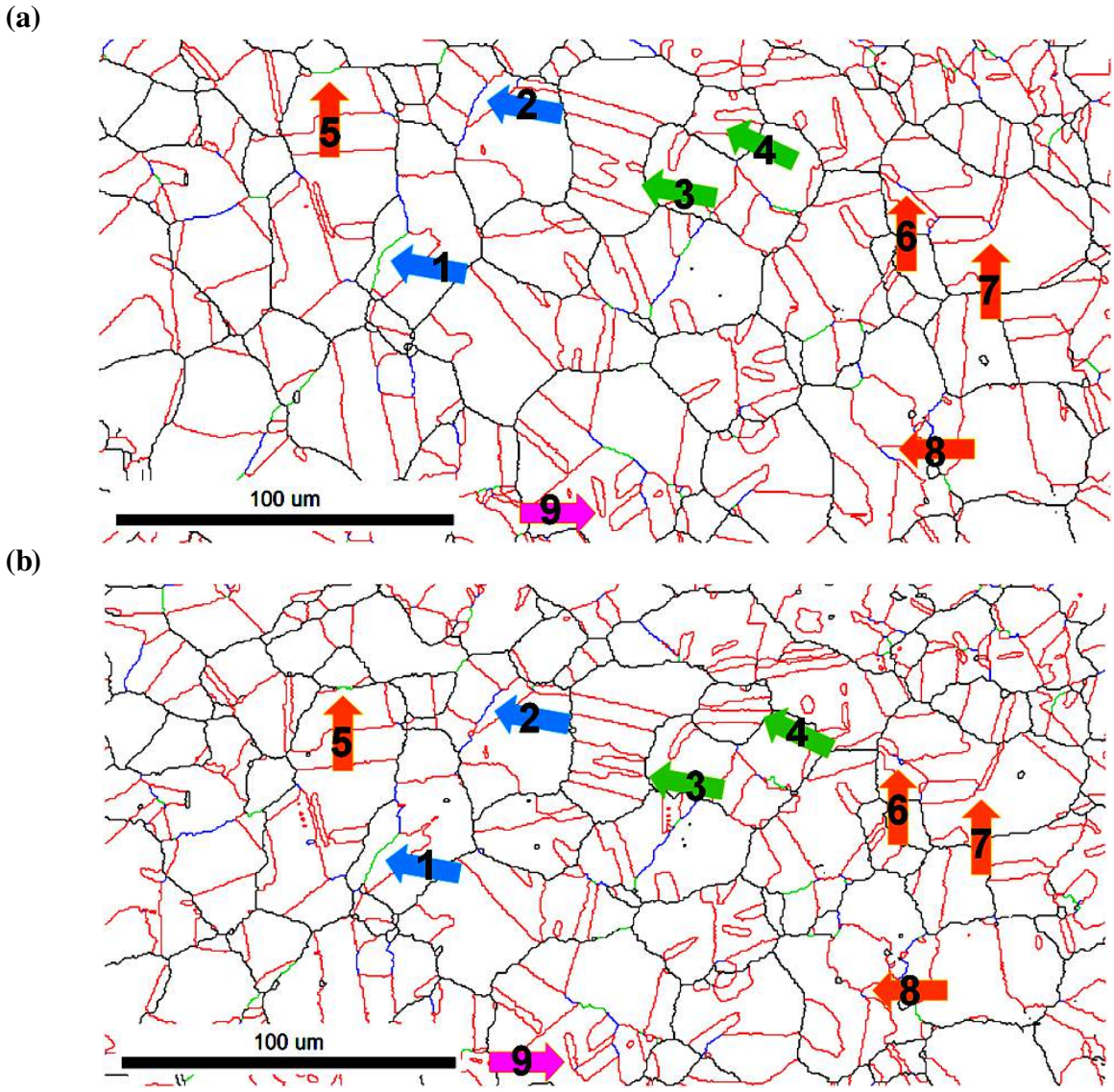

Fig. 6.9. *GBCD of cold rolled SS304HCu steel subjected to(a) treatment A and (b) treatment A1; 1 and 2 represent straightened grain boundaries, 3 and 4 represent Σ3 migration, 5 to 9 represent interactions of Σ3 and changes in CSL boundary in the same region; (Random boundary (>5°) - black, Σ3 – red, Σ9 – Blue and Σ27 – Green line).*

The most likely secondary phases reported in SS304HCu are MX (Nb(C, N)), $M_{23}C_6$ and Cu-rich phase [118]. However, the equilibrium MX phase (~0.35% volume fraction) is stable until ~1623 K (1350 ℃) in contrast to Cu-rich and $M_{23}C_6$ phases which dissolve at about 1123 K (850 ℃) and 1253 K (980 ℃) respectively [118]. During prolonged annealing, the MX (Nb(C, N)) precipitates at boundaries tend to pin the grain boundaries restricting their migration (Zener pinning effect) [157], which leads to the observed corrugated and nonlinear boundary contours (Fig. 6.9(b)). In addition, orientation pinning has also been reported to have strong influence on grain growth in FCC alloys [257]. However, CSL boundaries posed low Zener/solute drag [176] and were observed to be less corrugated in comparison to random boundaries during the second step of annealing in 'A1' specimen.

From the above observations, it is concluded that, the CSL boundaries were essentially annealing twins formed during recrystallization, whose fraction increased from 32% to 56-60% during high temperature annealing, in contrast to annealed ferritic steels where the fraction was only about 16%. Thus, it is evident that diffusional transformation during annealing in ferrite leads to random character of grain boundaries, whereas special boundaries (especially Σ3 CSL boundary) are enhanced in austenitic steel. Further, a methodology has been evolved to extend the EBSD analysis to characterize grain boundaries in three dimensions using serial sectioning method. The five-parameter GBCD is evaluated for polygonal grain structure obtained through diffusional transformation and after subsequent annealing in ferritic and austenitic stainless steels. In addition, interpretation of GBCD by various attributes and representations are discussed by comparing the results with the theoretical random GBCD. Further, special boundaries in austenitic steels, being low energy boundaries (especially Σ3 CSL boundary), 2D

characterization of such boundaries is incomplete. Hence, five parameter GBCD analysis of Σ3 interface plane has been carried out in annealed 304HCu austenitic stainless steel.

6.4. Procedure for Estimation of Five Macroscopic Parameters

EBSD microtexture analysis of planar section of the specimens gives ω, $\hat{r}$ and γ parameters of grain boundary, whereas stereological analysis or serial sectioning methods are required for the calculation of polar angle β. In literature, stereology based analysis of single planar section has been adopted to indirectly deduce the fifth parameter β of specific boundaries (such as Σ3), but a large number of boundary traces are necessary in this procedure [236, 258-260]. In recent times, Focused Ion Beam (FIB)-SEM has been used for serial sectioning to obtain series of EBSD maps at several parallel surfaces and construction of the microstructure in 3-dimensions (3D). However, analysis is generally restricted to a maximum scan volume of approximately 50 μm x 50 μm x 50 μm due to long FIB milling times, and this poses a limitation in study of materials with large grain sizes [261-263]. Alternatively, automated/manual mechanical polishing methods could be utilized for controlled removal of material by serial sectioning. By careful optimization of the procedure for controlled uniform removal of section thickness and accurate alignment in the subsequent scan, it is possible to evaluate larger sections of about 500 μm x 500 μm [138, 246, 264].

6.4.1. Serial Sectioning Method

The procedure involved controlled mechanical polishing to remove surface layer for serial sectioning, and EBSD characterization of the two sections (before and after sectioning) at the same region of interest (ROI). Vickers hardness indentation was used to make 4 fiducial marks near the ROI. The surface pile-up around the hardness indentation mark was removed by

polishing, before the ROI characterization of first section. Parallel alignment of specimen reference edge with the 70° pre-tilt SEM specimen holder was visually ensured during mounting, and re-checked from SE imaging before EBSD scans.

The indentation marks were additionally utilized for correcting small rotational misalignment of ROI between the two sections. The diagonal length of the indentation mark made by the diamond square pyramidal indenter (with dihedral angle of about 136º) and the depth of the indentation are related by, a constant factor of 7 [138, 139]. The size of indentation mark measured before and after serial sectioning was used to calculate the separation distance between the two sections.

6.4.2. Fine Alignment of EBSD Scans

The sample mounting procedure and indentation marks were used to assist in tracking the same ROI. The grain boundary trace of planar boundaries is expected to be parallel straight lines in the two sections, whereas misalignment of ROI would lead to systematic angular deviation of trace lines. A small lateral shift and minor rotational deviations grain boundary traces between the two ROI were visually recognized from the superposed EBSD maps, and was accordingly offset by re-rotating the second image.

The individual grains were identified based on 10° misorientation angle criterion for boundary [234, 265], and the 'grain average' routine was employed to calculate the mean Euler angles and the grain center locations for the two scans. If the ROI location was exact for the two scans, then there should be no net average displacement of grain centers (averaged for many grains). Grain centers of many grains were considered to calculate the small average (horizontal and vertical) shift of ROI, and corrected accordingly to achieve proper alignment of ROI scan data for further analysis.

6.4.3. Estimation of Five Macroscopic Parameters

The microtexture data of aligned ROIs was analyzed for extracting the five macroscopic parameters of a grain boundary namely the lattice misorientation (ω, $\hat{r}$) across the boundary, and grain boundary plane inclination angles of β, γ. Figure 6.10 illustrates the schematic of superimposed grain boundary trace of two consecutive sections with reference to X-Y axis of the rectangular ROI. The X-Y reference frame of the viewed image is in-plane rotated by 180º compared to X′-Y′ reference frame of EBSD scan. The Euler angle data ϕ_1 was thus offset by 180º ($\phi_1 \rightarrow 180^\circ + \phi_1$), and the Euler angle set (ϕ_1, Φ, ϕ_2) now describes the orientation with respect to X-Y-Z axis, utilized for further calculation/analysis.

Grain Boundary Misorientation

The homophase grain boundaries are planar defects separating the two grains having same crystal structure but different crystallographic orientation. If grain boundary is a flat plane, then it would intersect the sample plane sections at straight lines, and MN, OP in Fig. 6.10 denote the parallel set of grain boundary trace for the two sections. A single section is sufficient to evaluate the three parameters associated with crystal misorientation, and the azimuth angle (γ) of grain boundary trace. The quaternion corresponding to the Euler angles (ϕ_1, Φ, ϕ_2) (with respect to sample reference frame) of crystal orientation is given by the following expression [238] (Section 2.5),

$$\boldsymbol{q} = \cos\left(\frac{\Phi}{2}\right)\cos\left(\frac{\phi_1+\phi_2}{2}\right) + \sin\left(\frac{\Phi}{2}\right)\cos\left(\frac{\phi_1-\phi_2}{2}\right) + \sin\left(\frac{\Phi}{2}\right)\sin\left(\frac{\phi_1-\phi_2}{2}\right) + \cos\left(\frac{\Phi}{2}\right)\sin\left(\frac{\phi_1+\phi_2}{2}\right) \quad (6.4)$$

The relative orientation of grain 2 with respect to grain 1 can be calculated using quaternion equation (Eq. 6.4). The effect of rotation symmetry of cubic crystal has been considered to determine true misorientation angle $\omega = \theta_{min}$, and the associated rotation axis ($\hat{r}$) [237].

$$q(\theta,\hat{n}) = \cos\left(\frac{\theta}{2}\right) + \sin\left(\frac{\theta}{2}\right)(n_1 i + n_2 j + n_3 k) = q_1^{-1} \bullet q_2 \bullet qs \quad (6.5)$$

Grain Boundary Plane

The fourth parameter of grain boundary plane is the azimuth angle γ made by grain boundary trace with the positive Y-axis of reference frame [237]. A single (first) section was considered to determine the trace angle γ with the +Y, within the range [-90º, 90º] (Fig. 6.10). The alignment corrected second section image was superposed on the first, and the end co-ordinates of line segments MN/OP was used to evaluate their midpoint and common slope. The parallel line equation could then be stated for estimating the separation distance D between them.

The fifth parameter polar angle β (that denotes the angle between specimen surface normal and grain boundary interface normal) is calculated as,

$$\beta = tan^{-1}\left(\frac{d}{D}\right) \quad (6.6)$$

where, d is separation distance between the two sections (measured along z-axis) and D is the apparent distance between boundary line segments in the overlapped image. The value of 'd' is calculated to be one seventh of the fraction of the difference between the diagonal length of square indent marks of two sections [139]. By convention, grain 1 and grain 2 are assigned to be on left and right side of boundary respectively (Fig. 6.10), and grain boundary plane normal is taken to be pointing outwards from the surface of grain 1. Thus, when the grain boundary segment tends to move towards grain 2 in the second section, then the $\hat{g}$ vector would have positive z term, and the d value is taken to be positive in Eq. 6.6 to obtain angle β in [0,π/2] range. On the other hand, when grain boundary segments shift to left side (towards grain 1) in the second section, then the separation distance between line segment is considered to be negative, and Eq. 6.6 gives β in [π/2,π] range.

The normal vector of the grain boundary plane ($\hat{g}$) in terms of angles γ and β can be given as,

$$\hat{g} = cos\gamma sin\beta\hat{\imath} + sin\gamma sin\beta\hat{\jmath} + cos\beta\hat{k} \tag{6.7}$$

The above ĝ vector represents the orientation of interface plane normal with respect to sample coordinate axis. Let ĝ′ denote the same plane normal vector but described with reference to crystal axis of the grain. If quaternion expressions of g and g′ are considered as ĝ and ĝ′ respectively (with imaginary terms equal to resolved components of vector & their real part set as zero), then it is possible to determine ĝ′ through the quaternion relation,

$$\hat{g}' = q^{-1} \bullet \hat{g} \bullet q \tag{6.8}$$

where, q denotes the corresponding orientation quaternion of either of the two grains. The above equation can be used to calculate the two interface plane normal on either side of the grain boundary, and it gives the crystallographic description of the meeting planes at the interface. If {h1 k1 l1} and {h2 k2 l2} denote the crystallographic character of the meeting planes, then the interplanar angle (ψ) between them is,

$$\psi = \cos^{-1}\left(\frac{h_1h_2 + k_1k_2 + l_1l_2}{\sqrt{\left(h_1^2 + k_1^2 + l_1^2\right)\left(h_2^2 + k_2^2 + l_2^2\right)}}\right) \tag{6.9}$$

Grain boundaries can be classified as twist or tilt boundary, based on the angle between rotation axis n̂ and the interface plane normal ĝ [266]. Rotation axis (r̂) corresponding to misorientation angle (ω) has been specifically considered for determining the angle it makes with ĝ [267]. Rotation axis r deduced from Eq. 6.5 is with respect to crystal axis of grain-1 and the equivalent vector r^* in terms of sample co-ordinate axis can be found through the associated quaternion relation,

$$\hat{r}' = q_1 \bullet r \bullet q_1^{-1} \tag{6.8}$$

where, r̂ and r̂* are the equivalent quaternion expressions of the vector r and r*. Then, the angle between rotation axis and grain boundary normal is,

$$\xi = cos^{-1}[\hat{r}^* \bullet \hat{g}] \tag{6.11}$$

The ξ value close to 0° and 90° denotes twist and tilt nature of boundary respectively, whereas intermediate values signify a mixed character [266].

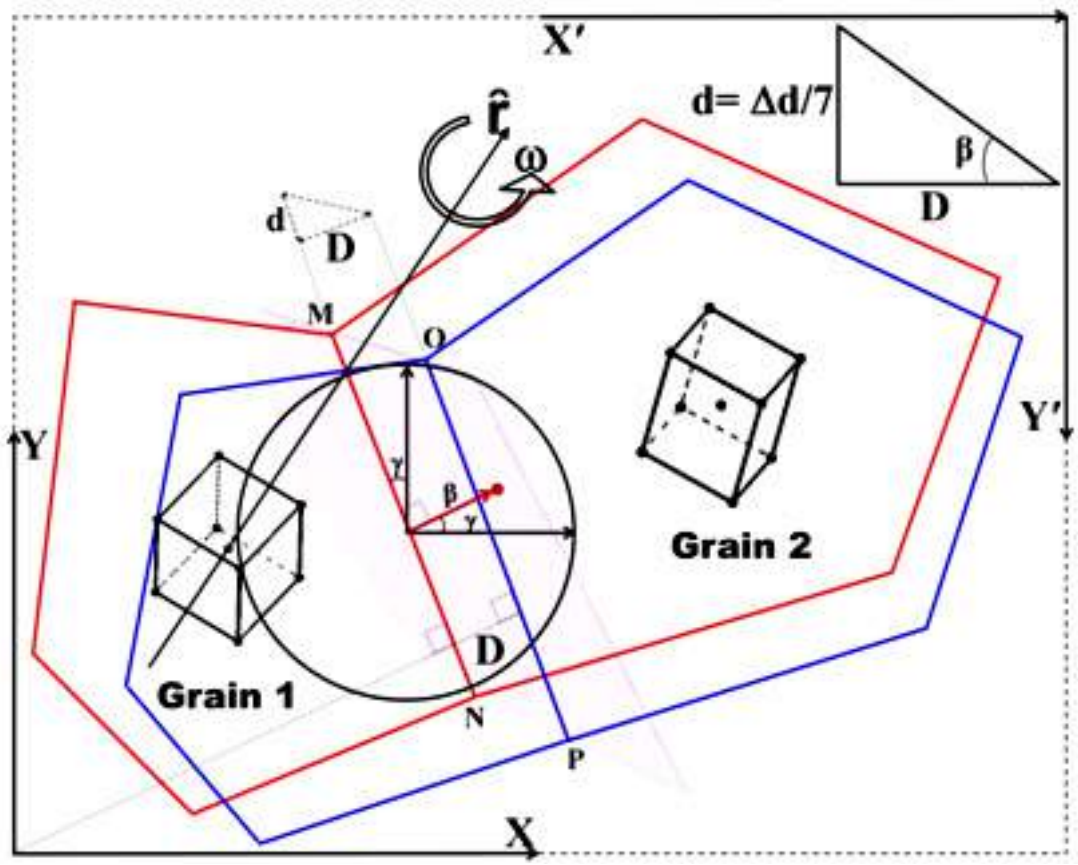

Fig. 6.10. *Schematic representation of two cross section segments used for calculation of polar angle (β) and azimuth angle (γ) where D and d are the distance between grain boundary segment and distance between two sections respectively.*

The 5-Parameter grain boundary description established using the above procedure has been applied to annealed BCC 9Cr-1Mo and FCC SS304HCu steels, the details of which are explained in the following sections.

6.5. 5-Parameter Grain Boundary Determination in Annealed BCC Ferrite Structure of 9Cr-1Mo Steel

6.5.1. Reconstruction of EBSD Maps

The EBSD scans were repeated on a selected ROI, with a serial sectioning separation distance of 8 μm for both IA and IAA specimens referred in section 6.2.

(a)

(b)

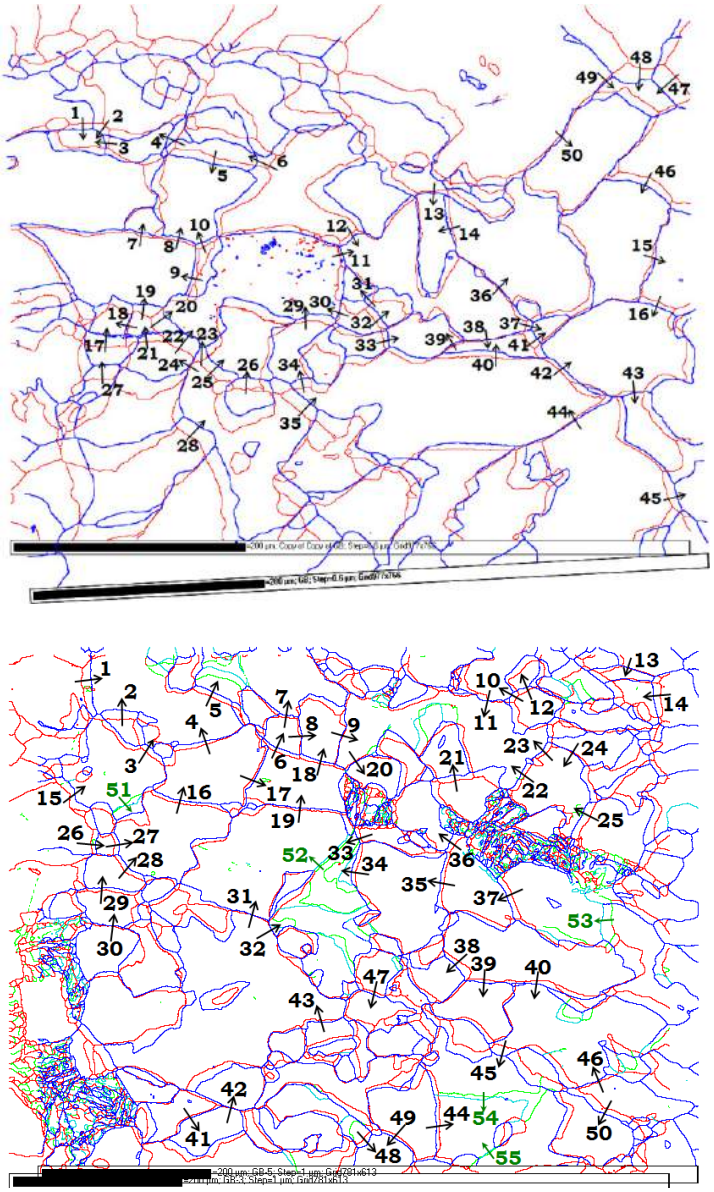

Fig. 6.11. *Superposed maps of the grain boundary (red-Section A and blue-Section B) in 9Cr-1Mo steel after (a) IA and (b) IAA treatment. Numbers indicating the analyzed boundary sequence and the alter direction of boundary trace is represented by the arrow marks (black-high angle boundaries and green-sub grain boundaries).*

EBSD maps of the ROI before and after serial sectioning (denoted by Section A and Section B respectively) are correlated by translation and rotation operations to reconstruct the stacking of images. Figure 6.11 illustrates the overlapped image of grain boundary maps of two sections. From the stacked image, it is possible to correlate the grain structure and track the shift of grain boundary contours. The grain boundary contours were approximated as straight line segments for the calculation, though most grain boundaries contours were not straight. Around 50 high angle boundaries with nearly straight contours were selected, and considered for detailed GBCD analysis (Fig. 6.11). In addition, five more boundaries of low-angle type were also analyzed in the IAA specimen.

6.5.2. Rotation Axis Distribution

The distribution of common axis of rotation ($\hat{r}$) pertaining to minimum misorientation angle ω is shown in Fig. 6.12. A large scatter in the distribution was observed for both the specimens. The average distribution of the three macroscopic parameters (ω, $\hat{r}$) of grain boundaries is inferred to be random. Similar results of random distribution have also been reported in fully equiaxed ferritic microstructures [268, 269].

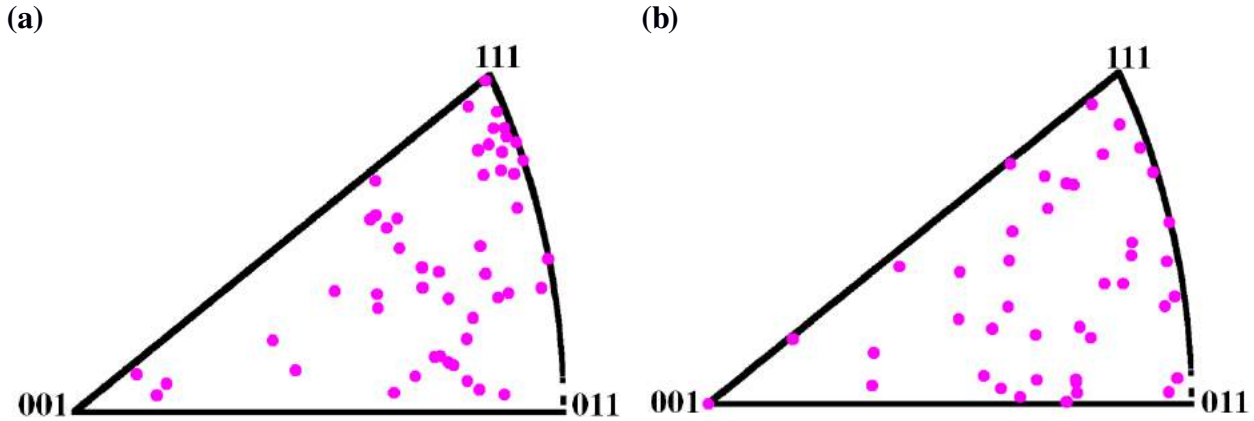

Fig 6.12. *Distribution of the misorientation axis of the adjacent crystallites of the analyzed boundary trace in 9Cr-1Mo steel after (a) IA and (b) IAA treatments.*

6.5.3. Grain Boundary Plane Normal Distribution

The inclination of the grain boundary planes with respect to specimen axis is in principle unrelated to crystal orientations, and it is possible to evaluate its morphology by serial sectioning technique. In an ideal isotropic and equiaxed grain structure, the azimuth angle would be distributed uniformly within $[-\pi/2,\pi/2]$, whereas the polar angle (β) distribution is expected to follow sine function [139]. Using Eq. 6.6, the grain boundary normal vector was studied in terms of the two crystal axis, and the crystallographic description of the meeting planes was determined.

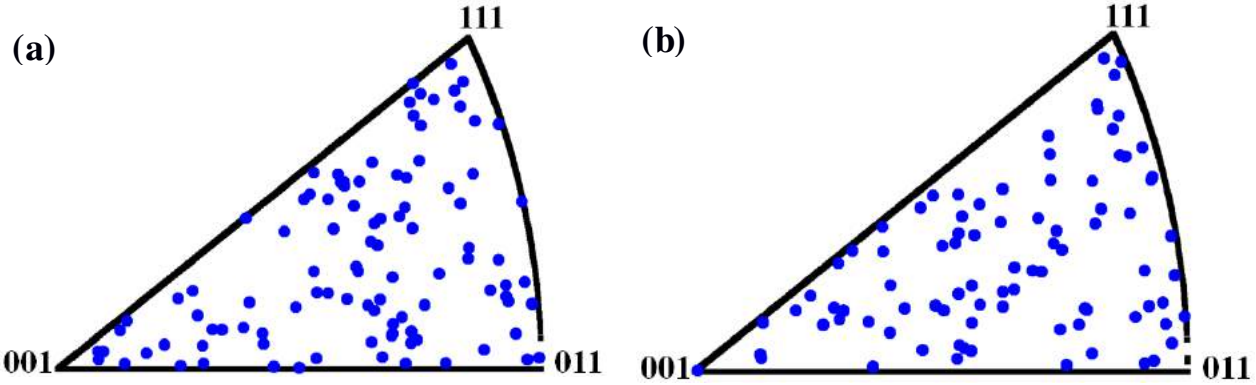

Fig 6.13. *Crystallographic depiction of grain boundary interfaces through their normal in 9Cr-1Mo steel after (a) IA and (b) IAA treatment.*

Considering the crystal rotational symmetries, the distribution of interface plane normal vector in the unit triangle is illustrated in Fig. 6.13. It again shows a random distribution of poles, with no specific tendency for clustering in both IA and IAA specimens. In literature, grain boundary planes of simple (h k l) types have been reported to preferentially form [244, 270], whereas in this study, such a trend was not observed.

6.5.4. Character of meeting (h k l) Planes

In a given crystal system, the interplanar spacing depends on the (h k l) indices of the plane. If the meeting planes are crystallographically of similar type, then they share a common

[h k l] direction as a rotation axis, although it may not necessarily correspond to misorientation angle. The coherent CSL boundaries, in fact have the same type of (h k l) as the grain boundary, with rotation axis of 180º. The experimental GBCD data set after various annealing treatments in 9Cr-1Mo ferritic steel is analyzed to check the above possibility of meeting of similar type of crystallographic planes at the grain boundary plane. The interplanar angle (ψ) between (h_1 k_1 l_1) and (h_2 k_2 l_2) meeting planes was calculated, and its normalized frequency distribution is shown in Fig. 6.14. The observed distribution has been assessed by comparison with the theoretical distribution estimated from a computer generated random pair of crystallographic planes. Around a million cycles of random data set were considered, and the resultant theoretical plot is shown in Fig. 6.14. The angle between crystallographic planes determined from the experimental data set was comparable to that derived from the theoretical data set. Thus, the meeting planes of adjoining grains were mostly uncorrelated, and no tendency for commonality of (h k l) planes was observed.

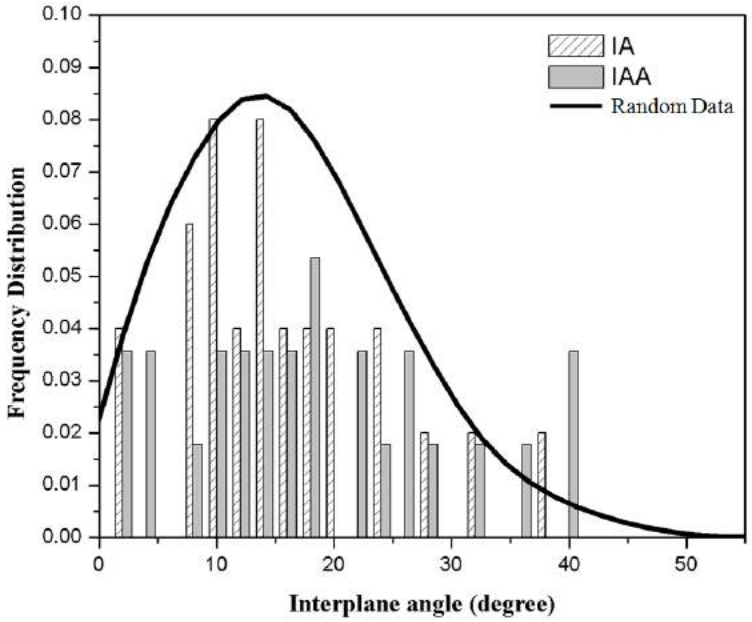

Fig. 6.14. *Interplanar angle distribution for experimental and random generated data set in 9Cr-1Mo ferritic steel.*

6.5.5. Analysis of Tilt or Twist character of Boundaries

The tilt or twist boundary is reported to be associated with the mechanism of energy minimization of the grain boundary plane orientations [237]. The macroscopic parameters of boundary planes can be used in identifying these boundaries [237, 244, 267]. The grain boundary plane normal and the rotation axis with respect to sample coordinate axis were calculated using Eq. 6.10. The angle (ξ) between them was also calculated [Eq. 6.11] and its distribution is illustrated in Fig. 6.15. for 9Cr-1Mo ferritic steel after various annealing treatments. It exhibits a random behavior, without any clustering around 0° or 90°, which indicates that there is no appreciable preference for occurrence of pure tilt or twist type boundary.

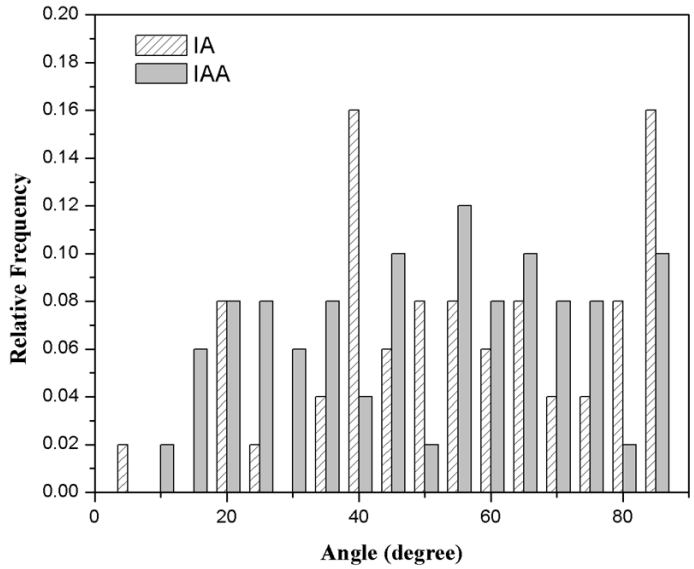

Fig 6.15. *Misorientation angle distribution of rotation axis with the grain boundary plane normal in 9Cr-1Mo ferritic steel.*

It is well known that the driving force for grain growth process is minimization of grain boundary surface energy. In the present system, the energy minimization after extended annealing is attributed primarily to reduction in grain boundary area, and persisting low-angle boundaries, as other GBCD attributes were found to be unaltered during grain growth process.

Also, the five additional low-angle boundaries analyzed in IAA [Fig. 6.11(b)] did not show any discernable preference for rotation axis $\hat{r}$, crystallographic planes or the tilt/twist character.

6.5.6. Comparison with Theoretical Set

The GBCD attributes depicted in Fig. 6.5, 6.14 and 6.15, are, and comparison with theoretical random distribution aided in qualitative assessment. Further, the observed data could be statistically compared with the theoretical distribution. The average (μ) and standard deviation (σ) are two important parametric quantities for assessing the distribution, and can be used to quantitatively gauge the similarity with theoretical distribution [271]. The GB parameters γ, β, ω, and $\hat{r}$ (through its angle with [001]/[101]/[111]) and GBCD attribute of ψ were statistically analyzed to determine μ and σ for both the experimental data sets, while the comparable values of the theoretical random distribution was determined using known formulae or from computer generated random data set. Table 6.5 lists the average and standard deviation values of various attributes of grain boundary parameters determined by serial sectioning method for the two specimens, and their comparison with the theoretical random case. Within the limited statistics of 50 grain boundaries assessed in the present study, the GBCD of both IA and IAA samples largely exhibited a random trend only.

Table 6.5. Comparison of grain boundary attributes of experimental and theoretical data set

Particulars		Average (μ)			Std. dev. (σ)		
		IA	IAA	Theoretical	IA	IAA	Theoretical
γ		91	92	90	46	48	52.3
β		87	81	90	41	32	39
ω		38	39	41	11	14	11
RA	001	39	37	35	10	13	11
	101	21	22	22	7	13	9
	111	21	27	26	11	14	11
ψ		17	19	15	9	14	8
ξ		58	53	57	21	23	22

6.6. 5-Parameter Grain Boundary Analysis in Annealed 304HCu Austenitic Steel

A systematic study has been carried out to address the effect of cold rolling and annealing on the grain boundary character distribution (GBCD) in FCC system on SS304HCu using EBSD analysis. The effect of annealing treatment on the Σ3 network and its interaction (Σ9 and Σ27) has been assessed, and for the first time, the change in boundary structure has been traced during annealing by combination of serial sectioning and EBSD analysis. To establish the micromechanism associated with the energy minimization during annealing in the present steel, a 5-parameter description of Σ3 interface plane is provided and quantitative deviation from the coherent (1 1 1) plane is also assessed.

6.6.1. Coherency of Σ3 Boundary

Although Σ3 type twin boundary is the commonly observed CSL boundary in FCC alloys, the coherency of boundary plane has a crucial impact on the properties of the boundary like GB Energy. It is reported [272] that there exist 41 types of Σ3 boundary sets possibly with the same misorientation between the grains and different boundary planes. In such cases, the low index boundary plane with misorientation angle 60º about (1 1 1) is coherent and contributes to the lowest boundary energy [272, 273]. The deviation angle from exact Σ3 is derived from the orientation data of specimens annealed at different temperatures after cold deformation using a single parameter (deviation angle from exact (1 1 1) plane). The fraction of Σ3 type boundaries for a given deviation angle within the Brandon criteria (8.66º) [127] is plotted in Fig. 6.16. The twin boundary shows a deviation of 2º from the ideal case. However, in the steel annealed at 1073 K (800 ºC, treatment 'R'), a secondary peak is observed, which indicates a high amount of incoherent boundaries with deviation >2º. Further, the high-angle random boundaries exhibit higher mobility and contribute substantially to the kinetics of growth of coarse grains (with

annihilation of fine grains) leading to a microstructure with low energy boundary configurations such as the low angle and coherent Σ3 boundaries. The linear grain boundaries in the steel annealed at 1373 and 1573 K (treatments 1100 ℃, 'A' and 1300 ℃, 'EA' respectively) indirectly indicate a considerable minimization of surface energy. The steel annealed at 1573 K (1300 ℃, 'EA'), which shows the highest amount of Σ3 boundaries, is chosen as a representative case to confirm the coherency of Σ3 interface plane from its grain boundary trace. Figure 6.17 shows the superimposed (1 1 1) pole figure on a twin boundary taken from a subset of Fig. 6.8(c). In the (111) pole figure of grains (across Σ3), a typical (111) pole concentration is always observed, and the superposed boundary trace line was found to be 90° apart. Measurements based on single section indirectly suggested that these boundaries are coherent (111) type. However, the interface of twin plane marked in Fig. 6.17 is observed not to be of (1 1 1) type, which explains for the faster advancement of twin boundaries along the length than along the width, in the steel annealed at 1373 K (A and A1) as reported in the previous section (Section 6.3.4).

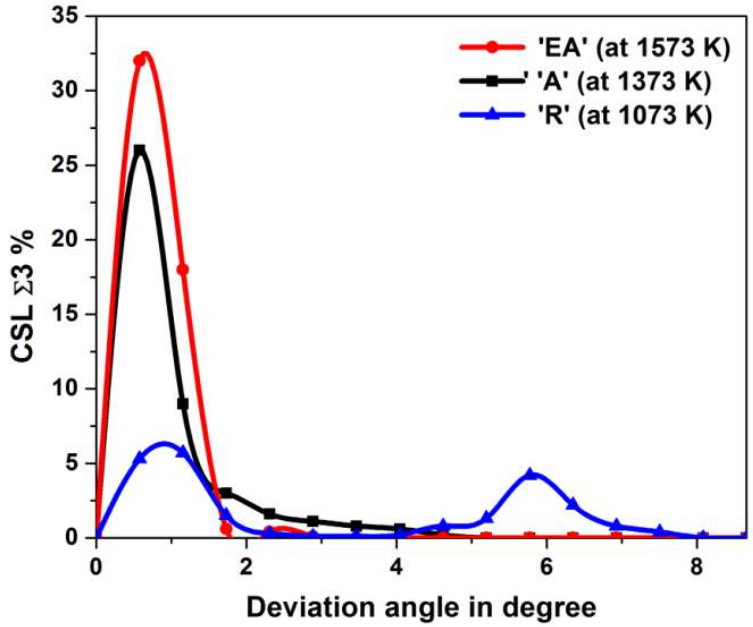

Fig. 6.16. *Amount of Σ3 type boundaries and deviation angle from ideal Σ3 type boundary in SS304HCu at different annealing temperatures.*

It is also observed from Fig. 6.17 that incoherent Σ9 and Σ27 boundaries formed due to interaction of Σ3 boundaries. Hence this trace analysis from a single section unambiguously predicts the boundary plane [255]; however, characteristics of the grain boundary interface such as dihedral angle is required to classify the boundary as twist or tilt type.

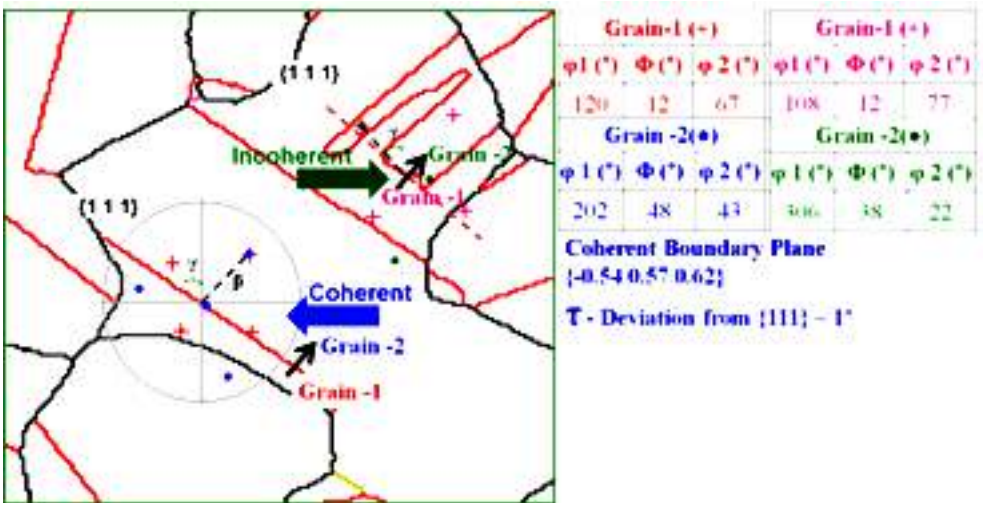

Fig. 6.17. *Σ3 boundary plane analysis from EBSD single planar section and {1 1 1} pole figure shows the pole distribution of the grains separated by the trace line in extended annealed SS304HCu. (γ and β represents the azimuth (trace of the boundary with +Y-axis), and polar (common pole concentration to the center of pole figure) angles respectively.)*

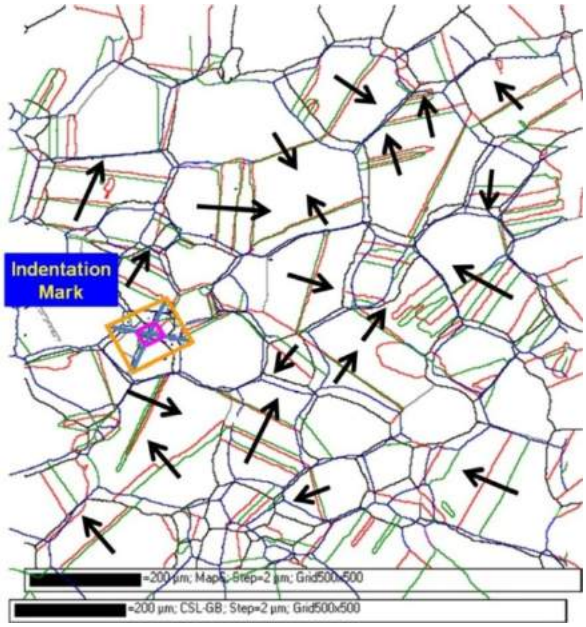

Fig. 6.18. *Superposed maps of the grain boundary in extended annealed SS304HCu and the analyzed Σ3 boundary (red and green line for section 1 and 2 respectively) traces indicated by arrow marks.*

Hence, the serial sectioning method with overlapping EBSD maps from successive sections (Fig. 6.18) was utilized to determine the grain boundary inclination angle and arrive at the 5-parameter description of the grain boundary. About 40 randomly chosen straight contours of the Σ3 type were analyzed to evaluate the small deviation angle from exact coherency. The Σ3 grain boundary plane was found to be very close to the expected coherent (1 1 1) plane with an average deviation of about ~6° (Fig. 6.19(a)).

The angle between grain boundary plane normal and the rotation axis with respect to sample co-ordinate axis (ξ) was calculated using Eq. 6.11. The frequency distribution of ξ is illustrated in Fig. 6.19(b). The distribution shows higher frequency at low angles, which suggests the formation of clear tilt type boundaries in this system. Hence persistence of low energy Σ3 boundaries is primarily responsible for formation of planar boundaries with low energy configurations during annealing, while GBCD of other $\Sigma 3^n$ CSL boundaries was found to be altered during the grain growth process.

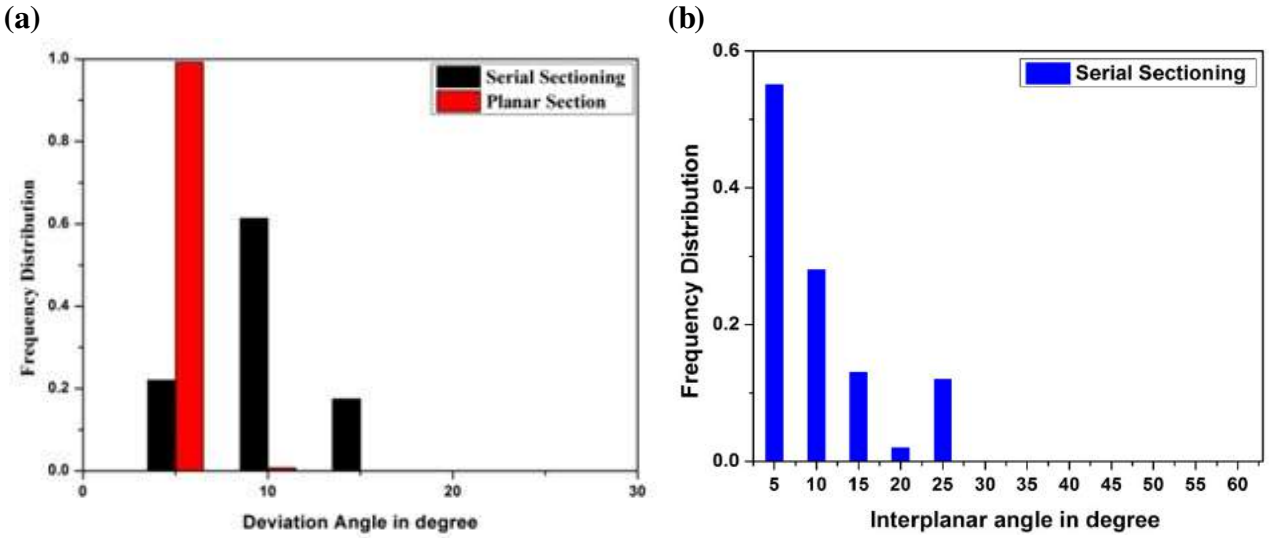

Fig. 6.19. *Distribution of (a) deviation angle of grain boundary plane from exact (1 1 1), and (b) angle between adjoining crystallographic planes at the boundary of extended annealed SS304HCu.*

From the above studies, it can therefore be concluded that the energy minimization after extended annealing is attributed primarily due to reduction in grain boundary area, and persistence of few low angle boundaries in ferritic steels, as other GBCD attributes was found to be unaltered in grain growth process. However, in SS304HCu, the energy minimization after extended annealing is primarily due to increase in fraction of low energy Σ3 boundaries, though interaction of other $\Sigma 3^n$ CSL boundaries was found to be altered during the grain growth process. In addition, the formation of tilt boundaries with low energy configuration during annealing process is also evident in SS 304HCu.

6.7. Summary

A systematic EBSD study has been carried out to understand the influence of SFE on grain boundary characteristics in ferritic (9Cr1Mo and 18Cr ODS) and austenitic (304HCu) steels using planar and serial sectioning methods. The salient results are as follows:

- Hot extruded 18Cr ODS ferritic steel possessed higher amount of CSL boundaries in both ED and TD due to deformation induced twinning, which decreased after recrystallization and annealing treatments, despite the persistence of low angle boundaries. A similar behaviour in 9Cr-1Mo ferritic steel after annealing suggests that grain size or presence of dispersoids does not influence the GBCD, while the high SFE of BCC matrix is responsible for the low amount of CSL boundaries during diffusional transformation.
- In 304HCu austenitic stainless steel, cold working followed by recrystallization treatment resulted in a higher fraction of annealing twins belonging to Σ3 type boundaries than ideal random case due to low SFE of FCC matrix, However, grain growth at higher annealing temperatures stabilized the low-energy Σ3 over Σ9 and Σ27 boundaries.

- Microtexture data in conjunction with serial sectioning method has been used to arrive at five macroscopic parameters of grain boundary for ferrite grains in 9Cr-1Mo steel and austenite grains in 304HCu austenitic stainless steel. This method enabled the direct measurement of all five grain boundary parameters of large grained microstructures, in contrast to stereological analysis or FIB-SEM technique.
- Based on the 5-parameter grain boundary distributions, it is proved that diffusion assisted phase transformations in 9Cr-1Mo steel lead to random type of boundaries, unlike displacive mode of phase transformation. The GBCD of high angle boundaries is found to be unaffected by the extended annealing treatment, while the length fraction of low angle boundaries increased. The grain boundary plane (h k l) distribution is demonstrated to be random, with no correlation between adjacent grains. Statistical analysis showed that experimentally evaluated distribution of GBCD follows the theoretical trend.
- In 304HCu austenitic stainless steel, the interaction of Σ3-Σ3 planes led to the formation of incoherent Σ9. However, the probability of formation of Σ3 and Σ27a/ Σ27b boundaries due to interaction of Σ3-Σ9 boundaries is predicted to be 0.4 and 0.6 respectively. The rate of migration of Σ9 and Σ27 interface is found to be higher during annealing in comparison to Σ3 type. In addition, the meeting planes at Σ3 boundary was calculated and found to be close to <1 1 1> type (with an average deviation of ~6°), and it suggested a preference for symmetrical tilt alignment of Σ3 boundaries.

Summary

7.1. Summary

The thesis entitled "STUDY OF MICROSTRUCTURE AND MICROTEXTURE DURING THERMO-MECHANICAL PROCESSING IN ADVANCED STEELS USING EXPERIMENTAL AND COMPUTATIONAL METHODS" presents the results of a study carried out to identify the cause and strategies to mitigate anisotropy in 18Cr Oxide Dispersion Strengthened (ODS) ferritic steel through optimization of consolidation methods and thermo-mechanical treatment. The major themes addressed in the thesis are,

- Optimization of consolidation conditions for 18% Cr ODS ferritic steel through evaluation of density, microstructure, microtexture and mechanical properties.
- Design of an effective/optimal thermo-mechanical treatment (TMT) to achieve an ultra-fine (~ 0.5 μm) equiaxed grain microstructure and randomization of texture during unidirectional cold rolling in a hot extruded 18Cr ODS ferritic steel starting with an initial elongated grain structure and a predominant α-fiber texture.
- Identification of optimum high temperature workability region during high temperature processing of 18Cr ODS ferritic steel.
- Description of grain boundary character distribution (GBCD) in 18Cr ODS ferritic steel during consolidation, deformation and annealing processes. Further, demonstration of a methodology is derived for describing the interface boundaries based on five parameter characterization in conventional ferritic and austenitic steels with high and low stacking fault energy (SFE) respectively.

The background information and existing literature on the research topic have been reviewed briefly in Chapter 1, and the relevant experimental design and procedures adopted in the study have been described in Chapter 2. The results and analysis of the four major themes have been presented in Chapters 3-6, and the salient findings are summarized below together with a brief outline of the scope of future work:

7.2. Optimization of Consolidation Conditions for 18Cr Oxide Dispersion Strengthened Ferritic Steel

- A maximum relative density of 92% was achieved by Cold isostatic pressing (CIP) followed by sintering at 1423 K (1150 ℃).
- Hot isostatic pressing (HIP) of CIP product at the optimized temperature of 1423 K (1150 ℃), and pressure of 200MPa yielded 97% of theoretical density.
- Spark plasma sintering (SPS) yielded a density of ~ 99%. Sintering temperature of 1323 K (1050 ℃) was found to be optimum based on kinetics of densification and resultant microstructure and microtexture;
- The steel consolidated by hot extrusion (HE) process showed higher densification (relative density >99%) and an anisotropic grain size distribution between the axial and transverse direction of extrusion while the overall grain diameters varied within 0.8 - 2 μm.

The relative density, morphology, average grain size, texture intensity and mechanical properties of the ODS steel consolidated by different methods were compared. Despite the morphological anisotropy, also reflected in the mechanical properties, the hot extruded steel showed a higher creep strength and rupture life in contrast to other processes, which highlights

density as the crucial parameter that governs the high temperature mechanical properties. Although HE is considered optimum, SPS is also a viable alternate process for consolidation of 18Cr ODS ferritic steel.

7.3. Design of Deformation and Annealing for Minimizing Anisotropy

Strategies for effective heat treatments have been identified to reduce/suppress anisotropy during unidirectional cold rolling of hot extruded 18Cr ODS ferritic steel. The following conclusions have been drawn from this study:

- The characteristic elongated grains structure obtained by hot extrusion is retained during further deformation by 50% cold working along the extrusion direction. Significant growth of recrystallized grains with aspect ratio upto 8 takes place during high temperature annealing at 1423 K (1150 °C) of the cold worked specimen, which is attributed to grain boundary migration associated with strain energy reduction.
- Distinct recovery and recrystallization temperature domains have been identified as 1350 and 1420 K (1077 and 1147 °C) and employing a heating rate of 7 $Kmin^{-1}$ by DSC thermograms. The start and finish temperatures of both recovery and recrystallization increased with heating rate, though it saturated at higher heating rates, due to lower rate of stored energy release.
- The higher incubation period in recovery region reduces the stored energy prior to recrystallization and is found to be beneficial to attain a fine grain size distribution, thus reducing the microstructural anisotropy in the steel and is achieved by the designed two step heat treatment.

- The fraction of ultrafine equiaxed grains increases progressively with repetitive deformation and two step heat treatments and the distinct bimodal grain size distribution become uniform, with a concomitant tendency towards texture randomization.
- The dislocation density is retained or enhanced despite the repeated two step heat treatment due to the pinning effect of dispersoids, which is also responsible for the progressive reduction in average grain size.

Although fraction of ultrafine equiaxed grains increases progressively with repetitive deformation and two step treatments, tube drawing process at high temperature (>973 K (700 °C)) and low strain rate ($<10^{-3}$ s^{-1}) is considered as an alternate fabrication process to achieve fine equiaxed grain structure in 18Cr ODS ferritic steel.

7.4. High Temperature Processing Domain of 18Cr Oxide Dispersion Strengthened Ferritic Steel

The optimum high temperature workability region has been identified for 18Cr ODS ferritic steel based on dynamic material model approach based on hot isothermal compression tests in a wide range of temperatures (1323 to 1473 K (1050 to 1200 °C)) and strain rates (0.01 to 10 s^{-1}). The following important conclusions are drawn from this investigation:

- Limited safe processing domains have been identified based on the influence of strain rate sensitivity (m), efficiency of power dissipation (η) and instability parameter ($\xi(\dot{\varepsilon})$) parameters.
- Instability domains have been identified in the temperature range of 1323 to 1423 K (1050 to 1150 °C) with strain rate > 0.1 s^{-1}.
- Based on superior workability region with peak efficiency up to 30-35%, the most favourable processing parameters have been optimized in the temperature range of 1350

to 1450 K (1077 to 1177 ℃) with a strain rate of 0.01 s^{-1} and 1473 K (1200 ℃) with a strain rate 0.1 s^{-1}.

- Low efficiency parameter in the safe processing domain resulted in shearing and retention of deformed microstructure at high (10 s^{-1}) and low strain rates (0.01 s^{-1}) respectively and a coarse grain size distribution is attributed to coalescence of grains during deformation.
- High temperature compression minimizes the <1 1 0> fiber texture; <1 1 1> fiber texture is obtained with strain rate <0.01 s^{-1} at 1373 K (1100 ℃) and a strain rate of <0.1 s^{-1} at 1473 K (1200 ℃).
- Intensity of γ-fiber is found to be dependent on the direction of applied stress. A higher reduction ratio of diameter to thickness favours the preferential growth of γ-fibers in contrast to α-fiber during high temperature processing of tube.

7.5. 5-parameter Interface Boundaries Characterization

A systematic EBSD study has been carried out to understand the influence of SFE on grain boundary characteristics in ferritic (9Cr1Mo and 18Cr ODS) and austenitic (304HCu) steels using planar and serial sectioning methods. The salient results are as follows:

- Hot extruded 18Cr ODS ferritic steel possessed higher amount of CSL boundaries in both ED and TD due to deformation induced twinning, which decreased after recrystallization and annealing treatments, despite the persistence of low angle boundaries. A similar behaviour in 9Cr-1Mo ferritic steel after annealing suggests that grain size or presence of dispersoids does not influence the GBCD, while the high SFE of BCC matrix is responsible for the low amount of CSL boundaries during diffusional transformation.
- In 304HCu austenitic stainless steel, cold working followed by recrystallization treatment resulted in a higher fraction of annealing twins belonging to Σ3 type boundaries than

ideal random case due to low SFE of FCC matrix, However, grain growth at higher annealing temperatures stabilized the low-energy Σ3 over Σ9 and Σ27 boundaries.

- Microtexture data in conjunction with serial sectioning method has been used to arrive at five macroscopic parameters of grain boundary for ferrite grains in 9Cr-1Mo steel and austenite grains in 304HCu austenitic stainless steel. This method enabled the direct measurement of all five grain boundary parameters of large grained microstructures, in contrast to stereological analysis or FIB-SEM technique.
- Based on the 5-parameter grain boundary distributions, it is proved that the diffusion assisted phase transformations in 9Cr-1Mo steel lead to random type of boundaries, unlike the displacive mode of phase transformation. The GBCD of high angle boundaries is found to be unaffected by the extended annealing treatment, while the length fraction of low angle boundaries increased. The grain boundary plane (h k l) distribution is demonstrated to be random, with no correlation between adjacent grains. Statistical analysis showed that experimentally evaluated distribution of GBCD follows the theoretical trend.
- In 304HCu austenitic stainless steel, the interaction of Σ3-Σ3 planes lead to the formation of incoherent Σ9; however, the probability of formation of Σ3 and Σ27a/ Σ27b boundaries due to interaction of Σ3-Σ9 boundaries is predicted to be 0.4 and 0.6 respectively. The rate of migration of Σ9 and Σ27 interface is found to be higher during annealing in comparison to Σ3 type. In addition, the meeting planes at Σ3 boundary was calculated and found to be close to <1 1 1> type (with an average deviation of ~6º), and it suggested a preference for symmetrical tilt alignment of Σ3 boundaries.

7.6. Scope for Future Work

A few areas related to the theme of the present thesis have been identified for future directions of work and are summarized below:

- Majority of the structural components involve plasticity as either macro scale phenomena during their production or micro scale phenomena in service. Understanding the micromechanisms of plasticity for a large class of materials has huge potential in technological applications. In this aspect, crystal plasticity based on crystallographic texture would help to model the material deformation behavior with good accuracy and need to be studied for these engineering materials.
- Finite element modeling in conjunction with EBSD analysis to address heterogeneous plasticity during deformation, and response of polycrystal aggregates in BCC system.
- FIB-SEM-EBSD in recent times has emerged as a powerful technique and useful tool for characterizing 3-D microstructure of polycrystalline materials. Serial sectioning technique also provides a more realistic evaluation of grain boundaries. This would enable a better understanding of the resistance of grain-boundary to slip transfer during deformation in a variety of materials.
- Precipitation of brittle [such as σ] phases during service temperature in high Cr ferritic steels are important issues to be studied for obtaining good performance of the steel components. Design of heat treatments to promote σ phase formation and the role of grain boundary plane on the evolution and kinetics of σ phase can be studied.

References:

1. K. L. Murty, I. Charit, J. Nucl. Mater. 383 (2008) 189.
2. Aitkaliyeva, L. He, H. Wen, B. Miller, X. M. Bai, T. Allen, Structural Materials for Generation IV Nuclear Reactors (2017) 253.
3. G. R. Odette, Scripta Mater. 143 (2018) 142.
4. C. Capdevila, M. Serrano, M. Campos, Mater. Sci. Tech. 30 (13) (2014) 1655.
5. V. de Castro, E. A. Marquis, S. L. Perez, R. Pareja, M. L. Jenkins, Acta Mater. 59 (2011) 3927.
6. R. L. Klueh, Int. Mater. Rev. 50 (2005) 287.
7. R. L. Klueh, N. Hashimoto, P. J. Maziasz, Scitpta Mater. 53 (2005) 275.
8. G. Junceda, M. H. Mayoral, M. Serrano, Mater. Sci. Engg. A 556 (2012) 696.
9. S. Ukai, M. Harada, H. Okada, M. Inoue, S. Nomura, S. Shikakura, K. Asabe, T. Nishida, M. Fujiwara, J. Nucl. Mater. 204 (1993) 65.
10. S. Ukai, S. Mizuta, T. Yoshitake, T. Okuda, M. Fujiwara, S. Hagi, T. Kobayashi, J. Nucl. Mater. 283 (2000) 702.
11. M. J. Alinger, G. R. Odette, G. E. Lucas, J. Nucl. Mater. 307 (2002) 484.
12. B. Raj, M. Vijayalakshmi, P. R. V. Rao, K. B. S. Rao, MRS Bulletin 33 (4) (2008) 327.
13. P. Rodriguez, What Happens to Structural Materials in a Nuclear Reactor: The Fascinating Radiation Enhanced Materials Science (2005).
14. B. Raj, M. Vijayalakshmi, P. R. V. Rao, K. B. S. Rao, MRS Bulletin 32 (3) (2009) 271.
15. D. O. Northwood, Materials & Design 6 (2) (1985) 58.
16. Z. Guo, N. Saunders, J. P. Schillè, A. P. Miodownik, Mater. Sci. Engg. A 499 (2009) 7.
17. S. Ukai, M. Fujiwara, J. Nucl. Mater. 307 (2002) 749.

18. S. Ukai, T. Nishida, H. Okada, J. Nucl. Sci. Tech. 34 (1997) 256.

19. S. Wurster, R. Pippan, Scitpta Mater. 60 (2009) 1083.

20. A. Kimura, J. Nucl. Mater. 417 (1–3) (2011) 176.

21. G. R. Odette, Annual Review of Materials Research 38 (1) (2008) 471.

22. G. R. Odette, Scripta Mater. 143 (2018) 142.

23. G. R. Odette, J. Miner. (JOM) 66 (12) (2014) 2427.

24. C. Cayron, E. Rath, I. Chu, S. Launois, J. Nucl. Mater. 335 (2004) 83.

25. H. Hadraba, B. Fournier, L. Stratil, J. Malaplate, A. L. Rouffie, P. Wident, L. Ziolek, J. L. Béchade, J. Nucl. Mater. 411 (2011) 112.

26. T. Okuda, Proc. Symp. Sponsored by the "TMS Powder Metallurgy Committee", Indiana, (1989) 195.

27. P. Olier, J. Malaplate, M. H. Mathon, D. Nunes, D. Hamon, L. Toualbi, Y. de Carlan, L. Chaffron, J. Nucl. Mater. 428 (2012) 40.

28. J. J. Huet, Powder Metall. 10 (20) (1967) 208.

29. A. de Bremaecker, J. Nucl. Mater. 428(1) (2012) 13.

30. S. Ukai, J. Nucl. Mater. 258 (1998) 1745.

31. T. Narita, S. Ukai, T. Kaito, S. Ohtsuka, T. Kobayashi, J. Nucl. Sci. Tech. 41(10) (2004) 1008.

32. S. Ukai, T. Narita, A. Alamo, P. Parmentier, J. Nucl. Mater. 329 (2004) 356.

33. P. Fauvet, F. Balbaud, R. Robin, Q. T. Tran, A. Mugnier, D. Espinoux, J. Nucl. Mater. 375 (2008) 52.

34. J. H. Lee, R. Kasada, A. Kimura, T. Okuda, M. Inoue, S. Ukai, S. Ohnuki, T. Fujisawa, F. Abe, J. Nucl. Mater. 417 (2011) 180.

35. A. D. Siwy, T. E. Clark, A. T. Motta, J. Nucl. Mater. 392 (2009) 280.

36. Z. Oksiuta, J. Mater. Sci. 48 (2013) 4801.

37. R. Novotny, P. Janik, S. Penttila, P. Hahner, J. Macak, J. Siegl, P. Hauˇsild, J. Supercritical Fluids 81 (2013) 147.

38. Y. de Carlan, J. L. Bechade, P. Dubuisson, J. L. Seran, P. Billot, A. Bougault, T. Cozzika, S. Doriot, D. Hamon, J. Henry, M. Ratti, N. Lochet, D. Nunes, P. Olier, T. Leblond, M. H. Mathon, J. Nucl. Mater. 386 (2009) 430.

39. Alamo, V. Lambard, X. Averty, M.H. Mathon, J. Nucl. Mater. 329 (2004) 333.

40. J. J. Huet, L. Coheur, L. de Wilde, J. Gedopt, W. Hendrix, W. Vandermeulen, Proceedings of Topical Conference for "Ferritic Steels for Use in Nuclear Energy Technologies", (Eds.) J. W. Davis, D. J. Michel, The Metallurgical Society of AIME, Warrendale (1984) 329.

41. T. Okuda, S. Nomura, S. Shikakura, K. Asabe, S. Tanoue, M. Fujiwara, in: A.H. Clauter, J. J. de Barbadillo (Eds.), Solid State Powder Processing, The Minerals, Metals and Materials Society (1990) 195.

42. Alamo, H. Regle, J. L. Bechade, Novel Powder Processing: Advances in Powder Metallurgy and Particulate Materials, Metal Powder Industries Federation 7 (1992) 169.

43. S. Ukai, M. Harada, H. Okada, M. Inoue, S. Nomura, S. Shikakura, T. Nishida, M. Fujiwara, K. Asabe, J. Nucl. Mater. 204 (1993) 74.

44. S. Ukai, T. Kaito, M. Seki, A. Mayorshin, O. V. Shishalov, J. Nucl. Sci. Tech. 42(1) (2005) 109.

45. M. Orai, Japan Atomic Energy Agency (JAEA) Research (2006) 042.

46. J. Bottcher, S. Ukai, M. Inoue, J. Nucl. Sci. Tech. 138(3) (2002) 238.

47. R. Kasada, S. G. Lee, J. Isselin, J. H. Lee, T. Omura, A. Kimura, T. Okuda, M. Inoue, S. Ukai, S. Ohnuki, T. Fujisawa, F. Abe, J. Nucl. Mater. 417 (2011) 180.

48. A. Kimura, R. Kasada, N. Iwata, H. Kishimoto, "Development of Al added high Cr ODS steels" for FGM 2012 IOP Publishing J. of Physics: Conference Series 419 (2013) 012036.

49. D. T. Hoelzer, J. Bentley, M. A. Sokolov, M. K. Miller, G. R. Odette, M. J. Alinger, J. Nucl. Mater. 367 (2007) 166.

50. G. R. Odette, M. J. Alinger, B. D. Wirth, Acta Mater. 57 (2008) 392.

51. D. K. Mukhopadhyay, F. H. Froes, D. S. Gelles, J. Nucl. Mater. 258 (1998) 1209.

52. M. Steckmeyer, M. Praud, B. Fournier, J. Malaplate, J. Garnier, J. L. Béchade, I. Tournié, A. Tancray, A. Bougault, P. Bonnaillie, J. Nucl. Mater. 405 (2010) 95.

53. B. Fournier, A. Steckmeyer, A. L. Rouffie, J. Malaplate, J. Garnier, M. Ratti, P. Wident, L. Ziolek, I. Tournie, V. Rabeau, J. M. Gentzbittel, T. Kruml, I. Kubena, J. Nucl. Mater. 430 (2012) 142.

54. M. Praud, F. Mompiou, J. Malaplate, D. Caillard, J. Garnier, A. Steckmeyer, B. Fournier, J. Nucl. Mater. 428 (2012) 90.

55. L. L. Hsiung, Microscopy: Science, Technology, Applications and Education, (2010) 1811.

56. S. Li , Z. Zhou, M. Wang, H. Hu, L. Zou, G. Zhang, L. Zhang, Journal of Physics: Conference Series 419 (2013) 12.

57. D. T. Hoelzer, B. A. Pint, I. G. Wright, J. Nucl. Mater. 283 (2000) 1306.

58. Z. Száraz, G. Török, V. Kršjak, P. Hähner, J. Nucl. Mater. 435 (2013) 56.

59. J. Rösler, Metal. Mater. Trans. A 23 (5) (1992) 1521.

60. P. K. Mirchandani, Aluminum base composite alloy. Google Patents (1992).

61. J. W. Martin, Micromechanisms in Particle Hardened Alloys, Cambridge University Press (1980).

62. F. Bergner, Metal. Mater. Trans. A 47 (11) (2016) 5313.

63. L. M. Callejo, I. Kaltzakorta, Mater. Sci. Tech. 30 (2014) 1658.

64. S. J. Zinkle, J. L. Boutard, H. Tanigawa, L. Tan, M. Rieth, G. R. Odette, D. T. Hoelzer, R. Lindau, A. Kimura, Nucl. Fusion 57 (2017) 092005.

65. Z. Shi, F. Han, Materials & Design 66 (2015) 304.

66. H. Springer, Materials & Design 111 (2016) 60.

67. T. Boegelein, Acta Mater. 87 (2015) 201.

68. H. Xu, Z. Lu, D. Wang, C. Liu, Nucl. Mater. Energy 7 (2016) 1.

69. M. Brocq, B. Radiguet, J. M. L. Breton, F. Cuvilly, P. Pareige, F. Legendre, Acta Mater. 58 (2010) 1806.

70. P. K. Parida, A Dasgupta, K. Jayasankar, M. Kamruddin, S. Saroja, J. Nucl. Mater. 441 (2013) 331.

71. C. Suryanarayana, Mechanical Alloying And Milling. Taylor & Francis (2004).

72. A. Y. Badmos, Some Properties of Mechanically Alloyed Oxide Dispersion Strengthened Metals. University of Cambridge, Cambridge (1997).

73. T. K. Kim, S. Noh, S. H. Kang, J. J. Park, H. J. Jin, M. K. Lee, J. Jang, C. K. Rhee, Nucl. Engg. Tech. 48 (2) (2016) 572.

74. S. Ukai, S. Ohtsuka, T. Kaito, Y. de Carlan, J. Ribis, J. Malaplate, Structural Materials for Generation IV Nuclear Reactors, Ch. 10, Elsevier (2017).

75. M. J. Alinger, G. R. Odette, D. T. Hoelzer, Acta Mater. 57 (2009) 392.

76. M. J. Alinger, G. R. Odette, D. T. Hoelzer, J. Nucl. Mater. 329 (2004) 382.

77. N. J. Cunningham, Y. Wu, D. Klingensmith, G. R. Odette, Mater. Sci. Engg. A 613 (2014) 296.

78. T. S. Chou, Mater. Sci. Engg. A 223 (1997) 78.

79. T. S. Chou, H. K. D. H. Bhadesia, Mater. Sci. Tech. 9 (1993) 890.

80. W. J. Yang, G. R. Odette, T. Yamamoto, P. Miao, M. J. Alinger, J. Nucl. Mater. 367 (2007) 616.

81. P. Unifantowicza, Z. Oksiutab, P. Olierc, Y. de Carlanc, N. Baluc, Fusion Engg. & Design 86 (2011) 2413.

82. M. A. Auger, V. de Castro, T. Leguey, A. Muñoz, R. Pareja, J. Nucl. Mater. 436 (2013) 68.

83. M. H. Mayoral, M. Serrano, E. On˜orbe1, A. G. Junceda, I. Hilger, B. Kloeden, T. Weissgaerber, A. Ulbricht, F. Bergner, B. Radiguet, A. Etienne, A. Shariq, C. D. Dewhurst, Mater. Sci. Tech. 30 (2014) 1669.

84. N. G. Rodriguez, M. Campos, J. M. Torralba, M. H. Berger, Y. Bienvenu, Mater. Sci. Tech. 30 (2014) 13.

85. H. Hadraba, B. Kazimierzak, L. Stratil, I. Dlouhy, J. Nucl. Mater. 417 (2011) 241.

86. M. Serrano, A. G. Junceda, R. Herna´ndez, M. H. Mayoral, Mater. Sci. Technol. 30 (2014) 1664.

87. S. Ukai, W. Izawa, N. Oono, S. Hayashi, Y. Kohno, S. Ohtsuka, T. Kaito, Mater. Sci. Technol. 30 (2014) 1709.

88. M. M. Baloch, Ph.D. Thesis, University of Cambridge (1989).

89. T. Narita, S. Ukai, B. Leng, S. Ohtsuka, T. Kaito, J. Nucl. Sci. Tech. 50 (3) (2013) 314.

90. S. Ukai, S. Mizuta, M. Fujiwara, T. Okuda, T. Kobayashi, J. Nucl. Sci. Tech. 39 (2002) 778.

91. N. Okuda, J. Nucl. Mater. 386 (2009) 974.

92. M. A. Auger, T. Leguey, V. de Castro, M. A. Monge, R. Pareja, Mater. Sci. Tech. 30 (2014) 13.

93. C. Capdevila, M. K. Miller, K. F. Russell, J. Chaoa, J. L. G. Carrasco, Mater. Sci. Engg. A 490 (2008) 277.

94. C. L. Chen, G. J. Tatlock, A. R. Jones, J. Microscopy 233 (2009) 474.

95. R. Gao, T. Zhang, H. L. Ding, Y. Jiang, X. P. Wang, Q. F. Fang, C. S. Liu, J. Nucl. Mater. 465 (2015) 268.

96. I. Hilger, X. Boulnat, J. Hoffmann, C. Testani, F. Bergner, Y. de Carlan, F. Ferraro, A. Ulbricht, J. Nucl. Mater. (2015) 1.

97. M. Serrano, M. H. Mayoral, A. G. Junceda, J. Nucl. Mater. 428 (2012) 103.

98. A. Chauhan, F. Bergner, A. Etienne, J. Aktaa, Y. de Carlan, C. Heintze, D. Litvinov, M. H. Mayoral, E. Onorbe, B. Radiguet, A. Ulbricht, J. Nucl. Mater. 495 (2017) 6.

99. C. Suryanarayana, Prog. Mater. Sci.46 (1-2) (2001) 1.

100. C. Suryanarayana, V. V. Boldyrev, Mater. Sci. Engg. A (2001) 151.

101. B. Murty, S. Ranganathan, Inter. Mater. Reviews 43 (3) (1998) 101.

102. E. Abdulkadir, J. Engg. Env. Sci. 26 (2002) 377.

103. M. Basaran, T. Z. Kattamis, R. Mehrabian, M. C. Flemings, Metal. Mater. Trans. A 4 (1973) 2429.

104. L. Gao, J. S. Hong, H. Miyamoto, S. D. D. L. Torre, J. Eur. Ceram. Soc. 20 (2000) 2149.

105. Z. A. Munir, U. A. Tamburini, J. Mater. Sci. 41 (2006) 763.

106. W. B. Zhou, B. C. Mei, J. Q. Zhu, X. L. Hong, Mater. Lett. 59 (2005) 131.

107. K. Rajan, T. Shanmugasundaram, V. S. Sarma, B. S. Murty, Metal. Mater. Trans. A 44 (2013) 4037.

108. K. M. Reddy, N. Kumar, B. Basu, Scripta Mater. 63 (2010) 585.

109. R. Chaim, Mater. Sci. Eng. A 443 (2007) 25.

110. G. B. Granger, C. Guizard, Acta Mater. 55 (2007) 3493.

111. T. Nagae, M. Yokota, M. Nose, S. Tomida, T. Kamiya, S. Saji, Metal. Mater. Trans. A 43 (2002) 1390.

112. U. A. Tamburini, J. E. Garay, Z. A. Munir, Mater. Sci. Eng. A 407 (2005) 24.

113. J. Hu, Grain Growth by Ordered Coalescence of Nanocrystals in Ceramics. Stockholm University, Stockholm, Sweden (2013).

114. M. Suárez, A. Fernández, J. L. Menéndez, R. Torrecillas, U. Kessel, J. Hennicke, R. Kirchner, T. Kessel, Challengs and opportunities for spark plasma sintering: a key technology for a new generation of materials, in: B.Ertuğ (Eds.), Sintering Application, In tech, Rijeka, (2013) 319.

115. M. Nagini, R. Vijay, K. V. Rajulapati, K. B. Rao, M. Ramakrishna, A.V. Reddy, G. Sundararajan, Metal. Mater. Trans. A 47 (2016) 4197.

116. F. B. Pickering, Meter. Tech. 7 (1980) 409.

117. S. Mandal, A. Bhaduri, V.S. Sarma, J. Mater. Sci. 46 (2011) 275.

118. M. K. Dash, T. Karthikeyan, R. Mythili, V. Vijayanand, S. Saroja, Metal. Mater. Trans. A 48 (2017) 4883.

119. V. Randle, Mater. Character. 60 (2009) 913.

120. S. Kikuchi, Jap. J. Phys. 5 (1928) 83.

121. M. N. Alam, M. Blackman, D. W. Pashley, Proc. Roy. Soc. 222 (1954) 224.

122. J. A. Venables, C. J. Harland, Philos. Mag. 27 (1972) 1193.

123. V. Randle, M. Caul, Mater. Sci. Tech. 12 (1996) 844.

124. T. Karthikeyan, M. K. Dash, S. Saroja, M. Vijayalakshmi, Micron 68 (2015) 77.

125. M. Calcagnotto, D. Ponge, E. Demir, D. Raabe, Mater. Sci. Eng. A 527 (2010) 2738.

126. J. Kumar, A. K. Singh, S. G. S. Raman, V. Kumar, Metal. Mater. Trans. A 48 (2017) 648.

127. D. G. Brandon, Acta Metall. 14 (1996) 1479.

128. M. Kamaya, Mater. Character. 60 (2009) 125.

129. M. Kamaya, Mater. Character. 66 (2012) 56.

130. J. J. Sidor, K. Verbeken, E. Gomes, J. Schneider, P. R. Calvillo, L. A. I. Kestens, Mater. Character. 71 (2012) 49.

131. S. Raju, B. J. Ganesh, A. K. Rai, R. Mythili, S. Saroja, B. Raj, J. Nucl. Mater. 405 (2010) 59.

132. S. Raju, B. Jeyaganesh, A. Banerjee, E. Mohandas, Mater. Sci. Eng. A 465 (2007) 29.

133. N. Ogasawara, N. Chiba, X. Chen, J. Mater. Res. 20(8) (2005) 2225.

134. Y. Li, E. Onodera, A. Chiba, Metal. Mater. Trans. A 51 (2010) 1210.

135. D. Samantaray, S. Mandal, A. K. Bhaduri, Mater. Sci. Eng. A 528 (2011) 5204.

136. ASTM E8/E8M-11, Standard test methods for tension testing of metallic material, ASTM international.

137. ASTM E139-11, Standard test methods for conducting creep, creep rupture and stress rupture tests of metallic materials, ASTM International.

138. F. X. Lin, A. Godfray, D. J. Jensen, G. Winther, Mater. Character. 61 (2010) 1203.

139. G. E. Dieter: Mechanical Metallurgy (2nd Eds.), McGraw-Hill Book Co., New York, NY, (1988).

140. M. Humbert, N. Gey, J. Muller, C. Esling, J. Appl. Cryst. (1996) 622.

141. J. H. Cho, A. D. Rollett, K. H. Oh, Metal. Mater. Trans. A 36 (2005) 3427.

142. http://www.sentesoftware.co.uk/jmatpro.aspx

143. http://www.thermocalc.com/start/

144. Y. Chang, D. Huang, C. Jia, C. Ge, D. Liang, P. Gao, Powder Metallurgy 57 (2) (2013) 103.

145. R. M. German, Powder metallurgy of iron and steels (John Wiley and Sons Ltd., New York, United States (1998).

146. D. S. Wilkinson, M. F. Ashby, Acta Metall. 23 (1975) 1277.

147. V. Mamedov, Powder Metal. 45 (4) (2002) 322.

148. P. Barnier, C. Brodhag, F. Thevenot, J. Mater. Sci. 21 (1986) 2547.

149. X. Wei, C. Back, O. Izhvanov, O. L. Khasanov, C. D. Haines, E. A. Olevsky, J. Nucl. Mater. 8 (2015) 6043.

150. H. J. Frost, M. F. Ashby, Deformation-Mechanism Maps: The Plasticity and Creep of Metals and Ceramics, Pergamon Press, New York, NY, (1982) 20.

151. M. Demuynck, J. Erauwa, O. V. Biest, F. Delannay, F. Cambier, J. Euro. Ceram. Soc. 32 (2012) 1957.

152. N. Chawla, X. Deng, Mater. Sci. Engg. A 390 (2005) 98.

153. D. Liu, Y. Xiong, T. D. Topping, Y. Zhou, C. Haines, J. Paras, D. Martin, D. Kapoor, J. M. Schoenung, E. J. Lavernia, Metal. Mater. Trans. A 43 (2012) 340.

154. S. Diouf, A. Molinari, Powder Tech. 221 (2012) 220.

155. Z. Trzaska, G. Bonnefont, G. Fantozzi, J. P. Monchoux, Acta Mater. 135 (2017) 1.

156. G. Ji, T. Grosdidier, N. Bozzolo, S. Launois, Intermetallics 15 (2007) 108.

157. E. Nes, N. Ryum, O. Hunderi, Acta Metall. 33 (1985) 11.

158. J. R. Groza, A. Zavaliangos, Mater. Sci. Engg. A 287 (2000) 171.

159. T. Furukawa, S. Ohtsuka, M. Inoue, T. Okuda, F. Abe, S. Ohnuki, T. Fujisawa, A. Kimura, Super ODS steels r&d for fuel cladding of next generation nuclear systems, in: International Congress on Advanced Nuclear Power Plants (ICAPP), Tokyo, Japan, (2009) 9221.

160. G. Pillonia, E. Quadrini, S. Spigarelli, Mater. Sci. Engg. A 279 (2000) 52.

161. T. Shresthaa, M. Basirat, I. Charit, G. P. Potirniche, K. K. Rink ,U. Sahaym, J. Nucl. Mater. 423 (2012) 110.

162. T. Sakthivel, S. P. Selvi, K. Laha, Mater. Sci. Engg. A 640 (2015) 61.

163. F. J. Humphreys, M. Hatherly, Recrystallization and related annealing phenomena, Elsevier, UK (1995).

164. P. Brozzo, G. Buzzichelli, Scripta Mater. 10 (1976) 235.

165. H. R. Wenk, P. V. Houtte, Rep. Prog. Phys. 67 (2004) 1367.

166. H. Okada, S. Ukai, M. Inoue, J. Nucl. Sci. Tech. 33 (1996) 936.

167. S. Ukai, T. Nishida, H. Okada, T. Okuda, M. Fujiwara, K. Asabe, J. Nucl. Sci. Tech. 34 (1997) 256.

168. S. Li, I. J. Beyerlein, A. M. Bourke, Mater. Sci. Eng. A 394 (2005) 66.

169. M. Ratti, Thèse de doctorat, Institut Polytechnique de Grenoble, (2009).

170. M. Rout, R. Ranjan, S. K. Pala, S. B. Singh, Mater. Sci. Engg. A 711 (2018) 378.

171. J. Baczynski, J. J. Jonas, Acta Mater. 44 (1996) 4273.

172. R. Przeliorz, J. Piątkowski, Archives of Foundry Engg. 10 (2010) 135.

173. J. G. Sevillano, E. Aernoudt, Mater. Sci. Engg. A 86 (1987) 35.

174. H. Tripathy, S. Raju, A. K. Rai, T. Jayakumar, Steel Research Int. 84 (2013) 1046.

175. F. J. Humphreys, Acta Mater. 45 (10) (1997) 4231.

176. R. D. Doherty, D. A. Hughes, F. J. Humphreys, J. J. Jonas, D. Juul Jensen, M. E. Kassner, W. E. King, T. R. McNelly, H. J. McQueen, A. D. Rollet, Mater. Sci. Engg. A 238 (1997) 219.

177. M. J. Luton, R. A. Petkovic, J. J. Jonas, Acta Metall. 28 (1980) 729.

178. D. J. Jensen, Mater. Sci. Tech. 21 (2005) 1365.

179. E. J. Mittemeijer, J. Mater. Sci. 27 (1992) 3977.

180. H. Altenbach, S. Kruch, Advanced materials modeling for structures, Springer, Berlin, Heidelberg (2013).

181. G. Mohapatra, S. S. Sahay, Mater. Sci. Tech. 27 (2011) 377.

182. A. Alamo, V. Lambard, X. Averty, M. H. Mathon, J. Nucl. Mater. 333 (2004) 329.

183. P. R. Rios, Acta Metall. 35 (12) (1987) 2805.

184. M. K. Dash, T. Karthikeyan, S. Saroja, Adv. Matt. Proc. 2 (5) (2017) 304.

185. S. D. Yadav, M. Tahawy, S. Kalácska, M. Dománková, D. C. Yubero, C. Poletti, Mater. Character. 134 (2017) 387.

186. A. Sarkara, M. K. Dash, A. Nageshaa, A. Dasguptaa, R. Sandhyaa, M. Okazakib, Mater. Sci. Engg. A 723 (2018) 229.

187. H. Yana, H. Bib, X. Li, Z. Xua, J. Matt. Pross. Tech. 209 (2009) 2627.

188. H. T. Liu, Z. Y. Liu, Y. Q. Qiu, G. M. Cao, C. G. Li, G. D. Wang, Mater. Character. 60 (2009) 79.

189. J. Isselin, R. Kasada, A. Kimura, T. Okuda, M. Inoue, S. Ukai, S. Ohnuki, T. Fujisawa, F. Abe, J. Nucl. Mater. 417 (2011) 185.

190. A. Steckmeyer, V. H. Rodrigo, J. M. Gentzbittel, V. Rabeau, B. Fournier, J. Nucl. Mater. 426 (2012) 182.

191. D. P. Field, Mater. Sci. Engg. A 190 (1995) 241.

192. D. P. Field, P. B. Trivedi, S. I. Wright, M. Kumar, Ultramicroscopy 103 (2005) 33.

193. S. Birosca, F. Di Gioacchino, S. Stekovic, M. Hardy, Acta Mater. 74 (2014) 110.

194. F. D. Gioacchino, J. Q. Fonseca, Intern. J. Plasticity 74 (2015) 92.

195. D. A. Hughes, Acta Metall. 41 (1993) 1421.

196. Y. Sugino, S. Ukai, B. Leng, Q. Tang, S. Hayashi, T. Kaito, S. Ohtsuka, ISIJ International 51 (2011) 982.

197. T. Watanabe, Mater. Sci. Engg. A 166 (1993) 11.

198. B. Fournier. H. Hadraba, EDFA workshop, Garching, Stockholm (2009).

199. Z. Oksiuta, P. Mueller, P. Spatig, J. Nucl. Mater. 412 (2011) 221.

200. D. Samantaray, S. Mandal, C. Phaniraj, A. K. Bhaduri, Mater. Sci. Engg. A 528 (2011) 8565.

201. T. Seshacharyulu, S. C. Medeiros, W. G. Frazier, Y. V. R. K. Prasad, Mater. Sci. Engg. A 325 (2002) 112.

202. L. J. Huang, L. Geng, A. B. Li, X. P. Cui, H. Z. Li, G. S. Wang, Mater. Sci. Engg. A 505 (2009) 136.

203. S. Venugopal, S. L. Mannan, Y. V. R. K. Prasad, Mater. Lett. 15 (1992) 79.

204. S. Venugopal, S. L. Mannan, Y. V. R. K. Prasad, Mater. Sci. Engg. A 177 (1994)143.

205. P. V. Sivaprasad, S. Venugopal, V. Maduraimuthu, M. Vasudevan, S. L. Mannan, Y. V. R. K. Prasad, R. C. Chaturvedi, J. Mater. Process. Tech.132 (2003) 262.

206. P. V. Sivaprasad, S. L. Mannan, Y. V. R. K. Prasad, Mater. Sci. Technol. 20 (2004) 1545.

207. G. Zhang, Z. Zhou, H. Sun, L. Zou, M. Wang, S. Li, J. Nucl. Mater. 455 (2014) 139.

208. M. Wang, Z. Zhou, H. Sun, Mater. Sci. Engg. A 559 (2012) 287.

209. E. I. Poliakt, J. J. Jonass, Acta Mater. 44 (1996) 127.

210. A. Sarkar, A. Marchattiwar, J. K. Chakravartty, B. P. Kashyap, J. Nucl. Mater. 432 (2013) 9.

211. G. V. Prasad, M. Goerdeler, G. Gottstein, Mater. Sci. Engg. A 400 (2005) 231.

212. A. D. Rollett, U. F. Kocks, Solid State Phenom. 35 (36) (1993) 1.

213. E. I. Poliak, J. J. Jonas, ISIJ Int. 43 (2003) 684.

214. C. M. Sellars, W. J. Mc Tegart, Acta Metal. 14 (1966) 1136.

215. H. Li, D. Wei, J. Hua, Y. Li, S. Chen, Comput. Mater. Sci. 53 (2012) 425.

216. H. Takuda, H. Fujimoto, N. Hatta, J. Mater. Process. Tech. 80 (1998) 513.

217. A. Galiyev, R. Kaibyshev, T. Saikai, Mater. Sci. Forum 419 (2003) 509.

218. T. Sakai, J. J. Jonas, Acta Mater. 32 (1984) 189.

219. D. Samantaray, S. Mandal, A. K. Bhaduri, Mater. Design 31 (2010) 981.

220. H. Ziegler, I. N. Sneddon, R. Hill (Eds.), Progress in Solid Mechanics, Wiley, New York, (1965) 91.

221. I. Prigogine, Science 201 (1978) 777.

222. Y. Prasad, J. Mater. Eng. Perform. 12 (6) (2003) 638.

223. Y. Prasad, T. Seshacharyulu, Int. Mater. Rev. 43 (1998) 243.

224. L. Wang, Y. Fan, G. Huang, Chinese J. Nonferr. Mett. 14 (7) (2004) 1068.

225. M. G. Stout, J. S. Kallend, U. F. Kocks, M. A. Przystupa, A. D. Rollet, Proc. 8 Int. Conf. on Textures of Materials, J.S. Kallend and G. Gottstein (Eds), TMS, Warrendale (1988) 479.

226. B. Verlinden, J. Driver, I Samajdar, R. D. Doherty, Thermo-mechanical processing of metallic material, Elsevier, UK (2007).

227. B. Sander, D. Raabe, Mat. Sci. Engg. A 479 (2008) 236.

228. J. W. Hutchinson, Bounds and self-consistent estimates for creep of polycrystalline materials. Proc. R. Soc. Lond. Ser. A, Math. Phys. Sci. (1976) 101.

229. I. Karaman, H. Sehitoglu, H. J. Maier, Y. I. Chumlyakov, Acta. Mater. 49 (2001) 3919.

230. B. Clausen, T. Lorentzen, T. Leffers, Acta Mater. 46 (1998) 3087.

231. B. Bishoyi, M. K. Debta, S. K. Yadav, R. K. Sabat, S. K. Sahoo, Mate. Sci. Engg. A. 338 (2018) 012.

232. S. Li, I. J. Beyerlein, C. T. Necker, Acta Mater. 54 (2006) 1397.

233. V. Randle, J. Mater. Sci. 44 (2009) 4211.

234. F. J. Humphreys, J. Mater. Sci. 36 (2001) 3833.

235. V. Randle, Texture Microstr. 20 (1993) 231.

236. D. M. Saylor, A. Morawiec, G. S. Rohrer, Metal. Mater. Trans. A 35 (2004) 1981.

237. T. Karthikeyan, S. Saroja, J. Appl. Crystal. 46 (2013) 1221.

238. T. Watanabe, J. Mater. Sci. 46 (2011) 4095.

239. T. Karthikeyan, M. K. Dash, S. Saroja, M. Vijayalakshmi, Metal. Mater. Trans. A 14 (2013) 1673.

240. J. K. Mackenzie, Canadian J. Mathematics (2012) 229.

241. H. I. Aaronson, W. T. Reynolds, Scripta. Mater. 21 (1987) 1599.

242. J. K. Mackenzie, Acta Mater. 12 (1964) 223.

243. K. J. Kurzydlowski, B. Ralph, The quantitative description of the microstructure of materials, CRC Press, USA (1995).

244. V. Randle, Mater. Character. 34 (1995) 29.

245. J. M. Howe, H. I. Aaronson, J. P. Hirth, Acta Mater. 48 (2000) 3977.

246. A. C. Lewis, J. F. Bingert, D. J. Rowenhorst, A. Gupta, A. B. Geltmacher, G. Spanos, Mater. Sci. Engg. A 418 (2006) 15.

247. M. K. Dash, T. Karthikeyan, S. Saroja, Trans. Indian Inst. Met. 70 (2017) 133.

248. G. Owen, V. Randle, Scripta Mater. 55 (2006) 959.

249. D. L. Engelberg, F. J. Humphreys, T. J. Marrow, J. Microscopy 230 (2008) 435.

250. R. Fullman, J. Fisher, J. Appl. Phys. 22 (1951) 1350.

251. H. Gleiter, Acta. Metall.17 (1969) 1421.

252. M. A. Meyers, L. E. Murr, Acta Metall. 26 (1978) 951.

253. V. Randle, The role of the coincidence site lattice in grain boundary engineering, Maney Pub. (1996).

254. V. Gertsman, Acta Mater. 49 (2001) 1589.

255. V. Randle, Acta Metall. 52 (2004) 4067.

256. J. Wang, N. Li, O. Anderoglu, X. Zhang, A. Misra, J. Huang, J. Hirth, Acta. Metal. 58 (2010) 2262.

257. R. D. Doherty, Prog. Mater. Sci. 42 (1997) 39.

258. D. M. Saylor, B. S. Dasher, A. D. Rollett, G. S. Rohrer, Acta Mater. 52 (2004) 3649.

259. G. S. Rohrer, V. Randle, C. S. Kimb, Y. Hu, Acta Mater. 54 (2006) 4489.

260. S. T. Doweney, N. Bembridge, P. N. Kalu, H. M. Miller, G. S. Roherr, K. J. Han, J. Mater. Sci. 42 (2007) 9543.

261. M. A. Groeber, B. K. Haley, M. D. Uchic, D. M. Dimiduk, S. Ghosh, Mater. Character. 57 (2006) 259.

262. W. Xu, M. Ferry, N. Mateescu, J. M. Cairney, F. J. Humphreys, Mater. Character. 58 (2007) 961.

263. M. D. Uchic, M. A. Groeber, D. M. Dimiduka, J. P. Simmons, Scripta Mater. 55 (2006) 23.

264. M. D. Uchic, Computational Methods for Microstructure-Property Relationships (2001) 31.

265. F. J. Humphreys, I. Brough, J. Microscopy 195 (1999) 6.

266. A. Morawiec, Scripta Mater. 61 (2009) 438.

267. H. Beladi, G. S. Rohrer, Metal. Mater. Trans. A 44 (2013) 115.

268. R .C. Reed, H. K. D. H. Bhadeshia, Mater .Sci. Tech. 8 (1992) 421.

269. H. K. D. H. Bhadeshia, Prog. Mater. Sci. 28 (1985) 321.

270. H. K. D. H. Bhadeshia, Scripta Mater. 21 (1987) 1017.

271. R. A. Ricks, P. R. Howellt, Acta Mater. 31 (1983) 853.

272. V. Randle, Acta Metall. 46 (1998) 1459.

273. D. L. Olmsted, S. M. Foiles, E. A. Holm, Acta Metal. Mater. 57 (2009) 3694.